Smart piezoelectric devices for X-ray optics applications

By

Daniel Rodríguez Sanmartín

A thesis submitted to the

for the degree of

DOCTOR OF PHILOSOPHY

School of Metallurgy and Materials
Engineering and Physical Sciences
The University of Birmingham
April 2011

Smart piezoelectric devices for X-ray optics applications

Daniel Rodríguez Sanmartín

Abstract

The development of active/adaptive X-ray optics, utilising piezoelectric actuation for the focussing of X-rays in large and small scale applications, has been studied as part of the UK Smart X-Ray Optics (SXO) consortium.

For laboratory based X-ray sources utilising micro-structured optical arrays (MOAs), a novel spider actuator structure, compatible with silicon wet etching of MOAs, has been developed. Test spider samples (20×20×0.100mm) have been bent to a 6.5cm radius using unimorph actuators, and to a 3cm radius without failure. FEA models predicted that a 4.5cm radius and +/-3mrad tip/tilt control of the MOAs could be obtained using unimorph actuators with segmented electrodes and optimized thickness, which would enable a tandem pair MOA configuration of suitable focal length.

A first generation prototype Wolter I optic for future high resolution X-ray telescopes exhibited kinks in the reflecting surface corresponding to the gaps between piezoelectric devices. FEA models have been used to develop second generation prototypes in which the gaps have been minimised or filled. These incorporate a brick wall arrangement of curved unimorph piezoelectric actuators (32×75×0.190mm) with radii from 160-200mm +/-6mm, manufactured using a VPP technique and laser machining for precise dimensional control.

Keywords: Smart X-ray optics (SXO), micro-structured optical arrays (MOAs), Wolter I X-ray optics, piezoelectric actuators, finite element analysis (FEA), viscous plastic processing (VPP).

Dedication

Dedico esta tese a miña nai Concha (1945-1997)

por todos os sacrificios que fixo por mín. Ela foi lembrada en cada paso do camiño.

I dedicate this thesis to my late mother Concha (1945-1997)

for all the sacrifices she made for me. She was remembered every step of the way.

ACKNOWLEDGMENTS

I would like to thank my supervisor Prof. Tim Button and the postgraduate tutor Dr. Alison Davenport for entrusting me to carry out this work. I would also like to thank Dr Ady James for the management of the SXO consortium and for helping to create a working environment in the quarterly project meetings which fomented creative thinking and open discussions.

I should also thank here my fellow researchers at the University of Birmingham Dr Dou Zhang and Mr. Carl Meggs for developing the manufacturing methods for the piezoelectric actuators. Carl also designed the assembly and packaging structure for the spider MOA and helped develop the integration procedures for both optics. They both showed a great deal of commitment to make this project successful.

I would also like to thank all the other researchers and technical staff working for the SXO project, in particular Dr. Hongchang Wang, from UCL, together we developed a piezoelectric actuators control system; Dr. Charlie Feldman, from the University of Leicester, with whom I carried out experiments to optimize the integration procedure of the Large optic; Mr. Graham Willis, from MSSL, whom carried out the laser machining of the piezoelectric devices; and Dr. Camelia Dunare, from the University of Edinburgh, who developed the silicon etching process to manufacture the spider MOA devices.

I should also mention here the principal investigators of the SXO research groups, Dr. Peter Doel, University College London, Prof. Alan Michette, Kings College London, Prof. Richard Willingale, University of Leicester and Prof. Tom Stevenson, University of Edinburgh. Their questions and discussions helped me to acquire a wealth of technical knowledge and develop as a researcher.

I would also like to thank my sister Pili, my aunt Manuela and my cousin Fina for their support at difficult times during my physics degree when I acquired some of the skills and knowledge put in practice in this work. Finally, but most importantly, I thank Berrak Kanbir for her unwavering love and support during the past three years. She has been a source of inspiration.

CONTENTS

INDEX OF FIGURES

INDEX OF TABLES

NOMENCLATURE AND ACRONYMS

Acronyms:

AFC	Active fibre composite
AO	Adaptive optics
CAD	Computer aided design
CT	Computer tomography
DM	Deformable mirror
ESA	European space agency
EPSRC	The UK's Engineering and Physical Sciences Research Council
EXOSAT	The European space agency X-ray observatory
FEA	Finite element analysis
HEAO-2	The Einstein X-ray observatory
IXO	International X-ray observatory
JAXA	Japanese space agency
KB	Kirkpatrick-Baez X-ray optics
KCL	Kings College London
LAXRO	Large adaptive X-ray optic (first generation prototype)
LTP	Long trace profiler
MEMS	Micro electro-mechanical systems
MPB	Morphotropic phase boundary
MOA	Micro-structured optical arrays
MSSL	The mallard space science laboratory
NASA	National agency for space and aeronautics
NEMO	New elliptical X-ray optic (second generation prototype)

PCB	Printed circuit board
PLZT	Lead Lanthanum Zirconate Titanate
PZT	Lead Zirconate Titanate
PZT-5H	Commercially available Lead Zirconate Titanate powder
Q	X-ray tracing software developed at the University of Leicester
SEM	Scanning electron microscopy
SoI	Silicon on insulator wafer
SPIE	International society for optics and photonics
STFC	Science and technology facilities council
SXO	Smart X-ray optics
TMAH	Tretra methyl ammonium hydroxide (for the wet etching of silicon)
UCL	University College London
UoB	University of Birmingham
UoE	University of Edinburgh
UoL	University of Leicester
VPP	Viscous plastic processing

Device parameters:

α_b	Angle of the tip of a piezoelectric bimorph
a_i	Segmented electrodes in the level a of the wet-etched spider design.
b_i	Segmented electrodes in the level b of the wet-etched spider design.
c_i	Segmented electrodes in the level c of the wet-etched spider design.
c_1,c_2	Level c of actuation in the wet-etched spider design.
δ_b	z displacement of the tip of a piezoelectric bimorph
ΔL_{st}	Length increment on a stack actuator
D_{ZC}	z displacement measured over the length of the chip
D_{ZM}	z displacement measured over the length of the MOA

E_{max}, E_{min}	Maximum and minimum electric field
F_{st}	Force produce by a stack actuator
G_{Ch}	Channel pith on a MOA array
h_b	Thickness of a piezoelectric bimorph
K_{sp}	Elastic constant of an ideal spring
K_{st}	Elastic constant of a stack actuator
L_{afc}	Distance between electrodes on an active fibre composite
L_b	Length of a piezoelectric bimorph
L_{LO}	Length of the large optic
L_{MOA}	Length of the MOA array
L_{Si}	Length of the silicon chip
L_{PZT}	Length of the PZT actuators
L_{st}	Length of a stack actuator
N_{st}	Number of layer on a stack actuator
ROC	Radius of curvature
ROC_{Front}	Radius of curvature of the large optic on the X-ray source side
ROC_b	Radius of curvature of a piezoelectric bimorph
ROC_{Back}	Radius of curvature of the large optic on the detector side
ROC_{MOA}	Radius of curvature of an MOA array
T_{bl}	Thickness of the bonding layer
T_{MOA}	Thickness of a MOA array
T_{Ni}	Thickness of the nickel substrate for the large optic
T_{Ch}	Depth of the channel on a MOA array
T_{Si}	Thickness of the silicon chip
T_{PZT}	Thickness of the PZT actuators
T_{st}	Thickness of each layer on a stack actuator
V_{ref}	Reference voltage
W_{afc}	Electrode width of an active fibre composite
W_A	Width of the non etched strips on the spider MOAs
W_{Ch}	Width of the channels on a MOA array
W_B	minimum width of the legs in the wet-etched spider model
W_F	Width of the beam between the MOA channels and the spider legs
W_G	Gap between legs in the wet-etched spider model
W_L	maximum width of the legs in the wet etched spider model

W_{LO}	Width of the large optic
W_{MOA}	Width of the MOA array
W_{Si}	Width of the silicon chip
W_{PZT}	Width of the piezoelectric actuators

Optical parameters:

α	Incident angle of incoming radiation
α^{crit}	Critical incident angle
f_{FS}	Focal length of a Fresnel-Soret zone plate
λ	Wavelenght
m_e	Mass of the electron
r_n	Radius of curvature of each of the rings in a Fresnel-Soret zone plate
ρ_e	Density of electrons on a reflecting surface
n	Refractive index

Piezoelectric and mechanical parameters:

d_{ij}	Piezoelectric coefficients
E	Electric field
E_c	Coercive electric field
E_p	Poling electric field
I_{mi}, I_{Mj}	Minimum and maximum input values
ν	Poisson's ratio
ε_{ij}	dielectric coefficients
P	Polarisation
P_r	Remnant polarisation
P_s	Spontaneous polarisation
r_i, R_j	Minimum and maximum response values
$\boldsymbol{S}$	Strain tensor
S_{ij}	Elastic coefficients
$\mathbf{T}$	Stress tensor
T_c	Curie temperature
T_p	Poling temperature
t_p	Duration of the poling procedure

T_{t1}, T_{t2}, T_{t3}	Compressive stress threshold before domain switching
Y_m	Young’s modulus

Units and constants:

c	Speed of light
ε_0	Vacuum dielectric permittivity
eV	Electron Volt
gnd	Electric ground (V=0)
MPa	Mega Pascal

CHAPTER 1

INTRODUCTION

One of the factors limiting the resolution of optical systems is the aberrations which can arise from two sources: introduced along the ray's path through inhomogeneous media, such as the atmosphere in astronomy or the eye tissues and fluid in ophthalmology; and introduced by defects originated during the manufacturing processes and/or due to gravitational or thermal effects in the optic surfaces. Adaptive optics is a concept in which the shape and position of an optical surface can be dynamically changed by the incorporation of actuation mechanisms in order to correct these aberrations, thus providing increased resolution. Adaptive optics have been used in astronomy, vision science and military applications for the last few decades and it is an ongoing field of research where devices for new applications such as active/adaptive X-ray and neutron optics are emerging.

X-rays, first discovered in 1895 by Wilhelm Conrad Röntgen, are used in a broad range of applications. Computer tomography scanners, third generation synchrotrons and X-ray telescopes are examples of technologies which enabled the further understanding of the human body, the microstructure of materials and the universe respectively. These technologies would all benefit from increased resolution if the X-ray optics they use were active/adaptive. However, this has only been demonstrated so far for large X-ray optics on synchrotron beam lines which consist of

Kirkpatrick-Baez type focusing mirrors manufactured on thick substrates where actuation was achieved using push/pull actuators such as piezoelectric stacks or voice coil actuators.

The Smart X-ray Optics (SXO) consortium, which was formed in 2007 following the steps of a proof of concept program in 2004, consists of seven research groups in the U.K. as described in detail in Appendix I. Two new prototype adaptive X-ray optics systems are under development in the SXO consortium with the aim of approaching the fundamental diffraction limit.

One proposed technology was micro-structured optical arrays (MOAs) to produce a micro-focused X-ray source, and which uses grazing incident reflection through consecutive aligned channels obtained using deep silicon etching. Such an optic would be an alternative to diffractive zone plates for the micro-focusing of X-rays with the main advantage of focusing by reflection rather than diffraction, therefore enabling up to two orders of magnitude of increased flux. Another advantage of MOA’s with respect to zone plates is that they would not suffer from chromatic aberration enabling the use of polychromatic X-ray sources. This would be of great advantage in laboratory based X-ray systems whose capabilities are limited by the maximum focused flux possible.

The second area of interest was actively deformable mirrors in large scale optics for the next generation of X-ray telescopes, with the aim to achieve a spatial resolution better than the currently available by Chandra (0.5”) whilst maintaining a thin optic section, below 1mm, which would enable a telescope design with high throughput via nested mirrors.

For both SXO applications piezoelectric actuation techniques were developed. These included the manufacturing of pre-curved piezoelectric shells using a viscous plastic processing (VPP) technique for the large optic; and the development of a novel actuator structure, the spider concept, to meet the application requirements of MOAs. Actuation methods for both applications were developed taking into consideration the manufacturing processes, of both the optics and the piezoelectric actuators, and their integration procedures. Their designs were optimized using FEA software and the testing results of manufactured prototypes.

This PhD thesis describes the development of piezoelectric actuated devices for Smart X-ray Optics applications. It begins with the literature review consisting on three chapters: Chapter II outlines actuation concepts in adaptive optics systems; Chapter III reviews the limits of current X-ray optics systems and Chapter IV reviews the physics, manufacturing processes and design of piezoelectric actuators. Following the literature review, the project objectives are outlined in Chapter V. Chapter VI presents the research methodology and experimental procedures used in this study. Chapter VII presents the piezoelectric actuated devices for Micro-structured Optical Arrays, followed by Chapter VIII where the development of piezoelectric actuators for large X-ray optics is presented. Finally, Chapter IX outlines the conclusions of this thesis and the proposals for future work.

CHAPTER 2

ACTUATION METHODS FOR ADAPTIVE OPTICS APPLICATIONS

2.1 Adaptive optics principles of operation

The concept of adaptive optics (AO) was first introduced by H.W. Babcock in 1953(1) to improve the resolution of ground based telescopes. Light has to travel through the atmosphere in order to reach a telescope's optics, and when it does so across turbulent areas of air distortions on its wave-fronts are introduced, which have the net effect of limiting the instrument resolution. Babcock's idea was to try to recover the original wave-fronts using a deformable mirror the shape of which would be controlled using the information provided by wavefront sensors as shown in the diagram in Figure 2.1. Firstly, an incoming flat wave gets distorted by the atmospheric turbulences; A deformable mirror (DM) is used to compensate for the atmospheric effects and recover the original flat wave; Secondly, using a beam splitter the corrected wave can be divided in two, one part travelling towards the optics of the telescope, and the other travelling towards the wavefront sensor; Finally the wavefront sensor and the DM are operated in a closed loop mode to keep track of the changes in the atmospheric turbulences.

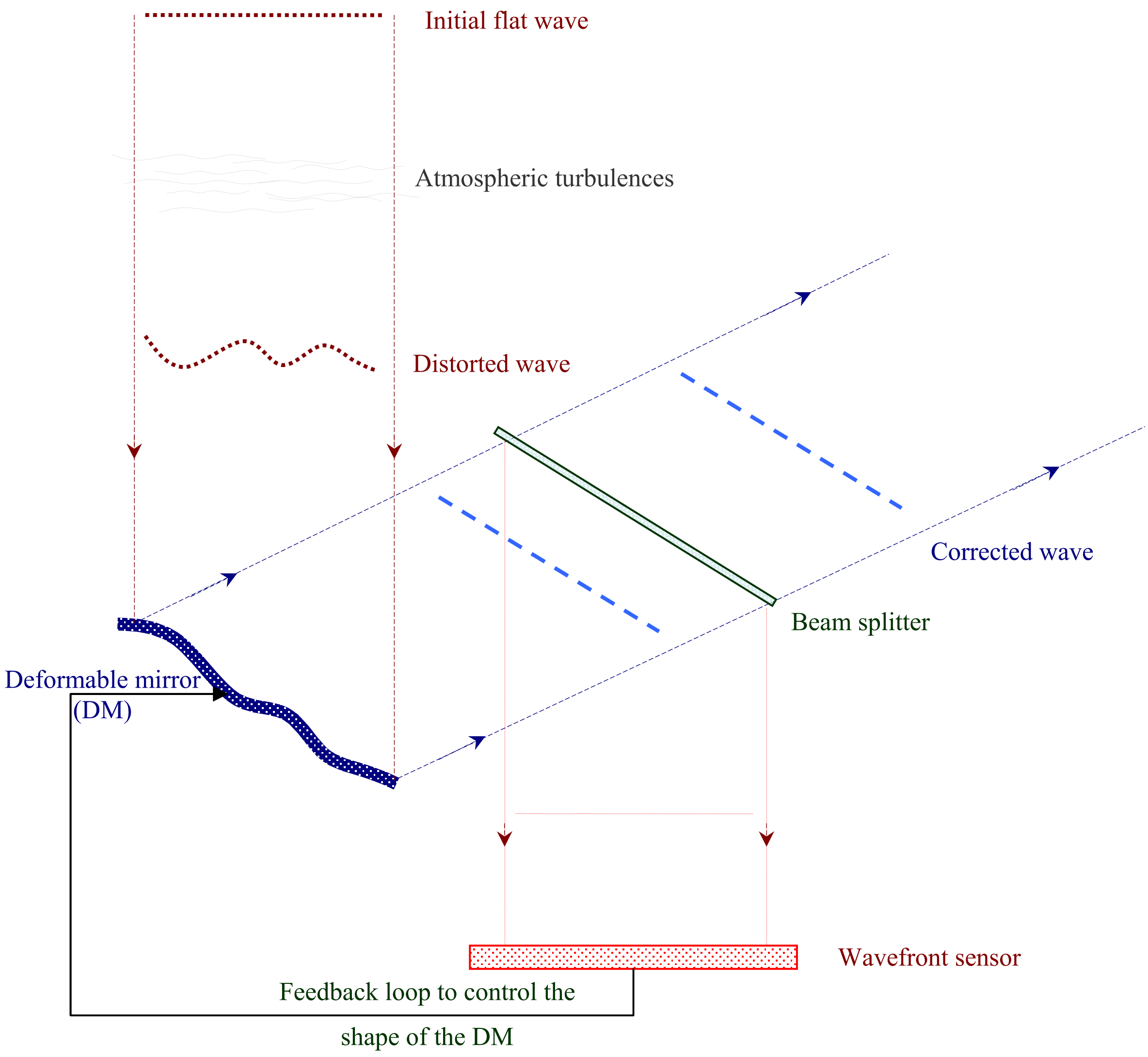

Figure 2.1: Diagram representing the operational principles of adaptive optics systems for ground based optical telescopes.

One of the key elements of this technology is the use of deformable mirrors. Babcock proposed the use eidomorphs, an early type of deformable mirror where the thickness of an oil layer over the surface of a mirror was controlled by a charge density distribution. Modern adaptive optics have benefited from all the technical advances of the last decades and are capable of incrementing the resolution of an optical telescope by a factor 100 until it is effectively diffraction limited(2).

However, real adaptive optics systems could be much more complex and their design goes beyond the scope of this work. For example for optical telescopes a big elliptical primary mirror has the function of collecting as many photons as possible and the adaptive optics are carried out in a small and flat secondary mirror.

The success of the first AO telescopes, and the advances in other technologies such as signal processing made it feasible for other applications, such as vision science and optical communications technologies to use similar techniques. Detailed descriptions of how the control algorithms and advances in wave-front sensor technologies are described in the literature(3, 4) and in reference books(5, 6) and go beyond the scope of this work. Figure 2.2 shows two pictures obtained in 1991 using COME-ON, a 3.6 meter diameter AO prototype telescope(7). The images show how a binary star system could only be resolved once the AO system was switched on.

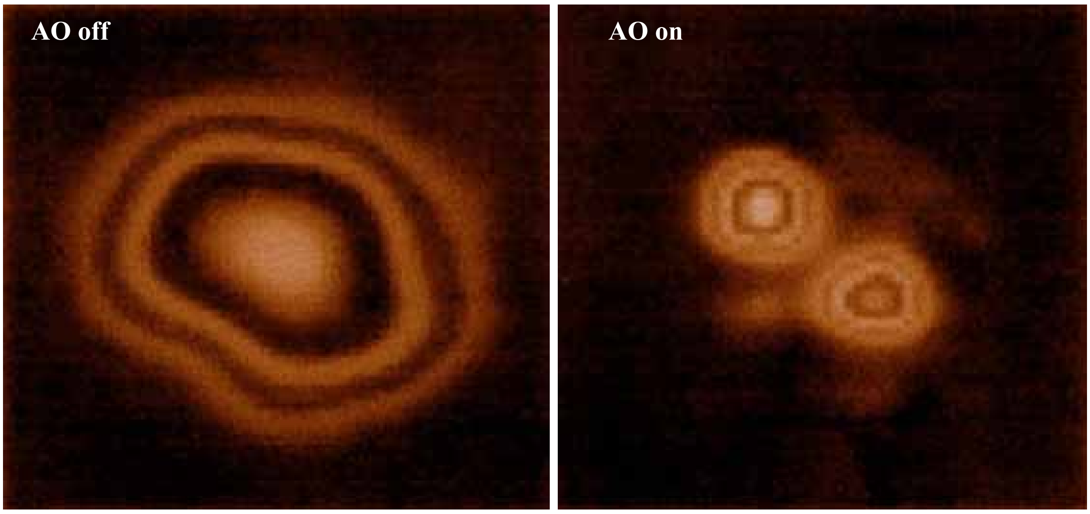

Figure 2.2: Images of a binary star obtained in 1991 using the COME-ON ground telescope(7). Left, image with the adaptive optics switched off. Right, image with the adaptive optics switched on.

As the technology evolved, adaptive optics techniques started to be used not only to reconstruct wave-fronts which had been distorted due to the interference of the propagating media, but also to improve the inherent resolution of the optical instruments themselves, and which could be compromised by the manufacturing processes of the optics, variations in temperature, or gravitational effects in space-based telescopes. The term active optic was then used for such systems, and in terms of operational principles the difference with adaptive systems is that the changes are slower, the order of 1Hz. Currently the term smart optics denominates systems with both active and adaptive capabilities.

2.2 Other applications of adaptive optics systems

Soon after the successful implementation of adaptive optics technologies to increase the resolution of ground based telescopes adaptive optics started to be developed in other fields such as vision science, optical communications. However, in other fields such as X-ray and neutron optics the technology is still in its infancy.

In vision science and ophthalmology the adaptive optics started to be used at the end of the 1990's to correct the aberrations introduced by the eye in real time. This has enabled the imaging of the in-vivo retina and would enable in future the early diagnosis of diseases affecting the eye. Latest advances in the field are described elsewhere in reference books(8) and in the literature(9).

Adaptive optics techniques have also been used for optical communications using laser beam through the atmosphere, and in other fields such as X-ray and neutron optics adaptive optics techniques are starting to be introduced. For all these applications actuation method needed to be developed to control the shape of deformable mirrors, and because of the different application requirements it has led to the use of different actuation technologies.

2.3 Large deformable mirrors (DM's): Push/pull, tip/tilt actuators

One of the ways of producing large DM's is to apply point forces on the back surface of a mirror using linear actuators. The linear actuators need to be bonded to a fixed reference surface and once activated could be used to create a piston motion, push, pull and tip/tilt the mirror surface as depicted in the schematic representation in Figure 2.3. In practice many more linear actuator are used to precisely control the shape of the mirrors and correct higher order aberrations. For example, the commercially available DM241 (Alpao, Biviers France, 2010) which consists of 241 voice-coil actuators arranged on a 17x17 matrix providing a DM with a pupil diameter of 4cm diameter and capable of correcting focus and astigmatism and higher order aberrations such as coma.

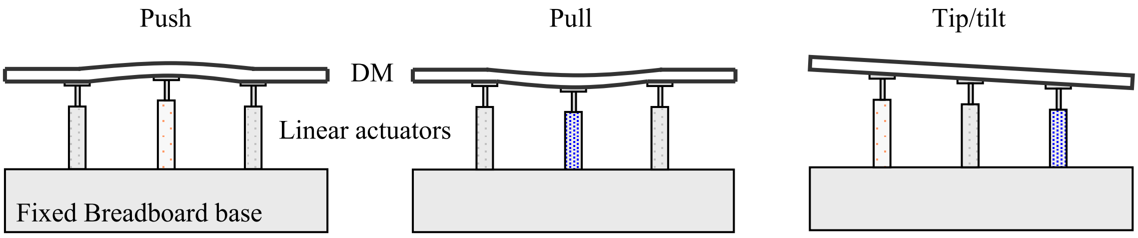

Figure 2.3: Schematic diagram of push/pull and tip/tilt actuation modes. The linear actuators are fixed to a reference surface at the bottom of the figure to control the deformable mirror at the top.

Figure 2.4a shows a picture of the Martini adaptive optics instrument developed by Doel et al in 2000(10) where a 120cm diameter mirror was segmented into six elements, each one of them controlled using three piezoelectric stack actuators.

Another push/pull actuation method is to use a membrane mirror which can be controlled using electrostatic forces. Figure 2.4b shows a photograph of a prototype device where both push and pull capabilities were added to the electrostatic membrane DM using transparent electrodes on the reflecting surface of the mirror and a patterned electrode on its bottom surface as shown in Figure 2.4c(11).

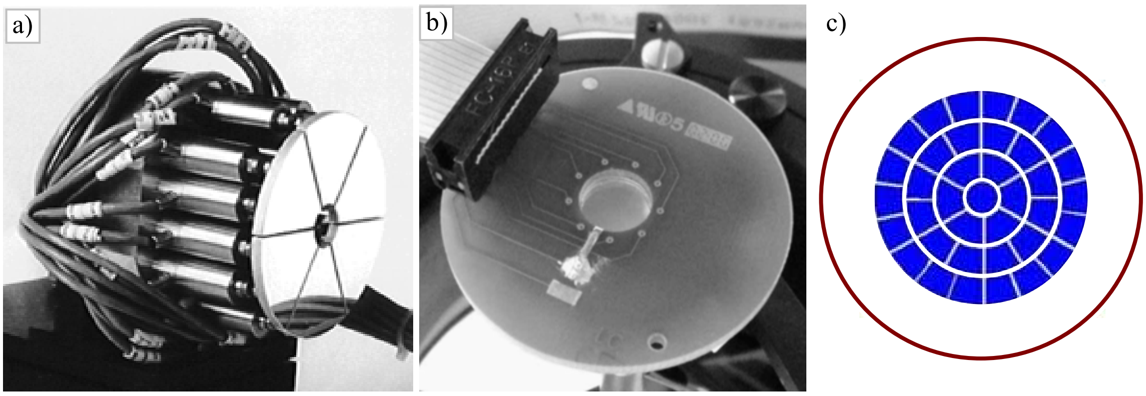

Figure 2.4: a) The Martini adaptive optics instrument, 120cm diameter, from Doel et al 2000(10) the positions of each segment of the mirror are controlled using three piezoelectric stack actuators. b) Push pull membrane mirror with a 2.5cm pupil diameter for vision sciences applications and c) Patterned electrode layout on the bottom side of the actuator, Bonora et al 2006(11).

2.4 MEMS for deformable mirrors applications

Advances in Micro Electro Mechanical Systems (MEMS) manufacturing methods have also being used to produce MEMS DM's. Figure 2.5 shows pictures of a 220x220μm micro-mirror manufactured by He et al(12) capable of tip, tilt, and vertical translation. The square mirror is fixed on its four corners and the actuation is provided by electrically driven actuators in a comb-drive configuration.

Another deformable mirror design manufactured using MEMS technologies by Kanno et al in 2005(13) is depicted in Figure 2.6. A membrane mirror has been coated on its back surface with thin film piezoelectric material, and then the hexagonal patterned electrodes are used to control its shape.

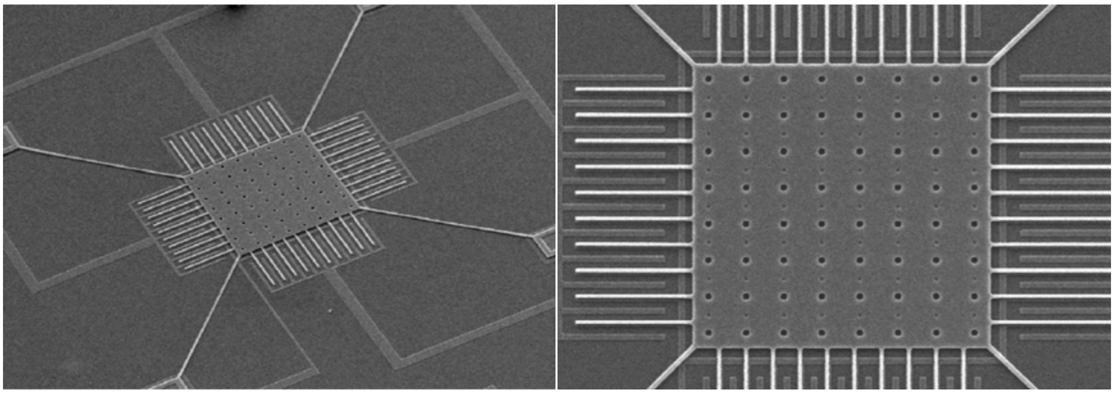

Figure 2.5: MEMS micro-mirror 220×220µm. The actuation is provided by comb drive actuators. Both the comb drive actuators and the mirror are micro-machined in the same silicon wafer. He et al 2005(12).

The electrode pattern is an important feature on the DM's design as an overlap of the actuation between adjacent areas is needed to assure a smooth transition between active areas on the reflecting surface and avoid the print-though of higher order aberrations which can not be corrected.

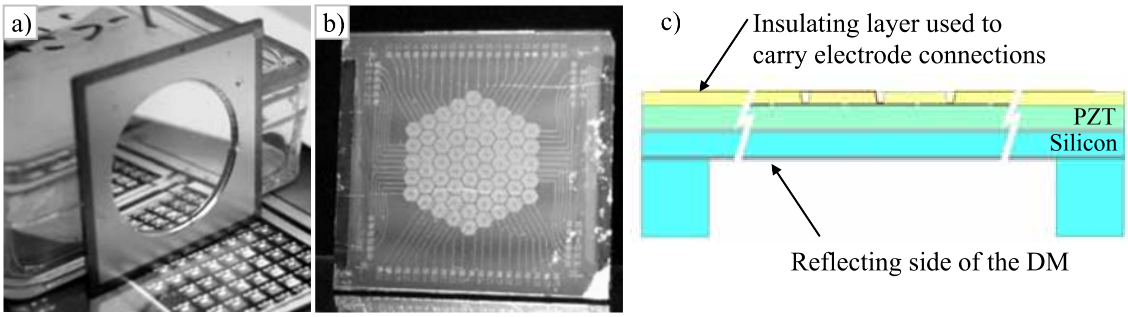

Figure 2.6: MEMS deformable mirror developed by Kanno et al(13). a) Reflecting side of the mirror. b) Hexagonal electrode pattern on the PZT thin film actuator layer at the back of the mirror. c) Schematic representation of a cross-section of the mirror.

2.5 Summary

A very wide range of techniques for implementing deformable mirrors can be found in the literature and in most cases these are manufactured on an ad-hoc basis depending on the application requirements. Different technologies are used ranging from: push/pull type actuators which could be made using piezoelectric stack actuators or voice-coil magnetic actuators; actuators manufactured using MEMS manufacturing methods, where thin mirror, can be manufactured using silicon processing methods and then manipulated using, for example, electrostatic or thermoelectric actuators; to unimorph structures consisting of a reflecting layer and a piezoelectric actuator layer bonded at its back with patterned electrodes, where the shape of the DM is controlled and by varying the voltages on the electrodes, with their design and control algorithms being critical.

In summary, to successfully introduce adaptive optics methods in a new application the DM's need to be designed to fulfil the application requirements integrating the optical properties of the DM's with an actuation structure in a single device. Moreover, the manufacturing methods of the optic part of the DM and the actuation part and their integration need to be compatible. Optics systems for higher energy physics (X-ray, neutron and gamma ray optics) are much more complex than their visible range counterparts and work with tolerances several orders of magnitude smaller which are the main reasons why these fields will be the latest to benefit from the use of adaptive optics methods to achieve increased resolutions.

2.6 References

1. Babcock, H.W., *The possibility of compensating astronomical seeing.* Publications of the astronomical society of the pacific, 1953. **65**(386): p. 229-236.
2. Ragazzoni, R., E. Marchetti, and G. Valente, *Adaptive-optics corrections available for the whole sky.* Nature, 2000. **403**(6765): p. 54-56.
3. Beckers, J.M., *Adaptive Optics for Astronomy - Principles, Performance, and Applications.* Annual Review of Astronomy and Astrophysics, 1993. **31**: p. 13-62.
4. Roggemann, M.C., B.M. Welsh, and R.Q. Fugate, *Improving the resolution of ground-based telescopes.* Reviews of Modern Physics, 1997. **69**(2): p. 437-505.

5. Potsaid, B. and J.T. Wen. *Optimal design of adaptive optics based systems using high fidelity MEMS deformable mirror models*. in *Optomechatronic Actuators and Manipulation III*. 2007: SPIE.

6. Qiao, D., Yuan W., Li K., Li X, Rao F. Comparative study on different types of segmented micro deformable mirrors. in 2nd International Symposium on Advanced Optical Manufacturing and Testing Technologies: Advanced Optical Manufacturing Technologies. 2006: SPIE.

7. Rigaut F., Rousset G., Kern P., Fontanella J. C., Gaffard J. P., Merkle F. and Lena P. Adaptive Optics on a 3.6-M Telescope - Results and Performance. Astronomy and Astrophysics, 1991. 250(1): p. 280-290.

8. *Adaptive optics for vision science: principles, practices, design and applications*. 1st ed. Microwave and optical engineering, ed. J. Porter, et al. 2006: John Wiley & Sons, Inc. 591.

9. Hampson, K.M., *Adaptive optics and vision.* Journal of Modern Optics, 2008. **55**(21): p. 3425-3467.

10. Doel A.P., Dunlop C.N., Buscher D. F., Myers R.M., Sharples R.M. and Major J.V. The MARTINI adaptive optics instrument. New Astronomy, 2000. 5(4): p. 223-233.

11. Bonora, S. and Poletto L., *Push-pull membrane mirrors for adaptive optics.* Optics Express, 2006. **14**(25): p. 11935-11944.

12. He, S.Y. and R. Ben Mrad, *Large-stroke microelectrostatic actuators for vertical translation of micromirrors used in adaptive optics.* Ieee Transactions on Industrial Electronics, 2005. **52**(4): p. 974-983.

13. Kanno, I., S. Tsuda, and H. Kotera, *High-density Piezoelectric Actuator Array for MEMS Deformable Mirrors Composed of PZT Thin Films*, in *2008 Ieee/Leos International Conference on Optical Mems and Nanophotonics*. 2008, IEEE: New York. p. 132-133.

CHAPTER 3

THE LIMITS OF CURRENT X-RAY OPTICS

3.1 Introduction: the challenge of focusing X-rays

The discovery of X-rays in 1895 by W.C. Röntgen(1) has made possible all the advances in medical imaging applications which revolutionized diagnostic medicine. For example, during the 20th century computer tomography (CT) scanners, consisting of rings of X-ray detectors surrounding the patient while being irradiated by an X-ray source, have been developed to a point where commercially available CT's(2) are capable of reproducing a 3D scan of the whole human body with a 0.5 mm resolution.

In other disciplines, X-ray optics are used for the focusing and acquisition of high resolution images and their geometries and designs depend on the specific application, with the three main ones being X-ray telescopes, optics for the focussing of X-rays in synchrotron beam lines and optics for laboratory based X-ray sources. These applications present different technical challenges and the technology is at a different level of development in each one of them.

This chapter intends to provide a general background of X-ray optics physics and summarize the limits in the three fields mentioned above and the implications these have on their bandwidth, resolution and sensitivity. An in depth description can be found in other tests in the literature(3, 4).

3.2 Physics limits on X-ray systems

3.2.1 X-ray reflection from ideal surfaces

The physics of X-rays is a field very well understood and is described in detail in several optics and electrodynamics bibliographies. David M. Paganin reviews in “Coherent X-ray Optics”(5) the X-ray wave-fields, their interaction with matter, X-ray sources, and optical elements and detectors.

X-rays operate at much higher energy than visible light and thus have a much shorter wavelength, λ, as it is shown in Figure 3.1. The wavelength is the ultimate physical limit to the resolution of imaging systems, therefore, X-ray optics have the capability of achieving much higher resolution than their visible equivalents. For example the commercially available X-ray computer topographer Xradia nanoXCT-100 can obtain X-ray images with a 50nm resolution using a combination of micro-focus X-ray sources and zone plate optics(6).

Another limitation is that X-rays are absorbed while they travel within most gases and therefore X-ray astronomy needs to be carried out in space to avoid the absorption of the X-rays in the atmosphere. The limits on the maximum launchable payload of satellites adds weight and size restrictions to the already high tolerances required due to the small wavelengths involved, and are the main technical reason why resolutions achievable in the visible range are beyond the reach of X-ray optics in astronomy.

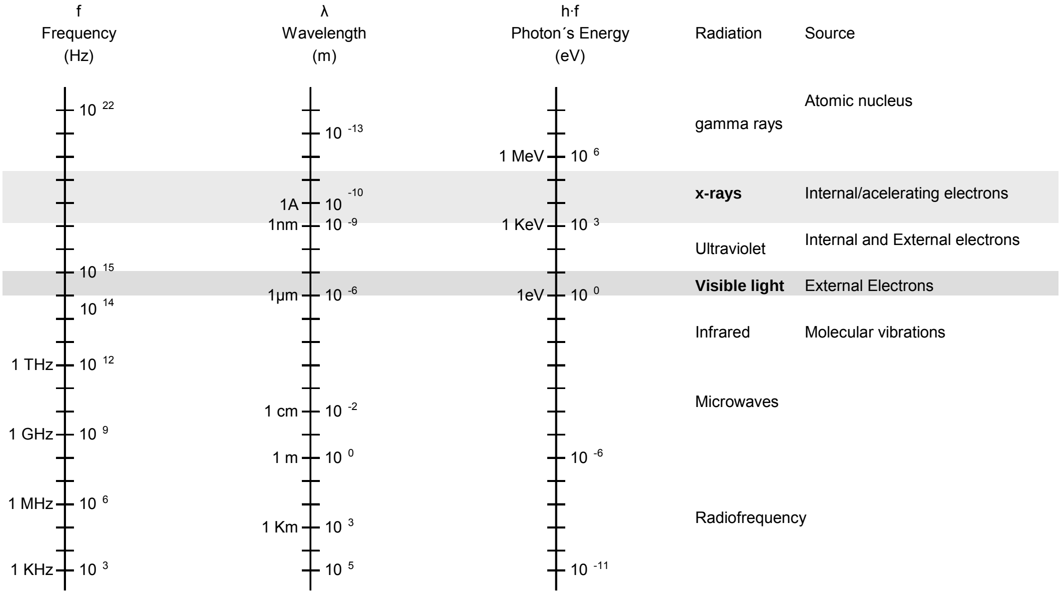

Figure 3.1: Orders of magnitude of the frequency, wavelength and the photons energy in the electromagnetic spectrum (Adapted from "E. Hecht and A. Zajac, Optics, Addison-Wesley, 1974").

In geometric optics X-rays are represented by rays propagating along one direction. When an X-ray encounters a discontinuity, i.e. two different propagating media, it divides itself into reflected and refracted rays following Snell's law given by 3.1, as in shown in Figure 3.2.

$$n_1 \sin\theta_1 = n_2 \sin\theta_2$$ **Equation 3.1**

Where:

n_1 and n_2	are the optical indexes of their respecting propagating medium.
θ_1 and θ_2	are the incident and refracted angles respectively measured with respect to the normal of the plane.
$\alpha_1 = 90^o - \theta_1$	is the angle between the incident wave and the discontinuity.

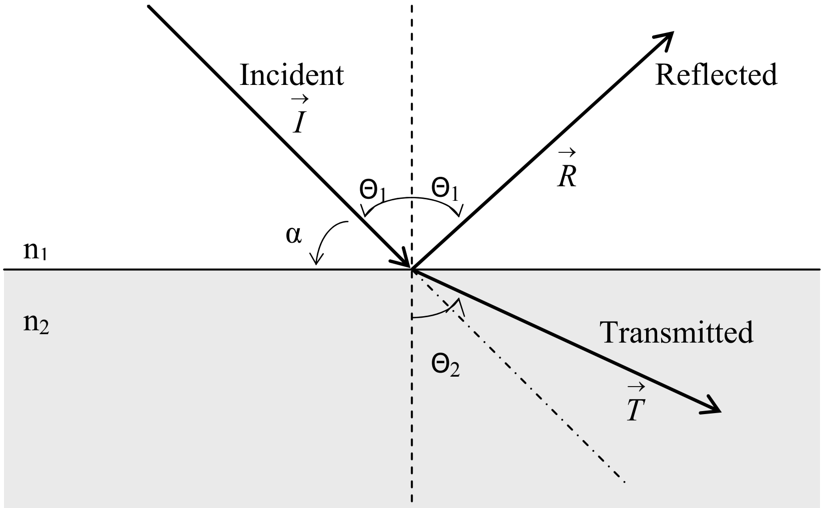

Figure 3.2: Incident; reflected and refracted rays in the discontinuity of two medium with different refractive index.

One important parameter relevant to X-rays is the critical angle (α^{crit}) which is the angle of the incident ray below which total reflection occurs. From the Snell law we can see that θ_2 increases as θ_1 increases. Therefore, the critical angle will occur when $\theta_2 = 90^o$, and the transmitted X-rays are parallel to the reflecting surface. Using an expression of the reflective index for isotropic materials (See D.M. Paganin for a detailed description$^{(5)}$).

$$\alpha^{crit} = \frac{e\lambda}{2\pi c}\sqrt{\frac{\rho_e}{\varepsilon_0 m_e}} \qquad \textbf{Equation 3.2}$$

Where:

α^{crit}	is the critical angle
λ	is the wavelength
c	is the speed of light
e	is the charge of the electron
ρ_e	is the electronic density in the surface
ε_0	is the vacuum dielectric constant
m_e	is the mass of the electron

The critical angle (α^{crit}), below which total reflection in a mirror is guaranteed, is directly proportional to λ which in practical terms means that X-ray mirrors can only operate effectively at very shallow angles (typically ≤3°), before the condition of total reflection is violated. One possible way of increasing α^{crit} is by increasing the density of electrons in the reflecting surface (ρ) using materials of higher atomic number. Most X-ray optics have their reflecting surfaces coated with a material of high atomic number, such as gold or iridium, as a means to increase the reflectivity.

When angles beyond α^{crit} are used only part of the incident X-rays will be reflected. The reflection coefficients are dependent on the incident angles, polarization of the incident X-rays (parallel or perpendicular to the reflecting surface) and the substrate properties (optical index). They are described by the Fresnel equations below which are calculated using the Snell law and the boundary conditions for electric fields which dictate the continuity of the tangential components of the electric field in the discontinuity. The deduction of these equations can be found in various text books, see Compton and Alison for a detailed description(7).

$$r_{\mathrm{II}} = \frac{R_{II}}{I_{II}} = \frac{nCos\theta_1 - Cos\theta_2}{nCos\theta_1 + Cos\theta_2}$$ **Equation 3.3**

$$r_{\perp} = \frac{R_{\perp}}{I_{\perp}} = \frac{nCos\theta_2 - Cos\theta_1}{nCos\theta_2 - Cos\theta_1}$$ **Equation 3.4**

Where

r_{II}	is the Fresnel reflective coefficient for the parallel component.
$r_{\perp}$	is the Fresnel reflective coefficient for the perpendicular component.
I_{II} *and* $I_{\perp}$	are the amplitudes of the parallel and perpendicular components of the incident field.
R_{II} *and* $R_{\perp}$	are the amplitudes of the parallel and perpendicular components of the reflected field.

3.2.2 X-ray reflection from real surfaces

For ideal surfaces, which are perfectly smooth, the reflection of the X-rays is limited by the critical angle and the Fresnel coefficients, both of which are dependent on the energy of the incident radiation. However, real surfaces are not perfectly smooth. They have a surface roughness, which originates from the manufacturing processes used for their fabrication, which has the undesirable optical effect of scattering part of the incident radiation. The larger the surface roughness, the more pronounced the scattering. This is a very well understood problem, and scattering equations for optical systems are widely available in the literature(7, 8). The percentage of the reflected energy from a surface is a function of the composition of the reflecting surface, the surface roughness and the energy and grazing incidence angle used.

For practical applications both the Fresnel reflection coefficients and the scattering from the surface need to be computed to calculate the reflectivity of a surface as a function of the energy and grazing angle of the incident radiation and the surface roughness of the surface. In the Centre for X-ray optics website(9) some of these calculations can be conveniently made on-line.

Figure 3.3 shows the reflectivity of a nickel substrate coated with a 30μm gold layer on its surface. The three sets of curves, which are typical for soft (<100eV) medium and hard (>10KeV) X-rays energy values, present different reflectivity vs. grazing incidence angle behavior (notice that the grazing angle scale is logarithmic). The solid lines represent an ideal surface, with zero surface roughness, and the dashed lines represent real surfaces with different values of surface roughness.

The reflectivity of soft X-rays is higher for all grazing angles and there is a smooth decrease of the reflectivity for increasing grazing angles; it can also be seen how surfaces with a higher surface roughness have lower reflectivity, as the roughness in the surface has the effect of dispersing the X-rays.

For hard X-rays it can be seen that only small angles, below 0.5 degrees, can be used as there is a grazing angle threshold value over which the reflectivity of the surface is dramatically reduced. The surface roughness has a negative impact on the reflectivity and on the range of usable grazing angles.

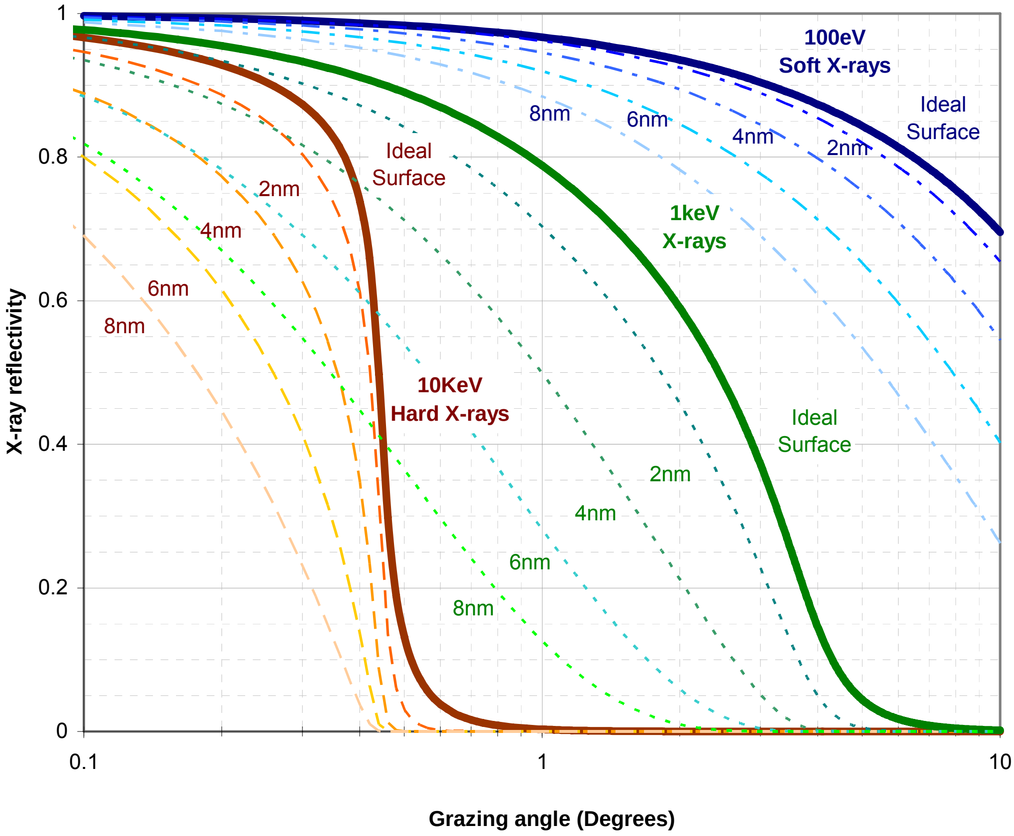

Figure 3.3: The change in reflectivity of a nickel substrate with a 30µm gold surface layer as a function of the surfaces roughness for soft (100eV), 1keV and hard (10KeV) X-rays at various grazing angles. This graph was calculated using the Centre for X-ray Optics website(9).

Other undesirable effects in reflecting surfaces are shadowing, where parts of the reflecting surfaces are hidden from incoming X-rays by imperfections in the surface, and scalloping where regular surface roughness patterns emerge as a result of the manufacturing processes, for example dry etching of silicon(10).

Understanding of the effects of the manufacturing processes on the surface roughness of the reflecting surfaces is crucial for the design of X-ray optics. In fact, most X-ray systems are limited by these effects and diffraction limited X-ray imaging it is not yet possible for most applications as the resolution is limited by the surface roughness rather than the physics limits of the theoretical surfaces.

3.3 *X-ray optics for astronomy*

3.3.1 Wolter I optics: The design compromise between resolution and active area.

There are 4 main types of X-ray optics that could be used to form X-ray telescopes: Kirkpatric-Baez(11), consisting of two orthogonal reflecting surfaces to create a double reflection, and Wolter 1, 2 and 3(12), which consist of concentric figures of revolution where the X-rays undergo a double reflection(13).

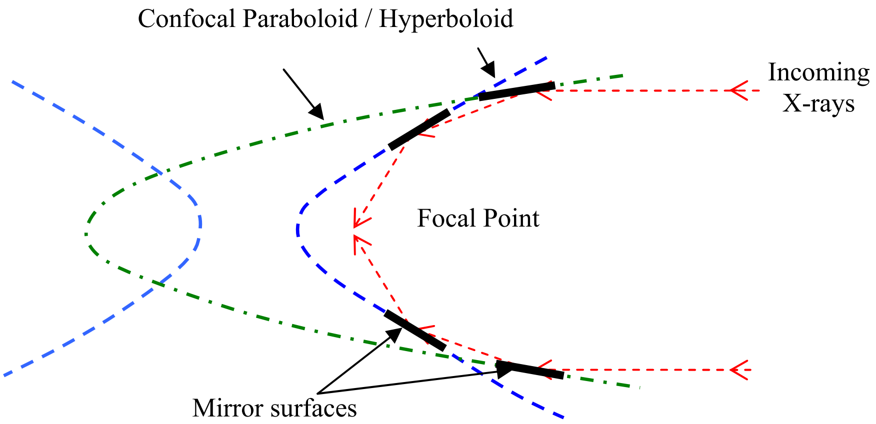

Figure 3.4: Schematic representation of a Wolter 1 optic(13). The X-rays are focused after being reflected on confocal paraboloid and hyperboloid surfaces. Adapted from Aschenbach(13).

Wolter 1 optics, consisting of a paraboloid/hyperboloid combination, is the dominant configuration in X-ray telescopes. It does not suffer from the aberrations present in Kirkpatric-Baez type of optics and presents the advantage over Wolter 2 and 3 configurations that the figures of revolution can be nested inside each other, and therefore the effective area of the telescope can be increased. Kirpatrick-Baez optics are the dominant configuration for X-ray focusing in synchrotron X-ray sources, where due to their high brilliance maximizing the flux is not an issue, and are described in the next section.

The most common manufacturing technologies for Wolter I X-ray mirrors are electroforming of nickel shells and slumping of glass. Weight restrictions to obtain a launchable satellite mass and limitations on these manufacturing processes mean that X-ray telescopes need to reach a design compromise between their resolution, for which perfectly smooth surfaces are needed, and the sensitivity of the instrument, for which as many shells as possible need to be nested inside each other in order to maximise the active area of the telescope.

Figure 3.5a shows a picture of 4 nested shells used on the Chandra X-ray observatory, the X-ray telescope with smoothest surfaces, and therefore highest resolution built to date(15). Centimetre thick zerodur ceramic (Schott AG, Germany) Wolter I shells were super-polished and then iridium coated to obtain the reflecting surfaces. Because of the thicknesses of the shells and the weight restriction of the telescope, Chandra is composed of only four nested shells.

The opposite design approach, maximizing the sensitivity, was taken on the XMM-Newton telescope, where fifty eight Wolter I nickel shells coated in gold where nested together as shown in Figure 3.5b, producing the most sensitive X-ray telescope built to date on the 250eV to 12KeV energy range. As the shells in XMM-Newton, with varying thickness' from 0.47mm in the most interior one to 1.07mm in the most exterior, are so much thinner those in Chandra ~2 - 3cm the surface roughness and precise positioning of the reflecting surfaces are more difficult to control and in turn the angular resolution is much smaller than that available in Chandra.

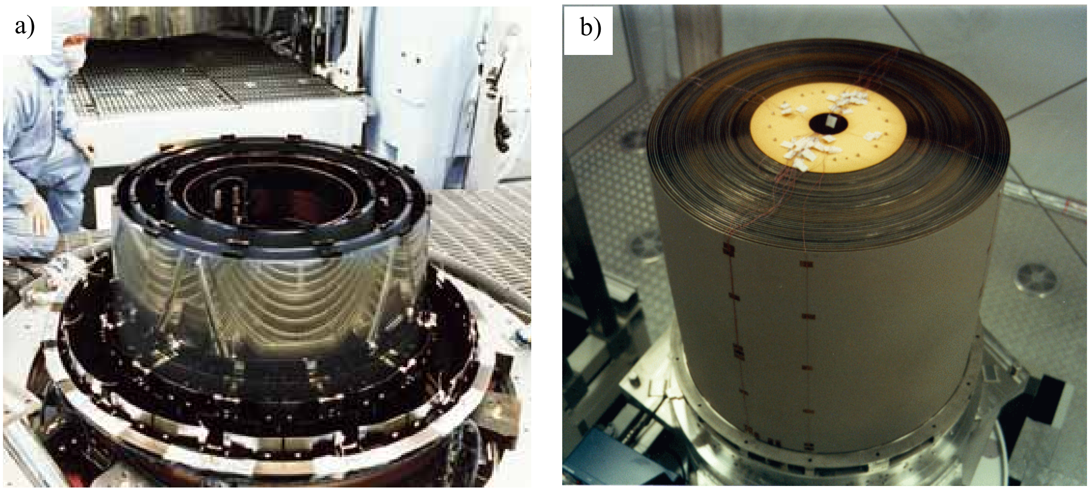

Figure 3.5:. a) The 4 Wolter I mirrors of the Chandra X-ray observatory(15). b) The 58 Wolter I optics nested to form one of the three modules of the XMM-Newton X-ray telescope(14).

3.3.2 Past, present and future X-ray telescopes.

Since the launch of the Einstein X-ray obserbatory HEAO-2 in 1978, the first one carrying Wolter I optics, successive X-ray missions have improved both the telescope resolution, 0.5arcsec is the smallest resolution currently available by Chandra, and sensitivity.

The graph in Figure 3.6 plots the values of resolution and effective area, which indicates the instruments sensitivity, of past present and planned future X-ray missions from all the major space agencies. Notice that both the effective area in the x-axis and resolution in the y-axis are plotted in a logarithmic scale.

To achieve the target resolution and sensitivity of future X-ray missions, the International X-ray Observatory (IXO) for ~2020, the manufacturing techniques of large X-ray optics will need to be improved to provide surfaces with sub-nanometer surface roughness on thin, below 1mm, substrates. For Constellation X, beyond 2020, an actuation mechanism will need to be devised which would cancel aberrations introduced during the manufacturing of the thin optics(16).

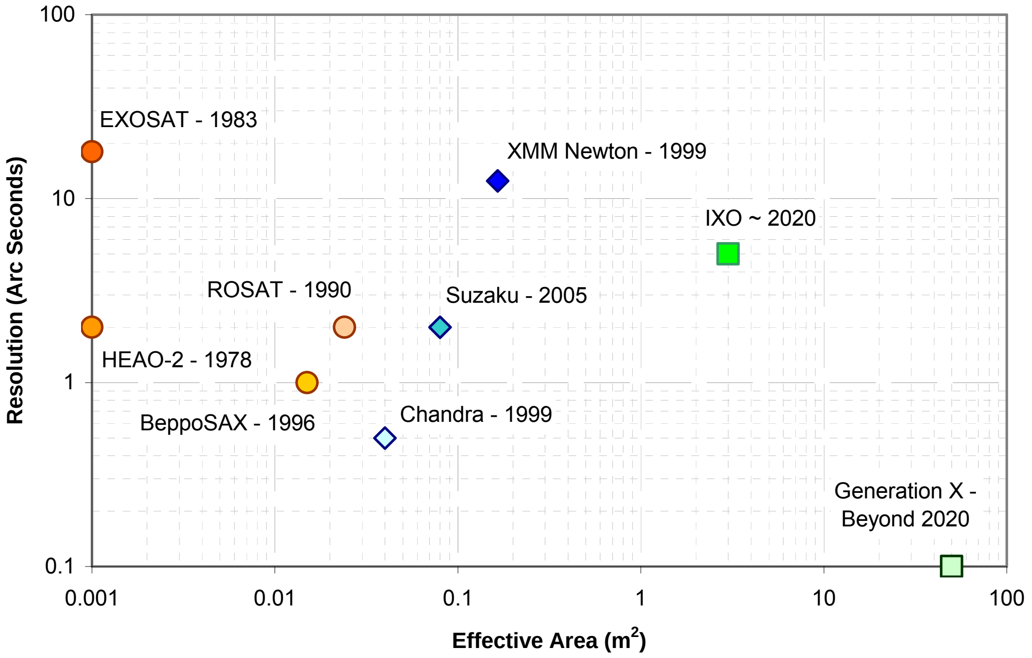

Figure 3.6: Resolution and effective area of past, present and future X-ray missions and their launch dates: The Einstein observatory HEAO-2, NASA, 1978; The European Space Agency (ESA) X-ray Observatory EXOSAT, 1983; The Röntgensatellit ROSAT, 1990, Germany; BeppoSAX, 1996, Italy; Chandra, 1999, NASA; XMM-Newton, 1999, NASA. Suzaku, 2005, Japanese Space Agency (JAXA); International X-ray Obsevatory IXO, NASA, ESA, JAXA collaboration; Generation X, beyond 2020, NASA.

3.3.3 Alternative X-ray telescope configurations

In recent years alternative telescope configurations, where substrates are deep etched to hollow fibres or micro channels(17-20). The individual chips can then be arranged to form a telescope, for example in a lobster eye configuration focusing the X-rays as described by the Wolter I configuration(21-23). In the lobster eye optics the Wolter I shapes are approximated by the arrangement of flat arrays instead of conforming to the ideal shapes which lowers the resolution. As the thickness of the mirror chips is limited and a significant area of the device would have to be sacrificed for mounting purposes, this configuration would result in a smaller effective and less focused flux than the Wolter I configuration. However, the advantage over X-ray telescopes consisting of nested concentric shells in a Wolter I configuration is that the structure as a whole is lighter, and therefore could be placed in interplanetary missions where the weight restrictions at launch are more demanding, even at cost of decreased flux and resolution. Figure 3.7 shows a proposed telescope configuration using microchannel plate optics developed by the Japanese space agency (JAXA)(22).

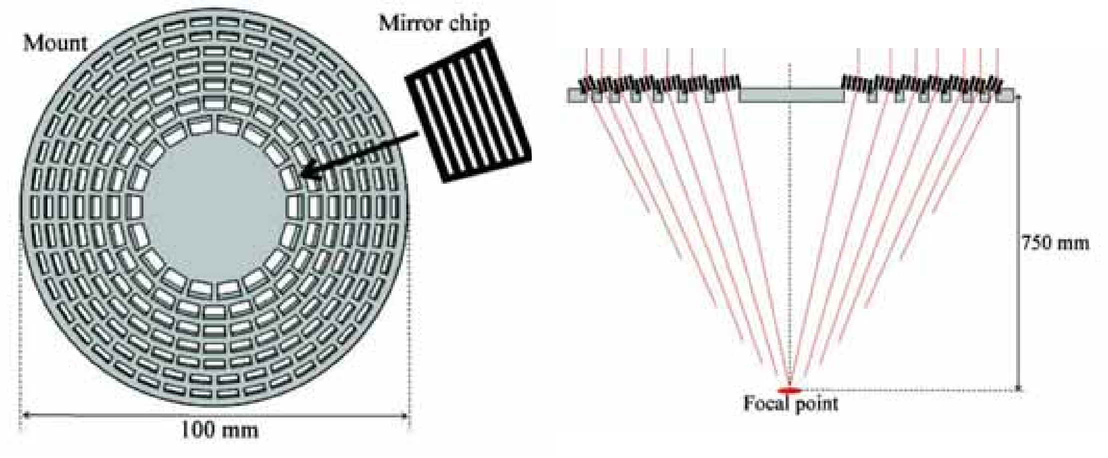

Plan view

Cross section

Figure 3.7: Lobster-Eye X-ray telescope arrangement using microchannel plate optics. Taken from M. Koshiishi et al Proc. SPIE 2007(22).

3.4 X-ray optics for synchrotron X-ray sources

The first generation synchrotron radiation was first produced as a by-product in particle accelerator facilities. The second generation of synchrotrons were purpose built for the generation of synchrotron radiation and therefore tried to maximise the brightness as it is a key parameter of any X-ray source. The higher the brightness the less time it takes to acquire an X-ray image and events changing faster over time can also be observed. The UK's Daresbury laboratory was the first of the second wave of synchrotron facilities and pioneered the technology for many others. This led to an inconceivable 10 orders of magnitude increase in brightness with respect of that available in rotating anode X-ray sources.

The third generation of synchrotrons, built on the technology developed by their predecessors, achieve increases in brightness of up to a further factor of five orders of magnitude. An example of a third generation X-ray source is the UK's Diamond light source facility. The operating principles of synchrotron X-ray sources for different generations of technologies are further explained in several text books in the bibliography(5, 24) and in the literature(25).

X-ray optics in beamlines within synchrotron facilities are used to define the energy, bandwidth, and focusing spot size and are customized depending on the particular science application the beamline is used for. Figure 3.8 below shows an example of the layout of the optical section in a beamline used at the Berkeley light source for micro X-ray absorption spectroscopy (μXAS)(26). In this system the X-ray source with a spot size 280×35μm is relayed toward the optical set-up using a toroidal mirror M1. The size of the beam is reduced using adjustable slits, and the energy of the beam is selected using the mirror M2 and a two crystal monochromators. Finally the mirrors M3 and M4, which are placed in a Kirkpatrick-Baez (KB) configuration to provide the y and x demagnification, focus the X-rays to a spot size up to 5×5μm.

For other applications requiring further demagnification of the X-ray beam a Fresnel zone plate, which focuses the X-ray beam by diffraction, would be placed between the M4 mirror and the sample. Both the Kirkpatrick-Baez configuration and Fresnel zone plates are discussed below.

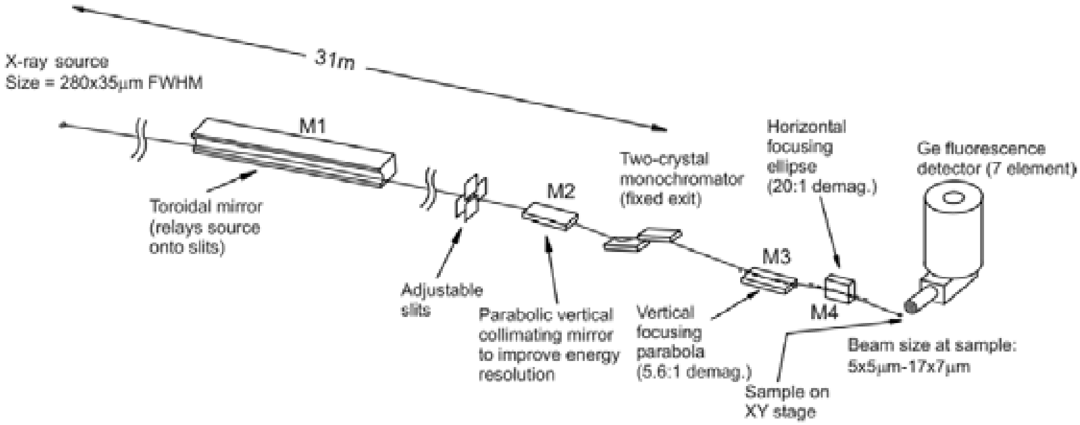

Figure 3.8: Layout of the beamline 10.3.2 at the advance light source in Berkeley. Taken from M.A. Marcus et al. 2004(26).

3.4.1 Kirkpatrick-Baez and elliptical X-ray mirrors

Kirkpatrick-Baez (KB) and elliptical X-ray mirror configurations are used in synchrotron facilities to obtain linear and point focusing respectively. In recent year research has been carried out to make these optics active/adaptive to obtain smaller focal points.

Figure 3.9 shows a schematic representation of a KB X-ray optic configuration used by PJ Eng et al.(27) at the Advance Photon Source in 1998, where the focusing was achieved after two successive reflections on X-ray mirrors which focused the X-rays on the x and y directions respectively.

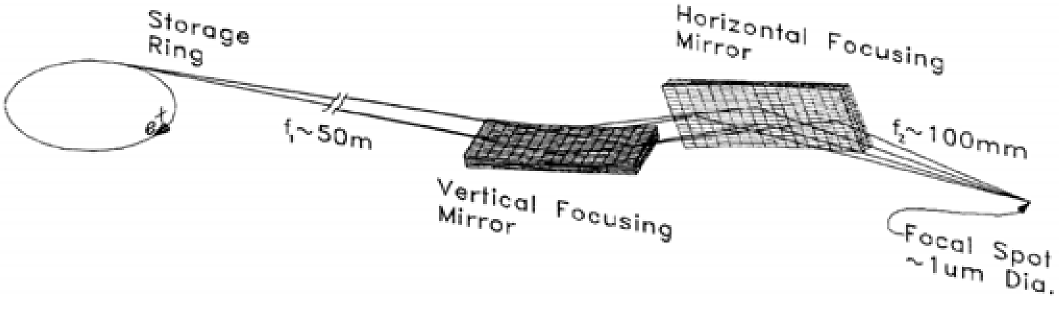

Figure 3.9: Schematic representation of a Kirkpatrick-Baez X-ray optic configuration. Taken from PJ Eng et al, 1998.(27)

In subsequent years further research followed where super-polished flat substrates were bent to make them conform to elliptical X-ray optics and therefore achieve point to point focusing. Figure 3.10 shows an diagram of one of the actuation methods proposed by M.R. Howells et al.(28) in 2000 in which forces were applied at the edges of the flat mirrors to bend them into elliptical shapes.

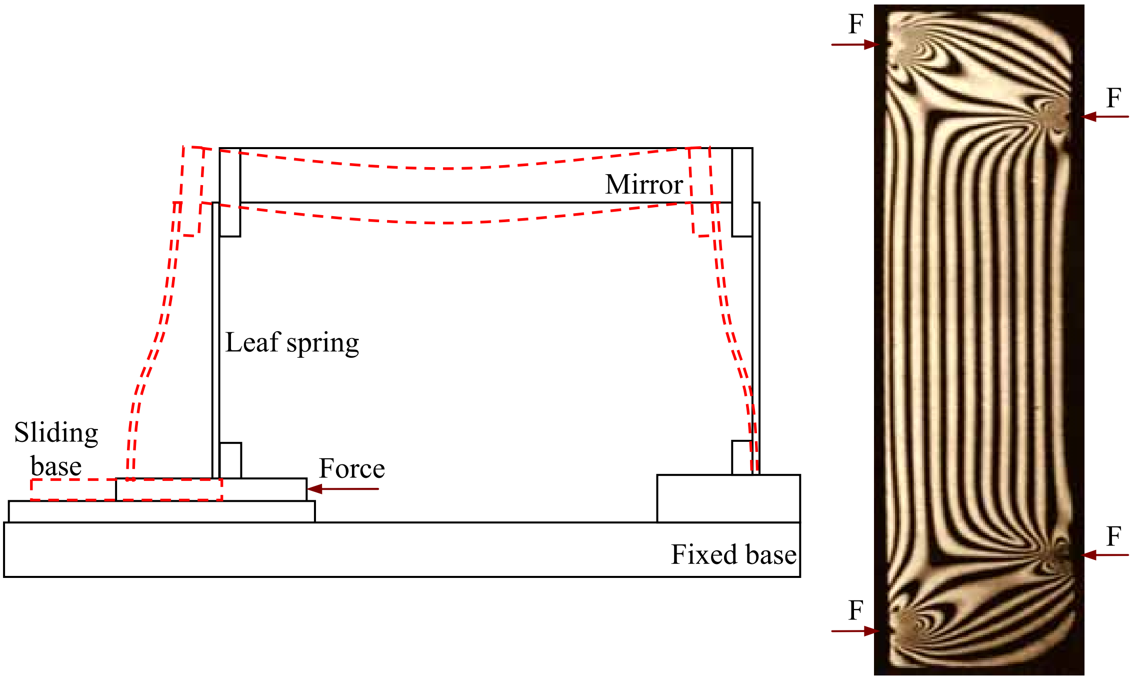

Figure 3.10: a) Possible scheme to bend a flat mirror into an elliptical shape so it can be used for focusing X-rays. The dashed lines represent the bent structure which curvature has been exaggerated for representation purposes b) Fringe pattern on a large X-Ray mirror whilst actuated using a 4 point bending system to create elliptical focusing at the centre area of the mirror. Figures adapted from Howells M.R. et al. 2000(28).

At the present time research is being carried out by several research groups where a number of push/pull type of actuators manipulate the back of the optics so they can be bent to elliptical shapes.

3.4.2 Diffractive X-ray optics: Fresnel zone plates

Fresnel zone plates, consisting of circular arrays of very fine trenches on thin substrates, are X-ray optics devices that obtain further demagnification of X-ray sources and have been in used as X-ray optics for several years. The width and separation of the circular trenches are engineered to focus the X-rays by Fresnel diffraction providing very small spot sizes. For example, Chao et al. from the Lawrence Berkeley national laboratory reported in 2009 a zone plate, designed for the soft X-ray energy range, capable of achieving a 12nm resolution(29).

The Fresnel diffraction equations have a dependence on the wavelength of the oncoming X-rays, as it can be seen in 3.5 for a Fresnel-Soret zone plate, and therefore X-rays with different wavelengths are focused at different focal distance from the Fresnel zone plate and therefore necessitates the use of monochromators. Another implication of 3.5 is that the wall thickness of successive rings of zone plate becomes smaller therefore limiting their physical size. This can be seen in Figure 3.11 depicting micrographs of Fresnel zone plates manufactured by Vila-Comamala et al.(30) using e-beam lithography. The wall thicknesses of the rings decrease from the centre to the outer edges of the opticfor a real example.

$$f_{FS} = \frac{r_n^2}{n\lambda}$$ **Equation 3.5**

Where:

f_{FS} is the focal distance of the Fresnel-Soret zone plate

r_n is the radius of each one of the n rings which constitutes the zone plate

λ is the wavelength of the incoming X-rays.

Fresnel zone plates are ideal optics to carry out microscopy studies in synchrotron facilities because of the high brilliance of the X-ray source. Images with resolution below 12nm can be obtained using these optics. However, they suffer from chromatic aberration and have very low efficiencies as they focus the X-rays by diffraction rather than reflection and they are size limited. This would make them the limiting factor on X-ray systems which do not have the benefit of high brilliance sources.

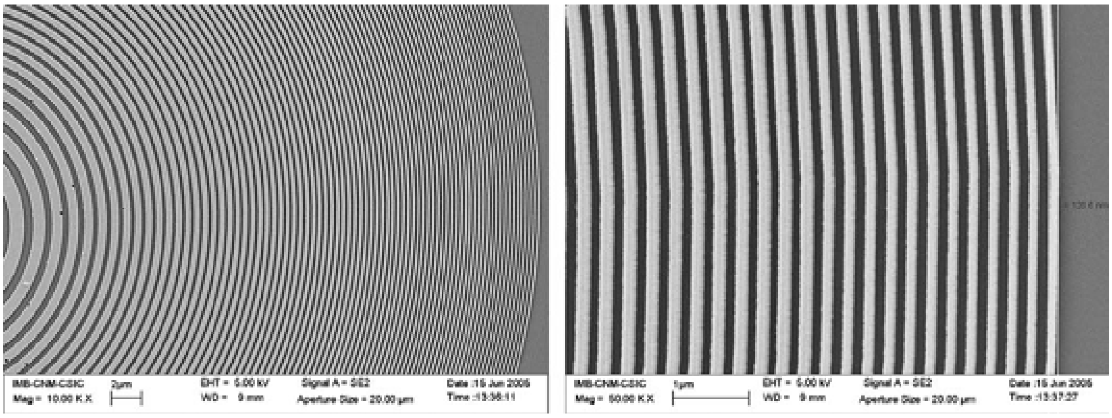

Figure 3.11: Micrographs of a manufactured Fresnel zone plate taken from J. Vila-Comamala et al 2006$^{(30)}$. The nickel rings constituting the Fresnel zone plate are 200nm high with a wall thickness of 50nm in the outer walls. They were manufactured using a combination of e-beam lithography and nickel evaporation methods over a thin silicon membrane.

3.5 X-ray optics for laboratory based X-ray sources

In laboratory based X-ray sources electrons are accelerated in a chamber using high voltages and then impact the anode. This in turn induces excited states on some of the atoms of the anode and X-rays with an energy distribution characteristic of the material of the anode are emitted when the electrons return from the excited state to the fundamental state.

Developments on the X-ray sources design have increased the brilliance of the sources. However they are still inferior by several orders of magnitude to those provided in synchrotrons as there is an upper physical limit on the electronic density of an electron beam due to their mutual repulsive forces between electrons, and heat dissipation issues arise in the anode at high electron fluxes. Another difference compared with the synchrotron radiation is that the focal lengths are much smaller (cm for the laboratory based sources instead of meters for the synchrotrons).

Laboratory based sources with small X-ray spot sizes and high fluxes would be a desirable research tool which would enable studies that otherwise would only be possible to carry out in synchrotron facilities, which in many cases would not be possible due to cost limitations. To obtain such sources X-ray optics need to be used to overcome the limitations on the X-ray sources.

From the optics design point of view, it means that an ideal X-ray optic for laboratory-based systems would need to be portable, in order to fit the "working distance" of the X-ray source, and would also have to maximise the X-ray flux. The first condition eliminates Kirkpatrick-Baez systems, which work well in synchrotron facilities where the "working distance" is very large, and the second eliminates Fresnel lenses which are diffractive optics and therefore very wasteful as only a small percentage of the incoming X-rays pass through the optic.

3.5.1 Reflective X-ray optics: micro-structured optical arrays (MOA's)

Micro-structured optical arrays (MOA's) are an X-ray optic concept based on polycapillarity and microchannel plate optics(17) to focus X-rays by grazing incidence reflection along actively aligned channels.

A design of a first MOA X-ray optic prototype was carried out by Prewett et al. in 2001(31) where the MOAs were manufactured using deep silicon etching techniques over a membrane and the actuation was obtained using a pressure differential between the two sides of the membrane as depicted in Figure 3.12a. Work on the MOA concept followed from 2005 to 2007(33-35).

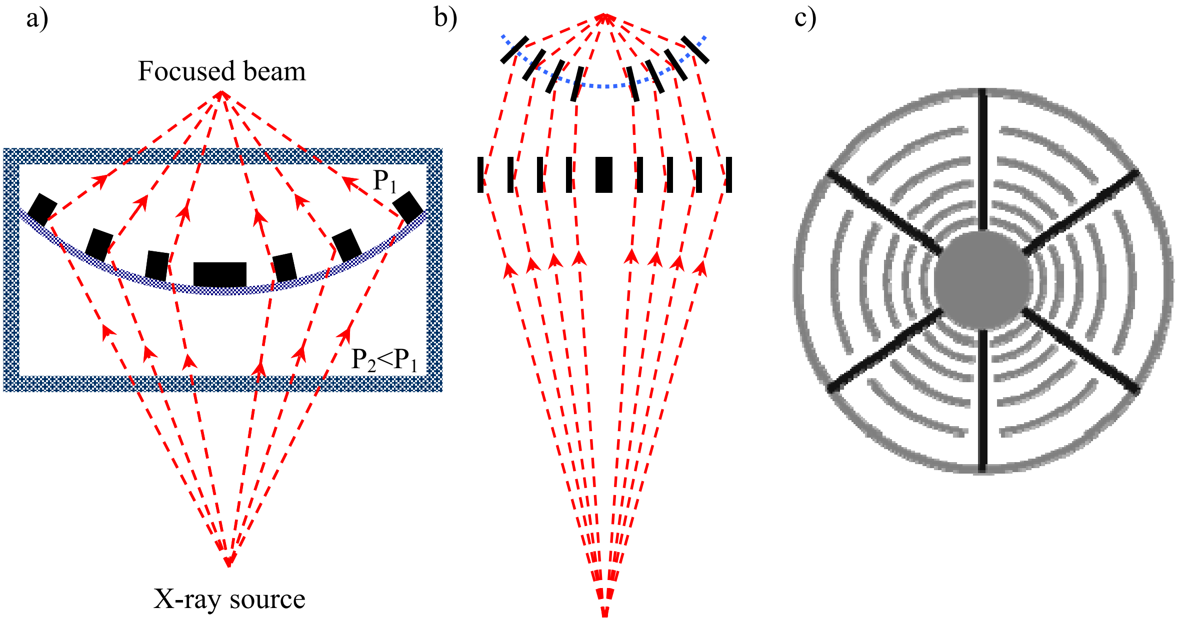

Figure 3.12: Conception of the idea of using MOA as focusing X-ray optics. a) Schematic representation of the first prototype device proposed by Prewett et al(31) where the actuation would be provided by pressure differential between the two sides of a membrane. b) Schematic representation of focusing using a flat and curved MOA's(32), and c) Schematic representation of a 2D arrangement from Michette et al(32).

The main obstacles at that moment in time were the need to obtain very smooth channels walls on the MOAs, with a surface roughness below 2nm, and at the same time find an actuation method capable of bending the MOA devices.

An even greater technical challenge would be to extend the MOA concept to obtain point focus as shown in the 2D arrangement depicted on Figure 3.12c.

Other approach was taken by Al-Aioubi et al.(33, 34, and 35) who developed X-rays optics mounted on thin cantilever beam where the actuation was provided using unimorph piezoelectric actuators.

3.6 Summary

The physics of X-rays imposes three restrictions on the design of reflective X-ray optics: they need to operate at glazing angles below two degrees; the optic surfaces need to have a surface roughness as small as possible (as least below 10nm); the surfaces need to be placed very accurately to conform to the shapes described by the Wolter I, II and III or the Kirkpatrick-Baez configurations to achieve X-ray focussing.

In practice this means that X-ray optics are customized depending on the application, with the three main applications being optics for X-ray telescopes, synchrotron X-ray sources and laboratory based X-ray sources. Each application faces different challenges.

For X-ray telescopes, which need to comply with the strict weight and size limitations, Wolter I is the dominant configuration as the optics can be nested inside each other providing increased flux. Current X-ray telescopes need to reach a compromise between the resolution, which is function of how well the optic conforms to the theoretical Wolter I configuration, and the throughput, which is function of how many shells are packed inside each other.

For synchrotron X-ray sources, which can provide very high fluxes, focusing can be achieved using a combination of Kirkpatrick-Baez mirrors, which can be made active using push/pull actuators, and Fresnel zone plates, enabling close to diffraction limited images.

X-ray optics for laboratory based X-ray systems are the less developed of the three. Current systems use diffractive Fresnel zone plates, but these produce very low focused fluxes and therefore limit their possible applications. Micro structured optical arrays, based on polycapillarity and microchannel plate optics, are reflective X-ray optics, where X-rays would be focused by the reflection on microchannels etched on a substrate providing increased fluxes compared to Fresnel zone plates. However, technical challenges for the development of these optics needed to be met and are objective of the present study and described in detail in Chapter VII.

3.7 References

1. Röntgen, W.K., *Ueber eine neue Art von Strahlen (On a new kind of rays).* Annalen der Physik, 1898. **300**(1): p. 1-11.
2. *Siemens Somaton Emotion Brochure, http://www.medical.siemens.com/siemens/en_GB/gg_ct_FBAs/files/brochures/SOMATOM_Emotion_Brochure_16705990_3.pdf (Last accessed 01-02-2010).*
3. *Modern developments in X-ray and Neutron Optics*. Springer series in optical sciences, ed. A. Erko, et al. Vol. 137. 2008, New York: Springer. 553.
4. Bass, M., et al., eds. *Volume III: Classical Optics, Vission Optics, X-ray Optics*. 1st ed. Handbook of Optics, ed. E.i.C. Michael Bass. Vol. III. 2001, McGraw-Hill: New York.
5. Paganin, D.M., *Coherent X-Ray Optics*. 1 ed. Oxford Series on Synchrotron Radiation. 2006, Oxford: Oxford Science Publications. 411.
6. *Xradia website, http://www.xradia.com/products/nanoxct-100.php (Last accessed 1-03-2010).*
7. Compton, A. and Allison S., *X-rays in theory and experiment*. Second ed. 1935, New York: D. Van Nostrand company, inc. 828.
8. Henke B.L., Gullikson E.M., and Davis J.C., *X-ray interactions: Photoabsorption, scattering, transmission and reflection at e=50-30,000eV, z=1-92*. Atomic data and nuclear data tables. Vol. 54:181. 1993.
9. *Centre for X-ray Optics, http://henke.lbl.gov/optical_constants/layer2.html (Last accessed 01-03-2010).*
10. Dunare C., Parkes W., Stevenson T, Michette A., Pfauntsch S., Sahraei S., Shand M., Zhang D., Rodriguez-Sanmartin D. Button T.W., Feldman C., Willingale R., Doel P., Wang H. and James A. Microstructured optical arrays for smart x-ray optics. EUV and X-Ray Optics: Synergy between Laboratory and Space, 2009. 7360(1): p. 736015.
11. Kirkpatrick, P. and A.V. Baez, *Formation of Optical Images by X-Rays.* Journal of the Optical Society of America, 1948. **38**(9): p. 766-774.
12. Wolter, V.H., *Verallgemeinerte schwarzschildsche spiegelsysteme streifender reflexion als Optiken fur riinfgenstrahlen (Generalized schwarzchil mirror systems with glancing incedence as optics for X-rays).* Annalen der Physik, 1952. **6**(10): p. 286-295.
13. Aschenbach, B., *X-Ray Telescopes.* Reports on Progress in Physics, 1985. **48**(5): p. 579-629.
14. The Telescopes of XMM-Newton, http://xmm.esac.esa.int/external/xmm_user_support/documentation/technical/Mirrors/index.shtml (last accesed 14-10-2010).

15. *The Chandra X-ray Observatory* *http://www.nasa.gov/mission_pages/chandra/main/index.html (Last accessed 02-03-2010).*

16. Cameron R.A., Bautz, M.W., Brissenden R.J., Elvis M.S., Fabbiano G., Figueroa-Feliciano E., Gorenstein, P., Petre R., Reid P.B., Schwartz D.S., White N.E., Zhang W.W. Generation-X: Mission and technology studies for an X-ray observatory vision mission, in Uv and Gamma-Ray Space Telescope Systems, Pts 1 and 2. 2004, SPIE-INT SOC OPTICAL ENGINEERING: Bellingham. p. 572-580.

17. MacDonald, C.A. and W.M. Gibson, *Applications and advances in polycapillary optics.* X-Ray Spectrometry, 2003. **32**(3): p. 258-268.

18. Beijersbergen M., Kraft S., Bavdaz M., Lumb D., Gunther R., Collon M., Mieremet A., Fairbend R., Peacock A., Development of X-ray pore optics: novel high-resolution silicon millipore optics for XEUS and ultra-low mass glass micropore optics for imaging and timing. Design and Microfabrication of Novel X-Ray Optics Ii, 2004. 5539: p. 104-115.

19. Price, G.J., Brunton A.N., Fraser G.W., Bavdaz M., Beijersbergen M.W., Boutot J.P., Fairbend R., Flyckt S.O., Peacock A. and Tomaselli E. Hard X-ray imaging with microchannel plate optics. Nuclear Instruments & Methods in Physics Research Section a-Accelerators Spectrometers Detectors and Associated Equipment, 2002. 490(1-2): p. 290-298.

20. Beijersbergen M.W., Bavdaz M., Peacock A., Tomaselli E., Fairbend R., Boutot J.P., Flyckt S.O., Brunton A., Price G., Fraser G., Herrmann C., Krumrey M., Ziegler E. and Freunde, A. High-resolution micro-pore X-ray optics produced with micro-channel plate technology. Advances in X-Ray Optics, 2000. 4145: p. 188-192.

21. Mutz, J.L., Bonnet O., Fairbend R., Schyns E., Seguy, J., Micro-pore optics: from planetary X-rays to industrial market - art. no. 64790F. Quantum Sensing and Nanophotonic Devices IV, 2007. 6479: p. F4790-F4790.

22. Koshiishi, M., Ezoe Y., Mita M., Maeda Y., Mitsuda K., Suzuki M., Osawa T., Hoshino A., Ishisaki Y., Takano T. and Maeda, R. The first light of a single-stage MEMS x-ray optic - art. no. 668814. Optics for Euv, X-Ray, and Gamma-Ray Astronomy Iii, 2007. 6688: p. 68814-68814.

23. Peele A.G., Lyngsjo H., Crocker R.M., Markham J., Bannister N., and Nugent K.A. Modeling of the Lobster-ISS x-ray telescope in orbit. Uv and Gamma-Ray Space Telescope Systems, Pts 1 and 2, 2004. 5488: p. 232-241.

24. Duke, P.J., *Synchrotron radiation: production and properties*. First ed. Oxford series on synchotron radiation, ed. C. J., H. J.R., and L. S.W. 2000, New York: Oxford University Press. 251.

25. Bilderback, D.H., P. Elleaume, and E. Weckert, *Review of third and next generation synchrotron light sources.* Journal of Physics B-Atomic Molecular and Optical Physics, 2005. **38**(9): p. S773-S797.

26. Marcus, M.A., MacDowell A.A., Celestre R., Manceau A., Miller T., Padmore H.A. and Sublett R.E. Beamline 10.3.2 at ALS: a hard X-ray

microprobe for environmental and materials sciences. Journal of Synchrotron Radiation, 2004. 11: p. 239-247.

27. Eng, P.J., Newville M., Rivers M.L., Sutton S.R, Dynamically figured Kirkpatrick Baez x-ray micro-focusing optics. X-Ray Microfocusing: Applications and Techniques, 1998. 3449: p. 145-156.

28. Howells M.R., Cambie D., Duarte R.M., Irick S., MacDowell A.A., Padmore H.A., Renner T.R., Rah S. and Sandler R., Theory and practice of elliptically bent x-ray mirrors. Optical Engineering, 2000. 39(10): p. 2748-2762.

29. Chao W., Kim J., Rekawa S., Fischer P. and Anderson E.H., Demonstration of 12 nm Resolution Fresnel Zone Plate Lens based Soft X-ray Microscopy. Optics Express, 2009. 17(20): p. 17669-17677.

30. Vila-Comamala J., Borrise X., Perez-Murano F., Campos J. and Ferrer S. Nanofabrication of Fresnel zone plate lenses for X-ray optics. Microelectronic Engineering, 2006. 83(4-9): p. 1355-1359.

31. Prewett, P.D. and A.G. Michette, *MOXI: A novel microfabricated zoom lens for x-ray imaging.* Advances in X-Ray Optics, 2001. **4145**: p. 180-187.

32. Michette A., Button T.W., Dunare C., Feldman C., Folkard M, Hart D., McFaul C., Morrison G.R., Parkes W., Pfauntsch S., Powell A.K., Rodriguez-Sanmartin D., Sahraei S., Stevenson T., Vojnovic B., Willingale R. and Zhang D. Active microstructured arrays for x-ray optics. in Advances in X-Ray/EUV Optics and Components II. 2007: SPIE.

33. Al Aioubi M.Y., Prewett P.D., Huq S.E., Djakov V. and Michette A.G. Design and fabrication of micro optical system for X-ray analysis of biological cells. Opto-Ireland 2005: Optoelectronics, Photonic Devices, and Optical Networks, 2005. 5825: p. 640-646.

34. Al Aioubi M.Y., Prewett P.D., Huq S.E., Djakov V. and Michette A.G., *A novel MOEMS based adaptive optics for X-ray focusing.* Microelectronic Engineering, 2006. **83**(4-9): p. 1321-1325.

35. Al-Aioubi, M.Y, Prewett P.D., Huq S.E., Djakov V. and Michette A.G. *Micro-opto-electro-mechanical system for X-ray focusing.* Microelectronic Engineering, 2007. **84**(5-8): p. 1252-1255.

CHAPTER 4

PIEZOELECTRIC ACTUATORS

PHYSICS, MANUFACTURING & DESIGN

4.1 Introduction

The piezoelectric effect was first discovered by the Curie brothers in 1880 when they discovered that variations in pressure in asymmetric crystals, quartz and topaz among them, generated electric polarization(1). In the decades that followed, physical models were developed to understand these effects but the advent of the first piezoelectric technology had to wait until World War I when piezoelectric transducers were developed for sonar applications. The capabilities of the technology were further increased with the discovery of multi-crystalline piezoelectric materials, first Barium Titanate and then with Lead Zirconate Titanate (PZT) which can exhibit high piezoelectric coefficients. At present, developments on the manufacturing techniques of multi-crystalline piezoelectric materials, for example enabling their integration onto silicon substrates, are driving forward the technology to an increased number of applications for Micro Electro Mechanical Systems (MEMS).

From the point of view of a device design there are four main points that need to be considered: the physics of piezoelectric materials; piezoelectric materials and their properties; the manufacturing processes of piezoelectric materials; and finally their design including possible geometries, operation modes and electrode configurations.

This chapter intends to give a general background of these four issues with emphasis on the application of piezoelectric materials as actuators. The aim is to provide the necessary knowledge to understand which design options are best for particular applications where piezoelectric actuation is required.

4.2 The physics of piezoelectric actuators

Piezoelectricity is a physical effect which couples two sets of variables; the applied stress with the voltage or the applied voltage with the strain. For example, assuming a piezoelectric material in the shape of a thin disk, an applied stress will generate a charge in its faces. This is known as the direct piezoelectric effect, where the piezoelectric material works as a generator. Conversely, if a voltage is applied to the faces of a piezoelectric disk both its thickness and radius changes, this is called the indirect piezoelectric effect, where the piezoelectric material is said to be working as a motor.

The definitions above represent a macroscopic description of piezoelectricity but in order to gain a deep understanding of piezoelectric behaviour several factors which determine its behaviour need to be understood:

i) The crystallographic structure of a material, which requires an imbalance in the charges of the unit cell, i.e. a net polarization, in order to be piezoelectric;

ii) The phase diagram of the materials system in question, so that the influence of conditions such as temperature and material composition on the crystallographic structures which generate piezoelectric behaviour can be understood;

iii) The distribution of the polarization at a microscopic level. This determines if the material presents piezoelectric behaviour. A random distribution would have zero overall polarization whereas an uniform alignment would provide maximum polarization;

iv) Materials with a random polarization distribution can be changed to materials with a preferred direction of polarization following a poling process.

Each of the four factors above dictate the behaviour of piezoelectric ceramics (which are multi-crystalline materials by definition), but when their behaviour is dominated by changes at the crystallographic level linear piezoelectricity theory can be used to describe stress/charge coupling. However, the linear theory is limited to small input fields and for larger fields non-linear effects such as hysteresis are exhibited.

4.2.1 The crystallographic structure of Perovskite Electroceramics

The piezoelectric behaviour is ultimately dependent on the crystallographic structure of the material and for a material to exhibit piezoelectric behaviour it needs to present polarization in its unit cell. Figure 4.1 shows the crystallographic unit cells for three phases of Lead Lanthanum Zirconate Titanate (PLZT) Perovskite ceramic (cubic, tetragonal and rhombohedral). The arrows indicate the polarization direction in the tetragonal and rhombohedral phases. Because the polarization direction is determined at the unit cell level, only certain polarization directions are compatible with the crystallography of tetragonal and rhombohedral structure with six and eight equivalent directions respectively. The same arguments are valid for other materials with the same crystallographic structures$^{(2)}$.

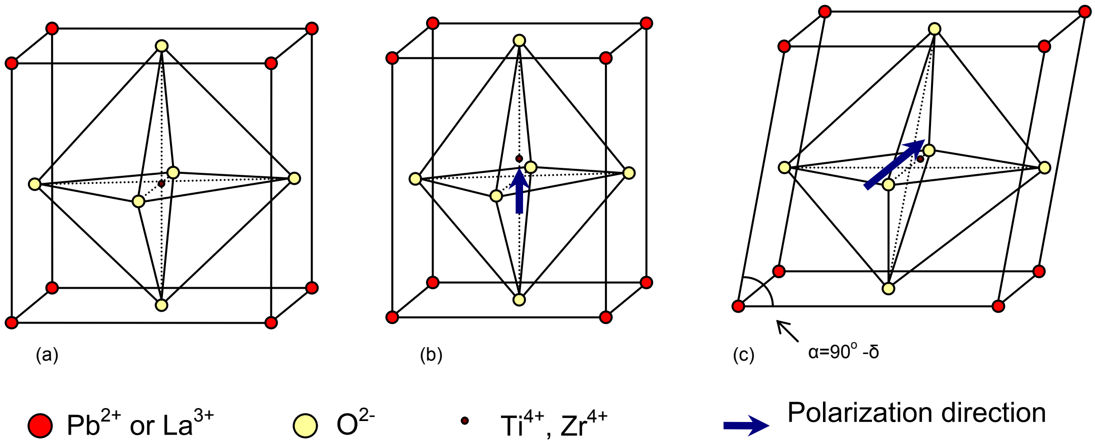

Figure 4.1: Crystallographic structure for the (a) cubic, (b) tetragonal and (c) rhombohedral phases in a PLZT Perovskite crystal. The arrow indicates the polarization direction. Only certain polarization directions are compatible with the crystallography of tetragonal and rhombohedral structures$^{(2)}$.

Materials with cubic symmetry do not exhibit piezoelectricity as all the charges within the unit cell are balanced. In the case of materials with tetragonal structure, the atom at the centre of the unit cell is slightly off-centre, which creates an imbalance in the charge distribution of the cell and therefore a net polarization. An applied pressure slightly changes the positions within the atoms of the unit cell and therefore the magnitude of its polarization (direct piezoelectric effect). On the contrary, an applied electric field would generate a change in the dimensions of the unit cell (inverse piezoelectric effect).

However, for sufficiently extreme conditions the arrangement of the atoms in the unit cell change which in turn changes the direction of the polarization. Figure 4.2 shows the six possible polarization directions for the tetragonal phase corresponding to the 90° and the 180° degree switching obtained using symmetry arguments on the tetragonal unit cell.

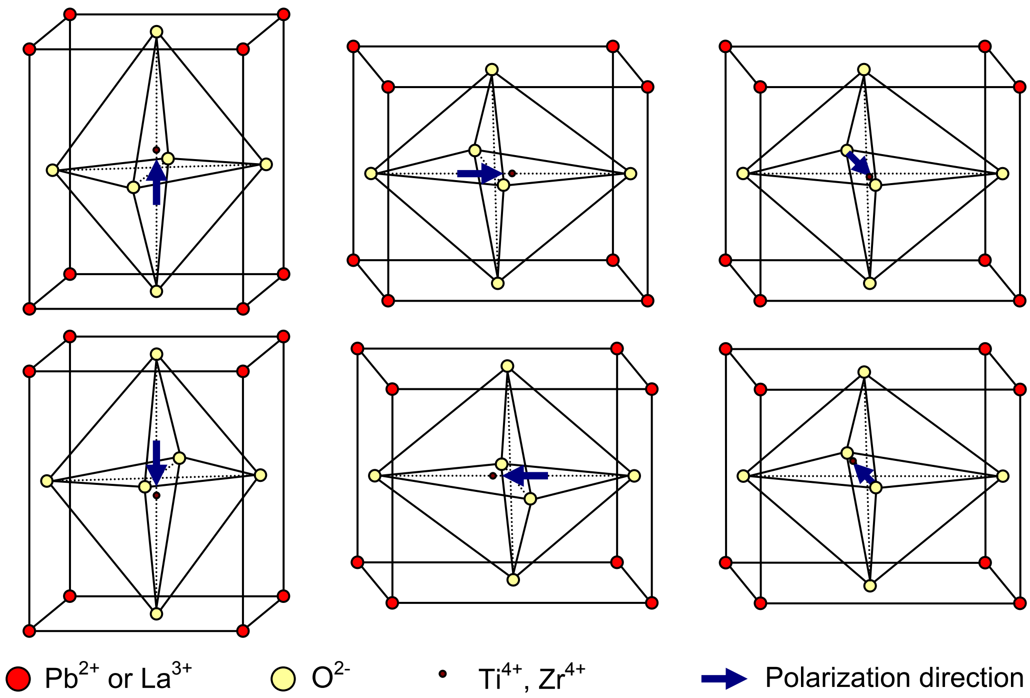

Figure 4.2: The six equivalent directions for the tetragonal phase corresponding to the 90^{o} and the 180^{o} degree domain switching obtained using symmetry arguments on the tetragonal unit cell (<100> directions). Symmetry arguments on the rhombohedral, <111> directions, unit cell can also be used to visualise its eight equivalent directions (190^{o}, 71^{o}, 109^{o} domain switching).

Symmetry arguments on the rhombohedral unit cell can also be used to visualise their possible polarization directions as summarised in the Table 4.1 below:

Table 4.1: Polarization switching directions allowed for tetragonal and rhombohedral structures$^{(2)}$.

Crystallographic Structure	**Polarization direction allowed**	
Tetragonal	180^{o}, 90^{o}	6 equivalent directions
Rhombohedral	180^{o}, 71^{o}, 109^{o}	8 equivalent directions

4.2.2 Piezoelectric domains

As a first approximation piezoelectric materials have a uniformly distributed polarization and changes in the applied stress or electric field have an impact on the dimensions of the unit cell which in turn changes the polarization of the material in what is referred to as intrinsic effects in the literature. However, as J.M. Merz found for $BaTiO_3$ in the 1950's(3), the distribution of the polarization in real materials is more complex as it is arranged in different regions, referred to as domains, with the same direction of polarization. From an energy perspective, the distribution of the domains is such that the material is in a stable state and minimises the energy within the material. Therefore, the net polarization seen in a material is the result of the average of the polarizations in each one of its domains. Figure 4.3 shows pictures and schematics of early work by J.M. Merz for $BaTiO_3$ in which piezoelectric domains and domain walls were first observed. Notice that the domains either have 90^o or 180^o changes which correspond with those allowed by the crystallography of the tetragonal crystals as previously described in Figure 4.2.

In a succession of papers in the early 1950's W.J.. Merz was the first to explain how domains changed for single crystals of barium titanate ($BaTiO_3$)(3-5). Using polarized light to visualise the domains in the surface of the $BiTiO_3$ samples he discovered that the domain switching is controlled by the nucleation of new domains and the speed at which the domains walls move. Both nucleation and domain wall movement are dependent on the applied field, stress and temperature. Further work was published by Berlincourt and Helmut in 1959(2) for lead zirconate titanate (PZT) ceramics and others followed for other piezoelectric materials(6). Even though there is a vast amount of data available in the literature, a unified and simple model capable of describing domain switching for all piezoelectric materials does not yet exist. Instead a variety of approaches and phenomenological models are used depending on the application.

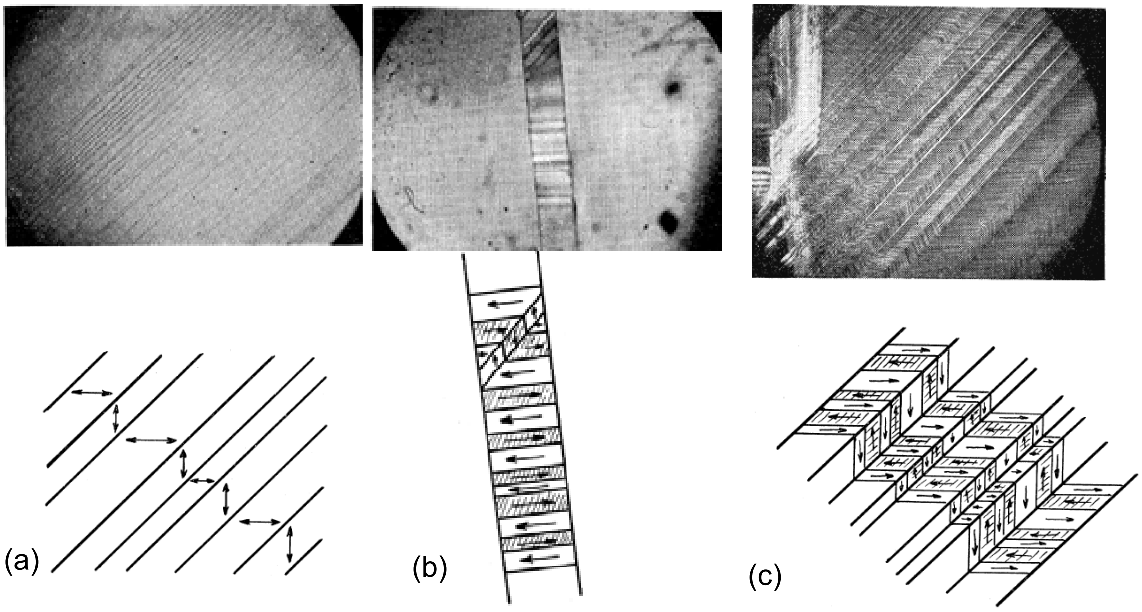

Figure 4.3: Photos and schematic sketches of domain walls in $BaTiO_3$ single crystals taken from WJ Merz, Physical Review, 1954 (3). (a) 90° walls between domains, (b) 180° antiparallel domain walls at the edge of a crystal, (c) 180° and 90° walls in the crystal surface.

4.2.3 The PZT phase diagram

The phase diagram is very useful tool for the visualisation of phase transitions. Figure 4.4 shows the phase diagram of PZT(7). For other commonly used piezoelectric materials (PMN-PT, $LiNbO_3$, $BaTiO_3$,) phase diagrams including the effects of dopants are available in the literature(8-10).

The Curie point marks the temperature at which the transition from the tetragonal or rhombohedral to cubic phase occurs. For PZT it is dependent on the Zr and Ti relative concentrations and also on the concentration of dopants. The material is no longer ferroelectric above the Curie temperature since only the cubic phase is present and instead it is paraelectric.

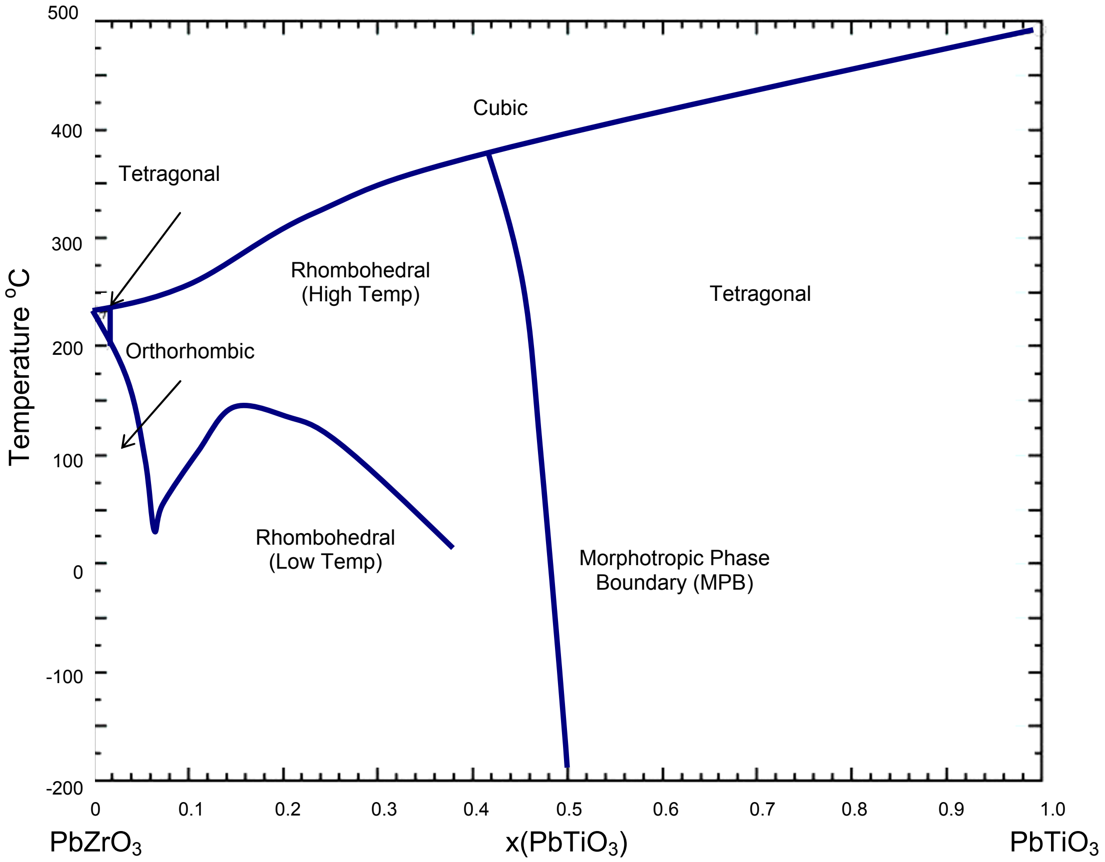

Figure 4.4: Phase diagram of Lead Zirconate Titanate. Bouzid et al 2005(7). The Curie temperature occurs in the transition between the cubic and the rhombohedral of tetragonal phases.

Another important feature in the PZT phase diagram is the morphotropic phase boundary (MPB) at which both the rhombohedral and tetragonal phases coexist. Compositions corresponding with the MPB are a popular choice as properties of both phases are present in the piezoelectric material leading to a maximum in the important properties.

For poled ceramics as the temperature increases the remnant polarization decreases until eventually, when the temperature reaches the Curie point, the polarization disappears as the piezoelectric phase is lost(11).

It is also known that as the temperature decreases the polarization remains constant although the material will become more resilient to a change in its polarization when an electric field or and stress is applied. Decreasing the temperature is a way of separating the intrinsic (ionic origin) and extrinsic (wall motion) contributions to the piezoelectric behaviour as at sufficiently low temperatures the piezoelectric behaviour is only intrinsic.

4.2.4 Poling of piezoelectric ceramics

Polycrystalline materials can also exhibit piezoelectric properties; in fact materials with the best piezoelectric properties are polycrystalline like lead zirconate titanate (PZT) or barium titanate. In these materials, as the crystallographic orientation and thus polarization direction of their grains are random the net polarization is zero on average. For all directions there are the same number domains pointing with the polarization oriented in that direction as there are with domains oriented in the opposite direction, so on average they cancel each other.

To make a polycrystalline exhibiting net polarization, which is referred in the literature as becoming active, it has to be submitted to a process in which the polarizations of each individual domain switch from their initial state to one of the other allowed states in a way in which, on average, the sample exhibits a net polarization. This process is referred to as poling, which needs to be carried out at a temperature below the Curie temperature (T_c).

During the poling process the piezoelectric ceramics are heated up to a poling temperature (T_p) below, but close to, their Curie temperature (T_c). The increase in temperature injects thermal energy into the material and increases the mobility of the domain walls. At the same time, the ceramic is subjected to a high poling electric field (E_p), typically E_p=2.5V/µm, which results in the growth of domains with directions approximately parallel to the applied external field at the expense of others which are not parallel. These conditions are maintained for a period of time (t_p), usually around 10-20 minutes, after which the sample is cooled down again to room temperature and the applied voltage reduced to zero. The exact poling temperature, electric field and duration of the poling conditions (E_p, T_p and t_p) can be optimized depending on the material, geometry and poling method used. Detailed information on the poling process has been published by Kamel et et al(11, 12).

When the temperature is reduced at the end of the poling process the new directions of polarization remain fixed which in turn means that the average polarization direction changes from being zero before poling to a net polarization in the same direction as the applied poling field. The domain configuration of the piezoelectric material for the cases, before, during and after poling is depicted in the schematic representation in Figure 4.5 below. The domains are reoriented during the poling procedure to produce a net polarization in the material.

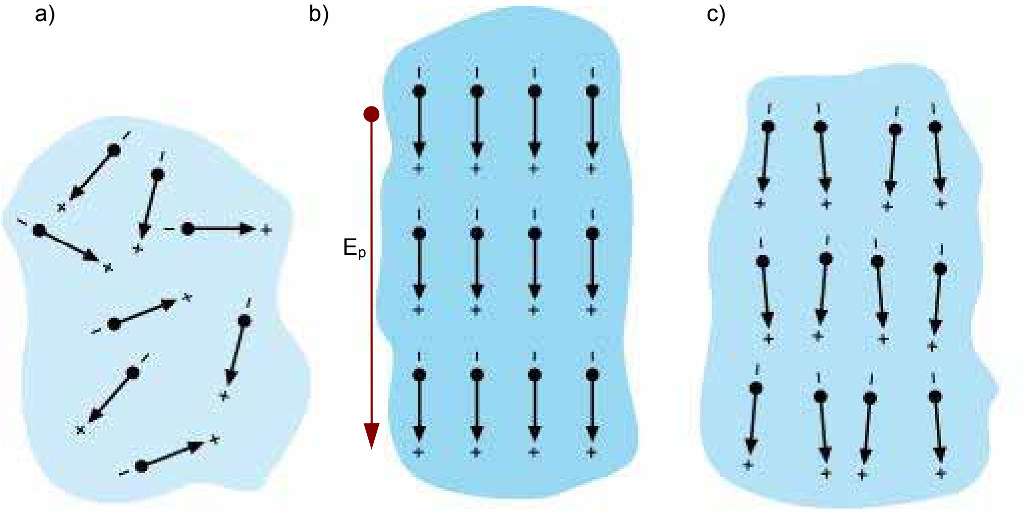

Figure 4.5: Schematic representation of the changes in the polarization direction in multi-crystalline materials. a) Domain orientation of un-poled material. b) Domain orientation during the poling process. c) Domain orientation after the poling process(13).

4.2.5 Linear Piezoelectricity

When small electric fields or external pressure are applied to piezoelectric ceramics their behaviour is dominated by the changes in atom positions in the unit cells of the ceramic. This is known as the intrinsic effect and the piezoelectric behaviour is approximately linear.

Linear piezoelectricity is a very well established theory, and as it is very well described in multiple reference books, see Moulson and Herbert for example(14). Equations 4.1 & 4.2 show the piezoelectric constitutive equations in the Strain-Charge form, other formulations are possible depending of the choice of independent variables. These equations couple the piezoelectric and elastic behaviour when an Electric Field (E) and a Stress (T) are applied to the material.

$$\vec{S} = S_{ij} \cdot \vec{T} + d_{ij} \cdot \vec{E}$$ **Equation 4.1**

$$\vec{D} = d_{ij}{}^{T} \cdot \vec{T} + \varepsilon_{ij} \vec{E}$$ **Equation 4.2**

Where:

$\vec{S}$	is the strain
S_{ij}	is the 6×6 matrix of elastic coefficients
$\vec{T}$	is the stress
d_{ij}	is the 3×6 matrix of piezoelectric coefficients
$\vec{E}$	is the electric field
$\vec{D}$	is the electric displacement
$d_{ij}{}^{T}$	is the transpose matrix of piezoelectric coefficients
ε_{ij}	is the matrix of dielectric coefficients

Notice that the equations are written in matrix form and therefore require the definition of a coordinate system in the material. A standard convention, as depicted in Figure 4.6 for a piezoelectric plate poled along its thickness, is normally used in the literature where the 3 axis (z) coincides in direction with the direction of polarization in the material and the 1 axis (x) and 2 axis (y) are orthogonal to the polarization direction and the 4, 5 and 6 indexes accounting for the shear direction along the x, y and z axes respectively. For more complex arrangements where the direction of the polarization is not uniform the axis convention need to be defined to account for this.

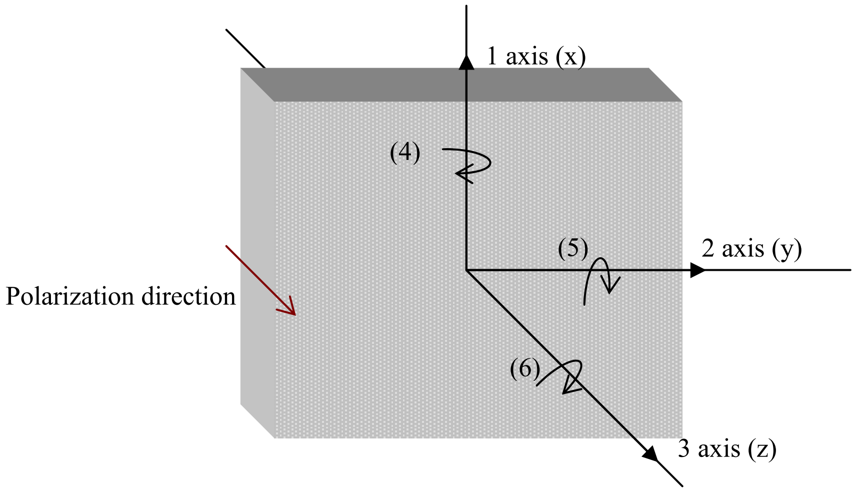

Figure 4.6: Axis convention for a square piezoelectric plate poled through its thickness. By convention the 3 axis (z) is chosen as the poling direction. The index 4, 5 and 6 are used to label the shear modes around the 1, 2 and 3 axis respectively.

In 4.1 & 4.2 d_{ij} represents a 6×6 matrix of piezoelectric coefficients which can be simplified for isotropic materials by using symmetry arguments, as shown in 4.3. The *i* index (which can take the values 1, 2 or 3) refers to the component of the applied electric field which the coefficient couples and the index j (which can take entire values from 1 to 6), refers to which axis the coefficient applies to.

$$d_{ij} = \begin{bmatrix} 0 & 0 & d_{31} \\ 0 & 0 & d_{31} \\ 0 & 0 & d_{33} \\ 0 & d_{15} & 0 \\ d_{15} & 0 & 0 \\ 0 & 0 & 0 \end{bmatrix}$$

Equation 4.3

In a similar way symmetry arguments can be used to simplify the compliance matrix as shown in the 4.4 below.

$$S_{ij} = \begin{bmatrix} S_{11}^{E} & S_{12}^{E} & S_{13}^{E} & 0 & 0 & 0 \\ S_{12}^{E} & S_{11}^{E} & S_{13}^{E} & 0 & 0 & 0 \\ S_{13}^{E} & S_{13}^{E} & S_{33}^{E} & 0 & 0 & 0 \\ 0 & 0 & 0 & S_{44}^{E} & 0 & 0 \\ 0 & 0 & 0 & 0 & S_{44}^{E} & 0 \\ 0 & 0 & 0 & 0 & 0 & S_{66}^{E} = 2\left(S_{11}^{E} - S_{12}^{E}\right) \end{bmatrix}$$

Equation 4.4

where the superscript E symbolizes that the elastic coefficients are measured for a constant electric field.

It is reasonable to make the assumptions that for randomly oriented polycrystalline piezoelectric materials their total volume would remain constant, and that their behaviour is isotropic in the x and y directions. These assumptions mean that that for a given change in the thickness along the z direction due to an electric field applied in this direction, which is given by d_{33} , a change in dimensions of opposite sign but half the magnitude would be observed in the x and y directions of the material, given by d_{31}. Therefore the expression 4.5 below applies for isotropic materials.

$$d_{33} \approx -2d_{31}$$

Equation 4.5

Another possible piezoelectric interaction is the shear mode which occurs when an electric field perpendicular to the poling direction generates a shear on the piezoelectric device and is quantified by the piezoelectric coefficient d_{15}. The equations above describe the thickness, transversal and shear coupling modes as depicted in the schematic representation in the Figure 4.7 below.

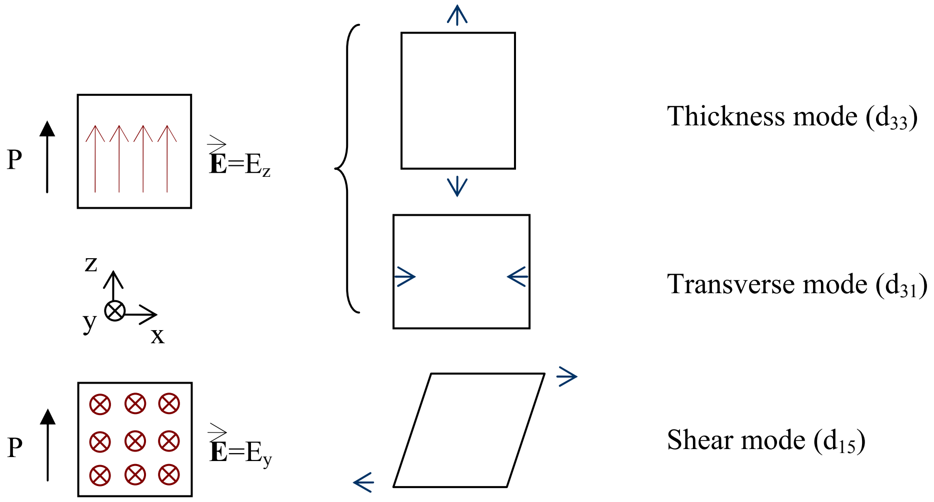

Figure 4.7: Two dimensional schematic representations of the thickness, transverse and shear modes when an electric field is applied along the thickness and parallel to the polarization in a piezoelectric ceramic.

4.2.6 Non-linear Piezoelectricity

Linear piezoelectricity is valid when small applied fields are used. However, when high external fields are applied new domains nucleate and/or grow at each other's expense until eventually a new domain configuration within the material is reached. These are known as extrinsic effects and these can introduce non linear behaviour such as hysteresis in the material. In practice this means that the material has a memory effect, and therefore future responses are not only dependent on the current condition but also on its electrical and mechanical history. Understanding which factors are dominant in controlling domain nucleation and domain wall movement is a very active field of research in the search for piezoelectric materials with ever increased properties.

4.2.6.1 Polarization and strain dependency of the electric field

The polarization and strain major hysteresis loops when quasistatic fields are applied are shown in Figures 4a & 4b respectively. There is a correlation between both diagrams as the polarization state of a sample determines its electric field / strain working regime.

The polarization diagram can be described as follows: Firstly, in order for the sample to present a net polarization it needs to be poled following the procedure previously described in Section 4.2.4. This is represented by the red dotted line which departs from a non-poled state at the origin, where the domain distribution is random, as represented by the striped yellow and blue hexagon. The poling process ends when the polarization reaches its spontaneous polarization value (P_S), which is represented by a completely blue hexagon with a white arrow indicating the direction of polarization.

Secondly, when the electric field is reduced from it maximum value back to zero the sample remains with a remnant polarization $P_R<P_S$, represented by a hexagon which is mostly blue in the diagram. Variations in the applied field around zero will now produce a linear piezoelectric response as changes in the polarization are small. However, if high negative fields are used, the domains in the sample will switch in directions favourable to the applied field, until eventually, for the coercivity value $-E_C$ the net polarization is zero as some of the domains switch their polarization in the direction of the negative electric field (state represented by a striped hexagon). Further increases in the magnitude of the electric field in the negative direction electric field

will pole the sample in the opposite direction, in a state represented by a yellow hexagon but with an arrow representing the polarization pointing downwards. A similar line of reasoning explains the other branch of the major hysteresis loop increasing the electric field from $-P_S$ to P_S.

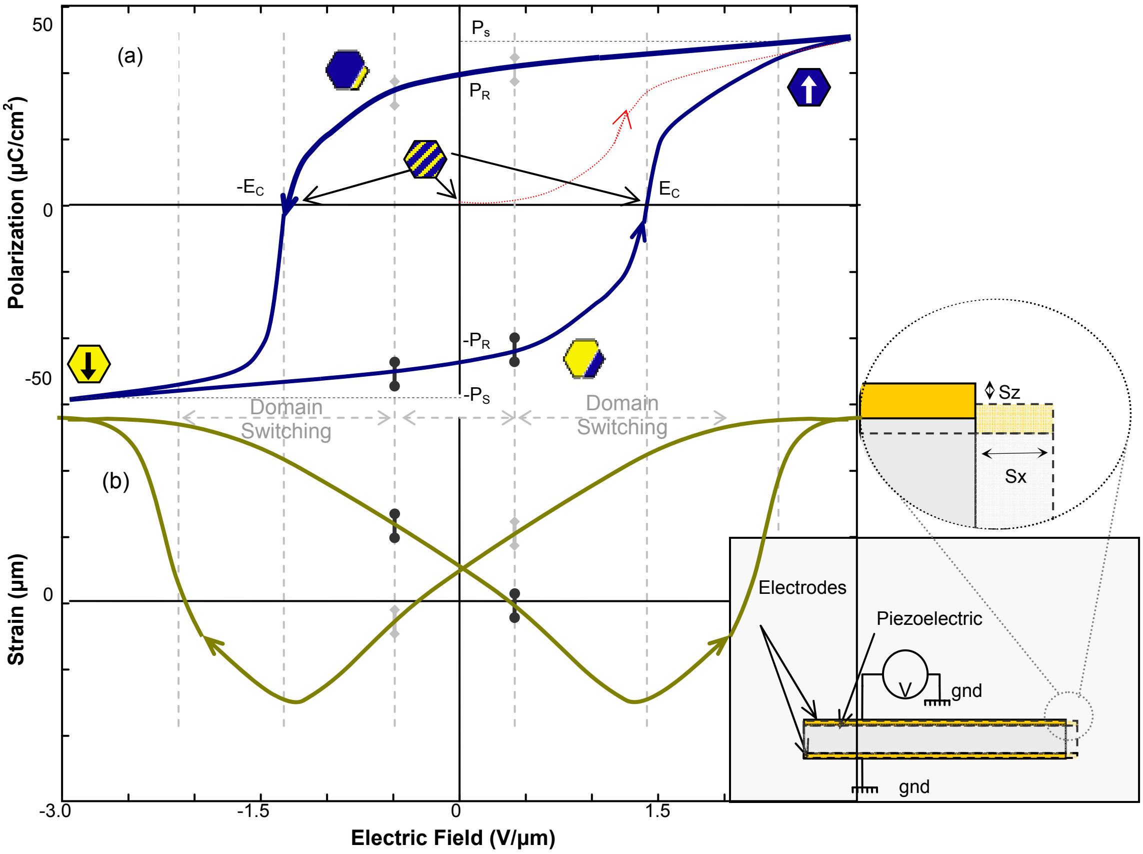

Figure 4.8: (a) Typical ferroelectric Polarization– Electric field (P-E) and (b) Strain-Electric field (S-E) hysteresis loops for a cantilever. The hexagons represent different states of polarization within the material at different points of the hysteresis cycle(15). The Inset shows typical sample and test configuration.

The lower part of the diagram (Figure 4.8b) represents the strain response to the applied field. It can be seen that for small electric fields the polarization is either P_R (positive) or $-P_R$ (negative) and in both cases remaining approximately constant. This means that the strain/electric field response is approximately linear. The limits of the two possible linear regimes are represented in the diagrams with the signs: ↕ for $P=P_R$ and ↨ for $P=-P_R$.

If it is assumed that the sample is within the linear regime for $P=P_{R,}$ and the electric field is decreased beyond the linear regime, domain switching would begin to occur in the sample as a response to the negative field taking the strain response out of the linear regime. Eventually domain switching will dominate and the strain increases rather than decreases as it would do if the behaviour were linear. If the electric field is further decreased to its minimum value the polarization direction completely changes and the strain reaches its maximum value. If now the electric field were reduced to zero, the strain/electric field response would follow the other branch of the hysteresis loop as the polarization in the sample has now changed to $P=-P_R$. A similar argument could be made to obtain the other branch of the hysteresis loop if the electric field is now increased to its maximum positive value and decreased again to zero.

4.2.6.2 Strain and polarization dependency of the applied stress

Schaufele and Hardtl set up an experiment in which they measured the compressive strain and depolarization as a function of the applied stress for different types of PZT ceramics(16). As a result of a phase change some materials may exhibit a spontaneous strain, what is normally know as ferroelastic behaviour. This was also investigated by Schaufele and Hardtl by applying simultaneously stress and an electric field to the piezoelectric samples.

Figure 4.9 shows a schematic representation of the stress and depolarization response for an applied stress. For compressive stresses below a threshold value T_{t1} the behaviour is linear (A-B). However, for compressive stress values over this threshold 90^o domain switching starts to occur in order to minimize the internal energy of the material (B-C). If the compressive stress is further increased a threshold value T_{t2} will be reached where all the domains have switched, and therefore the sample enters another linear regime (C-D). If now the stress is reduced the sample will maintain the switched state until a tensile stress threshold T_{t3} is reached to switch back the domains.

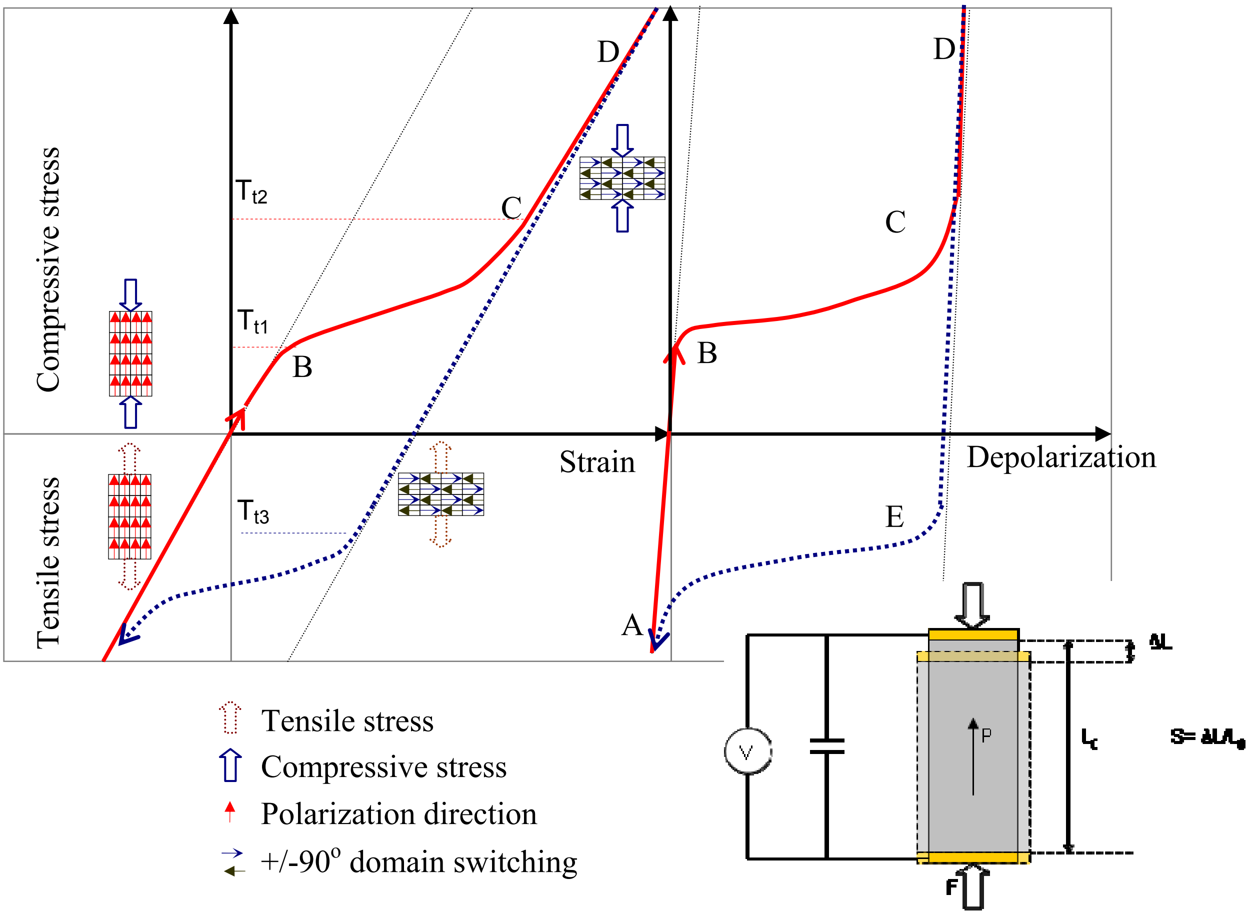

Figure 4.9: Schematic of the dependence of the strain and depolarization with the stress. Adapted from Schäufele and Härdtl, 1996, to include tensile stresses (16). A→B is the linear region. B→C is the non linear region, domain switching is occurring. C→D→E is a linear region, all the domains have changed direction. A→E is a non linear region (domain switching). Inset shows typical samples and test configuration.

4.2.6.3 *Other non linear effects*

A number of other effects also contribute to non-linear behaviour. After a piezoelectric sample is poled (applying a high electric field at a high voltage), it takes some time before the microstructure stabilizes and the sample provides a repeatable response. This process is known as ageing. Manufacturers usually supply samples in a aged condition.

Accommodation is a process by which a material stabilises its behaviour after being submitted to several cycles of an applied stress or electric field.

An increase in the applied stress or electric field, will have a instantaneous response, followed by a slow stabilization over the next few hours, an effect which is known as Creep(17). The ageing, accommodation and creep effects are schematically represented in Figure 4.10 below:

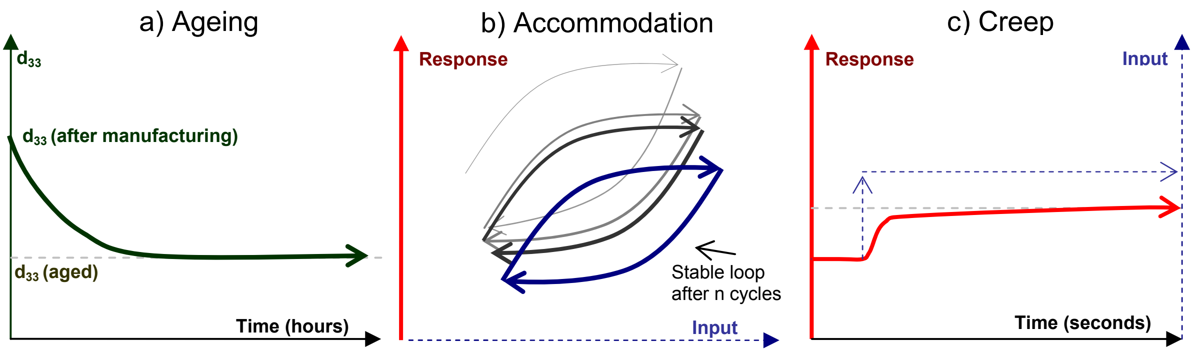

Figure 4.10: Schematic representation of the non linear processes: a) ageing, where x axis represents passed time since the manufacturing. The piezoelectric coefficients stabilize after several hours; b) accommodation and c) creep.

4.2.6.4 Non linear models of piezoelectricity

When a hysteretic system is cycled between its maximum and minimum input values (I_{min}, I_{Max}) the system's response is described by its primary hysteresis loop. However, when it cycled between other values ($I_m>I_{min}$, $I_M<I_{Max}$), the system's response is described by secondary hysteresis loops contained within the primary one. Figure 4.11 shows primary and secondary hysteresis loops and how the response R is not just dependent on the input but also of past extreme values, the system's history. In an

application where knowing the response at all times is critical, for example the position of the piezoelectric tip in an atomic force microscope, a model capable of predicting the response for any sequence of inputs would prove very useful.

The Preisach model of hysteresis is a mathematical formulation which deals with systems which present a hysteretic response. It was first published by F. Preisach in 1935(18) to describe hysteresis in magnetic materials. In magnetism it has become a well established technique but in other physical systems such as piezoelectricity, mechanical, superconducting, optical, and others it has also been used. However, as a mathematical formulation it is independent of the particular hysteretic system it is applied to.

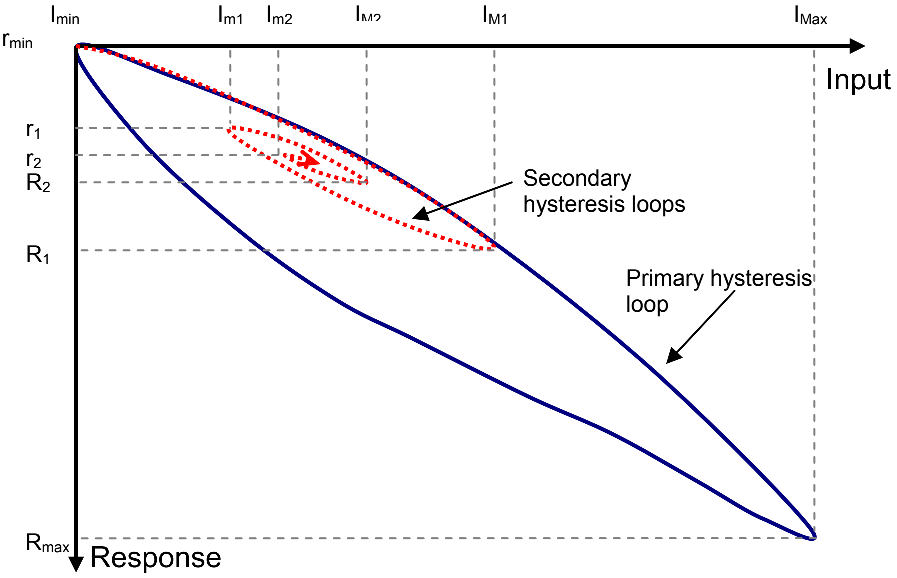

Figure 4.11: Schematic representation of a hysteretic system. The response not only depends on the input but also of the history of the system (past extreme values r_i and R_j).

The Preisach formulation for piezoelectric materials is a complex physical model and has been described in the book by I.D. Mayergoyz, “Mathematical models of hysteresis”, 1992(19), and the chapter by D. Damjanovic “Hysteresis in Piezoelectric and Ferroelectric Materials”(15). However, the complexity of the formulation means that it has only been applied with limited success to practical systems(20).

4.3 Manufacturing processes of piezoelectric actuators

The manufacturing processes of piezoelectric ceramics can be divided in two general categories: Powder-based routes, which require the milling of piezoelectric powders, consolidation and shaping, followed by sintering of piezoelectric ceramics to form dense structures. An alternative route for the manufacturing of piezoelectric ceramics is to use deposition techniques such as chemical vapour deposition or pulsed laser deposition. All the manufacturing techniques have their limitations and a different range of applications and are briefly discussed below.

4.3.1 Powder based manufacturing routes

Machining of bulk ceramics is a conventional technique for the fabrication of thin plates which could be used as actuators in a unimorph configuration. Firstly, a piece of bulk material is produced by, for example, uniaxial pressing followed by sintering. Secondly, two electrodes are applied to it, which are used for poling the bulk material under the appropriate temperature and voltage conditions. Finally, thin sheets of material can be obtained using a lapping machine until the required thickness is reached. However, there is a limit in how thin it is possible to go without revealing existing process related defects in the PZT or creating further defects, both of which would undermine its performance. In addition, only flat surfaces can be obtained.

The Viscous Plastic Process (VPP) is a technique which can be used for the fabrication of net shape ceramics(21). The size of the defects within the microstructure is minimised, obtaining enhanced mechanical and electrical properties. The main steps in the VPP are highlighted in Figure 4.12. Firstly, ceramic powder with small grain size is mixed with polymer in the green state. The presence of the polymer and the high shear mixing process avoid the reforming of agglomerates which would be responsible for large size defects. A paste is obtained which can be easily shaped. After sintering the sample, the polymer disappears and the final piezoelectric material is obtained. Shrinkage must be taken into account to achieve the desired final dimensions. Significantly for the present work, VPP can also create thin sheets of PZT (50µm) through calendering in the green state without the need to lap the material to make it thinner(22).

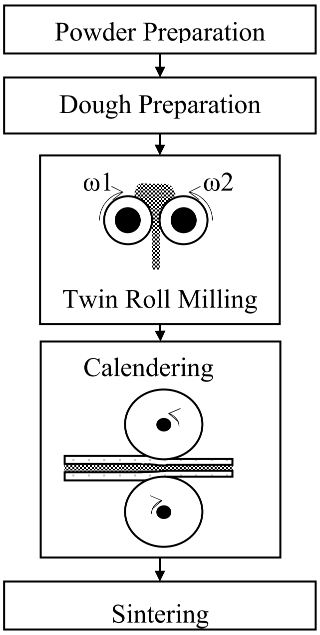

Figure 4.12: Main steps towards the fabrication of thin piezoelectric sheet in the VPP approach.

Tape casting is a conventional technique for the manufacture of plates or substrates and in which a blade is utilised to define the thickness of ceramic slurry deposited onto a moving film. Then the tape is dried out using infrared light until it gains enough strength to be removed from the carrier film. Finally the green tape is sintered. The powder preparation and the viscosity of the ceramic slurry are the main factors in control of the process.

Screen printing is a technique first developed in the 1930's to print images over a broad range of surfaces. The process has since been adapted for the printing of green PZT films, and can be referred to as a thick film process, suitable for making films of approximately 5-40μm in thickness. Firstly, the ceramic slurry or ink has to be prepared (powder, binder and solvent). Then, it is printed through a patterned screen onto a surface. In some cases the film is centrifuged and exposed to a heat treatment to increase its density. Finally the green tape is sintered. The powder preparation, the slurry viscosity, and the drying process are the main factors affecting the final quality of the film.

4.3.2 Thin film manufacturing methods

Thin Film technology is cited here to complete the possible range of technologies suitable for the fabrication of ceramic piezoelectric materials. In this approach layers of piezoelectric material are deposited over a substrate tens to hundreds of nanometres at a time(23) using techniques such as chemical vapour deposition (CVD) in which the composition of the piezoelectric layer can be controlled. The deposition process is repeated until the desired thickness is reached. However, the material fabricated in this fashion has inferior mechanical properties due to tensions between layers of piezoelectric and the substrate and difficulties in controlling the composition. Its applications are limited to micro-electromechanical systems (MEMS) sensors for which energy conversion efficiency is not so important, or for actuation where very small strains or forces are required. Lower temperature processes are also under investigation so the materials can be deposited directly on silicon(24).

4.3.3 Manufacturing methods limitations

The various manufacturing approaches discussed above results in piezoelectric ceramics with different properties, and are limited to different component scales and application areas as illustrated in Figure 4.13. The figure shows that thin film technologies are limited to build piezoelectric layers up to ~3µm thick before stresses within the piezoelectric layer build up and cause the piezoelectric to delaminate from the surface.

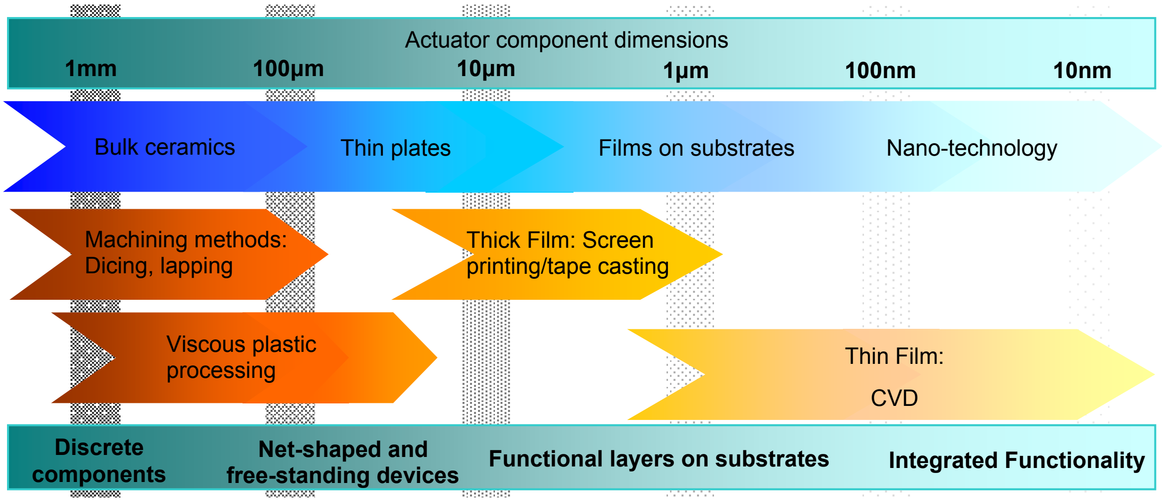

Figure 4.13: Schematic representation of different piezoelectric actuator manufacturing technologies for component dimensions scales ranging from mm to tens of nm. The diagram highlights how Viscous plastic processing bridges the gap between bulk ceramics, which are difficult to machine for feature sizes below 100µm and thick films which can only be grown on substrates up to a maximum thickness of 20-30µm.

For thick film technologies green films need to be sintered at temperatures over 600°C whilst applied on a substrate. This means that their sintering is uneven and imposes the limitation that only layers with maximum thickness up to ~25µm can survive the sintering stage without delaminating. There is also a minimum limit of ~1µm as the deposition of green films of such thicknesses becomes difficult.

Figure 4.13 also shows that there is a minimum limit for the machining of bulk ceramics which becomes difficult below 100µm and limited to flat devices. The gap between machining methods and thick film technologies is filled by the viscous plastic processing method capable of manufacturing net-shaped ceramics in the tens of microns range.

4.4 Piezoelectric materials

In polycrystalline piezoelectric ceramics, such as PZT, $Pb(Ti_{1-x}Zr_x)O_3$, the domain switching is controlled by the crystallographic structure (rhombohedral or tetragonal depending of the value of x), and the dopants used (acceptors for hard ceramics, and donors for soft ceramics). Grain size and pinning effects also have an effect on the wall mobility. In single crystals, such a $LiNbO_3$ the domains have more freedom to grow as they do not meet so many discontinuities, such as grain boundaries and defects within the material and therefore higher levels of domain switching occur under an applied field.

The key parameters of these materials when used as actuators are shown in Table 4.2. Materials with low piezoelectric coefficients such as single crystals $LiTaO_3$ and $LiNbO_3$, an anisotropic crystal which possesses a useful combination of piezoelectric and electro-optical properties, are included on the table for comparison purposes. PZT is a polycrystalline ceramic which is being used in a broad range of applications. Its piezoelectric and elastic coefficients depend on: Firstly, the PZT Stoichiometry, which is normally set to match the morphotropic phase boundary, MPB, which maximises piezoelectric properties; Secondly, the ceramic microstructure, with decreasing activity for increasing porosity which is ultimately dependent on the fabrication process. Generally, bulk and VPP ceramics have very low porosity compared with thick film ceramics; and finally, the level of dopants.

A wide range of commercially available PZT powders with different levels of dopants, see detailed explanation in Moulson and Herbert(14), are available which can be used to produce actuators with properties ranging between:

i) Acceptor dopants (such as Na, Mg, and Fe), which are compensated by oxygen vacancies, reduce domain wall motion, are used to produce relatively low activity are very linear and are difficult to depolarise as they have low losses. These are referred in the literature as “hard” ceramics.

ii) Donor dopants (such as Nb and Ta), which are compensated by the formation of cation vacancies, do not restrict domain wall motion, high activity, more hysteresis and are easier to depolarise as they have high losses. These are referred in the literature as “soft” ceramics.

Table 4.2 presents the properties supplied by the manufacturer of three commercially available ceramics (Morgan Technical Ceramics UK) which represent the piezoelectric properties ranging from soft to hard ceramics. The table includes PMN-PT which is a relatively newly discovered single crystal material with larger piezoelectric coefficients but much lower coercive field and Curie temperature than those corresponding to PZT ceramics, therefore limiting its maximum operational voltages and temperature.

Another alternative is to use composite materials, such as laminates to obtain materials with good piezoelectric and mechanical properties. The composite structure can also be used to pre-stress the device by means of adding a compressive or a tensile layer.

Table 4.2: Curie temperature (T_c), piezoelectric coefficients (d_{33} and d_{31}) and elastic coefficients at constant electric field for various piezoelectric materials. The top of the table represents text book values(14) where the bottom of the table represents the values provided by the manufacturer of four commercial ceramics (Morgan Technical Ceramics, UK). The (*) denotes single crystal piezoelectric.

Property	T_c	d_{33}	d_{31}	S_{11}^E	S_{12}^E	S_{13}^E	S_{33}^E	S_{44}^E
Units	°C	pCN^{-1}		μm^2N^{-1}				
$LiNbO_3$ (*)	1210	6	-0.85	5.8	-1.2	-1.42	5.0	17.1
$LiTaO_3$(*)	665	5.7	-3	4.9	-0.52	-1.28	4.3	10.5
$PbTiO_3$	494	47	-7.4	11	-	-	11	-
$PbNb_2O_6$	560	80	-11	29	-	-5 to -8	25	-
$NaKNb_2O_6$	420	160	-50	9.6	-	-	10	-
$BaTiO_3$	130	190	-79	8.6	-2.6	-2.9	9.1	23
PZT-501	330	405	-185	16.4	-	-	-	-
PZT-5A4	365	460	-195	16	-	-	18	-
PZT-5K4	137	950	-410	16.4	-	-	23.6	-
PMN-PT28(*)	143	1100-1700	-850	-	-	-	-	-

This design strategy has been used in the THUNDER and LIPCA devices(25) to obtain very large displacements using piezoelectric actuation. Figure 4.14 shows an example of commercially available actuators made using composite laminate materials (DuraAct™, Physique Instrumentik, Germany) and a schematic representation of these devices which includes important parameters such as the thickness of the piezoelectric and the encapsulating polymer. The combination of polymer matrix encapsulating the piezoelectric material enables these devices to be bent to a small radius of curvature without failure. Notice however in the schematic representations that some of the area of the device needs to be reserved to be used as the external electric connections.

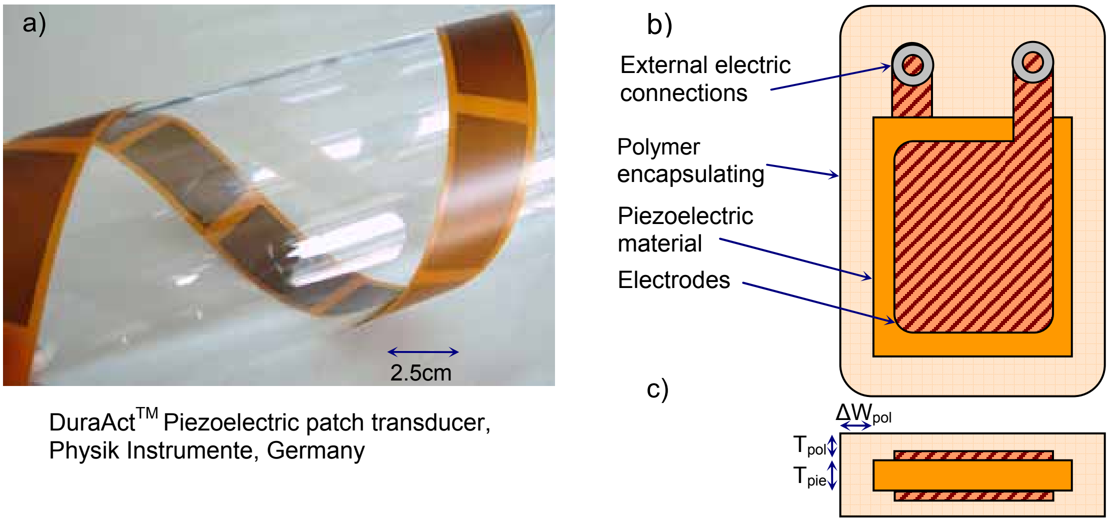

DuraAct^{TM} Piezoelectric patch transducer, Physik Instrumente, Germany

Figure 4.14: Examples of commercially available actuators made using composite materials. a) Laminate actuators DuraAct^{TM} manufactured by Physique Instrumentik, Germany. b and c) Schematic representation of these devices and important parameters such as the thickness of the piezoelectric and the encapsulating polymer.

4.5 Piezoelectric actuators geometry configurations

The design of piezoelectric actuator configurations is application driven as the system's performance depends both on the actuator configuration and the device they are applied to. Usually, a design compromise needs to be reached between maximising the strain provided by the actuator or its blocking force and/or limiting the maximum voltages applied. The actuator design parameters that can be optimized are its geometry, electrodes and poling configurations.

The simplest possible configuration is a unimorph actuator, a single piezoelectric plate or beam with electrodes in both faces and polarization across its thickness bonded to a substrate. When a positive voltage is applied the piezoelectric plate contracts along its thickness and expands along its length and width and if bonded to a substrate the stresses created at the bonding interface create a bending of the device. The amount of device bending depends on the piezoelectric properties of the actuator and the mechanical properties of both the actuator and the substrate and their relative dimensions.

4.5.1 Unimorph and bimorph configurations

The constitutive equations 4.1 & 4.2 can be solved in the time domain for a given geometry to obtain their oscillation modes, resonance frequency, losses, etc. However, for piezoelectric actuators the assumption can be made that the operating frequency is well below the lowest resonance frequency of the device and therefore a quasistatic assumption can be made. This in practice means that the constitutive equations can be solved assuming constant electric fields.

The most simple actuator geometries are the unimorph and bimorph cantilever configurations, for which the constitutive equations can be solved to obtain analytical models. Figure 4.15 below gives a schematic representation of bimorph, made up of two layers of piezoelectric material, and unimorph actuators where a single layer of piezoelectric material is bonded onto a substrate. For the bimorphs, different configurations are possible depending on the electrode and poling arrangements.

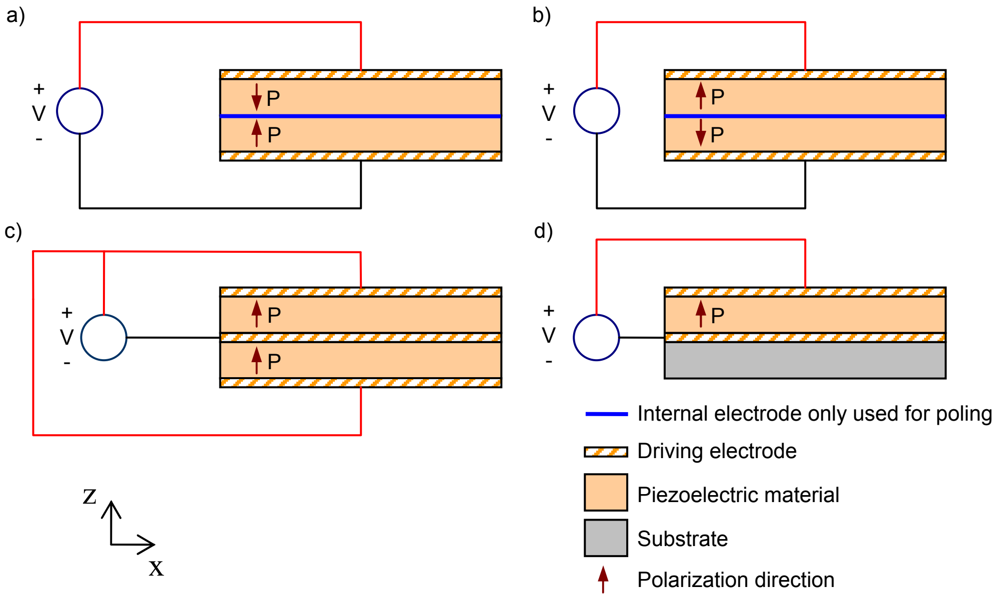

Figure 4.15: Geometry description of the bimorph and unimorph configurations: a) inward series bimorph; b) outward series bimorph; c) Parallel bimorph and d) Unimorph configuration with the piezoelectric actuator mounted onto a substrate.

The parameters describing the inwards series bimorph cantilever configuration are described in more detail in Figure 4.16 below. These include its geometry parameters, length and thickness (L_b, h_b); the applied electric field (E_z); the displacement at the tip of the bimorph δ_b; and the angle of the tip of the bimorph α_b.

Analytical models describing the inward series bimorph are available in the literature, see J.G. Smiths et al.(26) for a detailed description of their deduction. The equations 4.6, 4.7 & 4.8 below describe the radius of curvature of the piezoelectric bimorph, ROC_b, the displacement of the tip of the bimorph, δ_b , and the angle of the tip of the bimorph, α_b as a function of the applied electric field E_z:

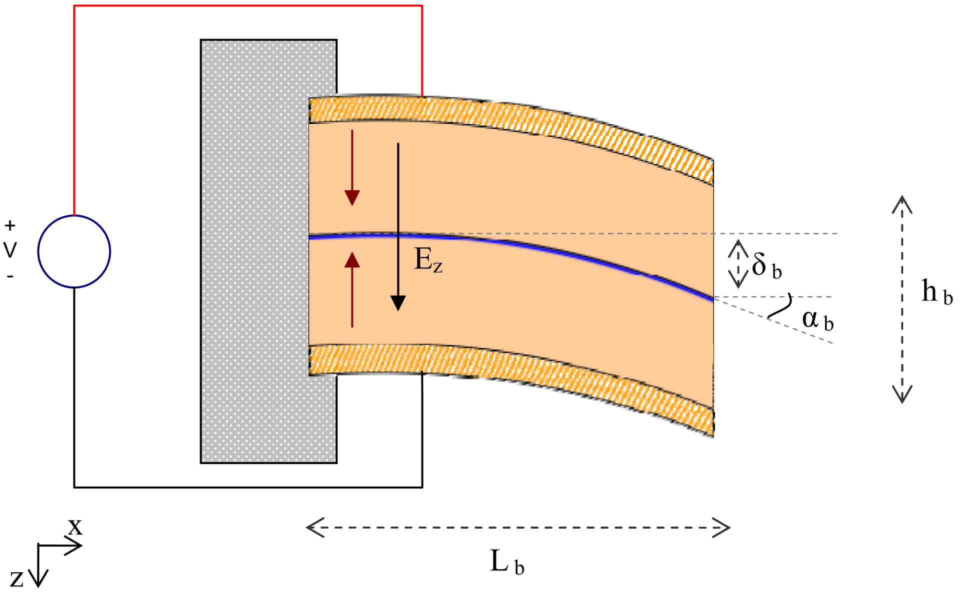

Figure 4.16: Schematic representation of a bent bimorph in state of equilibrium. The displacements are exaggerated in the figure for representation purposes.

$$\frac{1}{ROC_b} = \frac{\partial^2 z}{\partial^2 x} = \frac{3d_{31}E_z}{h_b} \qquad \textbf{Equation 4.6}$$

$$\delta_b = \frac{3d_{31}E_zL_b^{\ 2}}{2h_b} \qquad \textbf{Equation 4.7}$$

$$\alpha_b = \frac{3d_{31}E_zL_b}{h_b} \qquad \textbf{Equation 4.8}$$

Where:

ROC_b	is the series bimorph radius of curvature
d_{31}	is the transversal piezoelectric coefficient
E_z	is the z component of the electric field
h_b	is the thickness of the cantilever bimorph including both layers
L_b	is the length of the cantilever bimorph
δ_b	is the displacement of the tip of the bimorph
α_b	is the angle of the tip of the cantilever bimorph

These equations are derived using the constitutive equations for both piezoelectric regions constituting the bimorph and assume (a) a static situation where all the forces are balanced, (b) no external forces, or moments are applied upon it and (c) are only valid in the linear region ($E_{min}<E<E_{max}$). Substituting E_{max} in 4.6 we can see that the ROC_b of a bimorph is directly proportional to its thickness h_b.

A similar analysis can be made for the case of unimorph cantilever actuators. Their radius of curvature would be dependent on the thicknesses of the piezoelectric and the substrate as well as the material properties, such as Young's modulus, of the substrate.

4.5.2 Piezoelectric stack actuators and the displacement vs. applied force diagram.

For some applications large linear displacements, high applied force and low operating voltages are required. Figure 4.17 depicts a schematic representation of a stack piezoelectric actuator consisting of N_{st} layers of piezoelectric material with alternating ground and main electrodes. When an applied voltage $V=V_{st}$ is used the stack increases its height when zero voltage is applied, L_{st}, by a distance ΔL_{st}. The use of alternating ground electrodes allows the use lower operating voltages as described by 4.9 for a free actuator.

$$\Delta L_{st} \approx N_{st} \frac{d_{33}V_{st}}{T_{st}} = N_{st}^2 \frac{d_{33}V_{st}}{L_{st}}$$

Equation 4.9

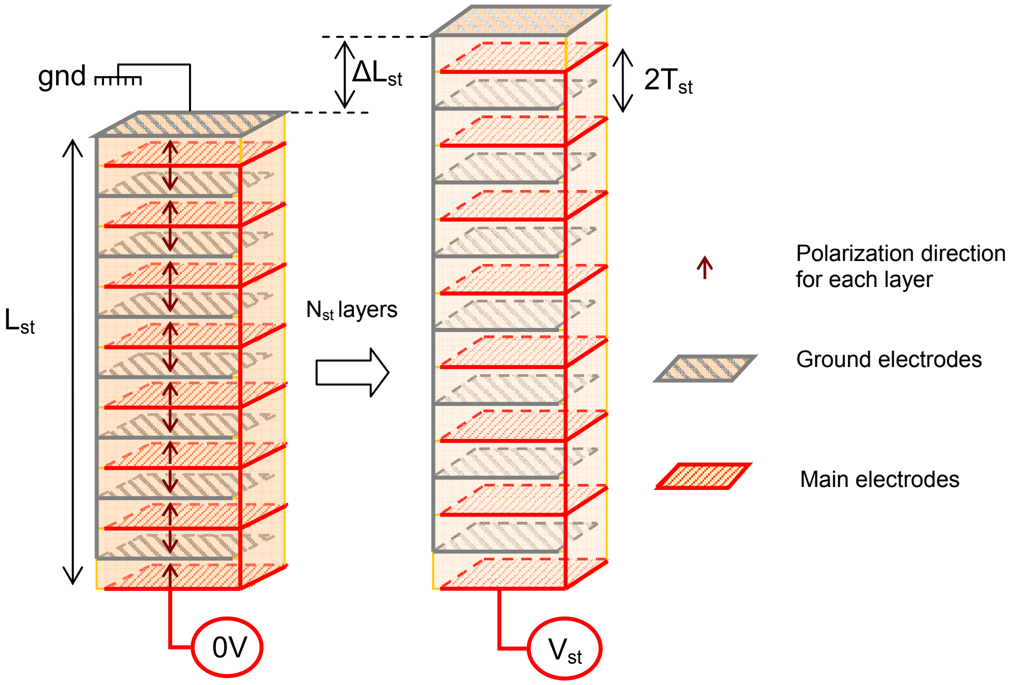

Figure 4.17: Schematic representation of a stack piezoelectric actuator consisting of N_{st} layers of piezoelectric material with alternating ground and main electrodes. The use of alternating ground electrodes allows the use lower operating voltages.

Depending on its working conditions the stack actuators may also be under the effect of an external applied force. Figure 4.18a gives a representation of the simplest external applied force, an ideal spring, to the piezoelectric actuator. Assuming that both the piezoelectric stack and the spring have ideal linear behaviour, the diagram in the Figure 4.18b illustrates the working regime of the actuator in the displacement / applied force domain as a function of the elastic constant of the ideal spring (K_{sp}), with all possible working regimes contained in the shadowed area. Three extremes cases to illustrate this behaviour can be considered:

i) A clamped actuator: In the model above the actuator would be clamped when the elastic constant of the ideal spring is very large compared with the elastic constant of the actuator (K_{sp}>>K_{st}). For that case the working regime of the actuator is represented along the x axis in the diagram as the displacement of the actuator is

$\Delta L_{st}=0$. For Vst=0 the applied force is zero ($F_{st}=0$) and as the voltage increases the applied force also increases until for $V_{st}=V_{max}$ the force reaches its maximum value F_{max}, which is normally referred as the blocking force of the actuator.

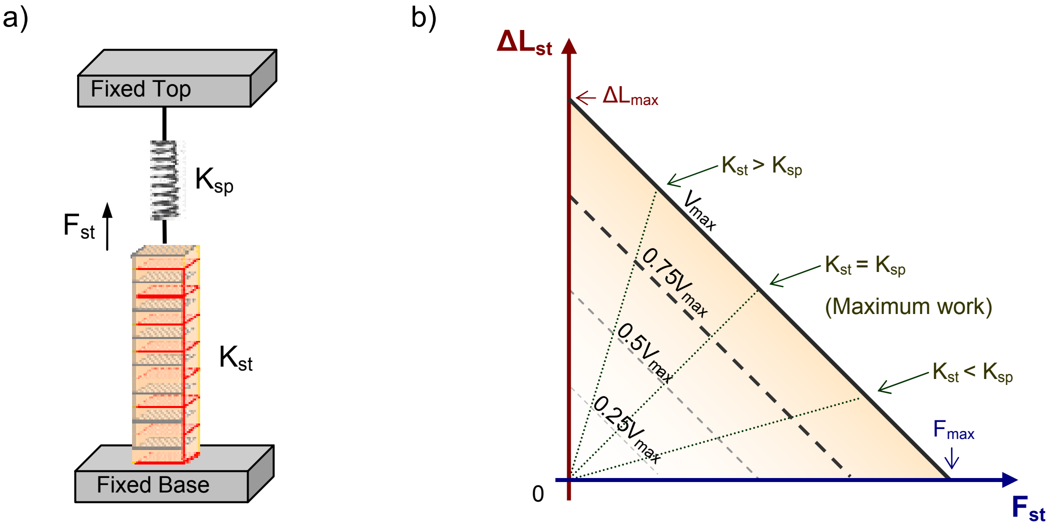

F_{st}	Force applied by the stack actuator
ΔL_{st}	Displacement of the tip of the stack actuator
K_{st}	Elastic constant of the stack actuator
K_{sp}	Elastic constant of the ideal spring
V_{max}	Maximum operating voltage
F_{max}	Blocking force, maximum possible force applied by the actuator (clamped)
ΔL_{max}	Maximum possible displacement (un-restrained stack)

Figure 4.18: a) Schematic representation of a stack actuator working against an ideal spring of elastic constant K_{sp}. b) Representation of all the possible force/displacement working regimes, inside the shadowed triangular area, as a function of the elastic constant of the ideal spring.

ii) A free actuator: In the model a free actuator would occur where the spring has $K_{sp}=0$, for which case the force applied over the spring is $F_{sp}=0$. This case coincides in the diagram with the y axis, as the applied voltage increases the displacement also increases until for $V_{st}=V_{max}$ the actuator reaches its maximum possible length $\Delta L_{st}=\Delta L_{max}$.

iii) Condition of maximum work: The third case considers the ideal spring to have the same elastic constant as the piezoelectric actuator $K_{st}=K_{sp}$ which is normally referred as the condition of maximum work. This condition is used for applications such as vibration damping as the most energy can be transferred between the actuator and the object which needs to be attenuated. This working regime is depicted by the dotted line in the Figure 4.18b which shows how as the applied voltage increases the displacement of the actuator and the applied force also increase.

The displacement vs. applied force analysis is made here for a stack actuator because its simplicity as the actuation occurs in only one direction, but it would be also be applicable to other actuator configurations where the definitions of the maximum displacement and the maximum applied force would need to be generalised. In the case of non linear effects occurring on the actuator the working regime would need to be represented by loops on the $\Delta L_{st}/F_{st}$ diagram instead of the straight dotted lines.

4.5.3 Active fibre composites

Active fibre composites (AFC's), which are sometimes also referred as multi fibre composites (MFC's) in the literature, are piezoelectric devices which take advantage of the higher piezoelectric coefficient d_{33} along the poling direction to obtain larger displacements along the length of the device. A picture of a commercial AFC (Smart Material GmbH, Dresden, Germany), and a schematic representation of its internal structure are depicted in Figure 4.19a & b. The AFC comprises piezoelectric fibres embedded in a polymer matrix. The electrodes are made in an inter-digitated configuration to allow for the poling of the AFC fibres along their lengths instead of through the thickness of the device. Figure 4.19c depicts the finite element analysis modelling of two adjacent segments within a single fibre in the AFC, which was carried out using COMSOL multiphysics. It can be seen that the poling direction in adjacent segments is in the opposite direction and that those regions under the electrodes are left un-poled. The widths of the electrodes, W_{afc}, and their separation L_{afc} are the most important parameters in order to optimise the actuation of these devices. It is also worth mentioning here the large inactive areas required in the device in order to accommodate the complex electrode configurations

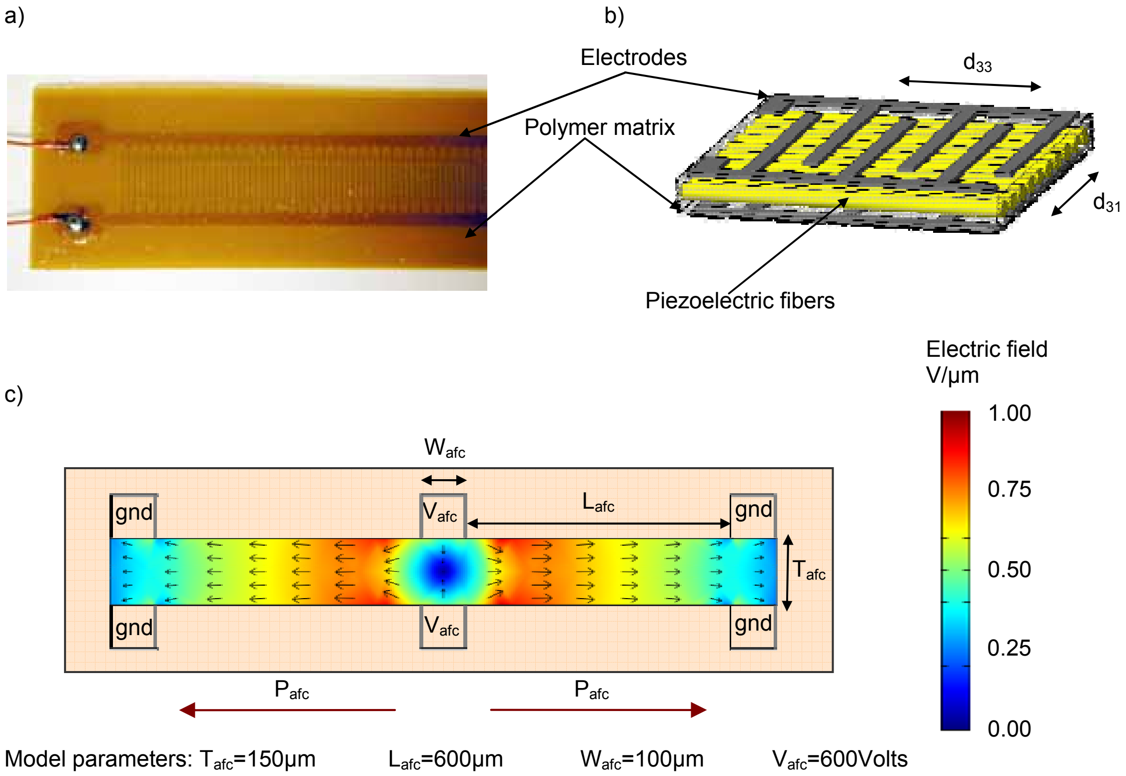

Figure 4.19: a) A picture of a commercial AFC (Smart Material GmbH, Dresden, Germany). b) Schematic representation of an AFC internal structure. c) 2D COMSOL modelling of electrostatic fields inside a PZT-5H fibre. The arrows show the polarization and electric fields direction during poling or while being actuated. There are regions of low field under the electrodes.

4.5.4 Net shaped helimorph actuators

Helimorph actuators are an example of piezoelectric devices where the geometry is engineered in three dimensions in order to maximise the displacement. Figure 4.20 shows pictures of prototype devices manufactured by Su, Pearce et al.(21, 27, 28) using a viscous plastic processing manufacturing technique in which a green VPP bimorph tape was rolled around a mould to give them their shapes and then co-sintered. These devices can provide displacements of up to several millimetres.

Figure 4.20: Examples of net-shaped helimorph actuators manufactured using a viscous plastic processing route. Pictures courtesy of Su, Pearce et al$^{(21, 27, 28)}$, 1998.

4.6 Summary

This chapter intends to give an introduction to the key issues: physics, fabrication methods and design of piezoelectric actuators.

From a microscopic perspective, piezoelectricity first originates from imbalances in the charge distribution of the unit cell of the piezoelectric material. At a higher level, the polarization within the piezoelectric material is distributed in different regions called domains which in the piezoelectric natural state are randomly orientated resulting in zero polarization on average at a macroscopic level. In order for the piezoelectric ceramics to present polarization as a macroscopic level, i.e. to become active, they need to be submitted to a process called poling in which the piezoelectric domains are re-orientated along the direction of an external applied field.

From a physics modelling perspective, the behaviour of piezoelectric ceramics is, as a first approximation, described by the linear theory of piezoelectricity which couples the piezoelectric and elastic behaviour of a piezoelectric device. However, linear piezoelectricity has its limits of application, as for sufficiently high electric fields and/or stresses domain switching begins to occur. This can give rise to memory effects in the material which can generate hysteresis.

In terms of manufacturing several methods can be used depending on device dimensions: deposited thin films for sub-micron piezoelectric layers on substrates; co-sintered thick film on substrates with thickness 1 and 20μm. Bulk ceramics for thickness above 100μm; and net-shaped viscous plastic processing ceramics which fill the gap between thick films and bulk ceramics thickness over 30μm. The composition and dopants of the ceramics can also be engineered to obtain different piezoelectric properties ranging from hard (low activity but high linearity) to soft ceramics (high activity but low linearity).

From a device perspective, different configurations are possible depending on the piezoelectric geometry, poling configuration, electrode configuration, and whether they are used on their own or as a part of a composite structure such as piezo/polymer laminates in active fibre composites. The equations for the exact solution of a simple case such as free (non-loaded) bimorph cantilever show that the thicknesses of the piezoelectric layers determine the performance of the device in terms of curvature and bending. Many other configurations are possible depending on the application demands: Unimorph, a simple layer over a substrate; active fibre composites, which use inter-digitated electrodes to pole the piezoelectric ceramics with the poling direction in the device plane to exploit the bigger value of d_{33}; helimorph actuators which are 3D engineered to provide large displacements; and stack actuators, which use several layers with alternate polarization directions to obtain large displacements in one direction and lower the operating voltages.

Finally, the analysis of a piezoelectric stack actuator working against an ideal spring showed the different working regimes such as free, clamped and the condition of maximum work which requires the elastic constants of the ideal spring and the stack actuator to match. The wider lesson of this simple model is that both the actuator and the objects it actuates against need to be considered as a whole device in order to optimise their design.

It is worth reminding the reader at this time that, within the context of this thesis on active/adaptive optics using, examples of active/adaptive optic systems using piezoelectric stack actuators(29) and deformable mirrors using piezoelectric unimorph actuators(30, 31) have been previously discussed in Sections 2.3 and 2.4.

4.7 References

1. Curie, J. and P. Curie, *Développement par compression de l'électricité polaire dans les cristaux hémièdres à faces inclinées.* Bulletin de la société minéralogique de France, 1880. **3**: p. 90-93.
2. Berlincourt, D. and H.H.A. Krueger, *Domain Processes in Lead Titanate Zirconate and Barium Titanate Ceramics.* Journal of Applied Physics, 1959. **30**(11): p. 1804-1810.
3. Merz, W.J., *Domain Formation and Domain Wall Motions in Ferroelectric $BaTiO_3$ Single Crystals.* Physical Review, 1954. **95**(3): p. 690-698.
4. Merz, W.J., *Domain Properties in $BaTiO_3$.* Physical Review, 1952. **88**(2): p. 421-422.
5. Merz, W.J., *Switching Time in Ferroelectric $BaTiO_3$ and Its Dependence on Crystal Thickness.* Journal of Applied Physics, 1956. **27**(8): p. 938-943.
6. Fatuzzo, E. and W.J. Merz, *Switching Mechanism in Triglycine Sulfate and Other Ferroelectrics.* Physical Review, 1959. **116**(1): p. 61-68.
7. Bouzid A., Bourim, E.M., Gabbay, M. and Fantozzi G. PZT phase diagram determination by measurement of elastic moduli. Journal of the European Ceramic Society, 2005. 25(13): p. 3213-3221.
8. Haertling, G.H., *Ferroelectric Ceramics: History and Technology.* Journal of the American Ceramic Society, 1999. **82**(4): p. 797-818.
9. Klein N., Hollenstein, E., Damjanovic D., Trodahl H.J., Setter N. anb Kuball M., A study of the phase diagram of (K,Na,Li)NbO3 determined by dielectric and piezoelectric measurements, and Raman spectroscopy. Journal of Applied Physics, 2007. 102(1).

10. Lemanov V.V., Smirnova E.P., Syrnikov, P.P. and Tarakanov, E. A., Phase transitions and glasslike behavior in Sr1-xBaxTiO3. Physical Review B, 1996. 54(5): p. 3151-3157.

11. Kamel, T.M., F. Kools, and G. de With, *Poling of soft piezoceramic PZT.* Journal of the European Ceramic Society, 2007. **27**(6): p. 2471-2479.

12. Kamel, T.M. and G. de With, *Poling of hard ferroelectric PZT ceramics.* Journal of the European Ceramic Society, 2008. **28**(9): p. 1827-1838.

13. *Piezotechnology: Fundamentals of Piezoelectricity,* http://www.piezo.ws/piezoelectric_actuator_tutorial/Piezo_Design_part2.php. (Last accessed April 2010), PI, Auburn, MA, USA.

14. Moulson, A.J. and J.M. Herbert, *Electroceramics: materials, properties, applications*. 1990, London: Chapman and Hall.

15. Damjanovic, D., *Hysteresis in piezoelectric and ferroelectric materials*, in *The science of hystereses*, G. Bertotti and I.D. Mayergoyz, Editors. 2006, Elsevier: Oxford. p. 337-466.

16. Schaufele, A.B. and K.H. Hardtl, *Ferroelastic properties of lead zirconate titanate ceramics.* Journal of the American Ceramic Society, 1996. **79**(10): p. 2637-2640.

17. Kaizuka, H. and B. Siu, *A Simple Way to Reduce Hysteresis and Creep When Using Piezoelectric Actuators.* Japanese Journal of Applied Physics Part 2-Letters, 1988. **27**(5): p. L773-L776.

18. Preisach, F., *Über die magnetische Nachwirkung ("On magnetic aftereffect").* Zeitschrift für Physik A Hadrons and Nuclei, 1935. **94**(5): p. 277-302.

19. Mayergoyz, I.D., *Mathematical models of hysteresis*. 1 ed. 1991, New York: Springer-Verlag. 207.

20. Viswamurthy, S.R., A.K. Rao, and R. Ganguli, *Dynamic hysteresis of piezoceramic stack actuators used in helicopter vibration control: experiments and simulations.* Smart Materials & Structures, 2007. **16**(4): p. 1109-1119.

21. Su, B., D.H. Pearce, and T.W. Button, *Routes to net shape electroceramic devices and thick films.* Journal of the European Ceramic Society, 2001. **21**(10-11): p. 2005-2009.

22. Abrar, A., Zhang D, Su B, Button TW, Kirk KJ and Cochran S. *1-3 connectivity piezoelectric ceramic-polymer composite transducers made with viscous polymer processing for high frequency ultrasound.* Ultrasonics, 2004. **42**: p. 479-484.

23. Seifert S., Sporn D., Hauke T., Müller G. and Beige H., *Dielectric and electromechanical properties of sol-gel prepared PZT thin films on metallic substrates.* Journal of the European Ceramic Society, 2004(24): p. 2553–2566.

24. Jianming Zeng, M.Z., Zhitang Song, Lianwei Wang, Jinhua Li, Kun Li and Chenglu Lina, *Lead–zirconate–titanate thin filmsnext term deposited on silicon using a novel technique at low temperature.* Applied Surface Science, 1999. **148**(3-4): p. 137-141.

25. Aimmanee, S. and M.W. Hyer, *A comparison of the deformations of various piezoceramic actuators.* Journal of Intelligent Material Systems and Structures, 2006. **17**(2): p. 167-186.

26. Smits, J.G., S.I. Dalke, and T.K. Cooney, *The Constituent Equations of Piezoelectric Bimorphs.* Sensors and Actuators a-Physical, 1991. **28**(1): p. 41-61.

27. Pearce, D.H., A. Hooley, and T.W. Button, *On piezoelectric super-helix actuators.* Sensors and Actuators a-Physical, 2002. **100**(2-3): p. 281-286.

28. Pearce, D.H., K.A. Seffen, and T.W. Button, *Net shape formed spiral and helical piezoelectric actuators.* Journal of Materials Science, 2002. **37**(15): p. 3117-3122.

29. Doel, A.P., Dunlop, C. N., Buscher, D. F., Myers, R. M., Sharples, R. M. and Major, J. V. , The MARTINI adaptive optics instrument. New Astronomy, 2000. 5(4): p. 223-233.

30. Bonora, S. and L. Poletto, *Push-pull membrane mirrors for adaptive optics.* Optics Express, 2006. **14**(25): p. 11935-11944.

31. Kanno, I., S. Tsuda, and H. Kotera, *High-density Piezoelectric Actuator Array for MEMS Deformable Mirrors Composed of PZT Thin Films*, in *2008 Ieee/Leos International Conference on Optical Mems and Nanophotonics*. 2008, IEEE: New York. p. 132-133.

CHAPTER 5

OUTLINE OF THE RESEARCH PROGRAMME

An emerging area of interest of adaptive optics is the design of actively controlled X-ray optics. The Smart X-Ray Optics (SXO) project comprises a UK-based EPSRC funded consortium, see Appendix I for ful details, developing prototypes for the next generation of large X-ray telescopes and small active/adaptive micro-structured optical arrays (MOAs) for X-ray microfocusing.

For the large optic, the overall aim of the project was to produce active X-ray mirrors using thin, below 1mm, structures, comprising nickel mirror shells with bonded piezoelectric unimorph actuators, and with a target resolution of ~0.1 arcs.

The MOA is designed to focus X-rays using grazing incidence reflection through consecutive aligned arrays of microscopic channels etched in silicon. The first objective of the project was to develop manufacturing techniques capable of producing vertical microchannels with a surface roughness below 2nm, which would make them useful as an X-ray optic. The second objective of the program was to develop an actuation method capable of bending the MOA’s arrays to a radius of 5 cm radius which would add to their focusing capability and would enable a tanden pair configuration of MOA’s with suitable focal lenghts.

To achive these goals the expertise of the seven SXO members with a wide range of multidisciplinary skills was required: Development of X-ray tracing sofware, optical design, manufacturing via electrodeposition of nickel shells, silicon manufacturing, Finite Element analysis modelling, and manufacturing of net-shaped piezoelectric actuators.

The work presented in this thesis comprises the development of actuation techniques for smart X-ray optics applications. For completeness, work from SXO collaborators has been included in the document where appropiate and this is acknowledged through the text.

Common to both large and small X-ray optics projects were the following objectives:

- To considere different piezoelectric actuator technologies and manufacturing methods. Explore if current piezoelectric devices (unimorph, bimorph and active fibre composites) could be adapted to bend the MOA arrays to a 5cm ROC.
- Design, manufacturing and optimization of piezoelectric actuated devices using finite element analysis (FEA) tools. Liaise with the SXO groups with the manufacturing expertise to translate optimized FEA models into drawings which could be use for the device manufacturing.
- Develop characterisation techniques for the piezolectric actuators. Curvature measurements of piezoelectric shells for the large optic and testing of prototype devices to demonstrate their capability to bend the MOA’s to the required 5cm ROC.
- Consider packaging/assembly issues. To devise an integration procedure of the piezoelectric actuatuators and the X-ray optics.
- Understand the influence of the sintering and poling procedure of the pre-curved piezoelectric ceramics on their curvature.

CHAPTER 6

RESEARCH METHODOLOGY AND EXPERIMENTAL TECHNIQUES

6.1 The process of evolving designs at the SXO

It is a general principle of engineering that for solving multidisciplinary problems, where a broad range of skills is necessary to solve a technical problem, requires good communication from all parties is required so the goals and the limits of the different manufacturing capabilities are understood so that the proposed solutions are feasible. Work within the smart X-ray optics (SXO) consortium was no different, with the seven UK research groups assuming different roles as described in the Appendix I.

The integration of the activities of the different research groups was achieved by several means:

i) Quarterly project meetings were held where all members of the consortium presented their work and open technical discussions were conducted.

ii) When a technical issue aroused requiring information from more than one the consortium members offline meetings where conducted as required.

iii) Joint experiments between the SXO research groups were carried out.

iv) The project manager, Dr. Ady James from the Mullard Space Science Laboratory (MSSL), kept an overview of the project, organizing human and physical resources and keeping a realistic view of what it could be achieved within the SXO timeframe.

The General design process at the SXO is represented in a block diagram form in Figure 6.1. It consists of three main stages: Concept generation; prototype design and manufacture and prototype testing.

The first stage is the concept generation, which were first validated using finite element analysis models (FEA), and if those were positive then manufacturing issues needed to be taken into consideration. In case of not being successful the concept was rejected and the concept generation process had to start again.

The second stage was the device design and manufacturing. At this stage detailed manufacturing drawings of all the elements needed to be produced. Silicon masks, piezoelectric element dimensions, laser machining files, device assembly drawings and parts drawings are the kind of elements that needed to be designed at this stage. This stage also included the manufacturing of the piezoelectric elements and their characterisation prior to their assembly and manufacturing of the X-ray optics. Once all the elements of the prototype assembly were manufactured the prototype assemblies needed to be carried out.

The final step was the device testing to verify that the expected performance calculated with the FEA models was obtained and to explore how the device could be optimized. After the device characterisation and the analysis of results the device design and manufacturing cycle was repeated to produce successive generations of prototype devices.

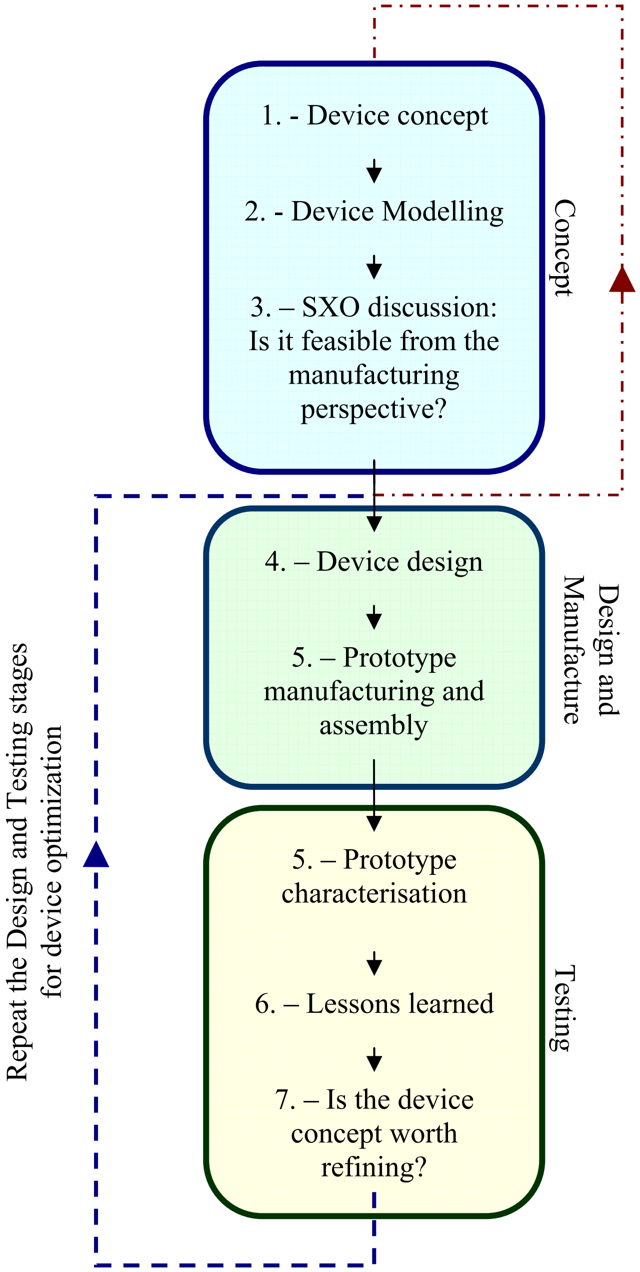

Figure 6.1: General design process at the SXO, with the concept generation, design, manufacturing and testing being main steps.

6.2 Modelling of physical problems

6.2.1 Analytical models

To produce analytical models of three dimensional piezoelectric actuated devices could prove very difficult, especially for complicated geometries such a hyperboloid or a paraboloid.

However, solutions to well know 2D problems can be used to make good guesses of some key dimensions such as the device thickness. For example: using 4.6 for the ROC of a piezoelectric bimorph; assuming that the device would have to be bent to a minimum radius lower than 5cm; and using the d_{33} values of 950 and 405pN^{-1} which correspond with those of commercially available for soft PZT ceramics as described in Table 4.2. It can be obtained that the device thickness of each one of the two layers of the piezoelectric bimorph would need to be lower than 142μm and 61μm for soft and hard PZT ceramics respectively when the maximum operating electric fields of 2V/μm are used.

This basic calculation points out that in order to bend the MOA to the required 5cm ROC using piezoelectric unimorph or bimorph actuator may require: thin devices, with device thickness below 150μm; a detailed analysis of the relative thicknesses of the PZT actuator and the substrate; and the actuator design configuration.

For the large optic project, where only small corrections on the ROC would be required, the PZT actuator thickness would not be a critical issue as in the MOA project.

6.2.2 Finite element analysis modelling (FEA)

Finite element analysis (FEA) modelling is a numerical technique which can be used to solve physical problems, and has the advantage of being capable of solving complex problems where analytical methods would be difficult to use due to the coupled physics involved and/or the complex geometries. A number of packages are commercially available, and some examples are: ANSYS by ANSYS Inc. Southpointe, *US;* ABAQUS *by* SIMULIA, a subsidiary of Dassault Systèmes, Providence, US; and LUSAS, a tradenmark of Finite Element Analysis Inc., Kingston upon Thames, Surrey, UK. Each one of them is specialized on certain type of applications, for example LUSAS is used for civil engineering projects.

The software package chosen to carry out the FEA modelling in this project was COMSOL Multiphysics (COMSOL, Inc., Burlington, US), as it has a module specialised in solving Micro Electro-Mechanical Systems (MEMS) where several physics effects can be modelled, including heat transfer, stress and strain, and piezoelectricity. Problems with 1D, 2D, and radial symmetry as well as 3D geometries can be solved in COMSOL, and it also provides a library of materials properties.

There are 7 steps to solve a problem in COMSOL multi-physics:

Selecting the physics to be solved: For example stress/strain, piezoelectric effects, thermal effects, electric fields, etc…).

Defining the geometry: First the kind of geometry needs to be selected, 1D, 2D, radial, or 3D depending on the symmetry of the problem to be solved. Then the geometry needs to be drawn, which can be done by importing a previously drawn geometry in other software such as SolidWorks (Dassault Systèmes SolidWorks Corp, Concord, US), or by drawing the problem using the CAD interface built in COMSOL.

Domain selection: in this step the equations to solve for each element of the geometry needs to be specified. For example, a stress/strain problem can be solved using the piezoelectric equations (as a stress/strain problem is a subset of a piezoelectric problem but with all the piezoelectric coefficients equal to zero). However, solving a stress/strain problem using the piezoelectric equations is not very efficient from the point of view of the use of the computer resources, which are limited. Therefore the problem to be solved needs to be as simple as possible, so it can then be modelled with more accuracy. In the domain settings it also needs to be specified how an object is orientated in the model if the orientation is relevant, as in the case of piezoelectric materials where it determines the poling direction.

Boundary conditions: These should be chosen to specify how the model interacts with the outside world and to associate a coordinate system with the model. For example, a system using the piezoelectric equations needs to specify the electrical boundary conditions (ground, applied voltages and which surfaces are left unconnected using the condition zero electric displacement (D=0). It also needs to be specified how the model is held in place, and if external forces are applied to the system.

Meshing: In finite element analysis the solution to a real problem is approximated by the solution of a simplified problem in which the materials are modelled as a group of points, each one of them interacting with its neighbours. The more points used the more precise the solution would be, but at the cost of increasing the size of the problem to be solved. The meshing process describes how these points are distributed and in what density, and it can be customised to obtain more precise solutions in particular areas of interest of the problem.

The solver: Different solvers can be used depending on the aim of the modelling exercise: time dependent for transient problems where the response of the model to initial conditions is modelled; stationary, where the stable position reached after the transient period is modelled; parametric, where the system can be resolved as a function of a parameter such as an external applied voltage or the Young's modulus of a material. In this step it also has to be chosen the particular numeric algorithm used to solve the FEA model. Finally, the order in which different physics effects are solved in the FEA model needs to be specified.

Data visualization: This is the final step of the modelling, where the information the results of the modelling process are presented. This can be done using 3D colour maps, deformed shapes, graphs, etc.

All these steps and example models are described in detail in the COMSOL multi-physics documentation.

The material properties contained in the COMSOL material library were used for the FEA modelling in this work including PZT-5H for the piezoelectric layer and polyamide which was used to model bonding layers. The substrates used in the modelling were nickel, for the large optic, and silicon for the MOAs. Their specific values are detailed in the Table 6.1 below.

Table 6.1: Material properties of PZT-5H, silicon, polyimide and nickel given by the COMSOL materials library which were used to model piezoelectric actuated devices. Silicon, polyimide and nickel were assumed to be isotropic in the modelling.

PZT-5H			**Silicon**			**Polyimide**		
Property	*Units*	*Value*	*Property*	*Units*	*Value*	*Property*	*Units*	*Value*
d_{33}	pC/N	593	Young modulus (Y_m)	Pa	$131*10^9$	Young modulus (Y_m)	Pa	$3.1*10^9$
d_{31}	pC/N	-274						
S_{11}^E	Pa^{-1}	$1.65*10^{-11}$	Poisson Ratio (ν)		0.27	Poisson Ratio (ν)		0.33
S_{12}^E	Pa^{-1}	$-4.78*10^{-12}$						
S_{13}^E	Pa^{-1}	$-8.45*10^{-12}$						
S_{33}^E	Pa^{-1}	$2.07*10^{-11}$	**Nickel**					
S_{44}^E	Pa^{-1}	$4.35*10^{-11}$	*Property*	*Units*	*Value*			
S_{66}^E	Pa^{-1}	$4..36*10^{-11}$	Young modulus (Y_m)	Pa	$219*10^9$			
$\varepsilon_{r11}=\varepsilon_{11}/\varepsilon_0$		3130						
$\varepsilon_{r22}=\varepsilon_{22}/\varepsilon_0$		3130	Poisson Ratio (ν)		0.31			
$\varepsilon_{r11}=\varepsilon_{33}/\varepsilon_0$		3400						

6.3 Manufacturing and assembly of test devices

For the MOA project there were two stages on the manufacturing of test devices: The first stage consisted on manufacturing prototypes to demonstrate the actuation capability of the device to bend the MOAs to a 5cm radius of curvature by means of piezoelectric actuation. For this stage test devices consisting of a silicon substrates manufactured at the University of Edinburgh (UoE) using dry or wet etching processes and piezoelectric actuators, manufactured at the University of Birmingham (UoB) were assembled using standard glues such as superglue (Superglue corp., US).

Once the proof of concept of the actuation method was successful, the second stage of the prototype manufacturing involved the manufacturing of complete prototype compatible with the X-Ray facility developed at KCL. The manufacturing steps are detailed in the Figure 6.2 below:

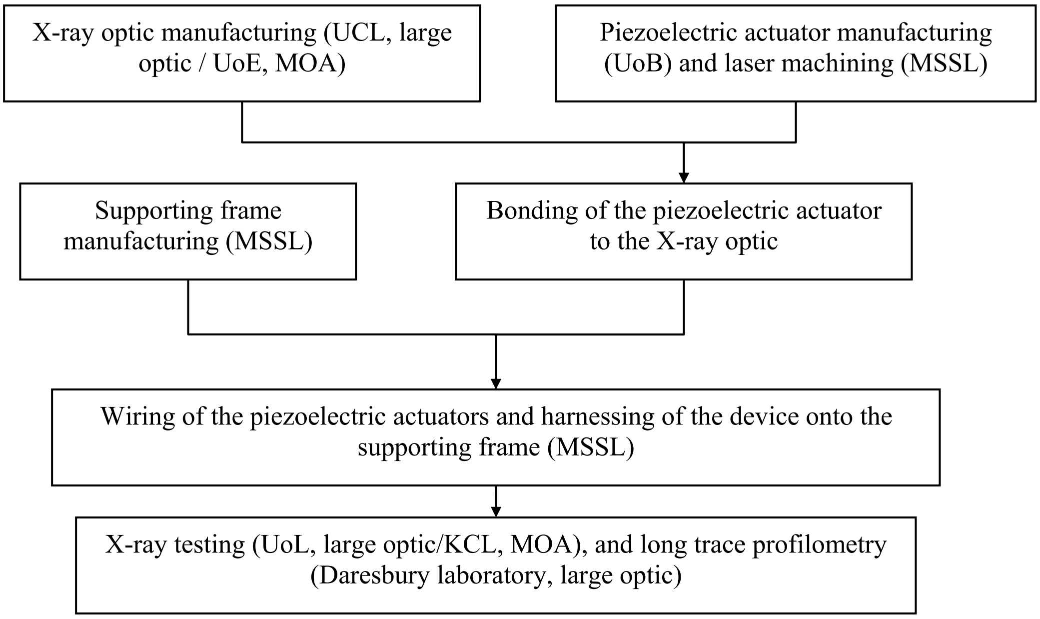

Figure 6.2: Block diagram representation of the manufacturing and integration processes involved complete devices for the MOA and the large X-ray optic projects. Laser machining was not used for the first generation of large X-ray optic prototypes.

For the large optic project two generations of prototypes were manufactured. The manufacturing processes involved, depicted in the block diagram in Figure 6.2, included: i) the manufacturing of the X-ray optics, which were carried out using electroforming of nickel over a gold coated stainless steel mandrel at UCL; ii) manufacturing of net-shaped piezoelectric actuators using a viscous plastic processing technique. iii) Manufacturing of a supporting frame; iv) bonding of the piezoelectric actuators to the back of the nickel shell. v) Wiring of the piezoelectric actuators and harnessing of the of the X-ray optic onto the supporting frame; and finally vii) X-ray testing (UOL) and profilometry testing (Daresbury laboratory) of the X-ray optic prototype.

The improvement of the manufacturing and integration procedures were part of the research objectives of the SXO programme and are described in more detail in Chapter 7 for the MOAs and Chapter 8 for the large optic.

6.3.1 Manufacturing of PZT plates

The manufacturing of PZT piezoelectric plates was carried out following the following steps:

6.3.1.1 Viscous plastic processing (VPP)

To obtain the green ceramic tape: Firstly the PZT-5H powder, polyvinyl alcohol-acetate (PVA) binder (KH 17s, Nippon Synthetic Chemical Industry Co. Ltd, Japan) and distilled water are mixed, with the amount of PVA binder, typically 5.0wt% of PZT-5H, optimized to obtain the breakdown of agglomerates during the process. Secondly, the mixed powders and solvents are milled using a twin-roll machine (Winkworth Machinery Ltd., UK) until a homogenous mixture is obtained. Then the green material was rolled in the shape of a cylinder. The cylinder of green material was then extruded using an extrusion machine (ElectroPuls™ E1000, Instron, High Wycombe, UK) a suitable dyes in the shape of tube which was cut to produce a 1mm thick green VPP tape. Finally the green tape was calendered until green sheets of the required thickness were obtained.

6.3.1.2 Sintering

The PZT-5H plates were place on a flat bed of ZrO_2 sand, which was loaded with PbO in order to control the lead stoichiometry, within an alumina crucible. The plates were covered with ZrO_2 sand and an alumina lid used to seal the crucible. The crucible was then placed in a furnace where the temperature was controlled as follows: a temperature ramp of 1^oC/min from room temperature until it reached 500^oC for the binder burn-out, followed by another ramp of 5^oC/min until the sintering temperature T_{sint}=1150^oC was reached. The temperature was maintained at 1150^oC for two hours after which the furnace was allowed to cool down to room temperature. The duration of the whole process was of about 22 hours depending on the thermal mass loaded in the furnace (bigger crucibles take longer to cool down to room temperature).

6.3.1.3 Electroding

Two different methods were used to apply electrodes to the PZT-5H plates. The first one involved the sputtering of gold electrodes using a peltier cooled sputter coater (Emitech K575 sputter Coater, Emitech Ltd., Ashford, UK). The second method involved the screen printing of platinum ink over the green PZT-5H tape which was then sintered as described above to produce PZT-5H plates with co-sintered electrodes.

6.3.1.4 Poling

Two different methods were used for the poling of PZT-5H plates: Oil poling, in which the piezoelectric plates were placed inside an oil bath at 110^oC and while an electric field of 2.5V/μm was applied. The other method which was used was corona poling, for which a custom made machine which was already available at the time of the project was used. The corona poling machine uses air instead of oil as an isolating medium and applies very high voltage of ~30.000V using a voltage amplifier between the main electrode and a hot plate set at 110°C. The hot plate also has the function of being the ground electrode. These conditions were maintained for 10min after which the samples were left to cool down using a fan and the voltage lowered to zero.

6.3.1.5 Cleaning

In order for the piezoelectric devices to be compatible with high vacuum systems, they needed to undergo a cleaning process to eliminate any residual contamination such as poling oil. The cleaning consisted of the use of a sequence of solvents: first the samples were placed inside a beaker which in turn was also placed inside ultrasonic bath (MXB6 Pulsatron, Grant) for 10 minutes; in order to remove the remaining acetone, the samples were then dipped in a series of beakers, for ~15 seconds each, of acetone, distilled water, 2-proponol, and distilled water; finally the samples were left to dry overnight on a 40°C oven.

6.4 Characterisation techniques

A range of standard characterisation techniques which were accessible at the time were used during the present work. These included scanning electron microscopy (SEM) and optical imaging for the microstructure analysis and documentation and impedance analysis for the electrical testing of ceramics.

Other characterisation techniques which needed to be developed involved the measurement of the ROC of piezoelectric elements along their length, to investigate how the manufactured samples matched the required ROC. This could not be done using standard profilometry techniques, which are meant for optical surfaces with surface roughness in the order of nanometers instead of micrometers as is the case for the piezoelectric elements. Additionally the ROC measurements were required over the whole area of the piezoelectric elements (up to 10cm×3cm). It was also required to measure the displacement and ROC of prototype samples as a function of the applied voltage. A computerized experimental set-up was designed to automatically make these measurements.

For the MOA project, one important measurement which needed to be carried out was the measurement of the ROC of the microchannels in prototype devices when these are actuated. This measurement could not be done using standard optical interferometers or profilometry instruments as these could not go over the MOA microchannels. An indirect measurement method, based on reflecting light over the top surface of the array, was used to estimate the ROC of the microchannels.

Both the standard characterisation techniques and the experimental set-ups developed are briefly described below.

6.4.1 Microstructural analysis: Scanning electron microscopy (SEM)

Scanning electron microscopy (Joel 6060, Oxford Instruments, UK) has been used to image cross-sections of prototype devices and at different magnifications. This allowed the inspection of manufactured devices, assessing features such as the porosity of the PZT ceramics, the thickness of screen printed platinum electrodes, the thickness and uniformity of bonding layers and inspection of laser machined trenches as described in later chapters.

Samples for which their surface needed to be investigated under SEM were bonded using a conductive tape (Conductive Adhesives Tabs, Ted Pella, Inc., Redding, US) to an aluminium substrate and then sputtered using an peltier cooled sputter coater

(Emitech K575 sputter Coater, Emitech Ltd., Ashford, UK), with a gold layer to improve their conductivity before being placed under the SEM microscope.

Samples for which a cross-section was needed were embedded in epoxy (Epo Fix Kit, Struers Ltd, Rotherham, UK), with the epoxy degassed on a vacuum chamber before left to cure. The samples were then polished using a polisher (Buehler metaserv grinder/polisher, Buehler, Lake Bluff, US). The polishing was carried out on several stages using polishing disks and diamond suspensions of decreasing grain size (MD-System Consumables and DiaPro diamond suspensions, Struers Ltd, Rotherham, UK). Once the polishing was finished the polished surface was gold coated for increased conductivity as described above.

6.4.2 Standard photography techniques

Optical photography has been used to document the different stages of the processed involved in this work. To improve the quality of some of the device images, where a large depth of field was required, a technique which entailed taken several pictures with both the digital camera and the sample in the same positions but manually varying the focal length of the camera at constant interval was used. The whole sequence of pictures was then digitally combined, using the commercially available software package (Helicon Focus, Helicon Soft Ltd., Kharkov, Ukraine), resulting in images where the whole of the image was in focus.

6.4.3 Impedance analysis

Impedance analysis was used as a characterisation method to check: that manufactured piezoelectric actuators were active at different stages of their manufacturing and assembly, measure material properties such as the dielectric constant of the piezoelectric ceramics, and check if low frequency resonances appear when the piezoelectric actuators are bonded to the devices. This was work was carried out using an Agilent 4294A impedance analyser (Agilent Technologies UK Ltd., Wokingham, UK).

6.4.4 Displacement measurements

A schematic representation and a photograph of the experimental set-up are shown in Figure 6.3. It comprises the following elements: a laser probe for displacement measurement (MEL Mikroelektronik GmbH, D-85386 M5L/2), a positioning system consisting of two motorized translation stages for the x and y axes (STANDA, models 8TM173-20-50, 8TM173-20) and a manual stage for the z axis (STANDA, 7T173-20) which positions the laser probe above the sample; and a voltage Amplifier (Agilent Technologies, OEM MODEL PA05039). Monitoring of the laser probe data and control of the amplifier voltage and the motorized stages is made using a National Instruments PCI-6052E acquisition card and LabView 8.5 software.

LabView programs have been written to control the voltage generation and the data capture. The LabView interfaces were designed to allow for selection of x/y positioning of the laser probe, the voltage pattern used, the maximum and minimum applied voltages and the averaging factor of the displacement measurement. These features allow, for example, the determination of Displacement-Voltage hysteresis curves, or scanning the sample for a given voltage to measure its radius of curvature. In both cases the data is plotted in real time, which is the main advantage over profilometer measurements. The main disadvantage is that stability measurements over several hours showed that the resolution was limited ~1μm.

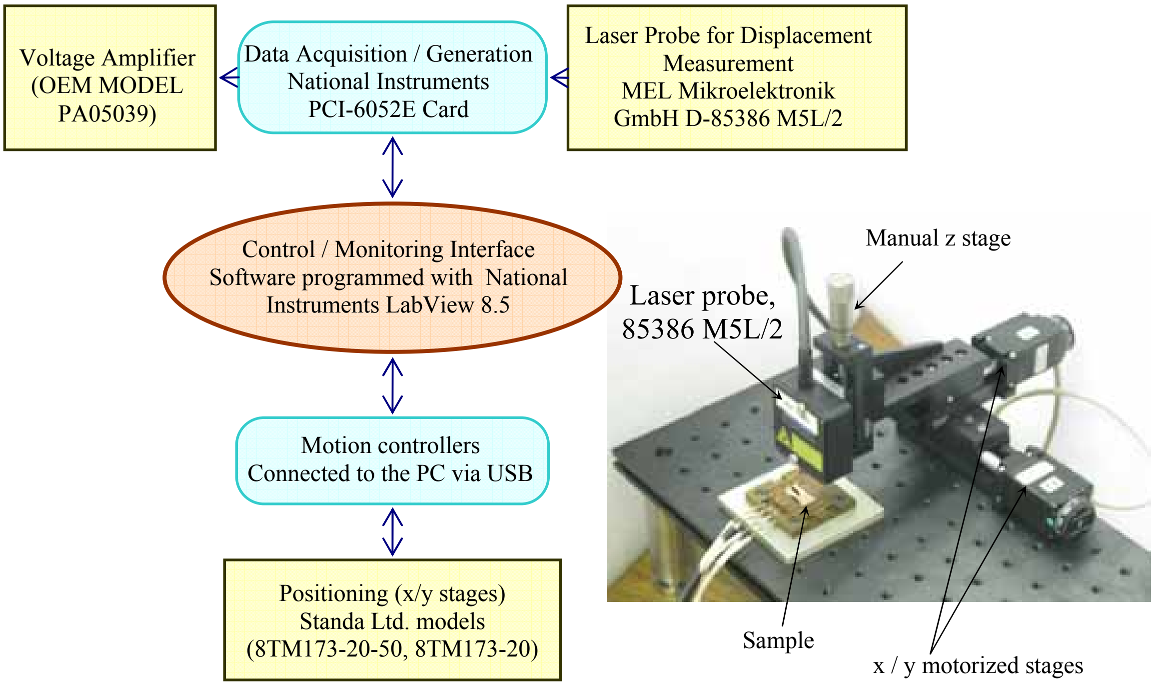

Figure 6.3: Block diagram and photograph of the experimental set-up for the measurement of displacement and radius of curvature. The set-up was computer controlled using a programme designed in LabView 8.5.

The set-up has been validated by measuring samples of the initial MOA and comparing the results with those obtained using TalySurf and *RST-500* profilometer, and by measuring the curvature of objects with a know radius of curvature, such as stainless steels dyes and plastic buckets, as shown in Figure 6.4 which showed that a correction factor $ROC_{measured}/ROC_{real}=1.11$ needed to be applied to the measurements. This systematic shift in the measurement originate from the laser probe 85386 M5L/2, which is designed to measured displacements over flat rather than curved surfaces.

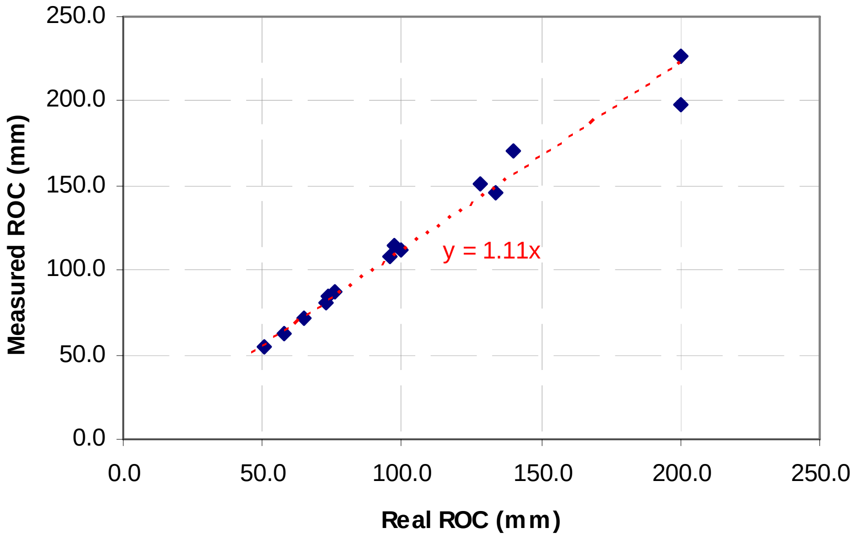

Figure 6.4: Calibration data for the radius of curvature measurements. The radius of curvature of objects of know curvature are plotted vs. the radius of curvature measured using the experimental set-up. The calibration detected that a correction factor $ROC_{measured}/ROC_{real}$=1.11 needed to be applied to the measurements.

Code and Lab-View interfaces designed to carry out the measurements described above are presented in Appendix III.

6.4.5 Curvature measurements

6.4.5.1 Direct measurements

Direct measurements of the curvature were obtained using the experimental set-up described in the previous section, a Talisurf profilometer and an interferometer at UCL and a long trace profilometer at the Daresbury laboratory.

6.4.5.2 Estimating the curvature using the z displacement

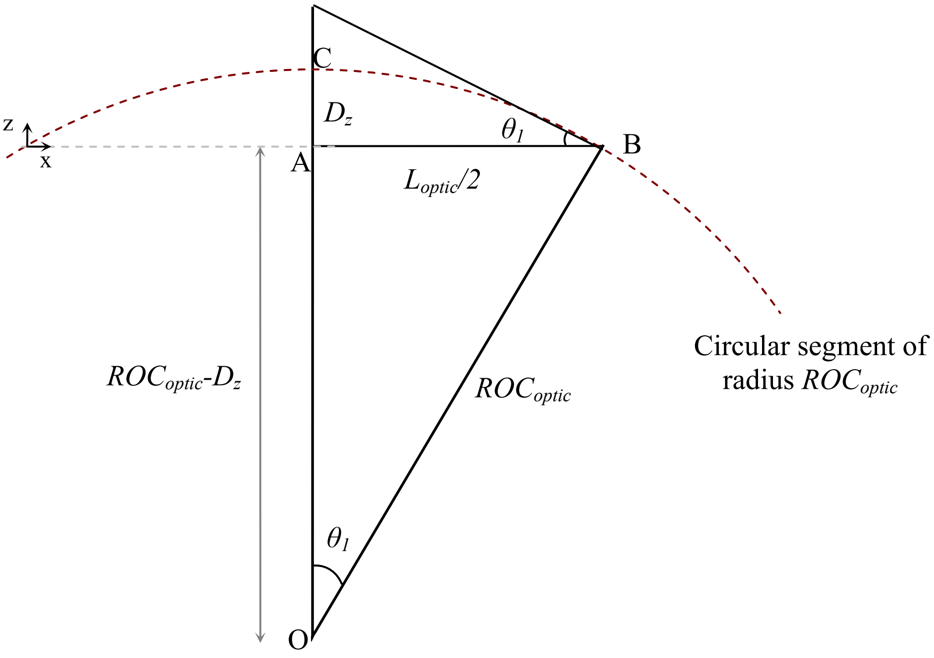

Figure 6.5: Schematic diagram to obtain the expression of the radius of curvature ROC as a function of the displacement along the z direction, *D_z*, and the length over which the displacement is measured *L_{optic}*.

Using the Pythagoras theorem in the triangle defined by the points O, A, and B the ROC can be obtained as shown in 6.1 below:

$$ROC = \frac{D_z^{\,2} + L_{optic}^{\,2}/4}{2D_z};\ if\ \ L_{optic} >> D_z \Rightarrow ROC \approx \frac{L_{optic}^{\,2}}{8D_z}$$ **Equation 6.1**

6.4.5.3 Estimating the curvature using the reflected image of a surface

A possible way of estimating the radius of curvature of a curved surface is by shining a laser beam light, and observing the reflected image on a screen as schematically shown in Figure 6.1. This problem is equivalent to solving an off-axis reflection on cylindrical mirrors, which is described in detail in several reference books (see for example Milton Katz, Introduction to geometrical optics, World Scientific Publishing, London, 2002).

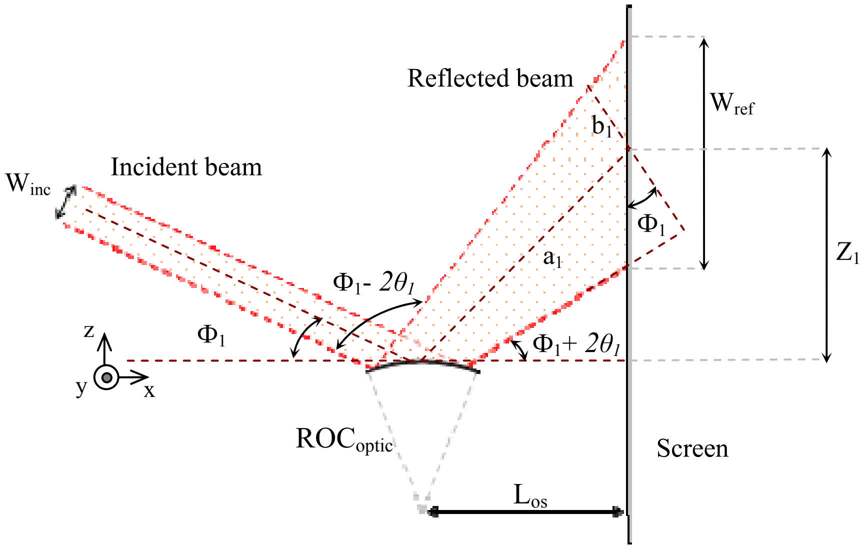

Figure 6.6: Estimating the radius of curvature of a curved surface by reflecting light on its surface and measuring the size of the image.

From the diagram in Figure 6.5, and using the Snell law on the edges of the optic surface it can be obtained that:

$$ROC_{optic} = \frac{L_{optic}}{2Sen(\theta_1)} \qquad \textbf{Equation 6.2}$$

And from Figure 6.6:

$$\tan(\theta_1/2) = \frac{a_1}{b_1} = \frac{L_{os}W_{ref}}{2((L_{os})^2 + Z_1)^2} \qquad \textbf{Equation 6.3}$$

Therefore, measuring the distance between the optic and the screen L_{os}, the width of the image W_{ref}, and the distance between the centre of the image and the plane of the optic Z_1, and if the length of the reflecting surface L_{optic} is known. In addition, if a cylindrical bend is assumed, the radius of curvature of the reflecting surface can be estimated substituting 6.4 in 6.2. In practice, as a 2D rather than a 1D surface is illuminated the size of the reflected image would vary along the y axis in Figure 6.6, therefore giving a 2D representation of how the curvature is in the optic.

CHAPTER 7

DEVELOPMENT OF SPIDER ACTUATORS FOR THE MOA'S

7.1 Introduction

The concept of micro-structured optical arrays (MOAs) was discussed at a SPIE meeting in 2001(1) and at the international X-ray Microscopy conference in Grenoble in 2002;(2) some progress followed(3, 4) but it was limited by lack of funding until the UK Smart X-Ray Optics (SXO)(5) consortium received funds initially for a pilot study in 2004 and then for a full programme of research, starting in 2006, under the Research Council UK's Basic Technology scheme(6). Work in different aspects of the project has been carried out since(7-11).

The MOA concept is largely based on polycapillary(12) and microchannel plate(13) optics, in which X-rays are guided by multiple reflections along a large number of small channels as previously described in Section 3.5. The main differences in MOAs are that the layout of the channels is more flexible and that there are single reflections in successive arrays which reduce aberrations as the Abbe sine condition is approximately satisfied. This is shown schematically in Figure 7.1a, where X-rays from a point source (at the top of the figure) are brought to a (quasi-) point focus at the bottom by two successive reflections. A central stop in the first array, not shown in the figure, prevents un-reflected X-rays from reaching the focus. In practice many more channels would be used. In the case shown the second reflection is from a bent array and by varying the radius of curvature the focal length can be changed.

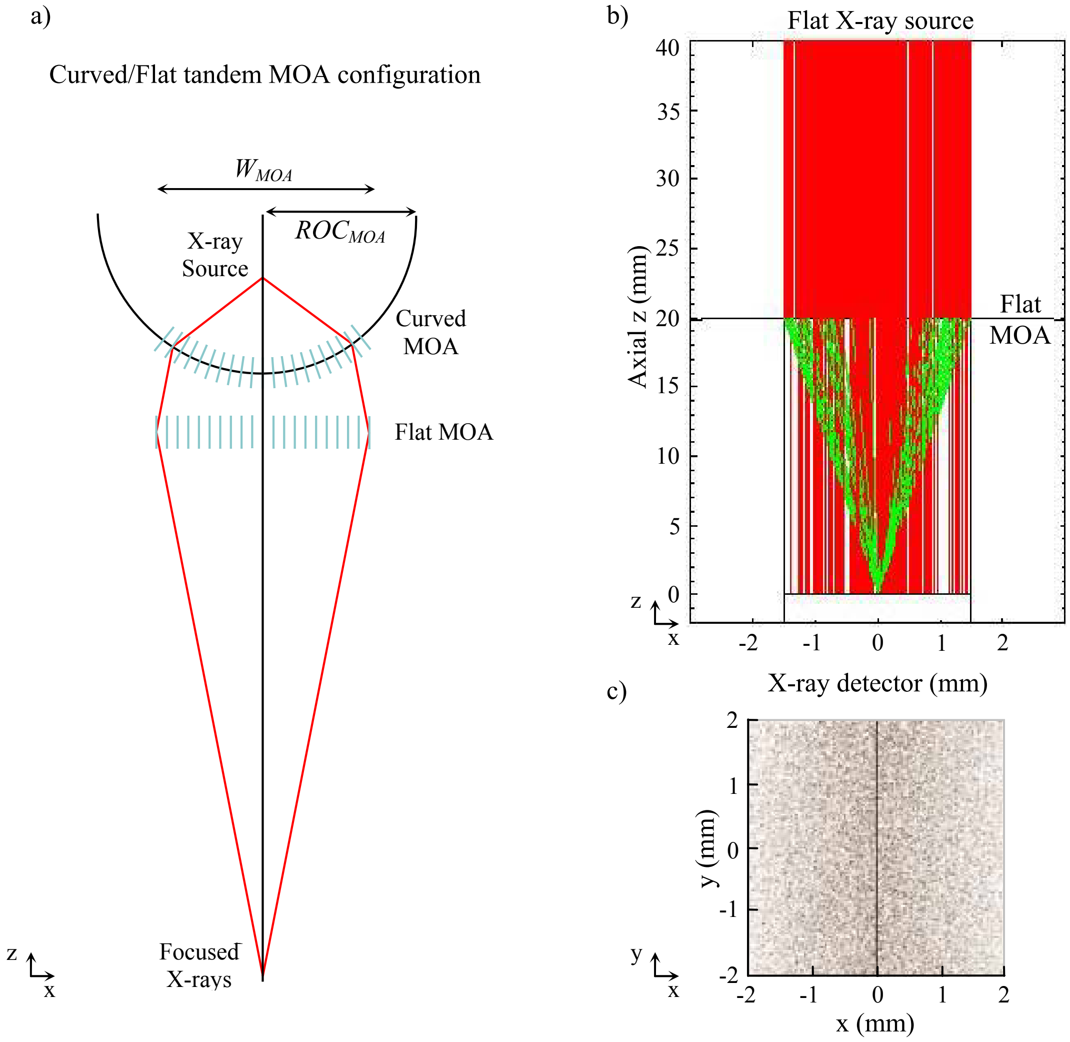

Figure 7.1: a) Operation principle of a curved/flat tandem MOA configuration. Oncoming X-rays from a line source (top) are brought to a line focus (bottom). b) Ray tracing modelling of an MOA with a cylindrical curvature with the incoming X-rays going from top to bottom. c) Line focus simulated on the X-ray detector (the picture shows an inverted image, i.e. black corresponds to high brightness and white to low brightness). The modelling was carried out using the X-ray tracing Q software at the University of Leicester(15).

Pictures of MOA channels manufactured in 2006 at the University of Edinburgh (UoE) using a dry-etching technique on silicon substrates are shown in Figure 7.2.

MOA channels with a 14:1 high to width aspect ratio were manufactured and a close up picture of the channels surface showing a regular pattern (scalloping) on MOA channel surface which increased their roughness.

Analytical models of how MOA channels could be used in different X-ray optic configurations such as line to line focusing or point to to point, and their dependence on the geometry of the MOAs are described in detail elsewhere(10, 14). Figure 7.1b shows X-ray tracing modelling of an MOA with a cylindrical curvature with the incoming X-rays travelling along the z direction. Figure 7.1c shows the results of the simulation at the detector where a line focusing is obtained (the picture shows an inverted image, i.e. black corresponds to high brightness and white to low brightness). The modelling was carried out using the X ray tracing Q software at the University of Leicester(14, 15).

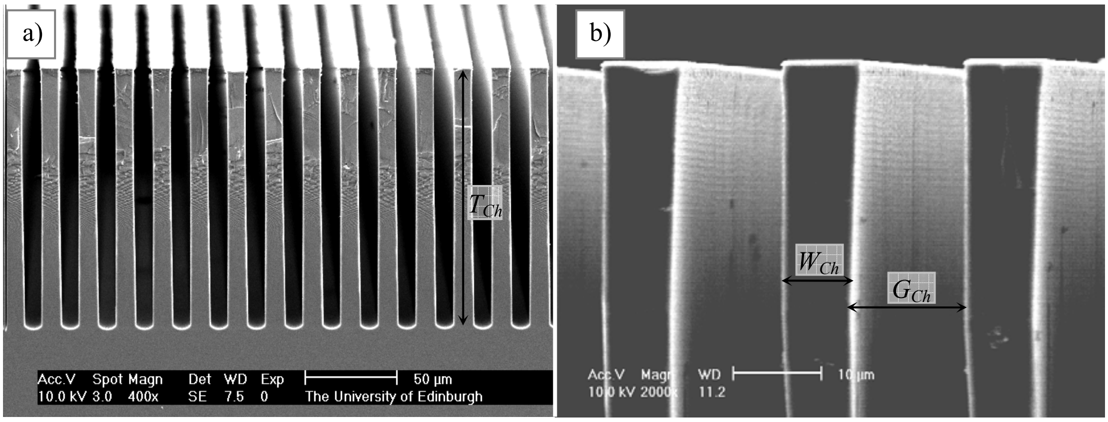

Figure 7.2: MOA channels manufactured using a dry-etching technique on silicon substrates. a) SEM picture showing the MOA channels with a14:1 high to width aspect ratio. b) Close up picture of the channels surface showing a regular pattern (scalloping) on MOA channel surface which increased their roughness. Pictures courtesy of the University of Edinburgh, October 2006.

Both analytical models and X-ray tracing reached the conclusion that the necessary requirements to enable the use of MOA structures as X-ray optics are:

i) The usable width of the MOA (W_{MOA}) is limited to 2mm as at higher W_{MOA} would also increase the incident angle on the external channels of the MOA and would reduce their reflectivity.

ii) There needs to be a high aspect ratio, over 20:1, between the depth (T_{Ch}) and widths (W_{Ch}) of the channels in order to increase the effective reflective area of the channels and therefore the focussed flux of the device.

iii) The surface roughness of the channels needs to be under 2nm in order to avoid scattering being the dominant factor on the X-ray reflectivity as has been described in Section 3.22.

iv) The other requirement was that an actuation method needed to be developed to bend the MOA's to a radius of curvature (ROC) below 5cm in order to provide enough demagnification of the microfocus X-ray source as discussed by Michette et al.(8)

An initial MOA and actuation concept design using piezoelectric unimorph actuators under a 2×1cm silicon wafer with the MOA channels at its centre was proposed as depicted in Figure 7.3, for which the relative dimensions of the wafer and the actuators needed to be investigated.

The use of piezoelectric actuators has a number of advantages over other actuation methods such as mechanical bending or the use of a membrane and a vacuum control system(3) to bend the channels: i) They would provide an electrically driven, compact and flat solution, which would have the advantage of freeing space in the optical system and simplifying the control mechanism. ii) As piezoelectric strips would be extended along the length of the chip, so are the stresses created, which is advantageous compared to mechanically driven three or four point bending solutions where the stresses would concentrate on the points where the forces are applied. iii) Finally, the use of segmented electrodes, thereby giving control of the curvature on the piezoelectric strips, could also make the optic adaptive, with the potential capability of reducing aberrations.

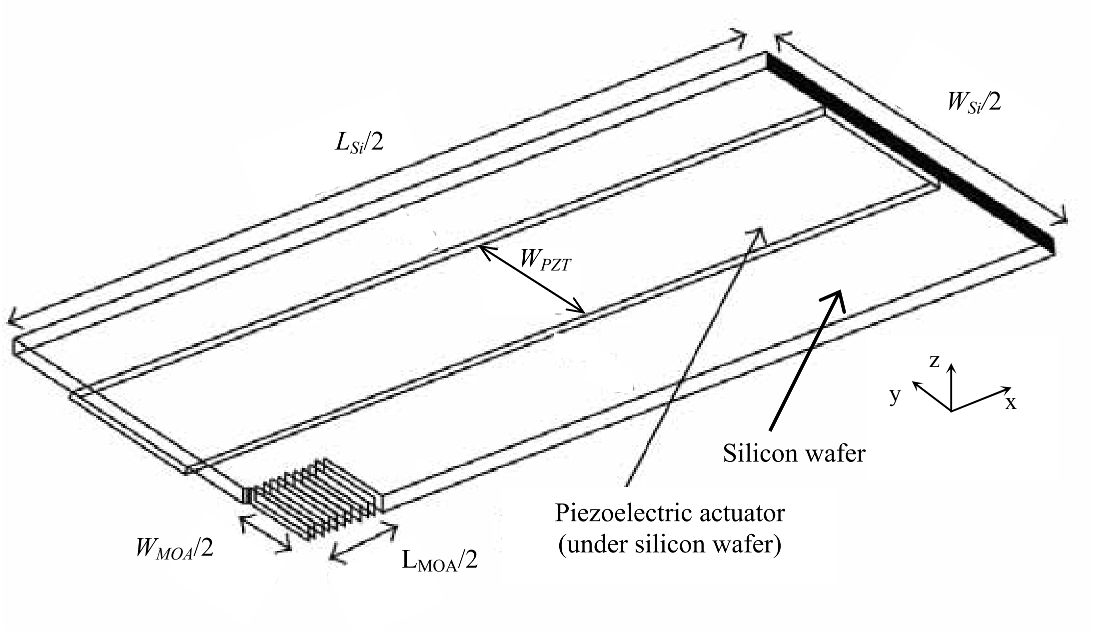

Figure 7.3: Shematic representation of the initial MOA and actuation concept design using an unimorph under the silicon wafer. For presentation purposes only a quater of the chip is drawn with the MOA channels in the bottom left corner of the figure.

From a manufacturing point of view, the piezoelectric actuators should be produced in a way which is compatible with the manufacturing process of the silicon channels. The material most commonly used for the actuators is lead zirconate titanate (PZT) because it has the highest piezoelectric coefficients, with the exception of PMN-PT which have other disadvantages (such as low coercive fields). Thick film is a manufacturing route commonly used in micro electromechanical systems (MEMS), normally used as sensors, where the PZT in the green state is screen printed with the desired pattern onto a substrate such as silicon. However, thick film has its drawbacks: i) The device needs to be sintered at high temperature bonded to a substrate (800–950^{o}C)$^{(16)}$ and therefore high thermal stresses in the MOA may be produced in the silicon channels and also there may be a chemical reaction between the PZT and the silicon. ii) Thick films usually have higher porosity and therefore lower piezoelectric properties and actuation than those seen in bulk ceramics. iii) The thicknesses of thick films are also limited with films more than 40µm being difficult to achieve. Thicker layers may be needed depending on the actuator arrangement and the thickness of the silicon chip. These three points indicate that an alternative manufacturing method to thick film needed to be sought.

Viscous Plastic Processing (VPP) was the manufacturing route chosen to manufacture the piezoelectric actuators at the University of Birmingham. VPP can produce free standing piezoelectric strips with piezoelectric properties close to those of bulk piezoelectric material, and with customized thicknesses ranging from several hundreds of microns down to a minimum of about 50µm. A TRS600 powder (PZT-5H equivalent) was used. Finally, the VPP piezoelectric strips can then be bonded at room temperature to the MOA chip as reported by Zhang et al.(7)

7.2 Manufacturing of MOA's at the UoE

Two deep silicon etching methods (wet and dry) were pursued at the University of Edinburgh as manufacturing routes with different degrees of success. Their main results have been presented elsewhere(9) and only summarised here.

For both wet and dry etched methods, an oxide mask on the silicon substrate to leave expose those areas on the silicon that needed to be etched. This was done using standard photolithography techniques as shown in Figure 7.4a.

The dry-etched process consisted of successive passivation and etching steps each lasting several seconds. The passivation step consisted of depositing a thin layer of the gaseous polymer C_4F_8 to stop further etching of the vertical wall of the channels, thus avoiding sloping the vertical walls. This was followed by a standard, nearly isotropic, plasma etching using sulphur hexafluoride, SF_6. The sequence was then repeated until the wafer was etched all the way through its thickness as shown in Figure 7.4b.

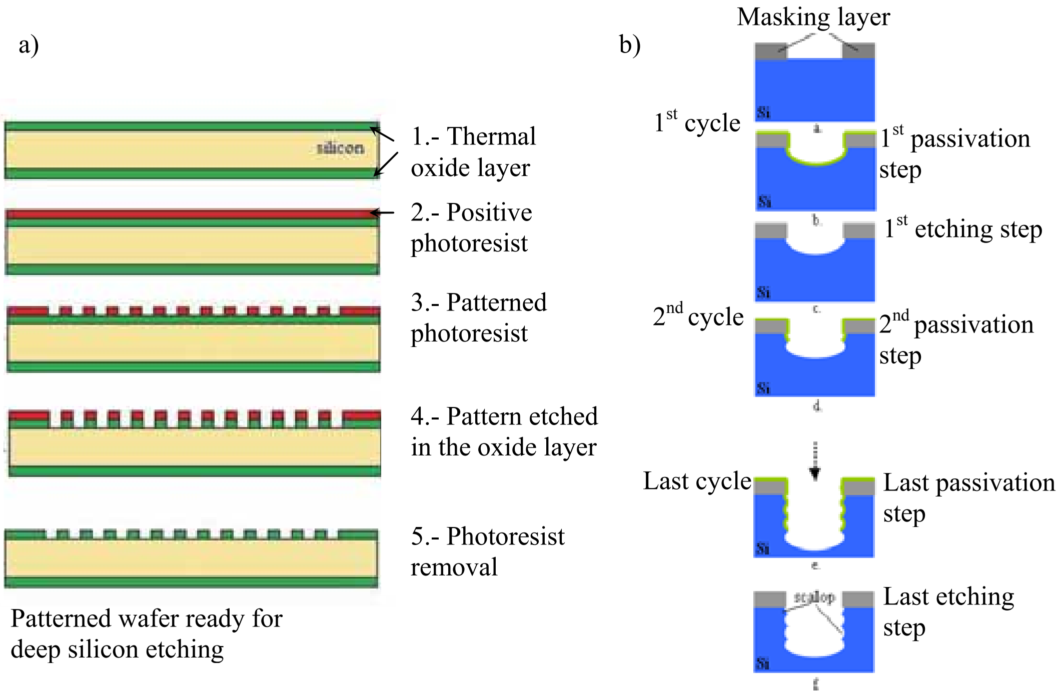

Figure 7.4: Manufacturing processes investigated at the University of Edinburgh as a possible manufacturing routes for the fabrication of MOA's. a) Pattern preparation b) Wet etching method alternating successive passivation and plasma etching steps.

One of the problems inherent in the dry-etching process is that it left behind a surface pattern on the MOA channels known as scalloping, as previously shown in Figure 7.1, thereby increasing the surface roughness of the vertical walls of the channels and creating shadowing effects. Average values of the surface roughness of the channel walls were found to be about 20nm, which made the dry-etching method unsuitable to produce X-ray optics.

Anisotropic wet etching, dependent on the crystallographic orientations, of silicon wafers with a (110) orientation, was the other manufacturing technique investigated at University of Edinburgh for the manufacturing of the MOA structures. This technique exploits the substantially different etch rates of different crystallographic planes in silicon. The technique required very precise alignment of the oxide mask relative to the silicon planes on the (110) wafers and alignment methods, including designing alignment masks to find the {111} silicon planes were developed to achieve this.

After the oxide mask was created the silicon substrates were immersed in a tetramethylammonium hydroxide (TMAH) solution which preferentially attacks the silicon substrate along the {111} planes until they were etched all the way through the wafers.

This fabrication method was able to generate MOA arrays with a surface roughness of 1.2nm, below the required 2nm, and was subsequently chosen as the appropriate method to manufacture the MOA arrays. Examples of MOA channels structures manufactured with both dry and wet etching methods are depicted in Figure 7.5 below, which highlights the improved surface roughness obtained with the wet etching method.

7.3 The Initial actuator design for the bending of the MOA's

Based on the optical equations of the MOA's, results from the X-ray tracing and what was achievable at the time in terms of silicon and PZT an initial MOA and actuator design with the following dimensions was chosen. The actuator arrangement initially assumed that the MOA channels would be etched in the centre 2×2mm of a silicon wafer with dimensions L_{Si}=2cm, W_{Si}=1cm and a thickness T_{Si}=100µm. The MOA would be in the centre 2×2mm (T_{MOA}=W_{MOA}=2mm). The actuation would be provided by two piezo strips, L_{PZT}=2cm, W_{PZT}=2mm and T_{PZT}=60µm, bonded along the length of the chip, would provide the actuation to bend the MOA channels as shown in the schematic representation in Figure 7.3.

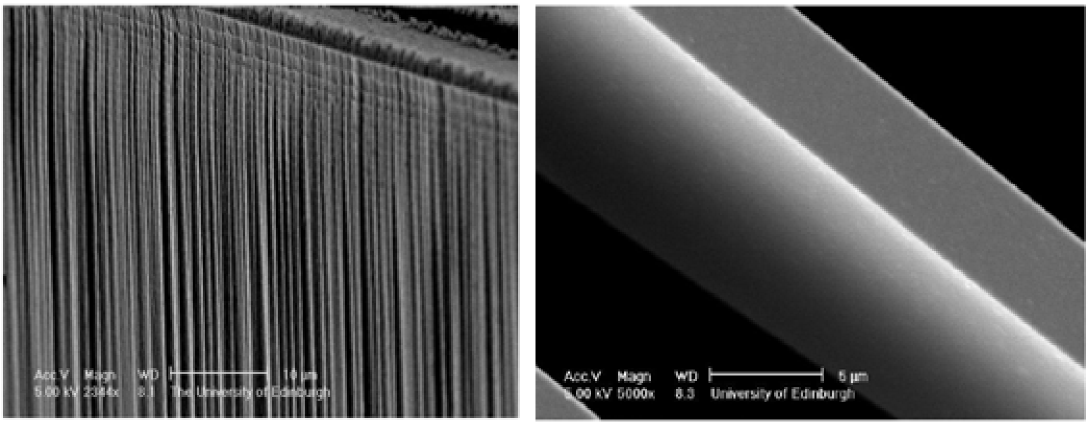

Figure 7.5: SEM pictures of MOA manufactured at the University of Edinburgh using dry etching (left) and wet etching (right) manufacturing routes. The dry etched route created scallops and curtain effect patterns on the vertical walls resulting on a 20nm average surface roughness, in contrast with the 1.2nm surface roughness of the channels manufactured using wet-etching techniques. SEM pictures courtesy of the University of Edinburgh (18).

7.3.1 FEA analysis of the initial model

A finite element analysis (FEA) model was set up, using the package COMSOL Multiphysics, with the dimensions described above and neglecting the thickness of the bonding layer. The applied voltages for the piezoelectric actuators are 120V, which corresponds with the maximum 2V/µm electric field within safe limits. The FEA analysis indicated higher stress points, highlighted in Figure 7.6b, showing where the risk of fracture is highest for a small bending radius. However, the maximum stresses of 108MPa do not exceed the breaking stress of silicon measured as 260MPa by a three-point bending test on silicon wafers as shown in the Appendix IV.

Figure 7.6b shows the 3D deformation of the centre 3mm strip along the y direction containing the MOA, the deformation has been exaggerated by a factor ×200 for visualization purposes. The deformation results in a complicated shape because the piezoelectric strips bend the MOA chip in both x and y directions. The radius of curvature of the MOA channels ROC_{MOA} in the FEA model is ROC_{MOA}=28cm, which was more than five times higher than the required 5cm target.

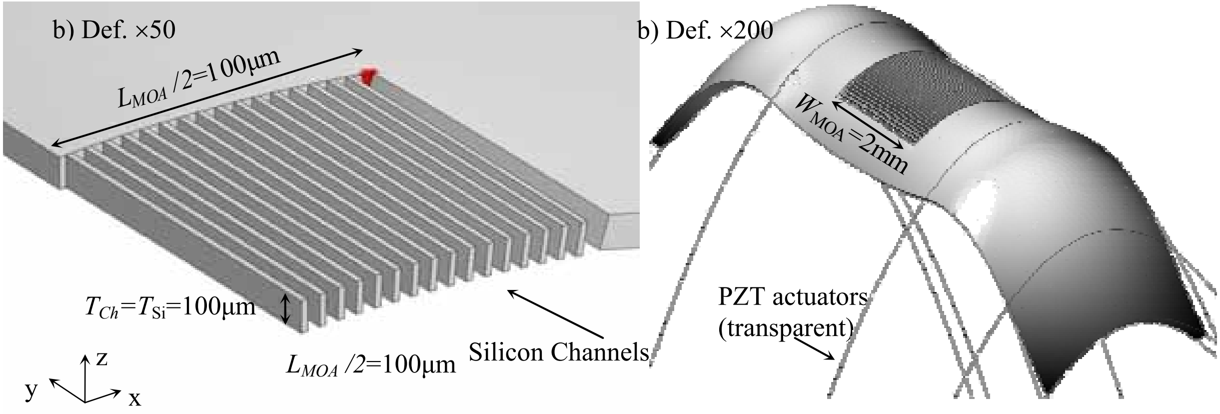

Figure 7.6: Finite element analysis of the initial MOA and actuator design. a) Displacement on the channels (1.9μm) (×50), only one quarter of the MOA chip is shown. The highlighted area shows where the largest stresses are (up to 108MPa). b) Deformation in the centre 3mm strip along the y direction containing the MOA. The curved solid lines indicate where the actuator would be under the chip.

7.3.2 Prototype device of the initial model

A prototype of the initial actuator design was built and the displacement of the actuators tested as shown in Figure 7.7a. It comprised two 20×2×0.15mm PZT unimorph actuators bonded onto a MOA silicon chip with dimensions 20×10×0.20mm, with the MOA microchannels etched onto the centre 2×2mm. The thicknesses used for the silicon chip and the PZT unimorph actuator were chosen according to the materials available at the time and are bigger that those used in the FEA model. Therefore it was expected than the device would bend less, larger ROC, than its corresponding FEA model.

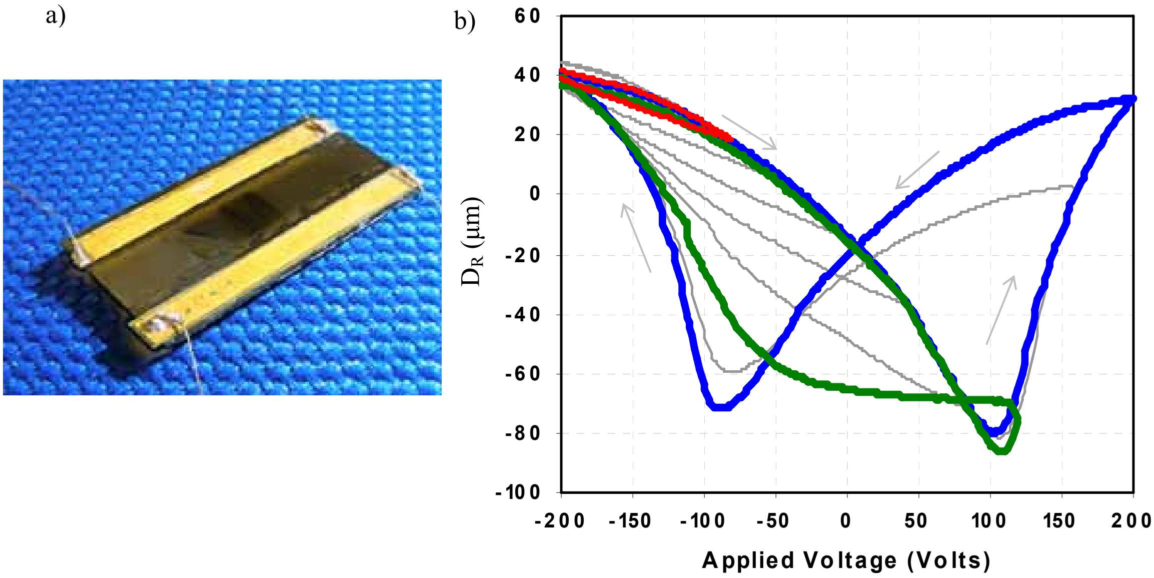

Figure 7.7: a) Test device of the initial MOA model. The test sample has two strips (20mm×2mm×150µm) PZT unimorph bonded on a MOA silicon chip (20mm×10mm×200µm). b) Complete hysteresis loops of the z-displacement at the centre of the sample vs. applied voltages for an MOA test sample.

Using 6.1 and assuming that the bending of the MOA chip is cylindrical and uniform, the z displacement measured over the lenght of the MOA chip ($D_Z=D_z^{Si}$ and $L=L_{si}$) can be to estimate ROC of the MOA channel structures. The bending performance of the device was tested using the experimental setup described in Section 6.4.4 and hysteresis curves obtained for different maximum and minimum applied voltages as shown in Figure 7.7b. The relative displacement D_R is a measure the distance between a point 2mm away from the laser probe and the sample. The D_R measurements show that the greatest change in z-displacement ΔD_z=120µm occurred when the sample is cycled between -200 and 100Volts. This would correspond to a maximum possible change in curvature from flat to 42cm, which is broadly in agreement with the FEA model, demonstrating that the initial design would not be capable of delivering the required ROC of the MOA structures and therefore further optimisation and/or redesigning of the actuation structure was necessary.

The different hysteresis loops in Figure 7.7b also highlight how different the device working regimes could be depending on working conditions used when a V_{min}=-200V was used as the minimum voltage for all the cycles: i) Almost linear (V_{min}=-200V; V_{max}=-80V), depicted in red in the figure. ii) Maximum possible displacements before the domain switching behaviour takes over (V_{min}=200V; V_{max}=120V), depicted in green. iii) Butterfly hysteresis loop dominated by the domain switching (V_{min}=-200V; V_{max}=200V), depicted in blue. Intermediate states at regular intervals are depicted in gray. The measurement was also repeated using V_{max}=200V as the reference voltage obtaining mirrored results.

7.4 Optimization of conventional actuation techniques applied to MOA's

Three possible configurations for the actuation of the MOA chip have been explored: unimorph, bimorph and active fibre composites (AFCs), with the unimorph single strips being the simplest of the solutions. Figure 7.8 shows the FEA of four different actuator configurations for the bending of a silicon substrate depicted in a darker gray tone. The red arrows show the piezoelectric poling directions and the deformation in the figures is magnified for visualization purposes.

The following design parameters were taken for all the devices: the electric fields were set up to be E=2V/μm; the silicon substrate thickness T_{Si}=100μm; the thicknesses of all piezoelectric layers were set up at T_{PZT}=100μm. Figure 7.8a shows the bending of a cantilever beam of length L_{Si}=2mm, width W_{Si}=100μm and thickness T_{Si}=100μm using an unimorph (a1), a bimorph (a2), and up & down unimorphs (a3).

Active fibre composites, which are commercially available(17), use piezoelectric fibres in a polyimide matrix which are actuated using interdigitated electrodes using the d_{33}

instead of the d_{31} mode ($d_{33} \approx -2d_{31}$), therefore providing greater and more directional actuation than unimorph actuators. However, much higher voltages with respect to a unimorph actuator would be needed to exploit these advantages (200V in a 100µm unimorph vs. 1.5kV in a standard AFC). Figure 7.8b shows the bending of a silicon plate with L_{Si}=4.5mm, W_{Si}=1.75mm, T_{Si}=100µm using an active fibre composite with: fibres thickness and width W_{PZT}=T_{PZT}=100µm, distance between electrodes L_{afc}=600µm, and electrode widths W_{afc}=100µm.

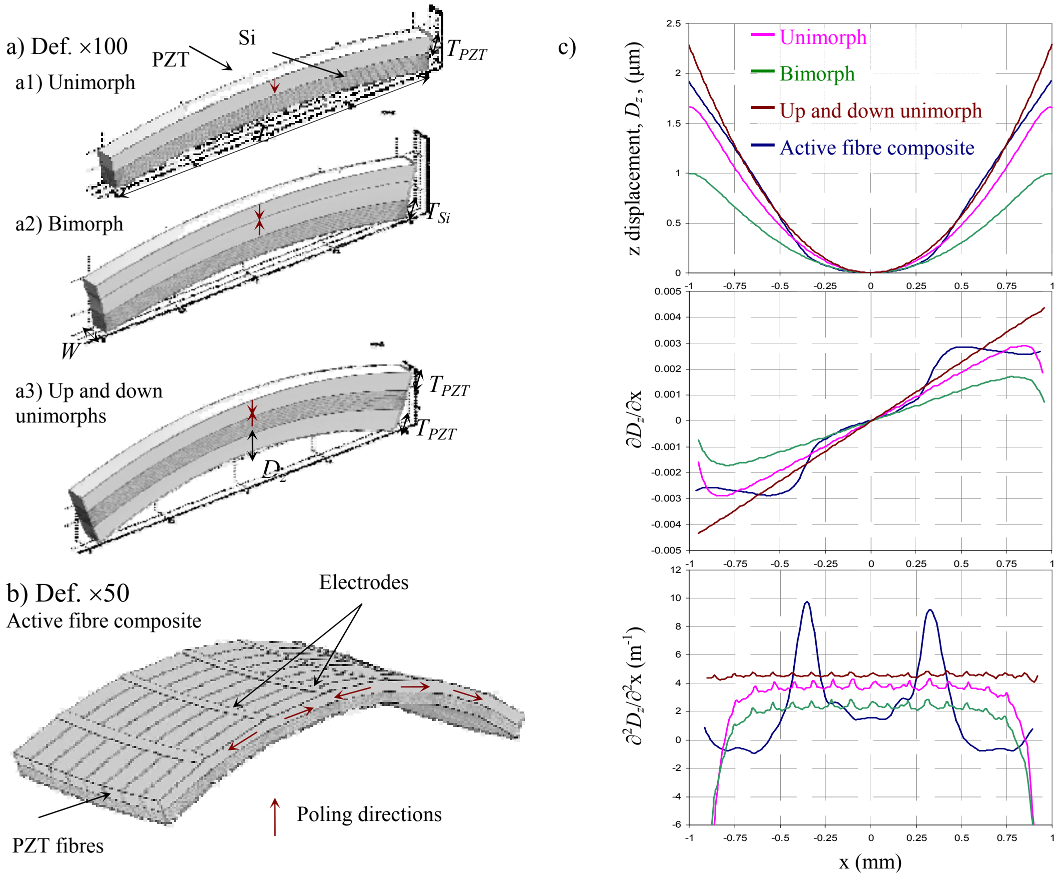

Figure 7.8: **FEA of four different actuator configurations for the bending of a silicon substrate depicted in a darker gray tone. The red arrows show the piezoelectric poling directions. The following design parameters were taken for all the devices: the electric fields were set up to be 2V/µm; the silicon substrate thickness T_{Si}=100µm; the thicknesses of all piezoelectric layers were set up at T_{PZT}=100µm a) Bending of a cantilever beam of length (L=2mm); width (W=100µm) and thickness (T=100µm); using a unimorph (a1), a bimorph (a2), and up and down (a3). b) Bending of a silicon plate with L=4.5mm; W=1.75mm; T=100µm using an active fibre composite. The strips at the top depict the inter-digitated electrodes. c) Comparison of the z displacement D_z and its first and second derivatives for all four actuator designs.**

In the FEA models all four actuators are ideally bonded (bonding layer with zero thickness) to the silicon substrate. The performances of the four actuator configurations are compared in Figure 7.8c where the following magnitudes were plotted for all actuator designs: the z displacement D_z; its gradient, which was calculated by using the first derivative of the z displacement (D_z) with respect to the x coordinate $\partial D_z/\partial x$; and its curvature, calculated using the second derivative the second derivative $\partial^2 D_z/\partial x^2$. Notice that the lower amplitude undulations on the second derivative are a modelling aberration due to the finite mesh size used.

The following conclusions can be extracted from the graphs:

i) The curvature of the AFC is very irregular along the length of the device. This is due to the way the electric field is applied along the lengths of fibres, reaching high values between electrodes and being very low under the electrodes. This behaviour is intrinsic to the AFC design as explained in Section 4.5.3, and therefore makes AFC unsuitable to be used to bend MOA as they require an uniform curvature.

ii) Less bending is obtained with the bimorph than with either of the two unimorph configurations. These can be visualised in force/displacement diagram following a parallel argument to that used in Section 4.5.2 for stack actuators. The bimorph is less effective than the unimorph because part of its energy is used to bend itself.

iii) Bimorph and single unimorph configurations present a range in x of constant curvature on the device and edge effects at both ends of the silicon substrate.

iv) The up and down unimorph configuration (Figure 7.10a3) is the one capable of bending the device more, and the curvature is constant along the whole length of the device. However, only a small increase in curvature, ~15% is obtained with respect to the single unimorph configuration (Figure 7.10a1) when only the centre region, where the MOA would be, of the device is considered.

The single unimorph has the second highest curvature at the centre of the device of actuator configurations considered, it is also the simplest, and it is this concept that is developed further below.

7.4.1 The influence of thicknesses and aspect ratios on unimorph actuators

Considering how to maximise the bending of the MOA chips, the obvious answer would be to go for thinner silicon wafers to reduce their stiffness. To take advantage of a thinner silicon wafer, thinner PZT is also necessary as will be argued in the next paragraph. However, there are practical limits on how thin the MOA device can be. In order to maintain the same amount of flux the aspect ratios (height/width) of the walls of the MOA also need to be maintained(10, 14), therefore using thinner silicon wafers would make the etching of the channels more difficult which, together with handling issues, sets the practical limit for thickness of the silicon wafer at 50µm minimum. From the piezoelectric perspective, free standing PZT sheets thinner than 50µm are difficult to manufacture using VPP manufacturing, and other routes such as thick film have disadvantages with respect to VPP as discussed in Section 4.3.

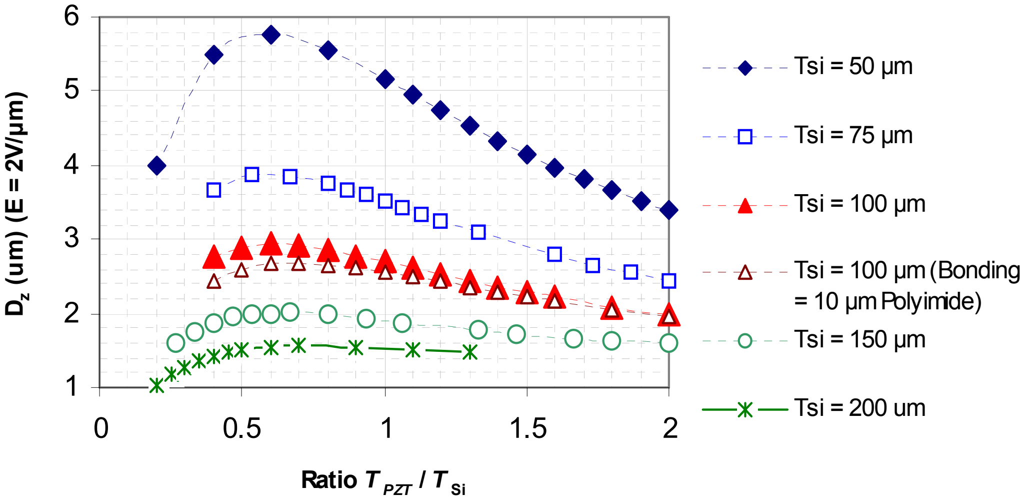

Figure 7.9: . a) Bending displacement (D) of a silicon cantilever beam with *L*=2mm and *W*=100µm and range of silicon thicknesses (T_{Si}) as a function of the T_{PZT}/T_{Si} thicknesses ratio. The electric field on the PZT actuators are 2V/µm.

In the case of unimorph actuators, such as the cantilever beam shown in Figure 7.8a1, the relative thicknesses of the silicon and the PZT can be optimized to maximise the bending. Figure 7.9 shows 2D-modelling results, considering the y direction infinite, for the dependence of the central displacement D of a 2mm long cantilever beam for a range of silicon thicknesses for a constant electric field of 2V/µm applied to the piezoelectric actuators, which is close to the working maximum. Assuming circular bending, the displacement for the target ROC of 5cm is 10µm. As would be expected, thinner silicon wafers are advantageous, but the graphs also highlight that the ratio T_{PZT}/T_{Si}~0.6 maximises the bending. The 2D modelling shown assumed a zero thickness of the bonding layer except for T_{Si}=100µm where both zero bonding and a $T_{pol.}$ =10µm bonding layer are shown for comparison. The bonding layer has the effect of slightly decreasing the amount of bending.

However, in piezoelectric material poled in the z direction, both x and y directions are equivalent. As shown in Figure 7.10, a unimorph will bend the silicon wafers in the x and y directions, leading to more complicated shapes of the bent structure. For example, if the structure were a disk instead of a square it would bend in the shape of a dome.

7.5 The initial spider MOA design

Since the use of the piezoelectric actuation alone has been shown not to produce sufficient actuation for the MOA structure, a new arrangement in which the piezoelectric strips are used to actuate a series of levers, in effect amounting to a mixed piezoelectric and integrated mechanical bending solution, was devised. The levers can be made by dry etching angled channels all the way through the silicon chip resulting in silicon levers which move independently when the piezoelectric strips are actuated. These levers effectively play the role of amplifying the curvature of the channels at the centre of the chip.

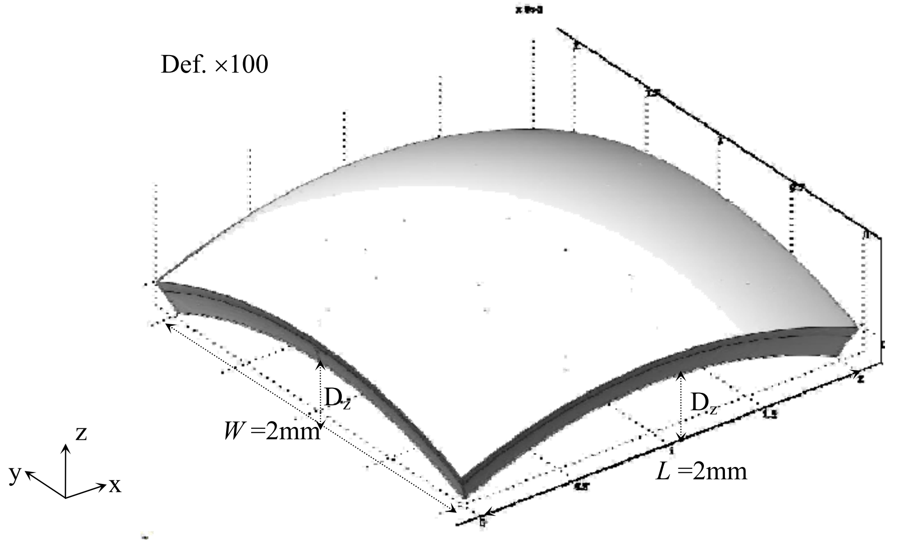

Figure 7.10: FEA of the bending of a square silicon plate using a square unimorph actuator with L_{Si}=L_{PZT}=W_{Si}=W_{PZT}=2mm, and thicknesses T_{Si}=100µm and T_{PZT}=60µm PZT unimorph. Notice that the plate bends the same amount in the x and y directions. The deformation is exaggerated by a factor ×100 for representation purposes.

7.5.1 Initial spider design: FEA analysis

FEA models were set as shown in Figure 7.11 with the so called spider MOA pattern drawn on a silicon wafer with thickness T_{Si}=100µm. The piezoelectric coefficients chosen were those corresponding to a PZT-5H ceramic and the bonding layer between the actuator and the silicon wafer was assumed to have zero thickness. The two piezoelectric strips with dimensions L_{PZT}=2cm, W_{PZT}=2mm and a thickness T_{PZT}=75µm were used in the FEA models as it would maximise the actuation for a T_{Si}=100µm(11).

Figure 7.11 shows the FEA modelling of the deformation (×20) of a 2×2cm spider array on a 100µm thick silicon wafer and an applied voltage of 150Volts to the piezoelectric actuators. The z displacements at the edges of the chip are 280µm, compatible with the curvature predicted for an unimorph cantilever beam. The displacements (×50) in the channels area with the highlighted areas at the end of the levers in the beam connecting the MOA channels at the centre of the chip representing the areas with highest tensile stresses on the chip (up to 100MPa). The ROC in the centre 2mm of the chip (across the channels) was 4.5cm, smaller than the 5cm target.

Silicon is the preferred material of choice for the substrate, as manufacturing techniques developed for the electronics industry are directly applicable to it. However, another possible manufacturing route would be to use etching techniques to create a silicon mould which could later be used to manufacture the final device (for example using electroforming methods).

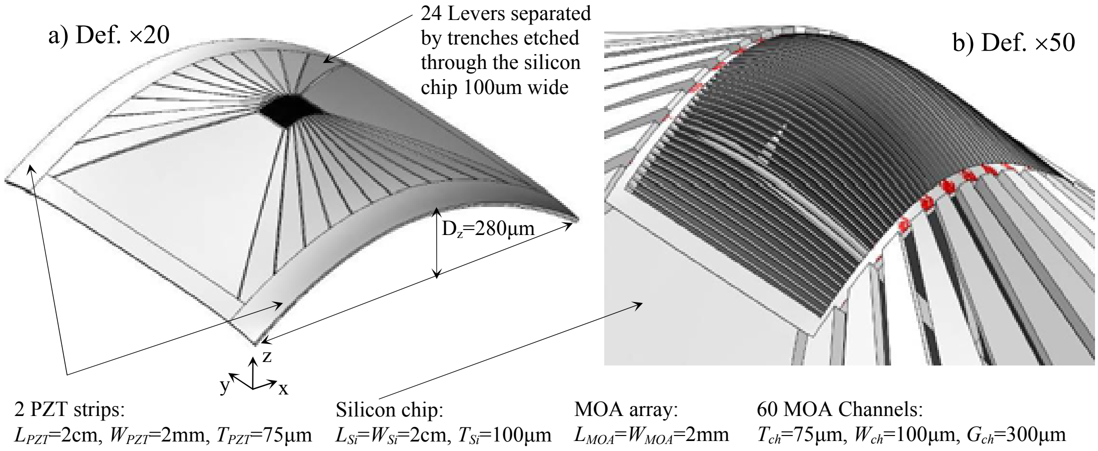

Figure 7.11: **a) Modelling of the displacements (×20) on the spider array when a voltage V_i=150Volts was applied to the piezoelectric actuators. b). Displacements (×50) on the channels. The highlighted areas in red are the points with highest stresses (up to 109MPa).**

Therefore, an exercise of interest from an academic perspective was to investigate what the dependence of the spider MOA behaviour as a function of the mechanical properties, Young's modulus and Poisson ratio, of the substrate. The FEA results are presented in the Figure 7.12, showing that for Young's modulus values 10GPa<Y_m<70GPa, such as aluminium with 69GPa and magnesium with 45GPa, ROC_{MOA} values lower than 3cm could be possible without any further optimisation of the device.

7.5.2 Initial spider design: Manufactured test samples

Test spider structures were manufactured at the University of Edinburgh using a dry etching process(9) with the intention to demonstrate the capability of the spider design to bend the centre 2x2mm of the chip to the required radius of curvature without breaking.

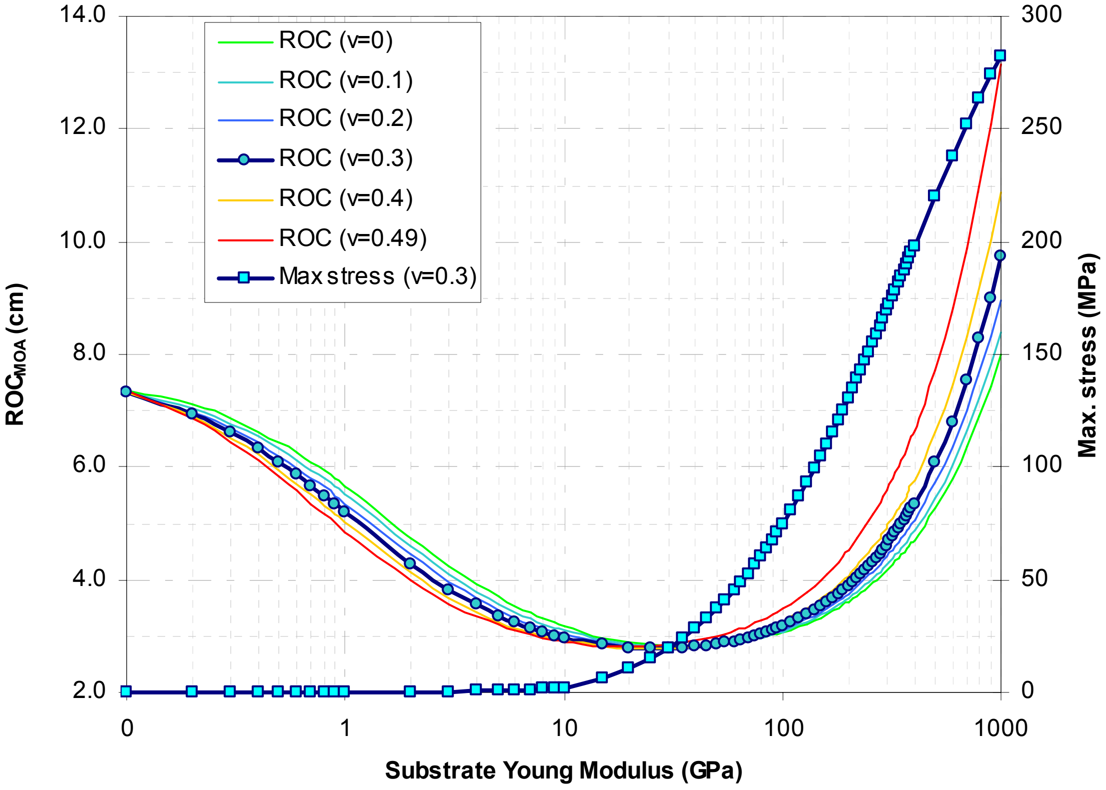

Figure 7.12: FEA modelling results for the dry eched spider MOA using the parametric solver to calculate the radius of curvature of the channels ROC_{MOA} and the maximun stress on the spider structure as a fucntion of the Young's modulus, Y_m, and poissons ratio, ν, of the material used as the substrate.

Figure 7.13a shows test samples where the spider pattern has been etched all the way through the wafer and Figure 7.13a when the etching process was stopped about 20µm before reaching the bottom face of the silicon wafer. Figure 7.13c shows a picture of a test device where two PZT actuators have been mounted onto the dry etched silicon wafer.

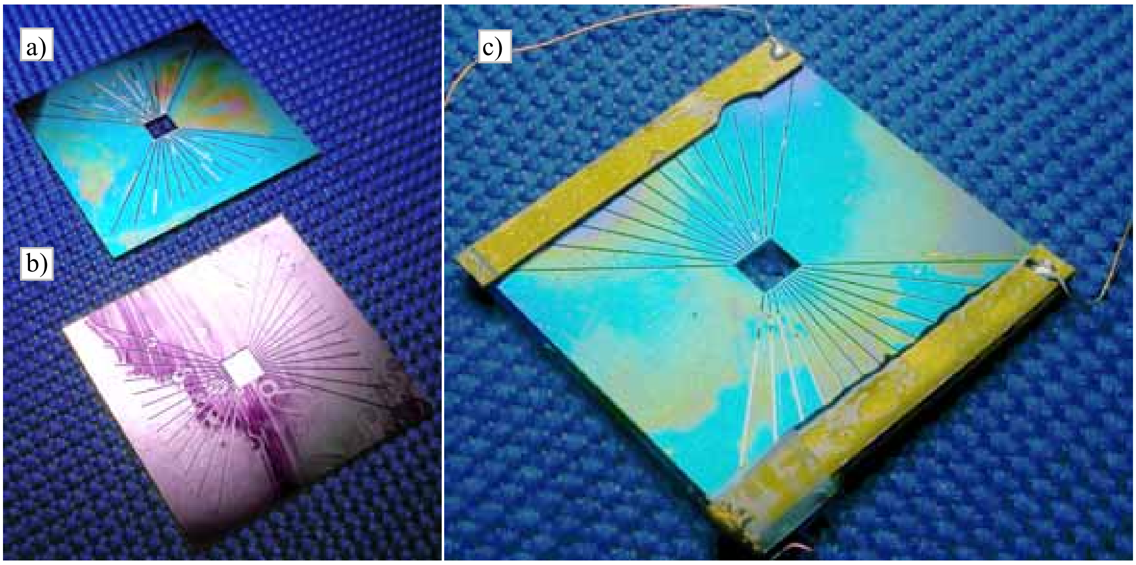

Figure 7.13: **a) and b) Dry etched spider pattern on a 2cm×2cm×100µm Si wafers. c) 2cm×2mm×120µm PZT piezoelectric actuators mounted on one spider device.**

7.5.3 The initial spider design: Characterisation results

Some of the samples which were not etched all the way through the wafer were mounted on pre-curved clamps with a 25cm ROC fitted on the outer 2mm as shown in Figure 7.14. The flat side of the sample is effectively a mirror for which the curvature can be measured. The curvature measurements of the centre were carried out using three different methods: a) Using a Talysurf profilometer to obtain a trace along the edge of the centre 2×2mm; b) using an interferometer; and c) measuring the size of a reflected laser image of the top surface as shown in Figure 7.14a. The laser beam was deliberately defocused to illuminate the whole of the test sample surface. The three measurements were consistent indicating that the clamped sample presents a ROC of 3cm at its centre. Figure 7.14b and Figure 7.14c show the difference in displacement using as a reference a flat surface and a 3cm ROC surface respectively.

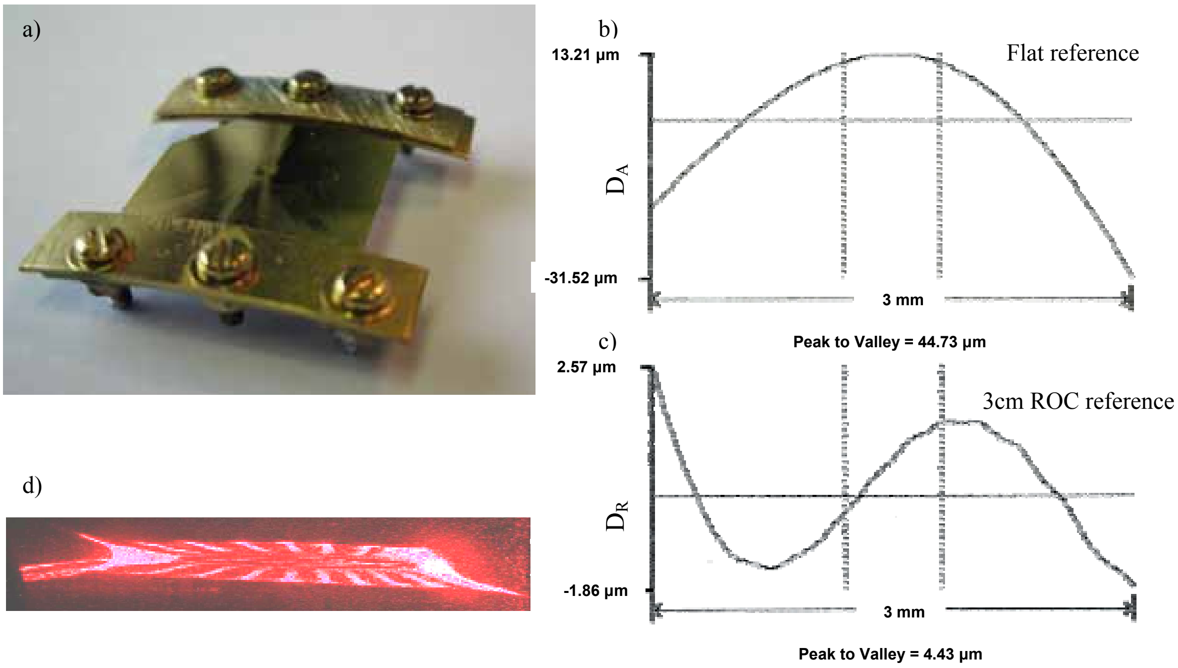

D_A ≡ absolute displacement, distance between the tip of the profilometer and the surface
$D_R = D_A - D_{Ref}$ ≡ relative displacement, where D_{ref} is the displacement of a reference surface of given ROC.

Figure 7.14: a) Clamped spider sample in a pre-curved jig. The sample was not dry etched all the way through so the top surface and centre area could be used as a mirror and characterised. b) Curvature profile over the beam adjacent to the centre area measured using a Talisurf profilometer with a flat reference and c) difference between the absolute measurement and a 3cm ROC reference, which is the best curvature estimate. d) Reflecting image off a laser light source when the whole of the top surface is illuminated.

Reflective images where also obtained for devices mounted with 2cm×2cm×150μm piezoelectric actuators. The reflective images indicated that the devices could be bent from flat to a ROC=8cm at their centre which is consistent with the values predicted by the FEA models as the PZT actuators were not at their optimum thickness of 75μm for 100μm thick silicon wafers.

7.6 Wet etching compatible spider MOA's

Characterisation results of the surface roughness of the MOA channels(9), together with the ROC measurements of the initial dry etched spider test samples mean that the two main technical challenges of the MOA technology, i.e. smooth channel walls with a surface roughness <2nm and controllable curvature to a ROC_{MOA}<5cm have been achieved. The remaining problem was to find a way of integrating both aspects of the design onto the same device.

Two spider and wet etched channels integration options were considered:

i) To use a double sided process on a "silicon on insulator" (SOI) wafer, where the spider pattern could be dry etched on one side of the wafer and the MOA channels wet etched on the other side with the oxide layer acting as a buffer zone. This was very challenging from the manufacturing perspective, as issues such as the front to back alignment of the masks would need to be solved;

ii) Re-design the spider pattern so it can be wet etched in the same manufacturing step as the MOA channels. This was much more attractive from the manufacturing perspective but it had the implication of having as a design rule to use the direction of the {111} silicon crystallographic planes on the (110) silicon wafers; i.e. parallel to the silicon channels or at a 70.53^{o} angle as explained in more detail in the Appendix II. The directions of both sets of planes are generally indicated by the directions of the main and secondary flat on (110) silicon wafers. Other sets of silicon planes could also be used to etch trenches in the silicon, such as the {110} planes, but their side walls would not be normal to the surface of the wafer when they were wet etched.

The second alternative was chosen, as it would produce more stable structures and would also be easier from the manufacturing perspective. It led to the design described below.

7.6.1 Design of the silicon chip

Figure 7.15 shows an alternative spider arrangement on a 2×2cm silicon chip. As with the previous arrangement the micro-channels would be etched in the central 2×2mm region, piezoelectric actuators, with dimensions 2cm×2mm×75μm, would be glued onto the 2mm wide strips at the top and bottom of the silicon chip. As with the model shown in the previous section the piezoelectric coefficients of PZT-5H were used and the thickness of the bonding layer was considered to be zero. The difference is that the levers of the spider MOA structure are drawn using two sets of planes: either parallel to the silicon channels; or at an angle of 70.53^{o} which coincides with the second set of {111} planes on (110) silicon; and therefore can be wet-etched in a single step.

The main design parameters are: the number of legs (N_L); the width of the levers when they meet the frame enclosing the micro-channels (W_B); the gap between them (W_G); the width of the frame supporting the micro-channels (W_F); and the distance between the end of the trenches defining the levers and the edge of the chip (W_A).

Figure 7.15 depicts a version of the model with N_L=20, W_G=W_B=W_F=100μm, and W_A=2mm, but other combinations would also be possible.

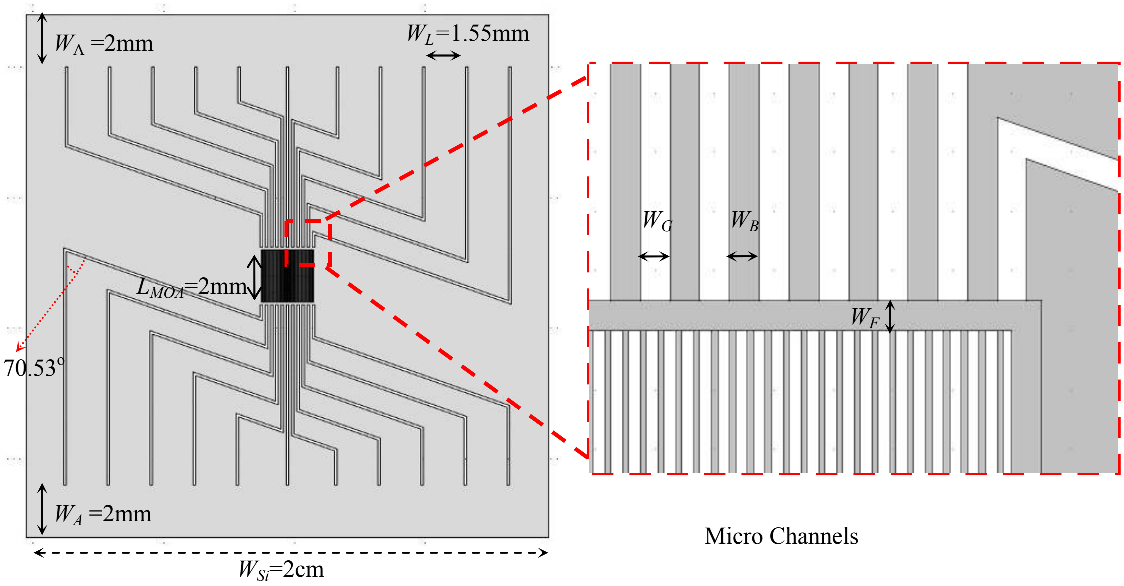

Figure 7.15: Wet etch compatible model definition for a spider design with number of legs NL=20. The micro-channels are located in the central 2mm×2mm region. The trenches are drawn parallel to the silicon channels and at an angle of 70.53° coinciding with the {111} planes in (110) silicon. The insert depicts the levers meeting the micro-channels.

7.6.2 Manufactured samples

Several spider-MOA structures have been manufactured using a wet etching process which is being developed at the University of Edinburgh. They included 6 different designs, with N_L, W_B and W_G values shown in Table 7.1, in order to allow comparison of FEA models with test results, and optimization of N_L and W_B. The micro channels in the central 2×2mm area have a width W_{Ch}=6μm and gap width G_{Ch}=4μm for all six models. The device thickness is determined by the initial thickness of the silicon wafer to be etched and the duration of the etching process. Samples corresponding to all six models have been successfully manufactured. Critical issues from the manufacturing perspective were alignment, handling and control of the wet-etch rates. Further details of the samples manufacturing were presented elsewhere by Camelia Dunare et al(18).

The silicon wafer was divided into 9 devices using six design variations. The device thicknesses are determined by the initial thickness of the silicon wafer to be etched and the duration of the etching process. M2, in bold characters in Table 7.1, was the design specification used for the FEA in the next section

Table 7.1: Design parameters of the 5 inch mask used to create the oxide mask on the silicon surface.

Model *Units*	N_L	W_B *μm*	W_G *μm*	W_L *mm*	W_A *mm*	W_F *μm*	W_{Ch} *μm*	G_{Ch} *μm*	L_{Si} *mm*	W_{Si} *mm*
M1	24	80	80	1.4	2	100	4	6	20	20
M2	**20**	**100**	**100**	**1.7**	**2**	**100**	**4**	**6**	**20**	**20**
M3	28	70	70	1.2	2	100	4	6	20	20
M4	20	80	120	1.7	2	100	4	6	20	20
M5	24	100	60	1.4	2	100	4	6	20	20
M6	20	120	80	1.7	2	100	4	6	20	20

7.6.3 Proof of concept: Preliminary results

Figure 7.16 shows optical pictures of two spider MOA samples manufactured at the University of Edinburgh for two different designs (M1 and M3 as described in Table 7.1), and SEM pictures of a partially etched device showing the levers and channel structures.

Test samples were mounted into a holder with two pivot points at the centre of the sample, so the lever action was not restricted, as shown in Figure 7.17a. Figure 7.17b shows one of the spider MOA's with a silicon thickness T_{Si}=120μm with two piezoelectric strips, 2cm×2mm×120μm, glued onto one surface. The PZT piezoelectric strips were manufactured using a viscous plastic processing technique and co-sintered with platinum electrodes, as described in Section 6.3.1. The top surface of the sample was then used as a mirror to estimate the ROC of the MOA once the spider structure was actuated.

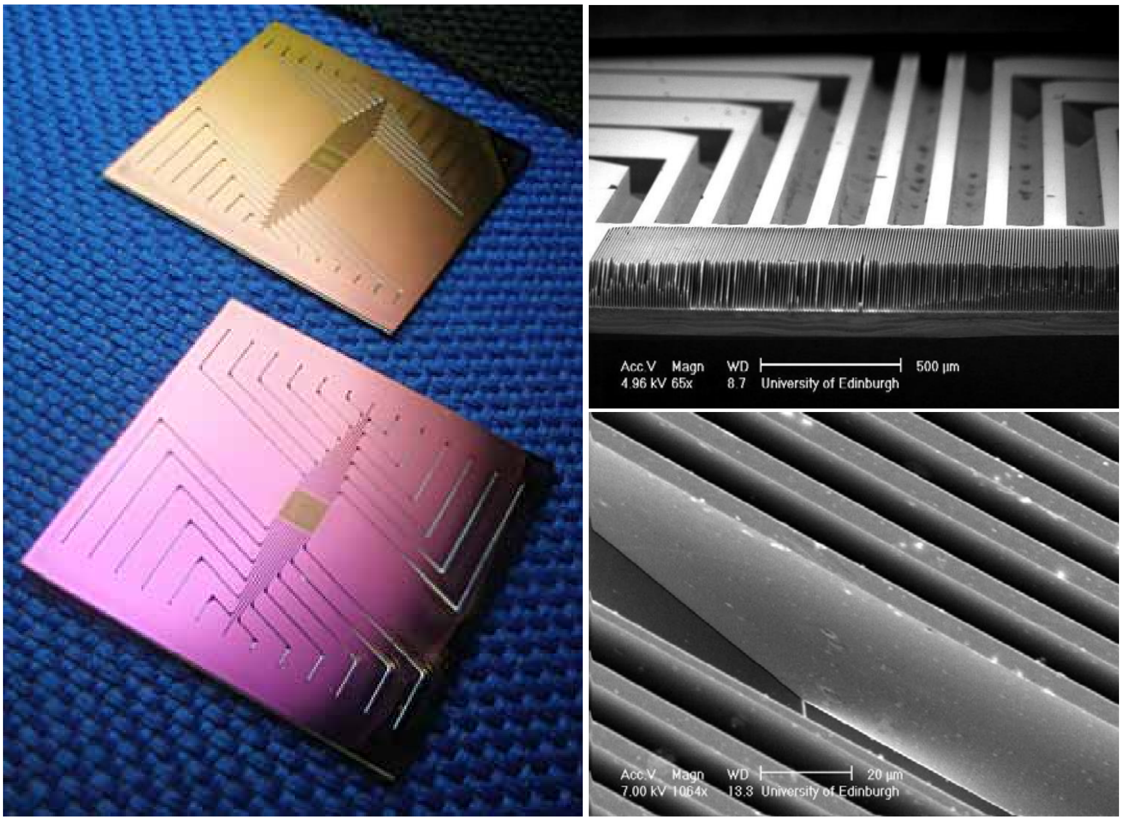

Figure 7.16: Optical and SEM pictures of wet etched spider devices (left). The SEM pictures, courtesy of the University of Edinburgh, showing a cross-section of a partially etched device (top-right) and smooth channel walls of the MOA arrays (bottom-right).

Figure 7.17c show images obtained when the whole of top surface of the MOA device is used as a mirror and is illuminated with laser light. Different applied voltages, V_i, to the piezoelectric strips were used. For V_i=0 the image is a line, corresponding to a flat sample. As the voltage is increased the image starts to split and for V_i=60V a central hole appears which corresponds to the place where the channels would be in the sample. The dimensions of this centre area were used to estimate that ROC_{MOA}~11cm at 60V. When V_i was increased to 195V the dimensions of the image increased, i.e.

the sample was more curved, but became less symmetric. The ROC_{MOA} from the dimensions of the image varies from 6.5cm on the left to 5cm on the right. The condition of the MOA's was inspected after a few actuation cycles, and all of them remained intact without additional defects on the channels themselves.

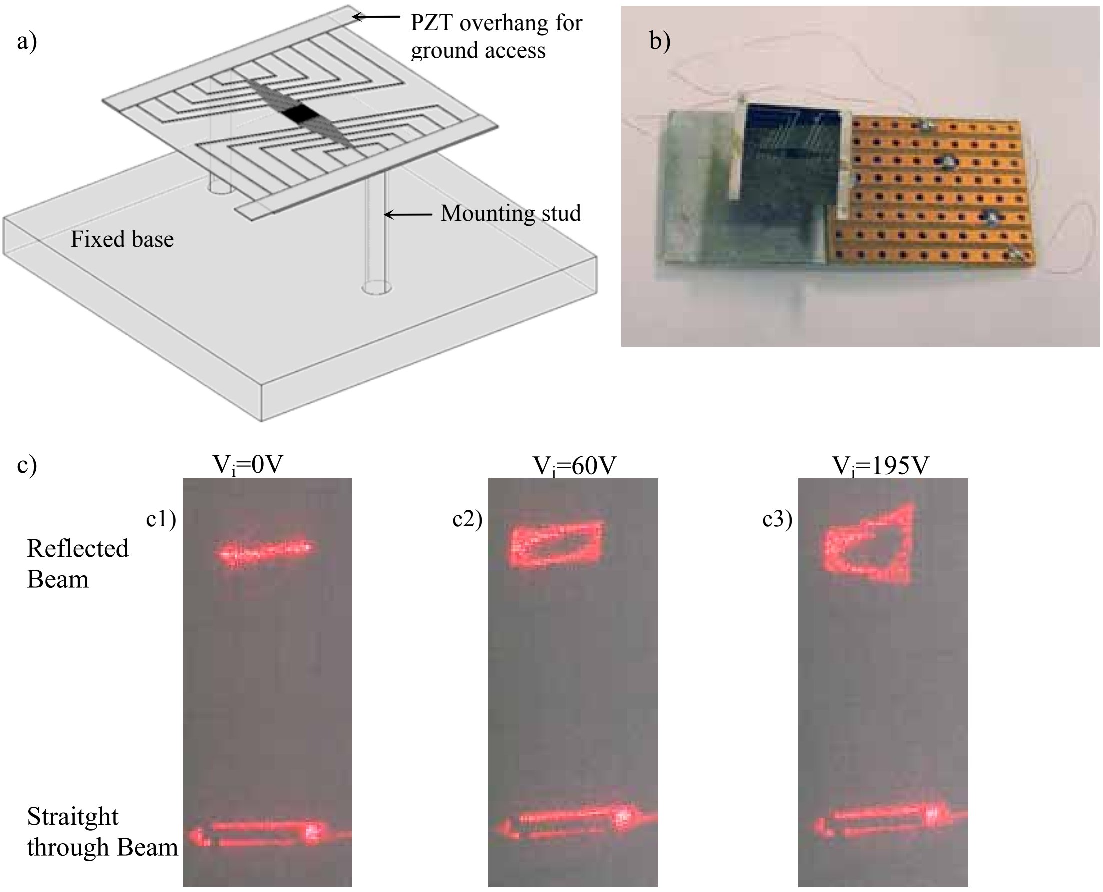

Figure 7.17: a) Schematic representation of how the spider MOA was mounted b) Spider MOA with two piezoelectric strips at its edges and mounted onto a holder. c) Reflective images of the top surface or the spider MOA (top) and straight through light (bottom) for 0V, 60V and 195V applied to both piezoelectric actuators (c1, c2 and c3 respectively).

7.7 Optimization of the Actuator Layout

The simple design of the piezoelectric layer, two piezoelectric strips, for the initial spider model used in two piezoelectric strips of dimensions 2cm×2mm×75μm bonded to the outside 2cm×2mm edges of the silicon, as this was also modelled for a 20 leg version of a wet etched spider MOA in 100μm silicon. As with the initial spider design the FEA models predicted a ROC below 5cm for the wet etched version when maximum electric field E_{max}=2V/μm were applied to the piezoelectric strips.

However, this simple actuator layer arrangement could be improved to add extra capabilities to the spider MOA chip in two ways: i) The piezo strips could have segmented electrodes which would bring the added benefit of controlling the curvature profile on the MOA channels and possibly cancelling out slight differences in the thicknesses of the piezoelectric and bonding layers. ii) Extending the piezoelectric actuators over the spider legs to actuate more areas of the silicon. This could have the benefit of adding extra degrees of freedom on the control of each individual leg of the spider.

To investigate these effects a FEA model was constructed for a 20 leg configuration, corresponding to that of the design variation M2 in Table 7.1 and a silicon thickness T_{Si}=100μm, in which the PZT actuator layer covered most of the silicon chip with trenches coincident with the gaps in the silicon. The same assumptions as in previous models were taken: piezoelectric coefficients equivalent to those in PZT-5H, and zero thickness of the bonding layer. The FEA model different areas of the actuator were separately addressed as shown by the regions labelled in Figure 7.18. The electrodes were arranged in four different levels: Level A, which would correspond with the piezoelectric strips in the simpler actuator design and provide the curvature and levels B, C and D. The areas not labelled in Figure 7.18 were not actuated in the models in order to keep where possible actuated areas of similar sizes and to try to maintain symmetry on the actuator layer of the chip. The labelling convention was to assign a number n=1, 2… 20 to each one of the legs with odd numbers at the top and even numbers at the bottom.

When all the electrodes in Level A are actuated to their maximum 150V and the electrodes in levels B, C and D are kept to 0V the silicon MOA channels are bent to a radius of curvature ROC_{MOA}<5cm in agreement with the initial simple model with two piezoelectric strips providing actuation. To investigate the effect on the MOA position actuation of several voltage combinations for the Levels B, C and D were modelled whilst voltages at the Level A where maintained at 150V. The FEA analysis shows that that the applied voltages on the Levels B and C could be used to control the z positioning (+/-20µm) and tip/tilt angles (+/-3mrad). The applied voltages to the Level D could be use to cancel out the unwanted bending along the y direction.

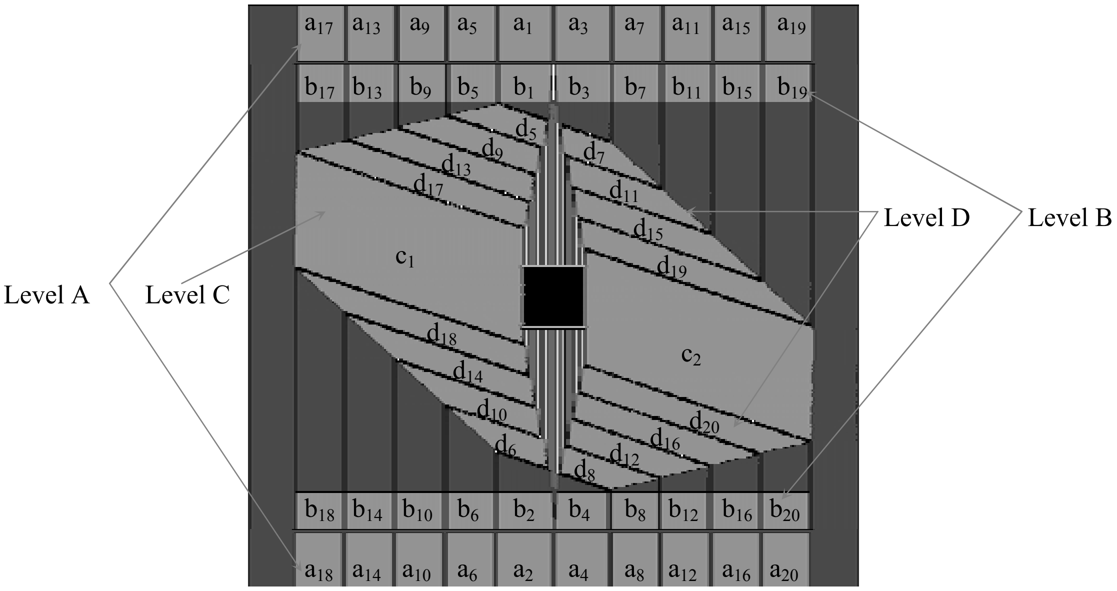

Figure 7.18: Modelled electrode areas for the wet-etched MOA configuration. The electrodes were arranged in four different levels: Level A, which would correspond with the piezoelectric strips in the simpler actuator design and provide the curvature and levels B, C and D. The areas not labelled were not actuated in the models in order to keep where possible actuated areas of similar sizes and try to maintain symmetry on the actuator layer of the chip. The labelling convention was to assign a number n=1, 2… 20 to each one of the legs with odd numbers at the top and even numbers at the bottom.

The Figure 7.19 depicts the FEA model of the actuated spider MOA where the deformations have been amplified by a factor of 20 (left) and 50 (right) for visualization purposes. The voltages in the Level D where selected to suppress the unwanted bending along the y direction. The coloured areas in Figure 7.19 represent those regions of the chip with the highest stress (maximum of 220MPa below the maximum breaking stress of silicon of 250MPa).

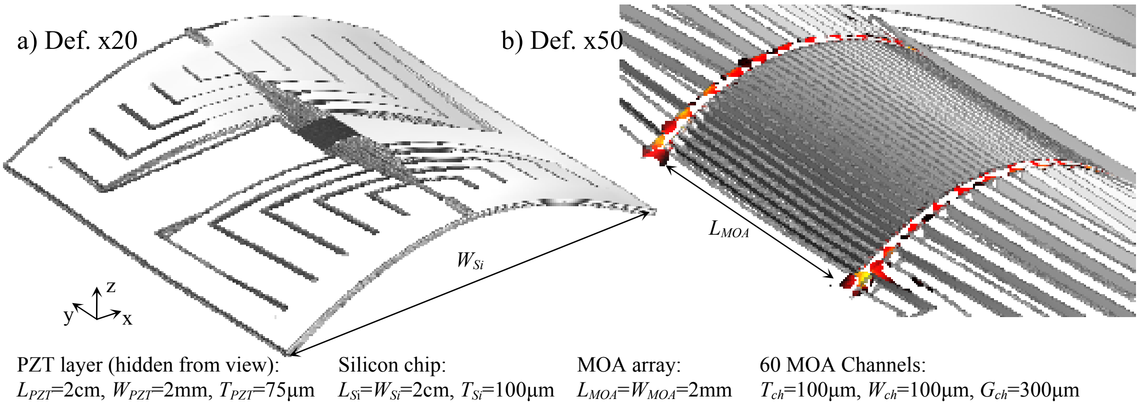

Figure 7.19: Results from the FEA models of a 20 leg spider MOA configuration. The deformations are multiplied by a factor of 20 and 50 in a) and b) respectively for visualization purposes. a) View of the whole spider MOA chip from the silicon side, the actuator would be beneath. b) Zoom image of the MOA area. The areas depicted in colour indicate the regions of highest stresses in the structure.

7.8 Spider unimorph actuators design and manufacturing

7.8.1 Design of the segmented electrodes on the PZT actuators

The FEA analysis shown in the previous section was a useful theoretical exercise which allowed an understanding of the effect of actuating different areas of the spider design. However, practical issues regarding how the actuator would be fabricated and assembled onto the spider MOA chip also needed to be considered. For example, the number of actuated areas should be minimised to simplify both the hardware and software used for their control. Modelling using X-ray tracing techniques (Q software) was carried out at the University of Leicester to investigate the effect of the unwanted curvature along the y direction on the MOA performance and it was found that it was the less critical of the issues in terms of reducing the width of the focused X-ray beam. Therefore the decision was taken to design the actuators without the Level D of actuation so there is no actuator over that region of the silicon chip as shown in Figure 7.22. In addition, adjacent electrodes on the Level A of actuation were joined together to reduce the number of electrodes. In the level B the actuation areas were divided so they coincide with the spider legs on the silicon underneath. These could be: physically separated by trenches through the actuator layer, in which case actuation of each one of them would be decoupled from that of neighbouring level B areas; or joined together with only electrode separation, in which there would be a degree of interaction between neighbouring actuator layers. Finally, the ground electrodes would be accessible by using the "ears" on the actuator layer, which would be joined with conductive silver epoxy to the other side of the actuator through the edges.

Three versions of the actuator layer were designed to match the 20, 24 and 28 legs spiders and the 24 leg version is shown in the Figure 7.20 below.

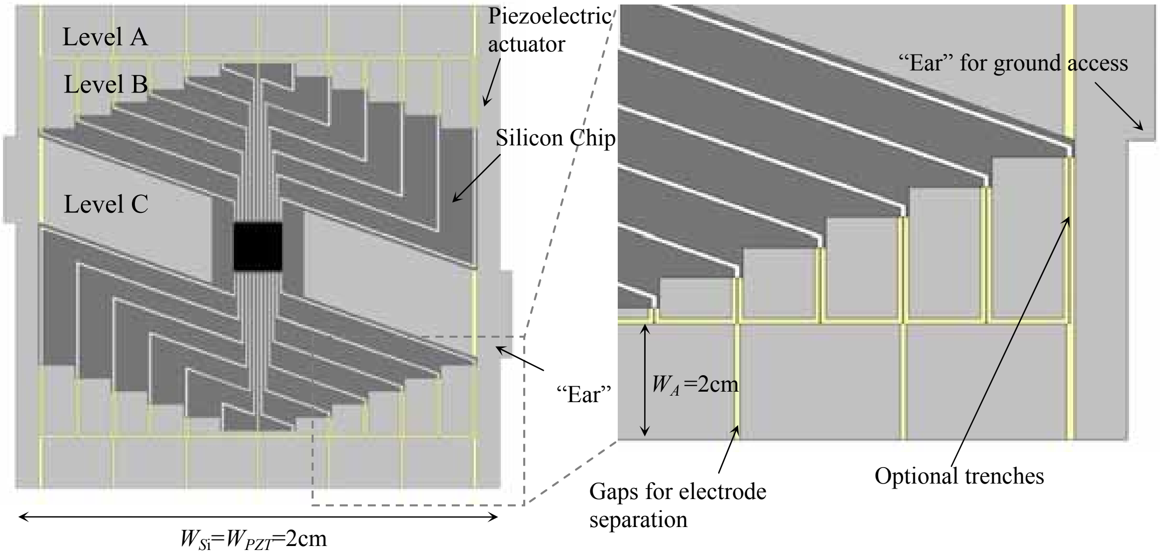

Figure 7.20: Proposed actuator design with 30 actuated areas for a 24 legs spider MOA configuration, 12 in the Level A, 16 in the Level B and 2 in the Level C, mounted on top of the spider MOA silicon chip.

7.8.2 Manufacturing of piezoelectric plates using Viscous Plastic Processing (VPP) technique

To enable the unimorph spider actuator design oversized unimorph piezoelectric plates needed to be manufactured. The viscous plastic processing (VPP), as described in Section 6.3.1, was used to create thin sheets (~100µm thickness) of green piezoelectric material. The green sheets were then screen printed on both sides with a layer of platinum ink (~20µm)[*]. The green PZT sheets with printed platinum electrodes were then cut to 3.5cm × 3.5cm squares. The samples were then sintered in batches of three at the time buried in layers of lead oxide sand in a crucible in other to maintain the lead stoichiometry of the samples.

After sintering the sample edges were polished to remove any bridging of the top and bottom electrodes and poled on an oil bath. The poling cycle used was the following: 5minutes at 190^{o}C and 150V and 5 minutes whilst cooling down with a fan outside the oil at 150V after which the samples were removed from the poling jig. The poling oil was cleaned using a sequence of solvents as previously described in Section 6.3.1.5.

The electric impedance was measured on an impedance analyser, Agilent 4294A, and to check they were active and presented the thickness and lateral resonances.

In terms of manufacturing yield 60% of the samples were successfully poled with most failures happening during the poling processes where build up of the charge

---

[*] The VPP processing of the green ceramic and the printing of the platinum ink was conducted by Carl Meggs at the University of Birmingham.

destroyed some of the samples. Optical and SEM pictures showing manufactured VPP plates and their microstructure are shown in the Figure 7.21 below.

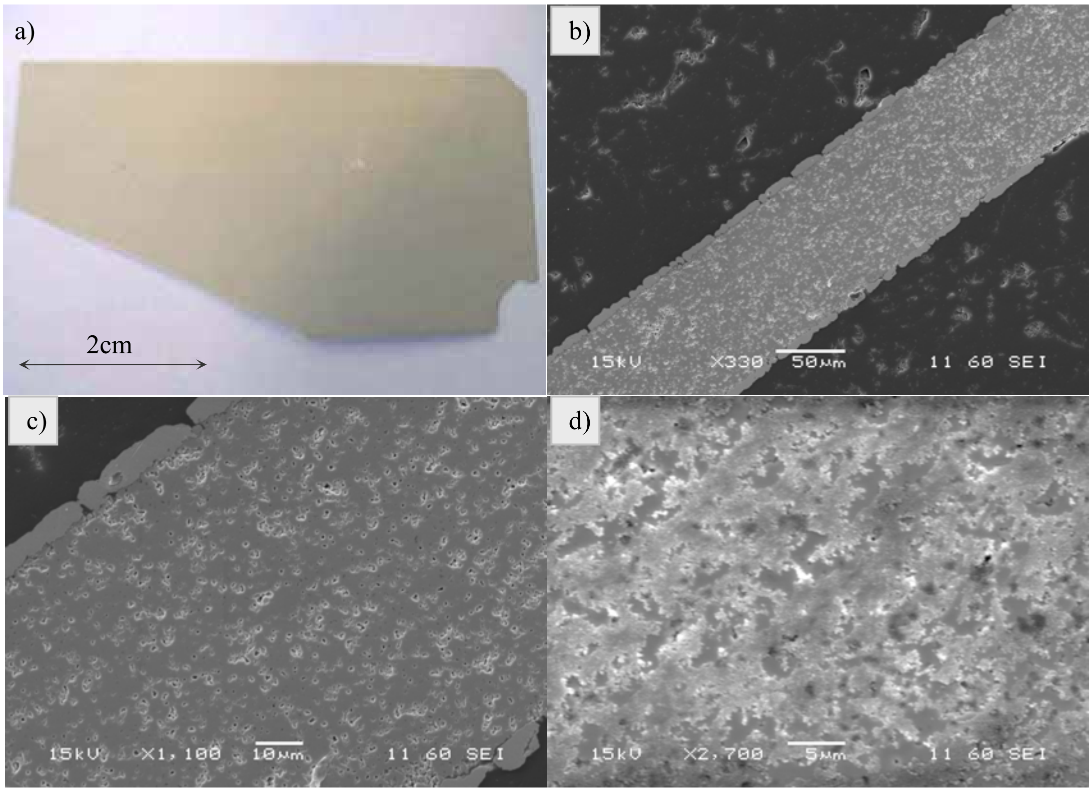

Figure 7.21: a) Photograph of a piezoelectric plate with sintered electrodes and thickness TPZT=80µm manufactured using a VPP technique. b, c and d) SEM pictures showing the microstructure of the plate.

7.8.3 Laser machining the of the piezoelectric actuator

The required machining steps to obtain the actuator layer for the spider MOA are shown in Figure 7.22 and entail: Cutting off the outside edges; cutting of the centre hole and, if required trenches to define the level B; and the removal of platinum on the yellow lines to define the segmented electrodes (top view) whilst maintaining an continuous ground electrode (bottom view).

The paths for the laser to follow would have to be defined for the laser machining of the PZT sample to define the areas to be machined whilst the number of passes would define the depth of the cuts to cut the PZT layer all the way trough or to just remove the electrodes to obtain the segmented electrodes. In practice, the steps defined in Figure 7.22a would be combined in the following sequence in order to minimise the number of laser machining steps and ease the handling of the PZT plate following the sequence: i) vertical electrode removal, ii) horizontal electrode removal; iii) cutting the centre hole and the trenches if required; iv) and cutting outside edges. The CAD files were drawn for each one of these steps, as shown for the 24 leg spider in Figure 7.22b, using the drawing of the silicon masks as a reference and then translated into a list of coordinates using a code compatible with the laser cutting machine at Mullard Space Science laboratory (MSSL). Three version of the drawings were made that will match the wet etched pattern on the spider MOA with 20, 24 and 28 legs respectively.

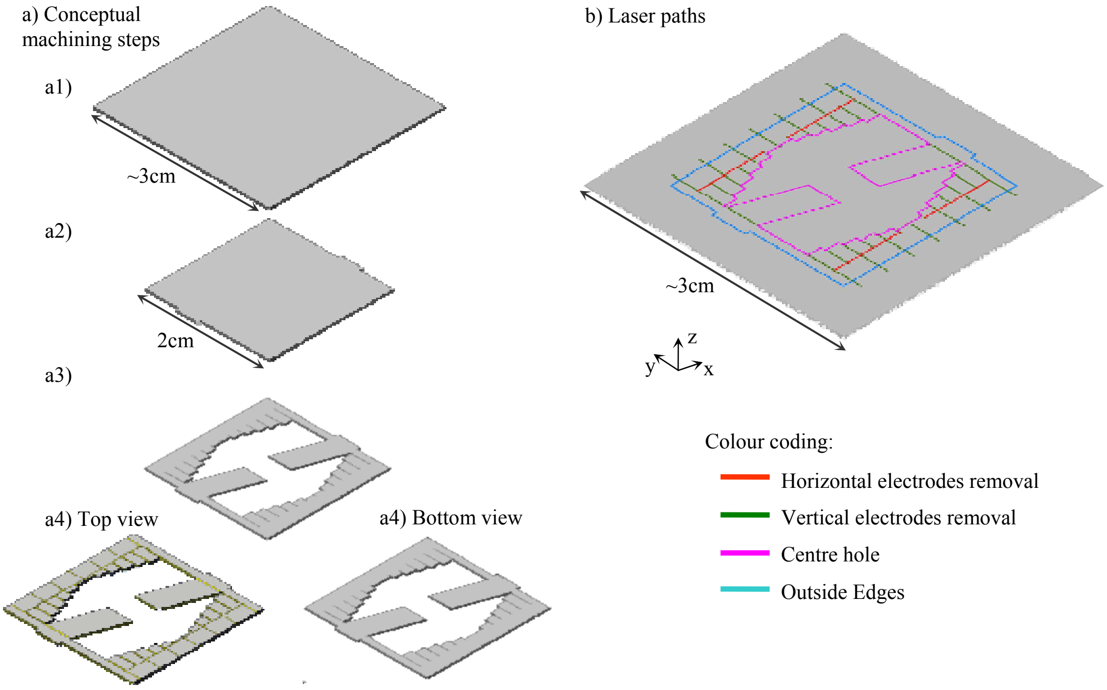

Figure 7.22: a) Required machining steps of an initially oversized PZT sheet with platinum electrodes to obtain the actuator layer for the spider MOA: Cutting out of the outside edges, Cutting of the centre hole and, if required the trenches to define the level B; and machining of the top platinum layer to define the segmented electrodes whilst maintaining an continuous ground electrode on the bottom layer of platinum. b) Laser paths to implement the conceptual machining steps for the 24 leg spider.

7.9 Actuator assembly and packaging considerations

A spider MOA device design was proposed which could be manufactured and integrated by following the steps:

i) Manufacture a 3cm×3cm×75µm PZT piezoelectric actuator with co-sintered platinum electrodes using Viscous Plastic Processing (VPP); and manufacture using a wet etching method of the of the spider MOA in silicon.

ii) Remove selected areas of platinum to define the segmented electrodes (using laser machining).

iii) Cut out the outer edges and the centre hole of the PZT actuator.

iv) Bond the PZT actuator and the spider MOA etched in silicon using the alignment jig shown in Figure 7.23.

v) Bonding the spider MOA onto the packaging structure (chassis and PCB) as described in Figure 7.24.

vi) Wire bonding to connect the segmented electrodes to the PCB.

7.9.1 Assembly and packaging of the spider MOA

Figure 7.24 shows an exploded view of the packaging design for the spider MOA which will provide a mounting method without restricting the lever action of the design. The packaging dimensions are such that the device would fit within the 35mm diameter constraint of the X-ray facility at Kings College London.

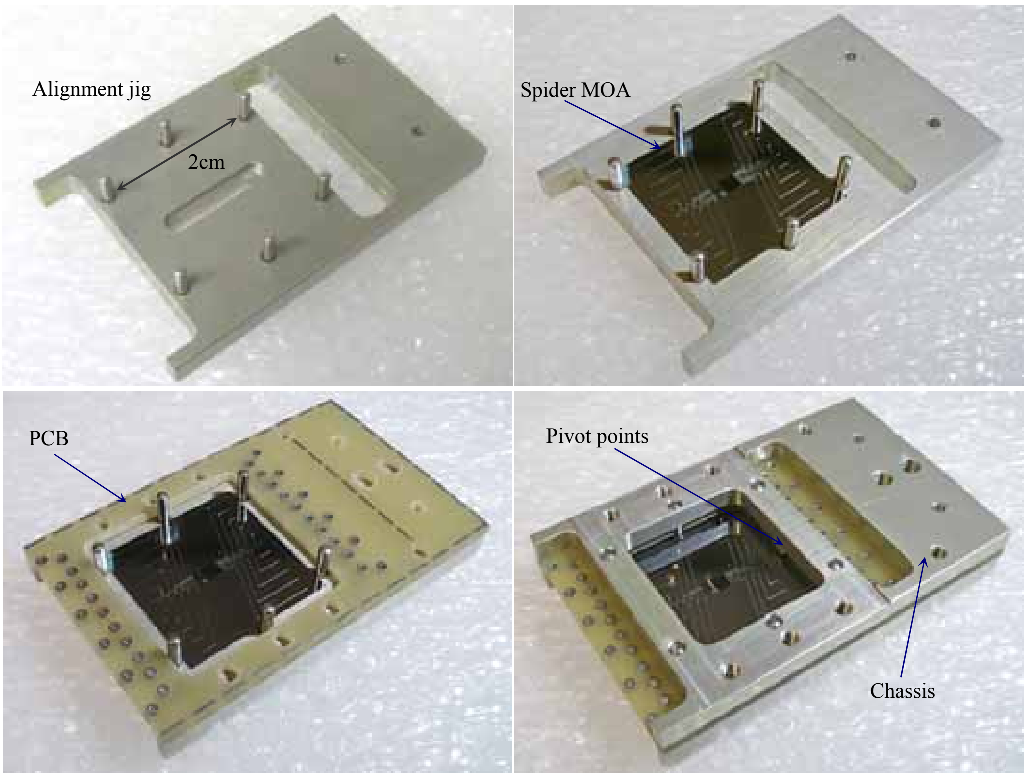

Figure 7.23: Pictures of the alignment jig which would be used to align and assemble the PZT segmented actuator, the 2cm×2cm silicon spider MOA the PCB and the mounting chassis. The packaging structure has been conceived and designed by Carl Meggs at the University of Birmingham and it was manufactured at MSSL.

The packaging consist of: a chassis with two raised points where the spider MOA would be mounted: a printed circuit board which will be glued to the chassis with the function of making the electrical connections to the segmented actuator of the spider MOA; and back and front covers for the device protection and filtering of the incident X-rays. During the packaging and device assembly an alignment jig is used to guarantee the relative alignment of the printed circuit board (PCB), the spider MOA and the chassis whilst the glue joining different parts set. An exploded view of how the final packaged device would look can be seen in Figure 7.24 below.

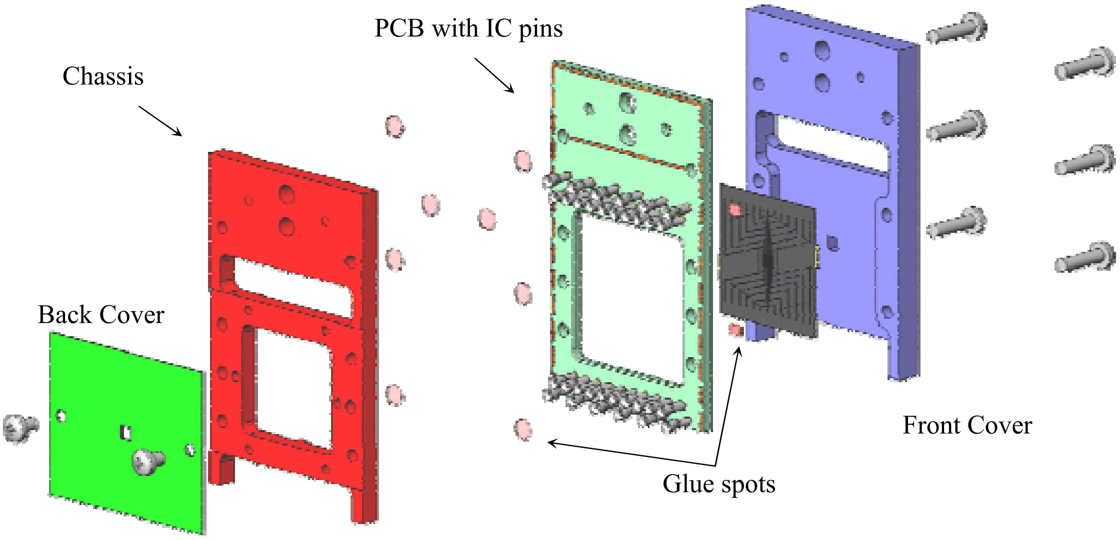

Figure 7.24: Exploded view of the packaging structure for the spider MOA

At the time of writing of this thesis the following tasks have been completed in order to manufacture and assemble prototypes of spider MOA with segmented electrodes:

i) More than 20 silicon chips, with all six design variations described in Table 7.1, have been manufactured using a wet-etching technique at the University of Edinburgh.

ii) More than 40 oversized PZT plates with a thickness T_{PZT}=80µm, have been manufactured using a VPP technique, poled, cleaned, their electric impedance checked, and delivered to MSSL where they await laser machining and assembly.

iii) 1 alignment jig, and 4 complete sets of consisting of chassis, PCB, and front and back covers have been manufactured at MSSL.

The remaining tasks to be carried out are: i) the laser machining of the PZT actuators; ii) the gluing of the actuator layer, silicon and the packaging structure; and the wire bonding of the electrical connections. These are planned for 2011 when time and resources (laser machining) availability allows.

7.10 Summary

The MOA concept is largely based on polycapillary(12) and microchannel plate(13) optics, in which X-rays are guided by multiple reflections along a large number of small channels and have potential applications for laboratory based X-ray sources where much higher focused flux are needed as current technologies (Fresnel zone plates) focus the X-rays by diffraction rather than reflection and suffer from very poor efficiencies.

The optical equations of different MOA configurations, such a flat/curved tandem pair, and X-ray tracing modelling carried out by other collaborators show that in order for the MOAs to be effective X-ray optics would need to have high aspect ratio (T_{Ch}/W_{Ch}>20), have a surface roughness better than 2nm in their vertical walls, and be able to be bent from flat to a 5cm ROC.

In order to achieve these goals it was necessary to gain an understanding of deep silicon etching manufacturing methods, piezoelectric manufacturing methods and the mechanics of piezoelectric actuation necessary to obtain small curvatures. FEA modelling and the results from test samples show that achieving the required ROC of the channels by means of piezoelectric actuation alone is not possible, indicating an alternative actuation arrangement was needed.

A spider array design is proposed as a possible actuation alternative in which piezoelectric and mechanical actuation are combined by etching trenches all the way through the silicon wafer, which in turn form levers to amplify the bending due to the piezoelectric effect alone. FEA analysis of the initial spider array design show that the required 5cm radius of curvature in the MOA chip can be obtained. This has been confirmed by measurements of the curvature in the centre region of test samples mounted on pre-curved clamps and using piezoelectric actuated samples.

To take advantage of the 1.2nm surface roughness of the vertical walls of the MOA channels achieved at Edinburgh University using a wet etch process, a new an novel spider arrangement has been designed which uses trenches parallel to the {111} planes in (110) silicon wafers. This means that the both the MOA arrays and the lever structure can be wet etched in the same manufacturing step and integrated in the same silicon wafer. Several spider MOA structures, with six different spider designs, have been successfully manufactured.

Preliminary results of a wet etched spider device actuated with two piezoelectric strips show that the MOA can be bent to a radius of 6.5cm without failure of the MOA channels. This is consistent with FEA models of the wet etched spider MOA design and with those of the initial spider MOA model showing that a two piezo-strip actuator configuration could bend the MOA structure to a ROC below 5cm if the thickness ratios of the PZT and the silicon are optimized.

An alternative actuator arrangement with segmented electrodes has also been modelled. The FEA results indicate that extra capabilities such as: more control over the curvature profile; +/-20μm z control; and +/-3mrad control over the tip/tilt angles could be obtained if precise micro machining of the actuator layer and assembly onto the MOA chip could be achieved.

The tasks carried out so far toward the manufacturing and assembly of complete spider MOA devices at the time of writing of this thesis include: the design drawings of an actuator with segmented electrodes have been produced; an integration procedure, including packaging and mounting procedures have been conceived; a set of spider MOA silicon chips with different design variant; the manufacturing of a set of flat piezoelectric plates of the required optimum thickness (T_{PZT}=75µm); finally, the packaging structure, and two sets manufactured.

The remaining tasks to be carried out in order to have full working prototypes are; the laser machining of the PZT actuators, the integration of the actuator layer, the spider MOA silicon chip and the packaging structure; and the wire bonding of the electrical connections. These are planned to be carried out in 2011 when time and resources (laser machining) availability allows. Once these issues are solved the intention is to carry out X-ray testing of the spider MOA devices at the X-ray testing facility being built at Kings College London to establish their capability as X-Ray optics, and show how the design of further prototype devices could be refined by optimizing design parameters or using a different substrate material.

7.11 References

1. Prewett P.D. and A.G. Michette, *MOXI: A novel microfabricated zoom lens for x-ray imaging.* Advances in X-Ray Optics, 2001. 4145: p. 180-187.
2. Michette A.G., Prewett P.D., Powell A.K., Pfauntsch S.J., Atkinson K.D. and Boonliang B., Novel microstructured adaptive X-ray optics. Journal De Physique IV, 2003. 104: p. 277-280.
3. Al Aioubi M.Y., Prewett P.D., Huq S.E., Djakov V. and Michette A.G. Design and fabrication of micro optical system for x-ray analysis of biological cells. Opto-Ireland 2005: Optoelectronics, Photonic Devices, and Optical Networks, 2005. 5825: p. 640-646.
4. Al Aioubi M.Y., Prewett P.D., Huq S.E., Djakov V. and Michette A.G. et al., *A novel MOEMS based adaptive optics for X-ray focusing.* Microelectronic Engineering, 2006. 83(4-9): p. 1321-1325.
5. *http://smartxrayoptics.org/*. (Last accessed 11-03-2011)
6. *http://www.rcuk.ac.uk/basictech/default.htm*. (Last accessed 11-03-2011)
7. Zhang D., Rodriguez-Sanmartin D., Button T.W., Atkins C., Doel P., Dunare C., Feldman C., James A., Michette A., Parkes W., Pfauntsch S., Sahraei S., Stevenson T., Wang H., Willingale R, Development of Piezoelectric Actuators for Active X-ray Optics. Journal of Electroceramics, 2009. Online Version: DOI 10.1007/s10832-009-9566-y.

8. Michette A.G., Pfauntsch S.J., Sahraei S., Shand M., Morrison G.R., Hart D., Vojnovic B., Stevenson T., Parkes W., Dunare C., Willingale R., Feldman C.H., Button T.W., Zhang D., Rodriguez-Sanmartin D., Wang H. and Smith A.D. Active microstructured x-ray optical arrays. EUV and X-Ray Optics: Synergy between Laboratory and Space, 2009. 7360(1): p. 736007.

9. Dunare C., Parkes W., Stevenson T., Michette A., Pfauntsch S., Sahraei S., Shand M., Zhang D., Rodriguez-Sanmartin D., Button T., Feldman C., Willingale R., Doel P., Wang H, James A, Microstructured optical arrays for smart x-ray optics. EUV and X-Ray Optics: Synergy between Laboratory and Space, 2009. 7360(1): p. 736015.

10. Michette A., Button T, Dunare C., Feldman C., Folkard M., Hart D., McFaul C., Morrison G.R., Parkes W., Pfauntsch S., Powell A.K., Rodriguez-Sanmartin D., Sahraei S., Stevenson T., Vojnovic B., Willingale R. and Zhang D. Active microstructured arrays for x-ray optics. in Advances in X-Ray/EUV Optics and Components II. 2007: SPIE.

11. Rodriguez-Sanmartin D., Zhang D., Button T., Atkins C., Doel P., Wang H., Brooks D., Feldman C., Willingale R., Michette A., Pfauntsch S., Sahraei S., Shand M., James A., Dunare C., Stevenson T., Parkes W. and Smith A. Progress on the development of active micro-structured optical arrays for x-ray optics. in Advances in X-Ray/EUV Optics and Components IV. 2009: SPIE.

12. MacDonald, C.A. and W.M. Gibson, *Applications and advances in polycapillary optics.* X-Ray Spectrometry, 2003. 32(3): p. 258-268.

13. Price G.J., Brunton A.N., Fraser G.W., Bavdaz M., Beijersbergen M.W., Boutot J.P., Fairbend R., Flyckt S.O., Peacock A. and Tomaselli E. Hard X-ray imaging with microchannel plate optics. Nuclear Instruments & Methods in Physics Research Section a-Accelerators Spectrometers Detectors and Associated Equipment, 2002. 490(1-2): p. 290-298.

14. Willingale R., Feldman C., Michette A., Button T., Dunare C., Folkard M., Hart D., McFaul C., Morrison G. R., Parkes W., Pfauntsch S., Powell A.K., Rodriguez-Sanmartin D., Sahraei S., Stevenson T., Vojnovic B. and Zang D., Active micro-structured optical arrays of grazing incidence reflectors. X-ray Optics and Instrumentation, 2009. doi:10.1155/2010/856836.

15. Feldman, C., *Smart X-ray optics for large and small scale applications*, in *Space Research Centre, Department of Physics and Astronomy*. 2009, University of Leicester: Leicester. p. 178.

16. Gebhardt S., Seffner L., Schlenkrich F. and Schonecker A. PZT thick films for sensor and actuator applications. Journal of the European Ceramic Society, 2007. 27(13-15): p. 4177-4180.

17. http://www.smart-material.com/Smart-choice.php?from=MFC. (Last accessed 11-03-2011)

18. Dunare, C., Parkes W., Stevenson T., Michette A., Pfauntsch S., Shand M., Button T. and Rodriguez-Sanmartin, D. MicroMachinning Optical Arrays (Accepted). in International Conference of Semiconductors. 2010. Sinaia, Romania.

CHAPTER 8

PIEZOELECTRIC ACTUATORS FOR LARGE X-RAY OPTICS

8.1 Introduction

The design of X-ray telescopes systems needs to reach a compromise between resolution and sensitivity as described in Section 3.3. A new area of interest in adaptive optics is the development of actively controlled thin X-ray mirrors, where aberrations would be corrected. The assembly of such optics on an X-ray telescope would provide an instrument with both high resolution and sensitivity.

The Smart X-Ray Optics (SXO) project has been developing prototypes for the next generation of X-ray telescopes. The overall aim is to produce X-ray mirrors using thin, below 1mm, structures. The X-ray optic would consist of a nickel substrate, with variable radius of curvature (ROC) along its length, and piezoelectric unimorph actuators bonded on its back. The piezoelectric actuators would be used to improve the resolution of the X-ray optic, having ~0.1 arcs as a target. Such an optic would enable the design of an X-ray telescope with both a greater resolution and collective area than the best currently available by Chandra (0.5 arcs) and XMM Newton (1650cm^2) respectively(1, 2).

Lead Zirconate Titanate (PZT) membranes with controlled surface finish, thickness and curvature have been developed for the SXO project using a viscous plastic process (VPP) technique(3). VPP generally provides improved material properties compared to conventional dry powder pressing and slip casting due to its capability of breaking down the agglomerates in a high solids loading paste system. Good plasticity in the green state facilitates complex shaping processes and the control of membrane thicknesses, i.e. 50-200µm in this study. The sintered density and piezoelectric properties are similar to the bulk values, but the process offers the flexibility of curving the membrane to the required radius of curvature.

This chapter presents the design and manufacture of the Large Adaptive X-ray Optic (LAXRO), a first prototype manufactured and tested in 2008, and how the lessons learned during its manufacturing, assembly, characterisation and finite element analysis were used for the subsequent design, manufacturing and assembly of the second generation of large X-ray optics prototypes, the new elliptical optics (NEMO1 and NEMO2), in 2010.

8.2 The first Large Adaptive X-ray Optic prototype (LAXRO)

8.2.1 The design of LAXRO

In a Wolter I X-ray optic configuration(4), such as that used in the Chandra and XMM-Newton X-ray observatories, X-rays are focused after a double reflection on paraboloid and hyperboloid surfaces as described in Section 3.3.

To demonstrate the principle that X-ray optics could be active, therefore increasing their resolution, an elliptical optic 30cm x 10cm, with a variable radius of curvature from 165.3mm to 169.8mm along its length was designed at the University of Leicester (UoL)(5). The length and width of the optic were chosen so they would be large enough to constitute a realistic test for the size of optic that would be required in an X-ray telescope. The variable radius of curvature along the length was chosen so X-rays could be focused within the University of Leicester X-ray testing facility. Detailed information about the optic design and its verification using X-ray tracing modelling is described in detail by C. Feldman in her PhD thesis(6). A summary of the specifications of the X-ray optic are presented in Figure 8.1 below.

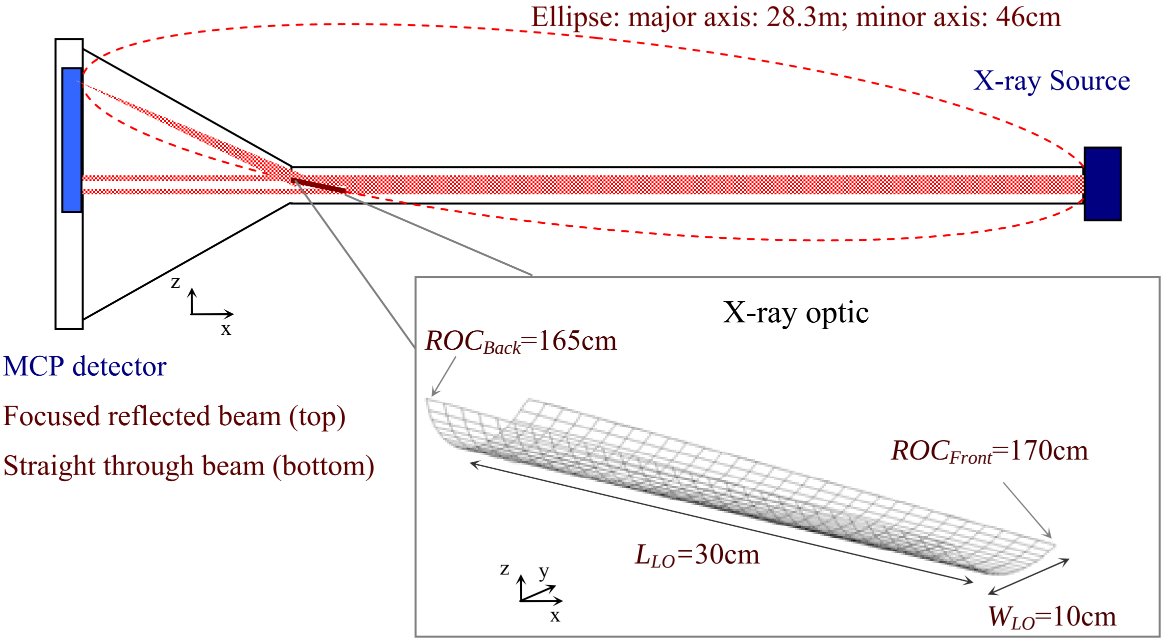

Figure 8.1: Schematic representation of the LAXRO design and its key dimensions. LAXRO was designed to achieve point to point focusing, using the focusing properties of ellipse geometry, inside the University of Leicester X-ray testing facility.

8.2.2 Actuator and substrate thickness optimization

The thickness of the optic was chosen to try to maximise the actuation provided by the piezoelectric actuators. The ideal thickness ratio T_{PZT}/T_{Ni} was calculated by setting up a finite element analysis (FEA) model of a cantilever beam, using the COMSOL multi-physics software package, and measuring the displacement of the cantilever as a function of the T_{PZT}/T_{Ni} ratio for different thicknesses of Nickel as shown in Figure

8.2. This exercise is identical to the one presented in Section 7.4, and the material properties used were those corresponding to PZT-5H for the piezoelectric material and nickel to the substrate as indicated in Table 6.1. The results were also similar, indicating that a ratio of T_{PZT}/T_{Ni}~0.8 would maximise the actuation.

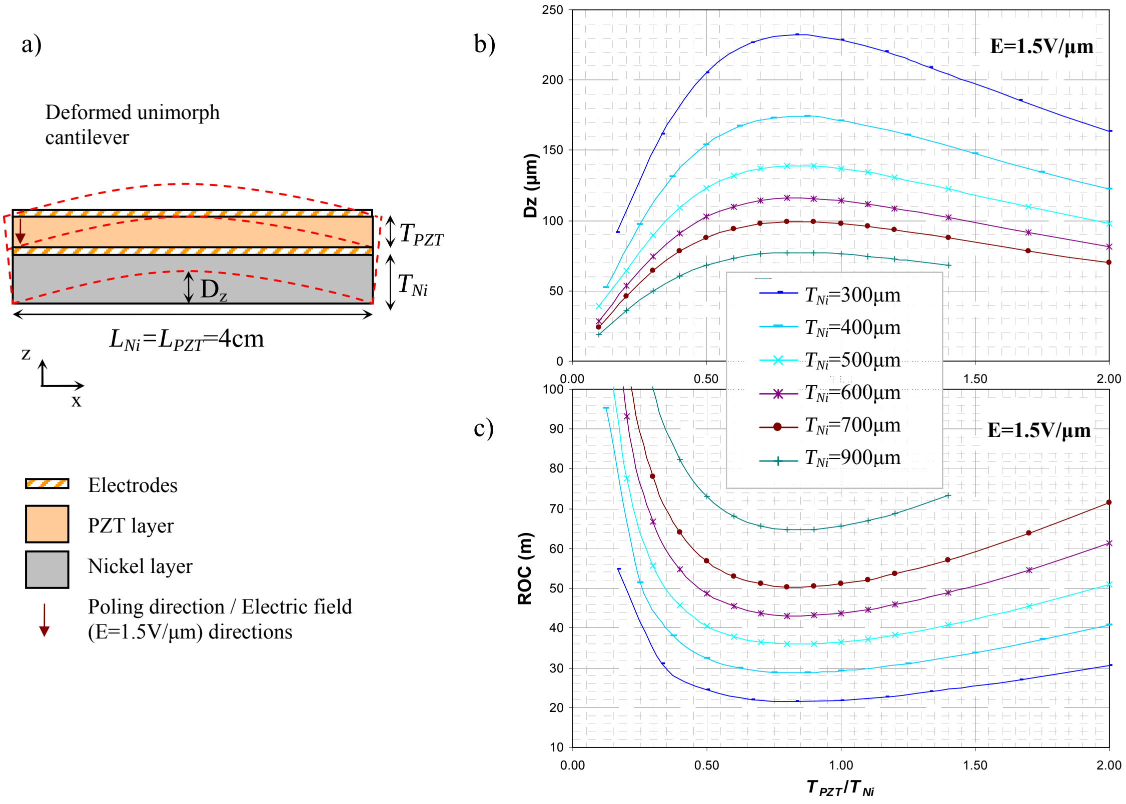

Figure 8.2: 2D FEA modelling an unimorph actuator using nickel as the substrate material. a) Actuator geometry definition. b) z displacement (D_z), and c) Radius of curvature (ROC) at constant electric field on the actuator layer for different nickel thicknesses as function of the PZT/nickel thicknesses ratios (T_{PZT}/T_{Ni}).

8.2.3 FEA analysis of the bonding layer

A similar approach was carried out to study the effect of the bonding layer between the piezoelectric actuators and the nickel substrate. A unimorph actuator model was set up as shown in Figure 8.3a, where the thickness of the nickel substrate, the PZT layer and the applied electric field were fixed to T_{Ni}=500µm, T_{PZT}=250µm and E=1.5V/µm. The ROC of the unimorph actuator was then calculated as a function of the young modulus (Y_m) of the bonding layer, assuming a Poisson's ratio ν=0.3, for different bonding layer thicknesses as shown in Figure 8.3b where the area highlighted by shadowed rectangle represented typical Y_m values of polymer bonding materials. The results show that the ROC of the unimorph actuator decreases linearly with the thickness of the bonding layer as the PZT layer needs to bend both the nickel substrate and the bonding layer.

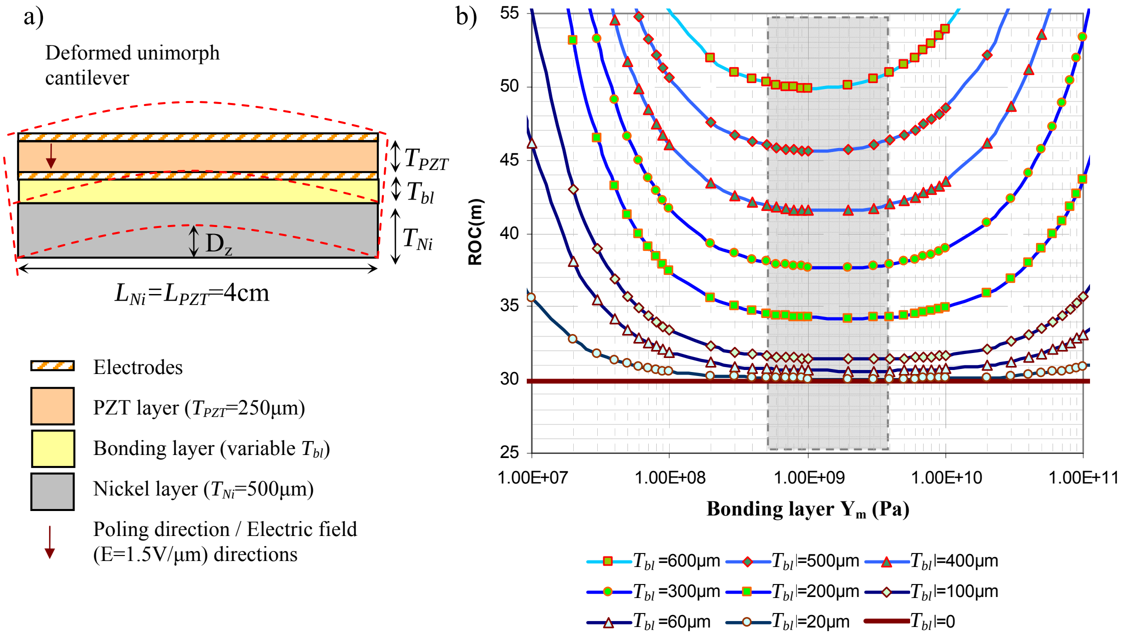

Figure 8.3: FEA analysis showing the influence of the bonding layer material and thickness (T_{bl}) on unimorph cantilever. a) Model definition b) ROC of the unimorph actuator vs. the Young modulus (Y_m) of the bonding layer assuming a Poisons ratio ν=0.3 for different bonding layer thicknesses and constant T_{PZT}, T_{Ni} and E. The Grey rectangle represents typical Y_m values of bonding materials.

8.2.4 Manufacture of the nickel shell

The manufacturing of the X-ray optics was carried out using an electroforming method developed at University College London (UCL). The electroforming process, developed by Carolyn Atkins[*] and explained in detail in her PhD thesis(7), consisted of the following general steps:

1. Super-polishing a stainless steel mandrel until it matched the curvature profile of the optic, and a surface roughness below 2nm.
2. Sputtering a layer of gold, typically 100nm thick, on top of the mandrel. This layer would create the reflecting surface of the optic.
3. Immersion of the optic in the electrolytic bath to carry out the electroforming of the nickel. The thickness of the nickel was controlled by the duration of the electroforming.
4. Release of the optic from the mandrel, this was achieved by immersing the optic in a cold bath

Several nickel shells were produced at UCL using this method and metrology was carried out on them to determine which ones conformed best to the required curvature profile. Figure 8.4a shows a picture of a mandrel after being gold sputtered, with the four areas around it so called “waster” having the function of guaranteeing uniform electro deposition of the optic without edge effects. Figure 8.4b shows one of the electroformed X-ray optics after being released from its mandrel.

---

[*] Other work carried out at UCL, which will not be repeated here, included: metrology of the manufactured nickel shells, so the ones conforming closer to the shell design would be used for the prototypes and FEA modelling of gravitational sag effects, mounting schemes and calculation of the influence functions of individual piezoelectric actuators.

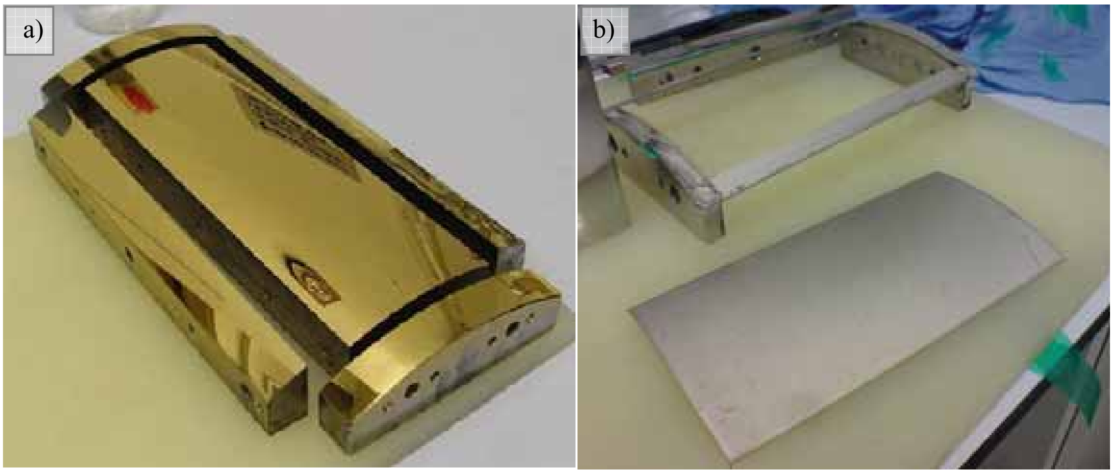

Figure 8.4: a) Stainless steel mandrel and wasters after they have been sputtered with gold. b) X-ray optic prototype released after the electroforming process.

8.2.5 Fabrication of the piezoelectric actuators

For LAXRO a configuration with 30 unimorph piezoelectric actuators each with dimensions 32mm×32mm×200μm was considered that would cover the whole length of the optic in a 3×10 configuration. The piezoelectric actuators were manufactured by Dou Zhang at the University of Birmingham using a viscous plastic processing (VVP) technique as described in Section 6.3.1.

Other commercially available piezoelectric actuators, such as active fibre composites, were also considered as possible ways of providing the actuation, but were rejected at the time as: i) they would have been difficult to customize to the large optic application, with the radius of curvature (ROC) and large dimensions being the parameters most difficult to match using commercially available actuators; ii) The FEA analysis in Sections 4.5.3 and 7.4 show that their actuation would be non uniform, with areas of low actuation under the inter-digitized electrodes when bonded to substrate.

The actuators needed to match the curvature profile of the optic (165-169cm radius), and therefore a technique to curve the piezoelectric actuators needed to be developed.

Two options were considered for the actuators of LAXRO both of which utilized zirconia formers machined to the required radius of curvature and then used to produce sintered zirconia plates with matching ROC. The components were then assembled inside a crucible as shown in Figure 8.5.

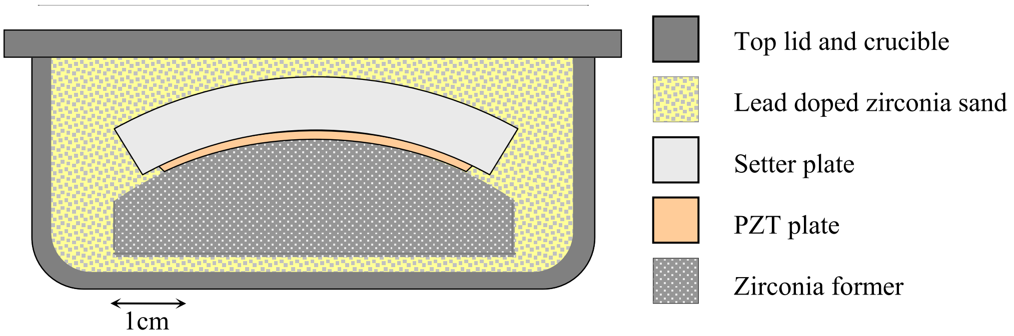

Figure 8.5: Schematic representation of the set-up for the sintering (green PZT plates) or slumping (sintered PZT plates) for the manufacture of curved PZT plates.

Both options differed as follow:

- The first one consisted of slumping sintered flat actuators onto the zirconia former with the right radius and then subject them to a heat treatment process so they could retain their curved shape (up to the sintering temperature ~1200°C).
- The second option consisted on co-sintering the green VPP samples sandwiched between a zirconia former and a zirconia setter plate, having the required ROC.

Both alternatives were investigated but the second option was found to be more reliable, as fewer breakages occurred during the process and it was therefore adopted for the manufacture of the piezoelectric actuators for LAXRO.

After sintering, gold electrodes were applied to both faces of the actuators using a sputter coater, (Emitech K575X, Quorum Technologies, UK). During this process low adhesion "Magic tape" was used to mask the edges of the actuators, so their edges would not be coated, which may have caused electrical shorting. Access needed to be gained to the ground (concave side) and electrode from the top face (convex side) of the actuators as the concave face would be glued to the optic. 2mm×2mm electrode pads were defined on the convex face of the actuator by removing a fine line of the sputtered electrode using sand paper. The electrode square pads were then bridged to the electrode on the concave face by painting around the edge of the actuator with conductive silver loaded epoxy (RS components, UK). Continuity of the pad at the top surface with the bottom electrode and isolation of the top and bottom electrodes were checked at this stage. The samples were then poled in an oil bath as described in Section 6.3.1.4. A schematic representation of the unimorph actuator and its basics dimensions and pictures of manufacture PZT actuators are shown on the Figure 8.6 below.

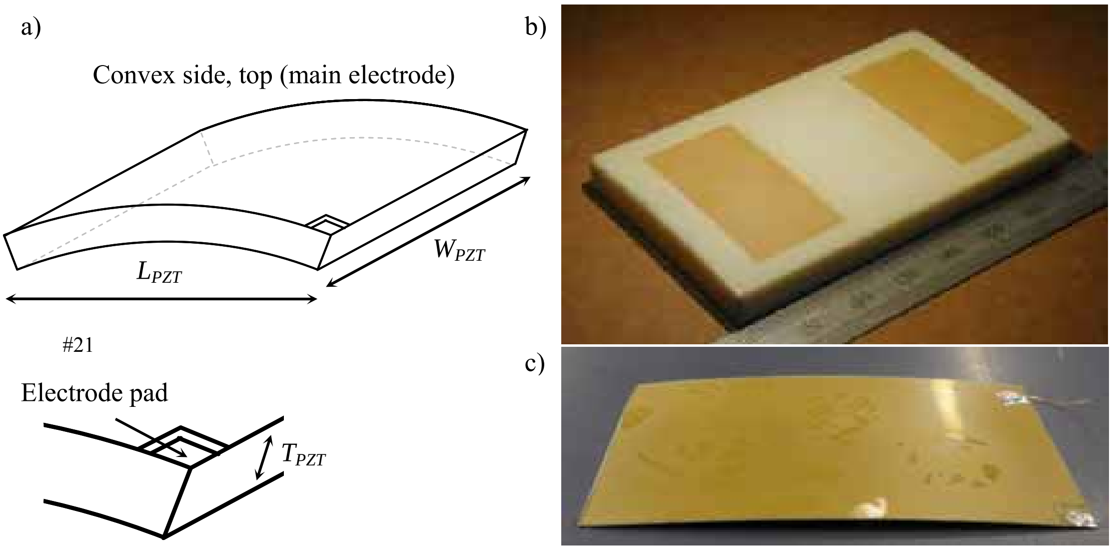

Figure 8.6: a) Schematic representation of the unimorph actuator and its basic dimensions. The main electrode is on the convex side and the ground electrode on the concave side (accessible from the top surface using the electrode pad). b) Zirconia former, 169cm ROC, with sintered PZT samples on top. c) PZT sample with dimensions: L_{PZT}=33mm, W_{PZT}=17mm, T_{PZT}=150µm and ~169cm ROC (right).

8.2.6 Actuators and X-ray optic integration

The integration process carried out at UCL, consisted of the following steps:

- Low shrinkage EP30 glue (Masterbond Inc., Hackensack, US) and a 5% concentration by weight of 80µm diameter glass beads, which would define the minimum thickness of the glue layer, were mixed and degassed in a vacuum chamber.
- The degassed glue was then applied to a small area on the back of the optic using a paint brush.
- A row of 3 piezoelectric devices were placed on top of the optic.
- Excess glue was cleaned using paper tissues and solvents.

Once the glue was sufficiently cured, the process was repeated several times with successive rows of piezoelectric actuators until the all 30 were bonded to the back of the optic.

Test samples were prepared in an identical way to the procedure shown above with the objective of obtaining a cross-section of the bonding layer of the device such as the one shown by the SEM micrograph in Figure 8.7 of a cross-section of a test device. In the image, glass beads can be seen embedded in the bonding layer and that delaminating occurred between the bonding layer and the PZT layer during the sample preparation. The thickness of the glue layer was not well defined across the length of the samples varying from a minimum of 100µm, as set by the glass beads, to several hundred microns thick.

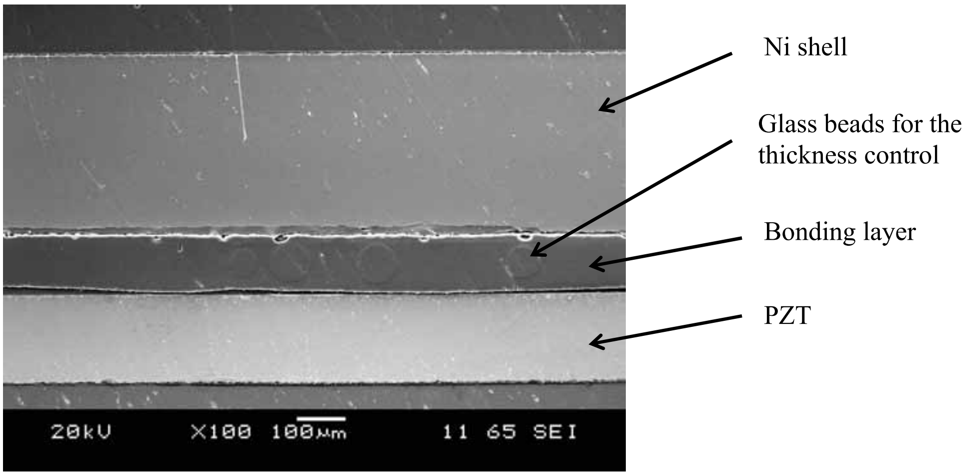

Figure 8.7: SEM micrograph of a cross-section of a test device. Glass beads of 80µm diameter can be seen embedded in the bonding layer. Some delamination occurred between the bonding layer and the PZT layer during the sample preparation. SEM pictures taken by Dou Zhang at the University of Birmingham.

8.2.7 Harnessing support and mounting structure

A supporting frame, which would hold the optic in place on top of one of the vacuum flanges at the X-ray testing facility at the UoL, was designed and manufactured in collaboration between the UoL and the Mullard Space Science Laboratory (MSSL). The support structure was also designed so pitch and yaw motors could be used to orientate the optic inside the vacuum chamber.

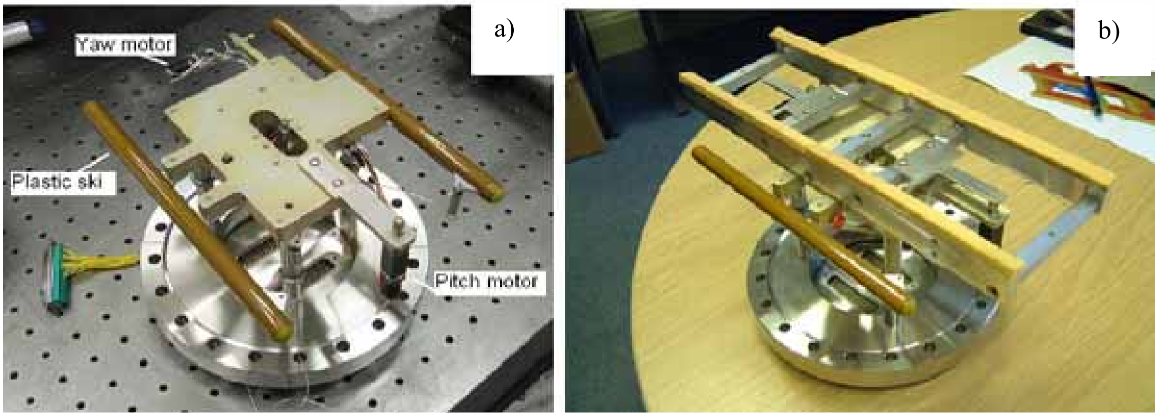

Figure 8.8: Support structure developed by the SXO team for the support of the large optic on one of the flanges of the University of Leicester X-ray facility. It includes pitch and yaw motors for the positioning of the optic.

The LAXRO was harnessed and mounted onto the supporting frame at MSSL. At the time it was decided to use a “soft clamp” option in which the optic was bonded to two 2mm wide strips of very compliant and vacuum proved space foam at the edges of the optic. In this way the action of the piezoelectric actuators could be de-coupled from any effects introduced by the mounting of the optic. The harnessing of the wires to the actuators was done by using indium soldering. Figure 8.1 shows various stages of the assembly and harnessing process.

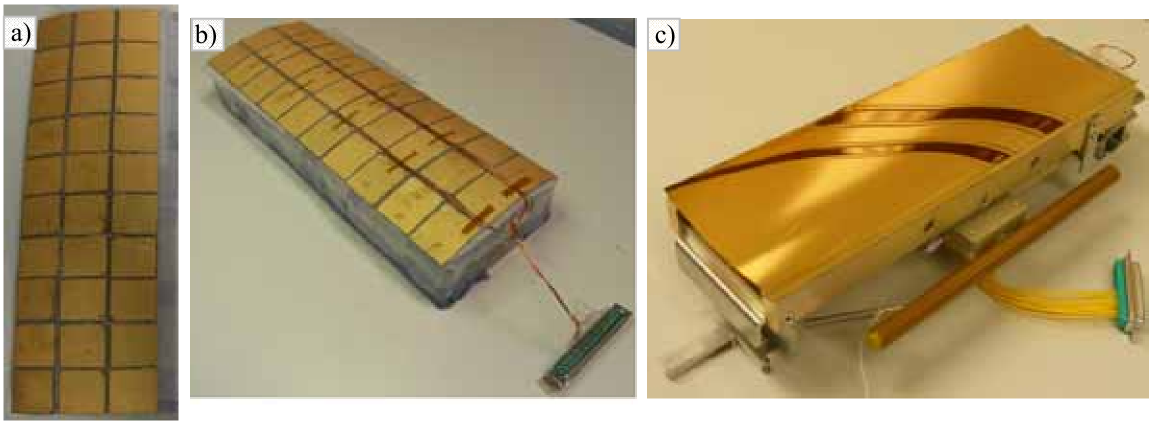

Figure 8.9: The LAXRO prototype. a) After bonding of the piezoelectric actuators. b) After harnessing. c) After bonding to the support structure.

8.2.8 Actuator control

As previously explained in detail in Section 4.2.6, the use of large electric fields to control the piezoelectric actuators may introduce in return hysteresis effects in their behaviour, and if not addressed would have the effect of compromising the repeatability of the actuators as their behaviour would depend, not only on the current applied field but also on previous ones.

A voltage amplifier (model E1463A, Agilent Technologies UK Limited, Wokingham, UK) with 32 output channels, each with +/-100Volts, was used to control the piezoelectric actuators. The amplifier was computer controlled using LabView software. From a device perspective, the hysteresis introduced by the piezoelectric actuators was an effect that needed to be minimized, and thus in order to obtain repeatability in the measurements it was not suitable to just linearly control the actuators. Instead two strategies were conceived to achieve repeatability and overcome some of the hysteresis effects:

i) Control method 1: To approach the target voltage using a cycling voltage and decaying voltage, to cancel out the hysteresis in the system. This approach has been used in the literature(8) to control other piezoelectric systems and was adapted to control the piezoelectric actuators.

ii) Control method 2: To use a maximum operating voltage as a reference (V_{ref}). To change the voltage in actuator from a value V_i to V_f , the actuator was linearly taken from V_i to V_{ref} and from V_{ref} to V_f. In this way all the voltages were approached always by the same top branch of the hysteresis curve, starting at V_{ref} and repeatability could be ensured.

Both approaches were tested using nickel shell samples with actuators bonded to their back surface as shown in Figure 8.12a. The sample was unconstrained and was simply kept in place by placing it of top of two fixed metal bar covered with foam as shown in Figure 8.12b. The z displacement (D_z) was then measured as a function of the applied voltage using the experimental sep-up described Section 6.4.4 and the LabView code and interface for the control software as shown in Appendix III.

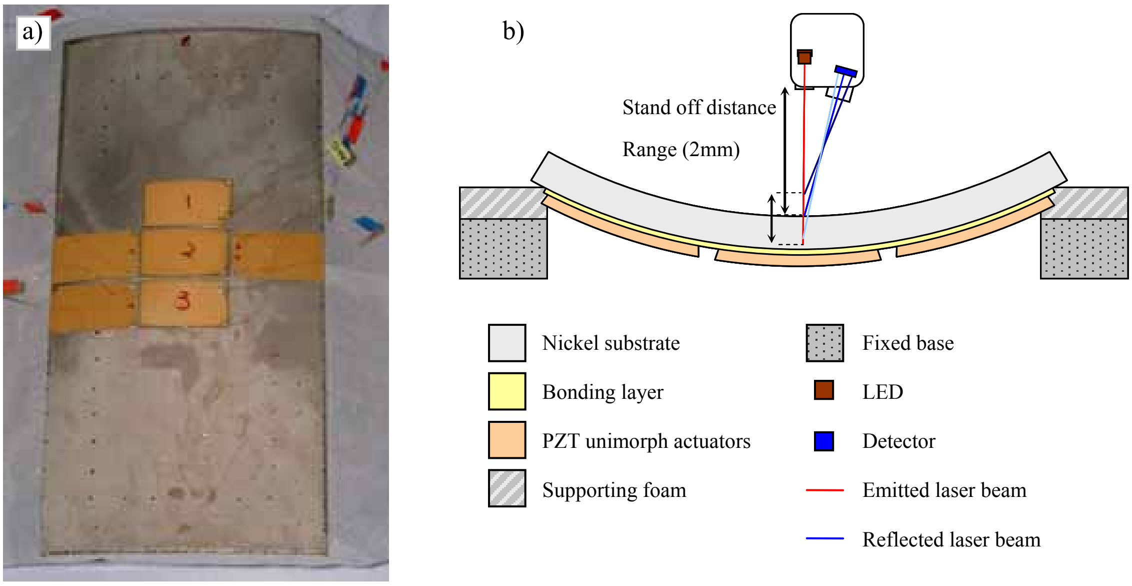

Figure 8.10: a) An electroformed nickel shell, manufactured at UCL, populated with six piezoelectric actuators. b) Schematic representation of the setup to measure the applied voltage vs. z-displacement curves at a point on the reflective side of the optic corresponding with the centre of the actuator.

To calibrate the experimental set-up, all the actuators were taken to 200V and then back to 0V. The z displacement was then measured over time with constant 0V on the actuators. The results are shown in Figure 8.11, where it can be seen that the drift rate ($\partial D_z/\partial t$) changes from 5µm/hour within the first hour to a constant 0.7µm/hour after a few hours.

This systematic drift was not completely understood, and could be due to a combination factors such as the way the sample was held in an unconstrained manner or residual tension due to the copper wires used to control the actuators.

Voltage and displacement curves were then measured as a function of time for both actuation methods. The results obtained when the sample was taken from V_i=100V to V_i=0V are plotted in Figure 8.12. For both set of measurements a large z displacement ΔD_z=60µm occurred, compared with the +/-1µm background noise of the raw data, which means that a change in the curvature profile of the optic would be inferred.

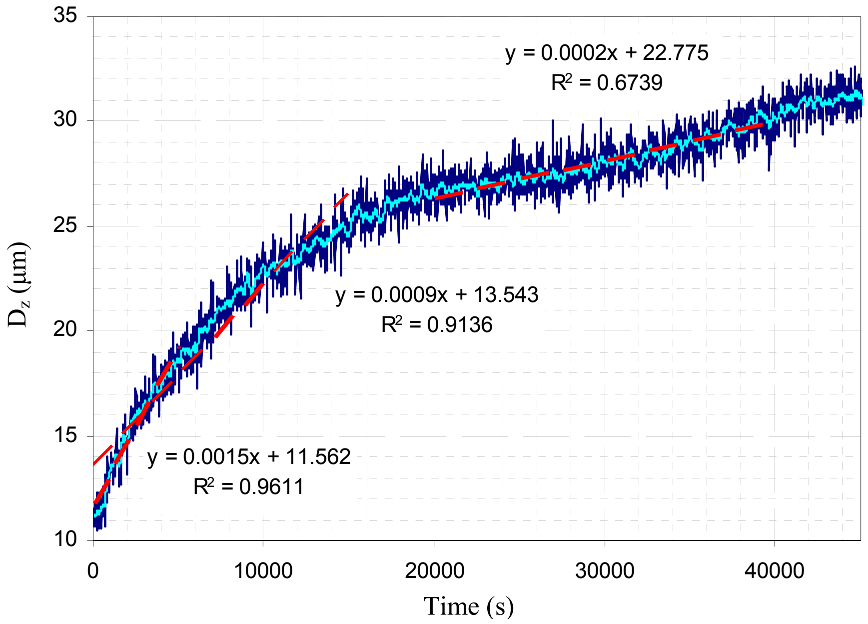

Figure 8.11: Drift of the measurement set-up over time when no voltages were used on the piezoelectric actuators. It varies from 5µm/hour at the beginning to 0.75µm/hour.

The data was further analysed by averaging the measurements over a period of time of one second, Avg D_z, in order to reduce the background noise. The results of both actuation methods are plotted together in the graph at the bottom Figure 8.12 and show that for the control method 1 the drift of the data was constant and of a magnitude of 6µm/hour and for control method 2 the drift was 10µm/hour (compared with the background drift of 5µm/hour).

Several actuation cycles were then carried out using different initial and final voltages for both control methods. The conclusion from the tests was that both actuation methods could achieve repeatability within the experimental error +/-1µm. However, these preliminary tests were based in measuring the displacement of a single point on a single actuator, and more research needed to be carried out to verify that this control mechanism was valid when all the actuators in the optic are active. Based on these initial experiments, the control programme was redesigned at UCL so the 30 actuators of the optic could be controlled simultaneously using both actuation methods.

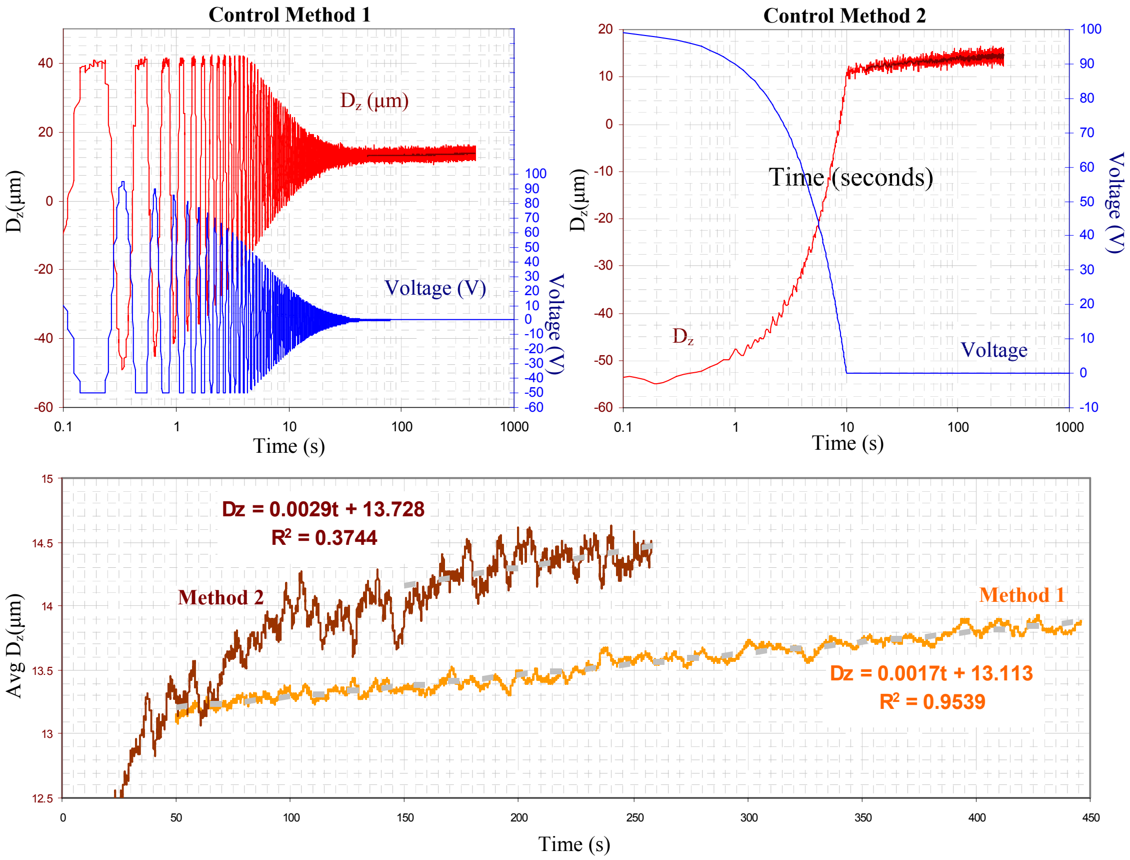

Figure 8.12: Stability test using a decaying cycling voltage to reduce the hysteresis. The tests were performed on an electroformed nickel shell manufactured at UCL. The displacement measurements show that the shell remains stable after the cycling voltage.

During the X-ray tests of the LAXRO prototype, and due to time constraints on the testing schedule, only control method 1 was used as these initial test indicated it may be marginally better than control method 2.

8.2.9 Characterisation of the LAXRO

X-ray test were carried out on LAXRO at the University of Leicester X-ray testing facility[†]. This facility is in very high demand and the SXO consortium only had

---

[†] These tests were carried out as a collaboration between the University of Leicester and University College London.

limited availability to it. It needed to be booked many months in advance to obtain a three week testing schedule and therefore the testing regimes were not always ideal.

In these X-ray tests several voltage patterns, such as rows, columns or individual devices, on the piezoelectric actuators were tried to investigate the effects of different actuators on the reflective surface of the optic.

However, two technical issues hindered these X-ray tests: Firstly, the motors for the control of the pitch and yaw angles of the optic became jammed, this in turn meant that the X-ray optic could not be placed in its optimum focused position with the pitch and yaw motors before the piezoelectric actuators were used. The second was a deficiency on the control software; the 30 actuators were cycled at the same time irrespectively of whether their voltages were changed or not, which defeated the objective of obtaining repeatability in the device.

In spite of the technical difficulties, which were not possible to be solved at the time due to the fixed an tight testing schedule, the X-ray tests were successful in demonstrating that LARXO was an active X-ray optic and that the piezoelectric actuators were capable of improving the focusing of the initial image as shown in Figure 8.13 below which shows the initial X ray image on the left of the figure and best X ray image obtained using the piezoelectric actuators on the right which had a smaller and brighter focal spot.

After the X-ray testing was completed further metrology of LAXRO was conducted at the Daresbury laboratory using a long trace profiler (LTP)[‡]. The LTP is designed to

---

[‡] These measurement were carried out by Charly Feldman (UoL) and Carolyn Atkins (UCL) with the assistance of Andy Smith (Daresbury Laboratory).

characterize flat surfaces so only traces along the length at the centre of LAXRO could be measured.

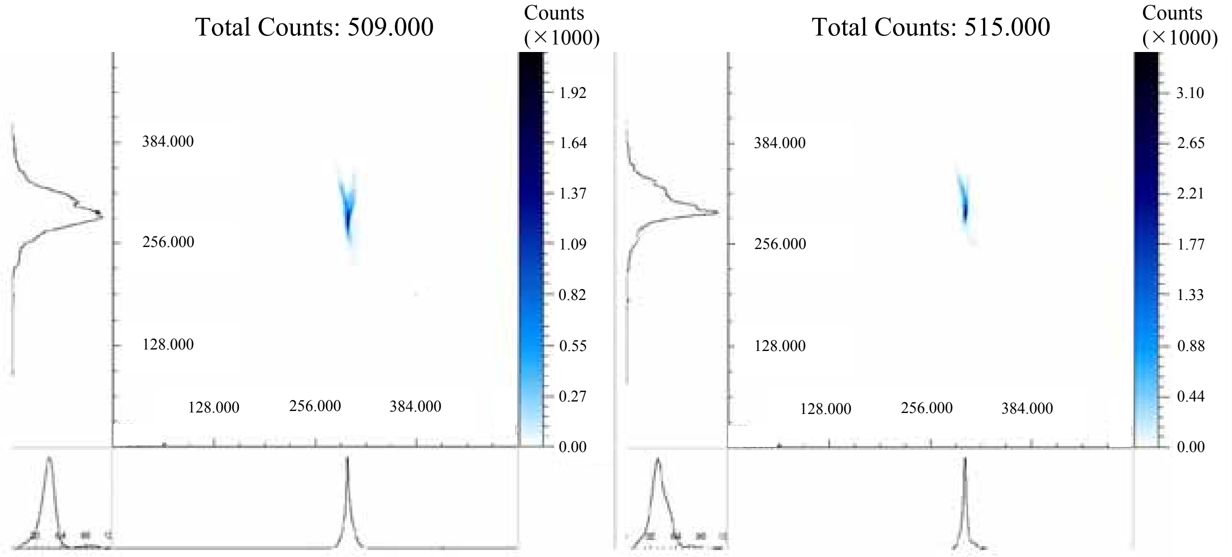

Figure 8.13: Initial X-ray image (left) and best X-ray image (right) obtained using the piezoelectric actuators, both images were obtained using similar number of counts. The image on the right has a smaller and brighter focal spot, notice the difference on the y axis scale in both images. Images courtesy of the University of Leicester.

The characterisation results revealed firstly that the actuators, as was intended, were able to significantly change the surface profile of LAXRO. And secondly, undesired distortions on the optic appeared between in the gaps between neighbouring piezoelectric devices when they were simultaneously actuated. The LTP results are summarised in the Figure 8.14 below. It should be noted here that during the assembly of the LAXRO described in Section 8.2.4 no particular spacing between the actuators was attempted, with typical gap being from 1mm to 2mm wide.

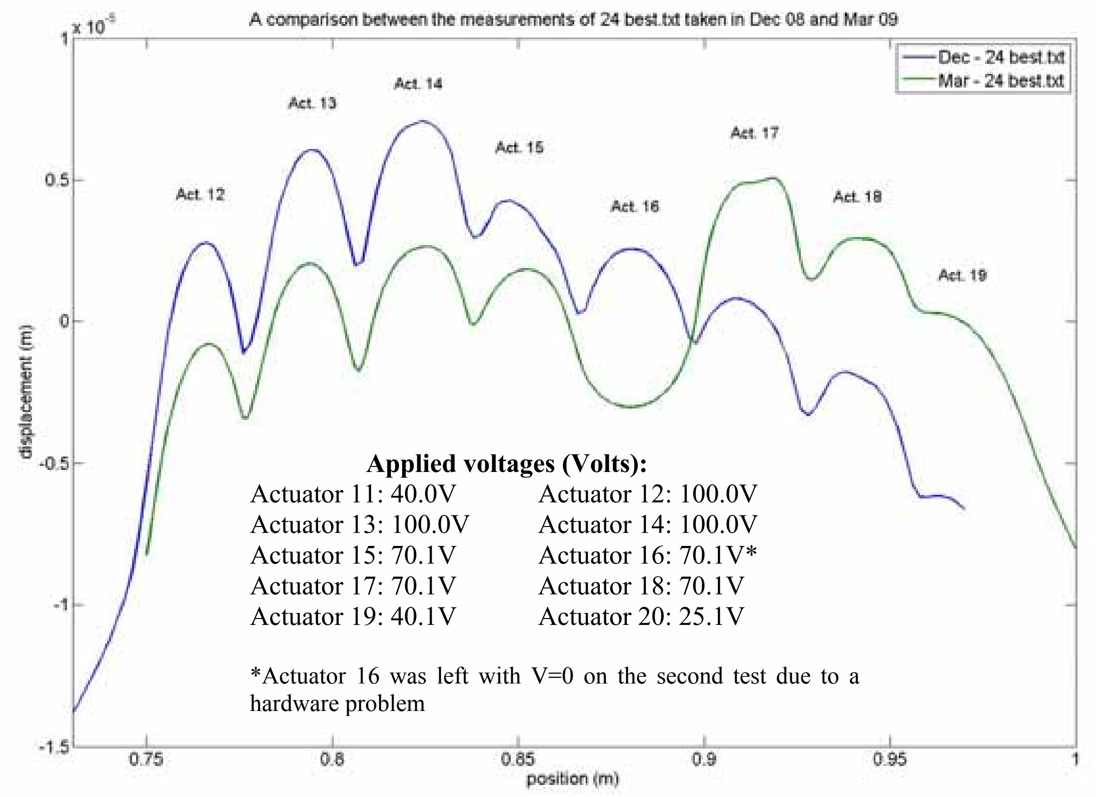

Applied voltages (Volts):

Actuator 11: 40.0V	Actuator 12: 100.0V
Actuator 13: 100.0V	Actuator 14: 100.0V
Actuator 15: 70.1V	Actuator 16: 70.1V*
Actuator 17: 70.1V	Actuator 18: 70.1V
Actuator 19: 40.1V	Actuator 20: 25.1V

*Actuator 16 was left with V=0 on the second test due to a hardware problem

Figure 8.14: Characterisation results obtained on LARXO using the long trace profilometer facility at the Daresbury laboratory taken at two different moments in time. Both measurements show that there is a kink on the reflective side of the optic in those places where there is a gap between piezoelectric devices.

8.2.10 FEA modelling of the gaps between piezoelectric actuators

The characterisation results from LAXRO show that the gap between adjacent piezoelectric devices created a corresponding kink effect on the optical surface. To further understand this problem, and how it could be solved, a finite element analysis (FEA) model was studied. The FEA model maintained the aspect ratios of the real problem, i.e.: T_{Ni}=400µm, T_{bl}=100µm and T_{PZT}=200µm, but its dimensions were a simplified version of the real problem, with just 9 actuators distributed in three rows and a much smaller radius of curvature in order to reduce the processing time required to solve the FEA model. Several versions of the model were made as shown in Figure 8.15.

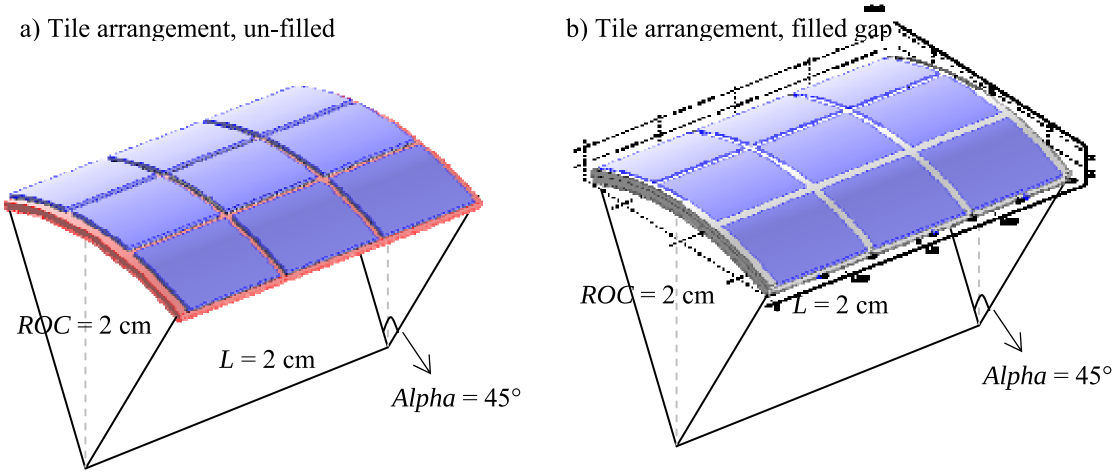

a) Tile arrangement, un-filled

b) Tile arrangement, filled gap

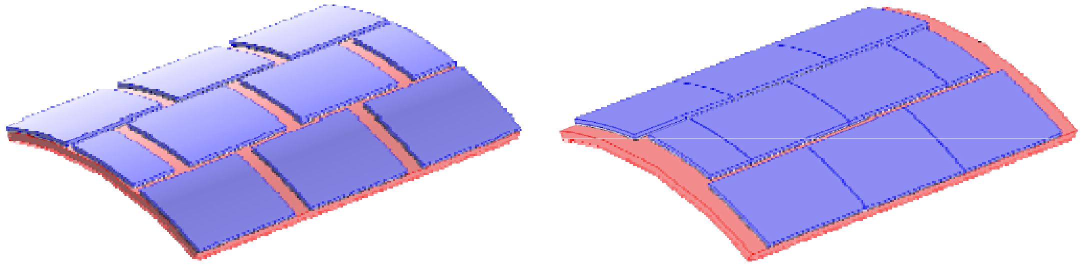

c) Brick wall arrangement (x-gap=1mm)

d) Brick wall arrangement (x-gap=100µm)

Nickel Shell: ROC=1.96cm, Alpha=45°; Length=2cm; T_{Ni}=400µm; Bonding layer: Polyimide; T_{bl}=100µm; Piezoelectric devices: PZT-5H, Alpha=14°; L_{PZT}=6mm; T_{PZT}=200µm; angular gap between piezoelectric actuators = 1.5°

Figure 8.15: FEA models used to investigate the kink effect as a function of the x-gap size in the actuator layer. a) Model with unfilled gaps b) Model with filled gaps with polyimide or PZT. c) Brick wall arrangement x-gap=1mm. d) Brick wall arrangement x-gap=100µm.

The influence of the size of the gaps in the optical surface of the FEA model were studied for both the tile and the brick wall arrangements for the following cases: when the gaps were not filled; when the gaps were filled with polyimide, which was chosen as a material with similar mechanical properties to those of the bonding layer; and when the gaps were filled with PZT, which equated to having a discontinuity on the top electrode. Each of these cases was redrawn, varying the size of the gap between adjacent electrodes from 1mm to 100µm, and modelled for the case when all the piezoelectric devices had an applied electric field E=0.5V/µm.

The kink effect was then quantified in terms of change in the derivative of the displacement, measuring the difference in the peak and valley values of the first derivative around the kink. The geometry of the model and a summary of its results are shown in Figure 8.15. They show that in the case of unfilled gaps the size of the kink decreases linearly with the size of the x-gap but does not tend to a zero value. In the case of filled gaps, with either polyimide or PZT, the results are almost coincident; the size of the kink also reduces linearly with the size of the x-gap but tends to zero. The results also showed that the brick wall arrangement was marginally better than the tile arrangement.

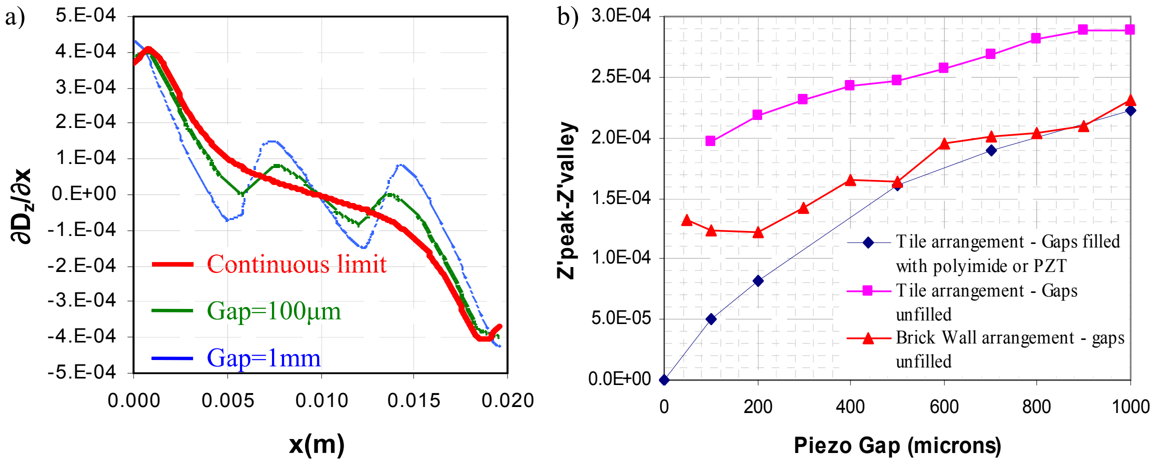

Figure 8.16: a) FEA model used to investigate the kink effect as a function of the gap size in the actuator layer. a) First derivative of the z displacement for the tile arrangement where the gaps are filled with polyimide for three different gap sizes: 1mm, 100µm and the continuous limit. b) Kink size, measured as the difference in the peak and valley values of the first derivative around the kink, as a function of the gap size for three different arrangement: Gaps filled, non filled, and gaps non filled but in a brick-walled pattern.

The effect on the kinks of varying the voltages between adjacent electrodes was also investigated. However, the modelling results indicated that the kinks could only be mitigated, but not eliminated.

The results from the FEA model lead to two conclusion that the kink effect could be significantly reduced if the gaps between the piezoelectric devices in the actuator layer were as small as possible and filled with some material to ensure the mechanical coupling between adjacent actuators and if a brick wall arrangement was used.

8.3 The new elliptical X-ray optic (NEMO)

8.3.1 Piezoelectric actuators design

The piezoelectric configuration of the second prototype was designed to minimise the kink effect on the reflective surface of the first X-ray optic prototype caused by the discontinuity of the piezoelectric layer bonded to the top surface. Finite element analysis (FEA) models carried out using COMSOL Multi-physics software indicated that kink effect has a dependence on the size of the gaps between piezoelectric devices and the filling material of those gaps. Therefore it was decided to minimise as much as possible those gaps, which in turn implied that precise control over the piezoelectric dimensions and electrode configuration was required.

Figure 8.17 shows drawings of the actuator elements with dimensions 75mm×32mm×0.2mm and 167mm ROC which matches the nickel X-ray optic. The top electrode (convex side) of each element is divided in two and the ground electrode (concave side) at the bottom of the piezoelectric element would be accessed using the 2mm×2mm square electrodes at each corner of the sample. The piezoelectric elements would not have electrodes along their 50μm edges to avoid shorting adjacent electrodes assembled in the optic. To cover the whole of the Nickel X-ray optic the elements would be staggered in a brick wall fashion, using 11 full and 2 half or 10 full and 4 half elements.

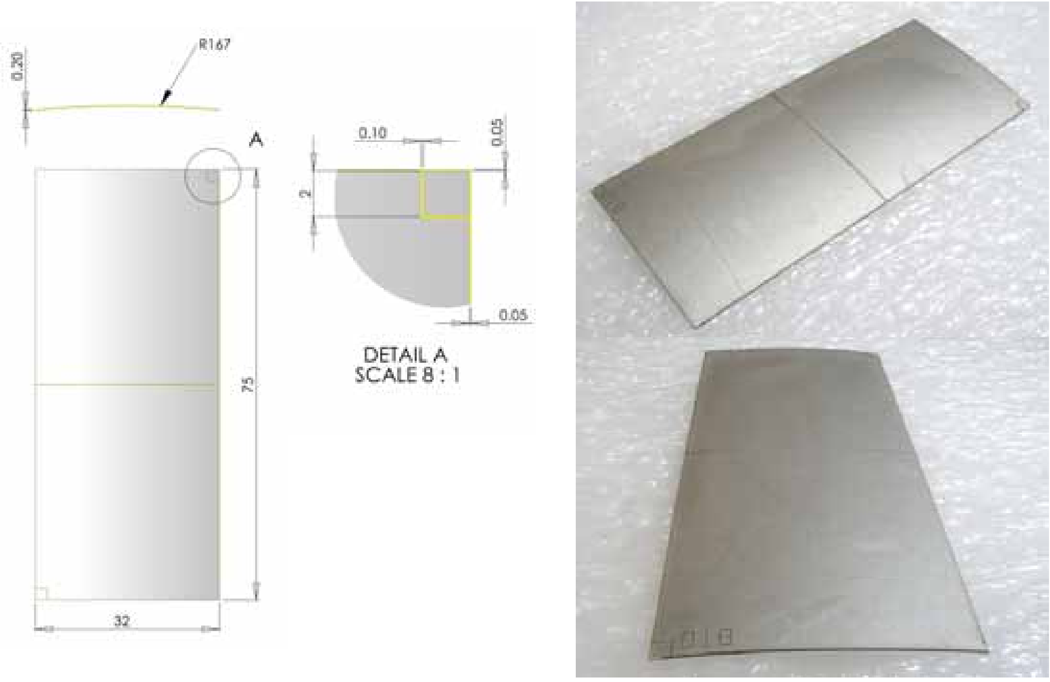

Figure 8.17: Drawings of the piezoelectric elements for the NEMO prototypes (with all dimensions in millimetres), and top and side views of the piezoelectric element with serial number 018.

8.3.2 Production of the piezoelectric actuators

8.3.2.1 Viscous plastic processing (VPP) manufacturing route for pre-curved plates

The piezoelectric plates for NEMO optics were manufactured using a Viscous plastic processing (VPP)$^{(3)}$ technique as described in Section 6.3.1. The VPP ceramic dough was shaped into membranes with controlled green thickness of 240µm using a calendering and laminating processes. The calendered tape was then: screen printed with platinum thick film ink (Gwent Electronic Materials) to form the top and bottom (ground) electrodes; cut to oversized green dimensions, typically 10cm×4cm, to allow for shrinkage during sintering; drying and pre-forming over moulds of the required ROC.

The sintering method used for manufacturing the samples of the first large X-ray optic prototype has been described by Zhang et al(9, 10) and summarised in Section 8.2.5. It consisted of using formers and setter plates to maintain the curvature of the samples during sintering. However, it was found that it was not successful on co-sintered samples as could not be scaled to produce larger dimensions required here. Trial samples caught on the former or the setter plate during sintering, and, as the sample was shrinking, defects such as edge cracks or blister were formed.

A new sintering method was developed by Carl Meggs at the UoB in which both the lead stoichiometry of the PZT sample and its shape were preserved without restricting the shrinkage of the samples. This was achieved using the following steps: i) Layers of zirconia and lead oxide sand of different grain sizes were laid in a zirconia boat; ii) An indentation using a pre-formed mould of 167mm ROC was made on the sand bed (the same mould that was used to pre-form the green samples during drying); iii) The pre-curved green sample was then placed on the indentation; the sample was covered with layers of fine and coarse sand as shown in schematic representation in Figure 8.18. This ensured a PbO-rich atmosphere and preservation of the sample curvature during sintering.

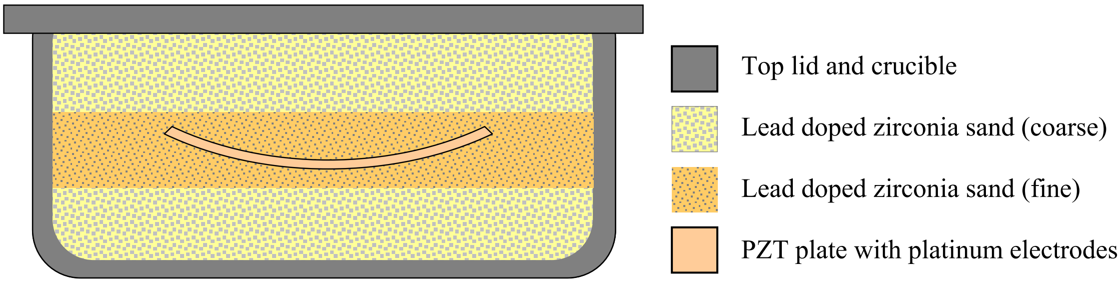

Figure 8.18: Sintered set-up of the piezoelectric plates for the NEMO X-ray optics. The green VPP plates with screen printed platinum electrodes were pre-curved to the required radius and placed on a pre-curved indentation on the fine zirconia sand inside the crucible. The sample was then covered with a layer of fine sand and a layer of course zirconia sand.

The sintered piezoelectric plates were then made active using a standard poling process in an oil bath. The poling conditions used were: an applied electric field of 2.5V/µm, at 110^{o}C for 10minutes. Pictures of a sample at different stages of the sintering process are shown in the Figure 8.19.

Figure 8.19: a) Pre-curved green sample laid on a pre-curved zircon sand with lead oxide. b) Sample after sintering. c) Sample after poling and cleaning.

8.3.2.2 Laser Machining

After the poling process the oversized piezoelectric actuators were laser machined at the Mullard Space Science Laboratory (MSSL) to obtain the dimensions described in Section 8.3.1. Code with the sample coordinates was written to carry out the laser machining in two steps: i) the top platinum electrodes were removed from unwanted areas to define the two electrodes and the two ground connections. The electrodes were also removed along the perimeter of the sample to define a 50µm gap on the top electrode at the edges of the sample and to prevent the shorting the top electrodes of adjacent samples. The depth of removed material was kept at 20µm and controlled by counting the number of laser passes over the same area of the piezoelectric actuator; ii) The PZT actuators were cut to the right dimensions of length and width. The laser set up at MSSL allowed for 10µm accuracy in both tasks. Figure 3 shows SEM photographs of laser machined trenches dividing the platinum electrodes on top of the PZT layer[§].

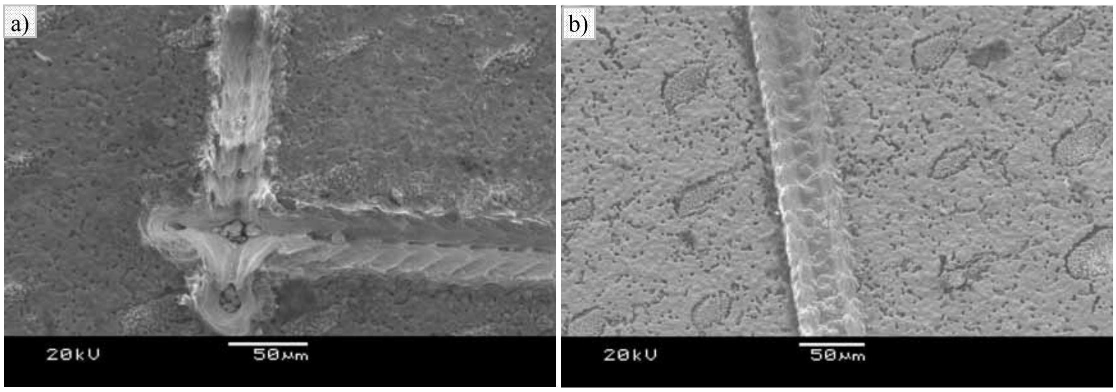

Figure 8.20: SEM micrographs of the laser machining of the piezoelectric actuators carried out at MSSL. The SEM pictures were taken with the assistance of Hana Hughes from the University of Birmingham.

8.3.2.3 Cleaning and connecting the grounds

Two cleaning stages were performed on piezoelectric devices, firstly to remove the poling oil before they were laser machined and then to remove the debris produced during the laser machining itself. The cleaning consisted of using a sequence of solvents and the use of an ultrasound bath as previously described in Section 6.3.1.5. After the cleaning process the ground electrodes at the top of the sample were connected with the bottom electrodes painting the edges of the sample with thin layer of silver loaded epoxy (RS Components Ltd, UK).

The cleaning process also highlighted in a qualitative way that the bonding strength between the co-sintered platinum electrodes and the piezoelectric actuators was superior to that of electrodes applied by sputtering of Cr and Au after sintering, which was the method used for fabricating the actuators of the LAXRO as none of the

---

[§] The SEM photographs of test devices shown in Figures 4 and 6 were taken with the assistance of Dr H. Hughes from the University of Birmingham.

samples for NEMO failed at this stage, where about 30% of the samples required re-sputtering of the electrodes after the cleaning stage.

8.3.2.4 Productivity summary

From a productivity point of view a total of 20 full and 10 half sintered actuator samples were made which were used to produce the NEMO1 and NEMO2 optics with a configuration consisting of 10 full samples and 4 half's places on the corners of the optic. Some samples manufactured whilst the sintering process was being optimized were discarded and used instead for the calibration of the laser machining setup at MSSL and for bonding tests.

8.3.3 Characterisation of the piezoelectric actuators

The radius of curvature (ROC) of the piezoelectric devices were measured using the experimental set-up described in Section 6.4.4. In order to learn what effect different stages of the manufacturing process have on the ROC of the piezoelectric elements, the ROC was measured at 1cm intervals after their sintering, but before their poling, and after their poling. It was found the ROC significantly changes after sintering, with respect to the preformed green samples, and after the poling. When data from all the manufactured samples are averaged a trend emerges. The ROC of the samples increases during sintering but decreases again after poling by 13mm on average. The data corresponding to the thickness measurements and ROC measurement for the samples that were finally assembled in the optic is presented in Table 8.1.

The thickness and ROC measurements for the samples used for the NEMO1 and NEMO2 assembly are presented in graphical form in Figure 8.21 where the three batches of samples, corresponding to different extrusions of green material, are presented. It can be seen that the thicknesses of the samples are T_{PZT}=190 +/-10µm for which the ROC varies in the range between 160 to 200µm.

Table 8.1: Thickness and radius of curvature measurements for the piezoelectric elements used for the NEMO1 and NEMO2 X-ray optics. The half samples are presented on the table under the dashed line.

					Before Poling		After Poling	
	Batch #	Serial #	T_{PZT} (µm)	stdev T_{PZT} (µm)	avg ROC (mm)	stdev ROC (mm)	avg ROC (mm)	stdev ROC (mm)
NEMO1	#1	#04	180	2.4	165	12.7	169	11.7
	#1	#05	199	4.4	184	4.2	179	3.7
	#2	#06	193	5.6	206	15.5	185	5.2
	#1	#07	192	7.5	203	-	184	6.2
	#2	#08	195	3.9	175	3.5	173	4.2
	#2	#09	194	1.7	184	8.8	180	6.9
	#2	#10	196	6.8	198	14.6	185	10.7
	#1	#12	196	5.8	211	9.3	168	2.4
	#1	#13	164	6.2	170	-	183	6.8
	#2	#14	216	6.9	195	7.3	183	8.2
	#2	#19	190	8.3	174	15.5	163	5.8
	#2	#21	186	2.9	227	18.0	175	6.6
	#1	#26	192	3.9	172	3.5	157	4.2
NEMO2	#2	#11	186	8.3	195	4.5	197	9.2
	#2	#15	219	6.6	205	3.6	172	9.3
	#3	#27	179	4.8	227	14.4	182	4.2
	#3	#28	190	9.1	208	9.0	193	3
	#3	#29	203	1.9	-	-	204	5
	#3	#30	191	5.9	204	7.3	199	8.6
	#3	#31	187	14.3	208	7.9	186	6
	#3	#32	199	9.9	209	17.1	192	10.3
	#3	#33	199	5.9	210	4.4	194	2.2
	#3	#35	192	6.0	-	-	187	10.0
	#1	#22	197	8.7	174.3	12.8	171	8.0
	#2	#23	222	3.9	194	8.2	188	3.5
	#1	#24	191	9.0	147	1.9	158	6.3
	#1	#25	197	8.7	215	14.8	160	7.4
Average of all samples used for the NEMO optics:			**194**	**6.3**	**195**	**9.5**	**182**	**6.6**

The radius of curvature measurements, in addition to be used as a selection criteria for which actuators that were to be assembled onto the optics, were also used to determine in which positions they were placed on the back of the optics. Those piezoelectric elements with smaller ROC towards the detector side of the optic and those with larger ROC towards the X-ray source side of the optic as shown in Figure 8.18.

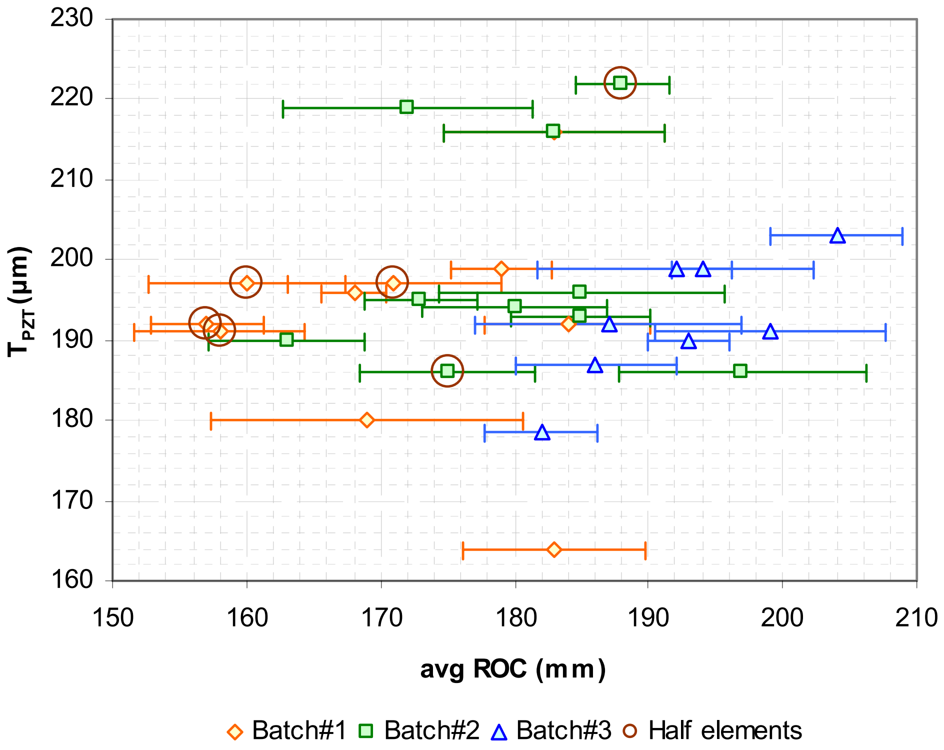

Figure 8.21: Thicknesses and average ROC for the samples used for the manufacturing of NEMO1 and NEMO2 X-ray optics. The radius of curvature measurements where used as a selection criteria for the actuators that were to be assembled onto the optics. The legend indicates the batch number and which samples where used as half samples, where the error bars indicate the spread of the ROC over the length of each individual element.

Assuming a constant shrinkage ratio during sintering for all samples, the variation in thickness indicates a variation on the green thicknesses of the VPP material which was not optimized for these trials. Further reduction on the thickness tolerances could be obtained by carrying out thickness measurements and selection of the green samples.

All the samples were tested using an impedance analyser (Agilent HP4294A) to ensure that they were active after the poling and laser machining processes.

8.3.4 Harnessing the piezoelectric actuators onto Nickel X-ray optics

A new integration procedure of the piezoelectric nickel shell was developed. Its main objectives were to increase the control over the thickness of the glue layer, the strength of the bond and maintain the alignment between neighbour piezoelectric devices on the optic. Two full optics were assembled: NEMO1 in which the nickel shell was released from the mandrel before bonding the piezoelectric devices; and NEMO2 which was released from the mandrel after the bonding of the piezoelectric devices and the harnessing to the support structure.

a) NEMO 1 piezoelectric devices layout

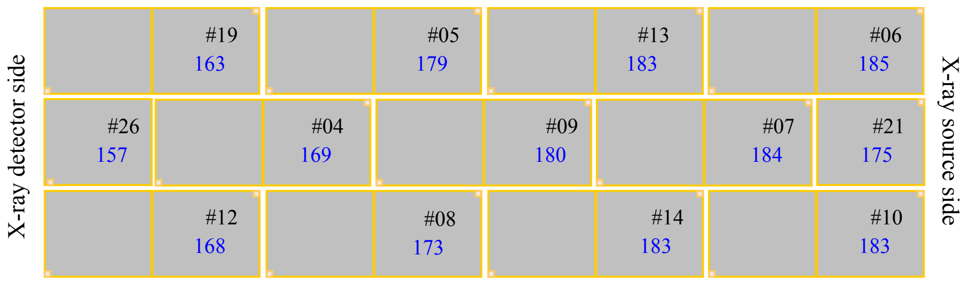

b) NEMO 2 piezoelectric devices layout

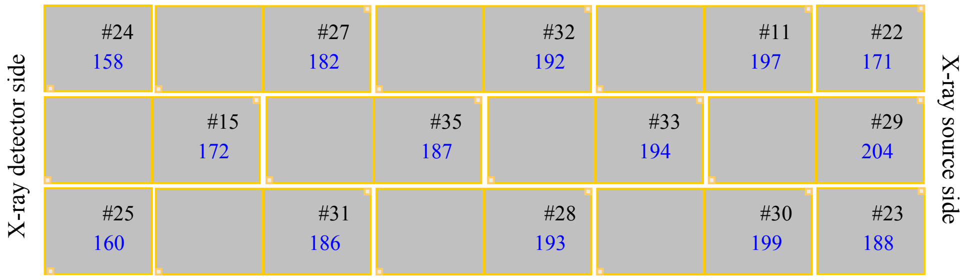

Figure 8.22: Piezoelectric devices brick wall layout for the NEMO 1, using two half elements and for NEMO 2, using four half elements. Each element is labelled with its serial number and average radius of curvature in millimetres. The gaps between the piezoelectric elements in the diagram are exaggerated for visualisation purposes.

To control the thickness of the glue layer a 5% volume content of glass beads with 80μm diameter was added to the EP30 glue (Master Bond Inc). The glue was applied to the optic using a doctor blade technique in which tape of defined thickness is used to define the separation between a steel blade and the nickel optic. The steel blade was then used to spread the glue leaving behind a glue layer of uniform thickness.

Initial tests were conducted to determine the weakest link of the nickel-glue-platinum electrodes-PZT structure and it was found that is was weakest at the nickel-glue interface. This was followed by another series of surface treatment tests to investigate if a surface treatment of the nickel surface would improve the strength of the bond. This assessed only in a qualitative manner by means of trying to detach the actuators using a scalpel 48 hour after bonding with the conclusion that the samples better bonded were those in which the surface treatment consisted of mechanical abrasion of the surface using sand paper combined with chemical etching using a 5% solution of nitric acid for 20 minutes. SEM pictures of cross-sections of one of the samples used for these test are shown in Figure 8.23.

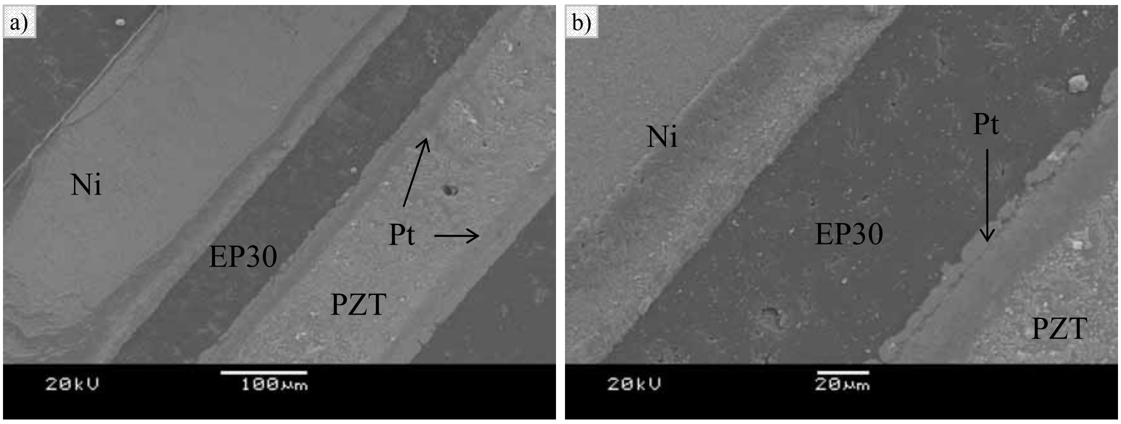

Figure 8.23: SEM pictures of a cross-section of a sample used for bonding test. The nickel surface was not treated prior to bonding.

However, when the final devices were made only the cleaning of the surface was carried out as both surface treatment methods would carry the risk of damaging the reflecting surfaces of the optics. It does not appear that the bond strength has a limiting factor on the performance of the current optics, but improvements of the bond strength between the glue layer and the nickel surface would need be revisited in future prototypes.

The piezoelectric devices were designed and accurately laser machined as previously described. The precise device dimensions enabled them to self align precisely with each other during assembly as long as they had a reference surface to be butted against during the bonding process. The reference surfaces were provided by two copper strips temporally bonded with double sided tape along 2mm wide strips along the length of the optic. A silicone rubber mould having the same curvature profile as the optic was placed on top of the piezoelectric devices after bonding thereby adding a small even pressure along the optic and making the piezoelectric devices conform better to the curvature profile of the optic. In the assembly of NEMO1 the copper strips were removed a couple of hours after bonding to avoid having them permanently glued to the optic. However, this proved to be too soon as the glue had not completely set allowing glue leak onto the reflecting surface. To avoid this problem for the bonding of NEMO2, more glue trials were conducted to determine if the copper wasters could be removed after the glue has set and the ideal time window for the application of the EP30 after it's mixing.

The conducted glue trials and the experience gained during the bonding of NEMO1 resulted in the bonding procedure of NEMO2, shown in Figure 8.24, consisting of the following steps:

1. Thorough cleaning of the bonding surfaces. The piezoelectric devices were cleaned using sequential cleaning in a series of solvents and an ultrasonic bath later left to dry in a 40^{o}C oven as described in Section 6.3.1.5.

2. Double sided tape was used along the 2mm edges of the optic to temporally bond two copper strips which would be used to align the piezoelectric devices on top of the nickel optic.
3. The edges of the optic were protected with PVC tape to avoid glue leaks onto the reflecting surface.
4. Use 100μm PVC tape along the two curved edges of the optic top to define the glue thickness.
5. Doctor blade the low shrinkage glue, EP30, over the nickel surface as shown in Figure 8.24a. The glue was prepared with 80μm diameter glass beads and left to set for 1h 20m to achieve a suitable viscosity.
6. The piezoelectric actuators were then positioned on the optic using a vacuum tool as shown in Figure 8.24b and c. The positions of the piezoelectric devices were chosen accordingly to their curvatures to match the changing ROC on the nickel optic.
7. Once all the piezoelectric devices were micro-positioned on the optic, small strips of ‘magic tape’ were used to join adjacent devices in order to maintain their relative alignments. The magic tape was masked over the piezoelectric boundaries so it could be removed after the glue was set even in the event of a glue leak through the gaps between piezoelectric actuators.
8. A transparent silicone rubber cast with the same curvature profile as the optic was placed on top of the actuators to keep them in position and apply pressure as the glue set.

After the glue had set for 15 hours the silicon rubber, copper waster and masking tape were removed and wires soldered, using indium solder, on the optic to provide the connections to the top and ground electrodes of the piezoelectric devices. The optic was mounted onto the support structure using two viton strips, 2mm wide, which were placed in the areas uncovered by the copper wasters. The final step was to release the harnessed optic from the mandrel using thermal shock. The harnessed NEMO2 device is shown in Figure 8.25.

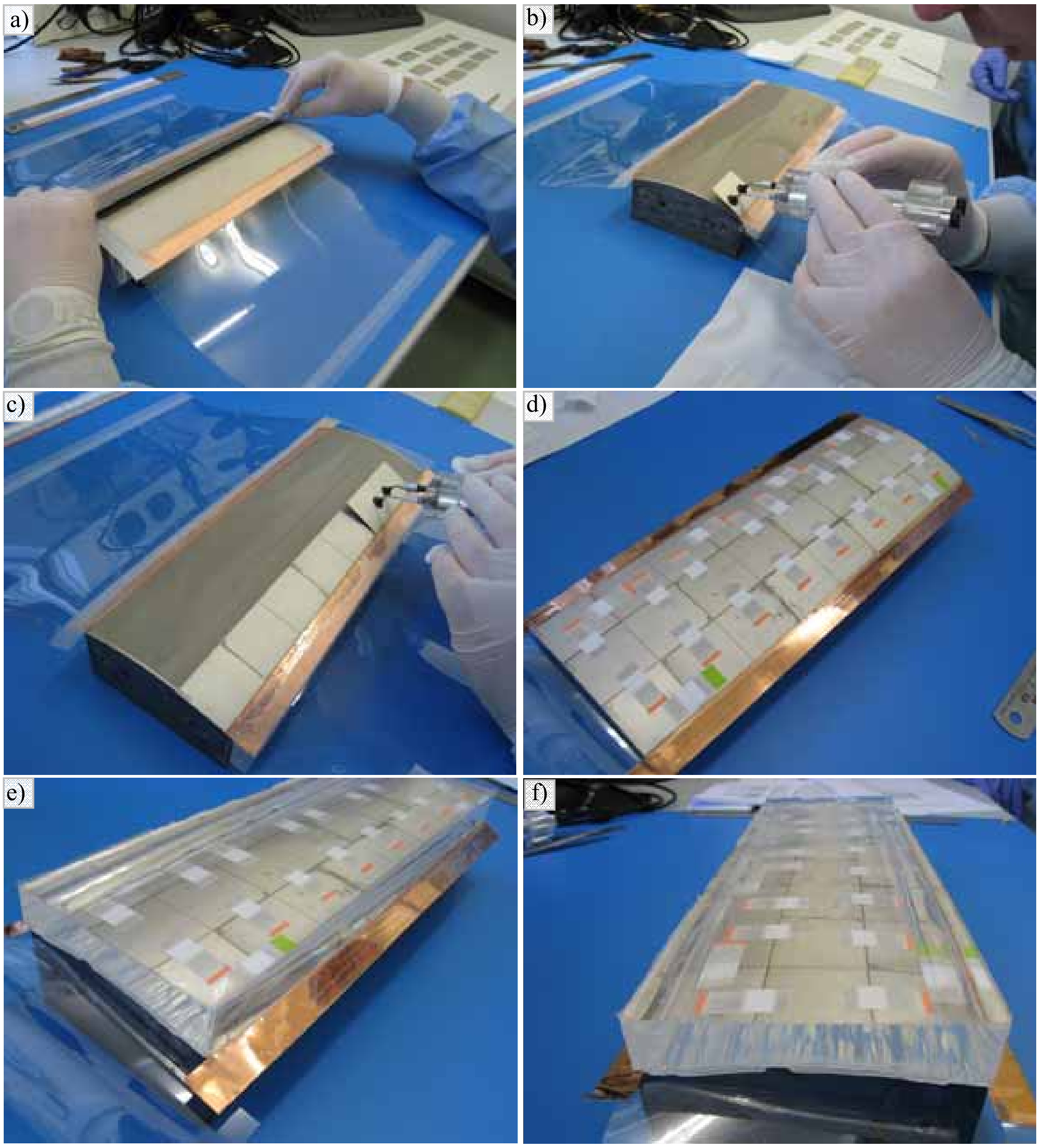

Figure 8.24: **Bonding procedure of NEMO2. a) Applying the EP30 glue using a doctor blade technique. b) and c) Positioning the piezoelectric actuators on the optic using a vacuum pen tool. d) The piezoelectric devices were glued together using magic tape to maintain their alignment. e) and f) A silicone rubber mould was used as a weight to maintain the positioning of the piezoelectric devices whilst the EP30 glue set.**

8.3.5 NEMO1 and NEMO2 characterisation

A new round of X-ray testing was scheduled to take place in May 2010 at the X-ray test facility at the UoL. Two upgrades were carried out with respect to the X-ray tests of LAXRO: The control programme of the piezoelectric devices was modified so each electrode could be controlled independently; and pitch and yaw motors on the support structure were changed and extensively tested at MSSL.

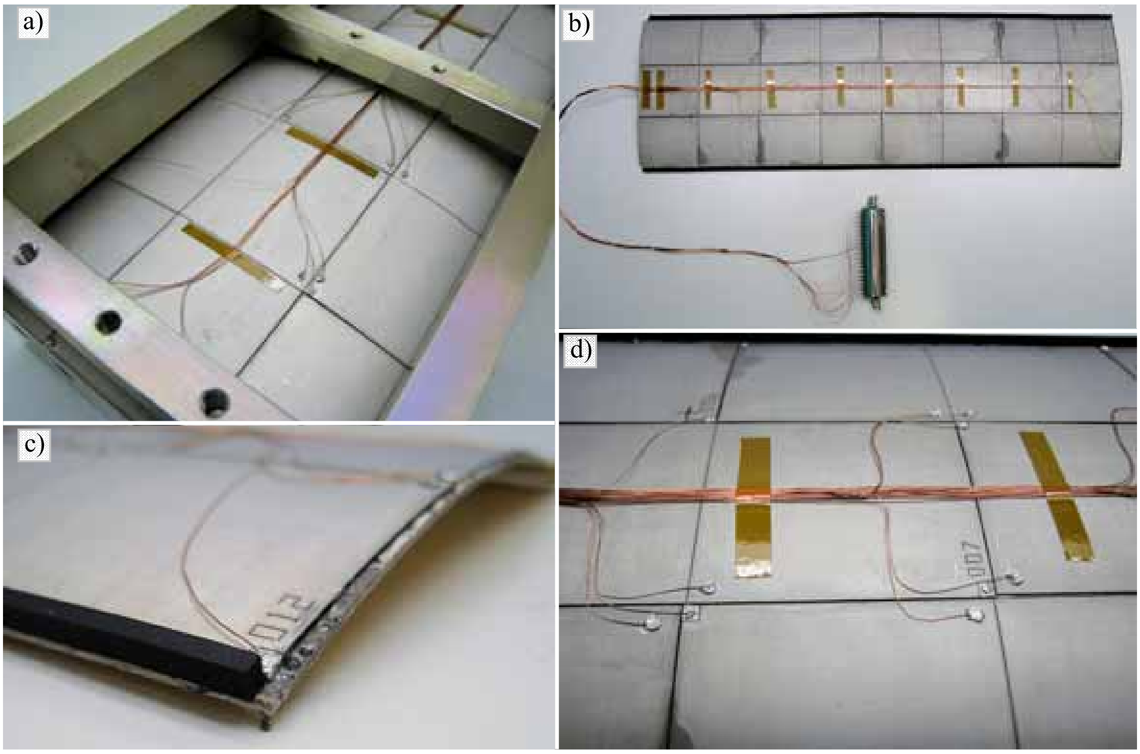

Figure 8.25: a) Close up picture of the harnessed NEMO2. b) Overall pictures of the NEMO2 optic. c) Close up view of the NEMO1 optic showing the mounting 2mm wide viton strip along the edge of the optic. d) Close up pictures of the NEMO2 showing detail of the harnessing and wiring. The harnessing and wiring was carried out at the MSSL by Graham Willis.

Both NEMO1 and NEMO2 were setup at the UoL X-ray testing facility and alignment tests using a laser beam demonstrated that both the pitch and yaw motors worked correctly. For NEMO2 all 24 electrodes were taken one by one from 0 to 100Volts, and in each case it was seen that they changed the laser image. However, the X-ray tests were not successful as it was found that NEMO2 focused the X-rays outside the detector range of the UoL facility. NEMO2 was still on the mandrel during the integration of the piezoelectric devices and the harnessing metrology of the optic so there was always the risk of this scenario happening.

Due to the glue leak that happened during the integration and defect on the surface that happened during the electroforming/release of the shell NEMO1 it was decided to mask 30% of the optic along its length to avoid stray reflections during the X-ray test. However the X-ray test results were inconclusive, just demonstrating that the X-ray image could be changed but not improved (11).

Technical problems in the UoL X-ray test facility meant that the test schedule could not be completed. However, further tests planned to be carried out by UCL and UoL to fully characterise the NEMO optics include the use of a Fizeau interferometer, a long trace profilometer, and possibly another X-ray test at the UoL facility.

8.4 Summary

The characterisation results of LARXO carried out in 2008 were very encouraging; as they demonstrated that its resolution could be improved using the pre-curved piezoelectric actuators bonded to its back surface, and therefore serving as a proof of principle device. However, they also highlighted that the gap between piezoelectric actuators created kinks on the reflecting surface which was an undesired effect as these kinks could not be actuated out.

A simplified FEA model of the problem was studied in COMSOL multiphysics reaching the conclusion that the gaps between piezoelectric devices should be as small as possible and be filled in order to achieve good mechanical coupling between adjacent piezoelectric devices and eliminate the kink effects on the reflecting surface.

Two sets of piezoelectric actuators have been manufactured and were used to produce two second generation X-ray optics prototypes, NEMO1 and NEMO2. The novel features of the actuators with respect of the first X-ray optic prototype included: First, the use of co-sintered platinum electrodes, instead of Au and Cu sputtered electrodes, which greatly improved the bond strength between the PZT ceramic and the electrode; secondly, a new sintering procedure was developed which allowed the sintering of piezoelectric elements more than twice the size; and finally laser machining was successfully introduced as a technique to define the electrodes within the same piezoelectric element and for the precise control of its dimensions.

From a design perspective the dimensions of the piezoelectric devices were chosen so they would cover the whole of the nickel surface, leaving very small gaps between piezoelectric devices. According to the FEA models previously presented this will reduce the kink effects that were present in the first prototype. An integration procedure of the piezoelectric devices, the nickel shell, and the support structure has been developed. The combination of the doctor blade technique to apply the glue and the use of 80µm glass beads allows control of the glue thickness. The precise laser machining of the piezoelectric devices enabled their alignment over the nickel surface.

Thickness and ROC measurements of the piezoelectric elements used show that: target thickness of 190µm can be achieved with 3% tolerances; For the ROC a wider distribution was obtained, which in principle is desirable as the optic also varies its ROC along its length, and the measurements show that samples with a target ROC within the bracket 160mm to 200mm with 6mm tolerances could be obtained using the same manufacturing methods.

For NEMO1 the piezoelectric devices integration and harnessing were carried out once the optic was released from the mandrel and a glue leak damaged part of the reflecting surface of the optic. For NEMO2 the nickel optic was left attached to the mandrel during integration and harnessing procedures which made both these processes easier as the mandrel served the function of temporary support structure and lessons learned from the integration of NEMO1 were applied to NEMO2. The problem with the second method is that the condition and metrology of the optical surfaces are unknown until the device is complete, and the nickel optic needs to be left attached to the mandrel for a longer period, which in turn may allow contaminants to enter the interface between the nickel shell and the mandrel.

Future work would concentrate on improving the manufacturing procedure of the piezoelectric devices to improve the curvature tolerance and space proving of the technology. One particular issue to be investigated is to improve the bond strength between the glue layer and the nickel shell.

As the testing of the NEMO1 and NEMO2 optics are still ongoing it is still unclear if the kinks on the gaps between piezoelectric actuators have been eliminated and/or minimised with the new integration procedure.

8.5 References

1. The Telescopes of XMM-Newton, http://xmm.esac.esa.int/external/xmm_user_support/documentation/technical/Mirrors/index.shtml (last accessed 14-10-2010).
2. *The Chandra X-ray Observatory* *http://www.nasa.gov/mission_pages/chandra/main/index.html (Last accessed 02-03-2010).*
3. Su, B., D.H. Pearce, and T.W. Button, *Routes to net shape electroceramic devices and thick films*. Journal of the European Ceramic Society, 2001. **21**(10-11): p. 2005-2009.
4. Wolter, V.H., *Verallgemeinerte schwarzschildsche spiegelsysteme streifender reflexion als Optiken fur riinfgenstrahlen (Generalized schwarzchil mirror*

systems with glancing incedence as optics for X-rays). Annalen der Physik, 1952. **6**(10): p. 286-295.

5. Feldman, C., Willingale R., Atkins C., Wang H., Doel P., Brooks D., Thompson S., Button T., Zhang D., Rodriguez Sanmartin D., James A. and Theobald C., Development of thin-shell adaptive optics for high angular resolution x-ray telescopes. in Space Telescopes and Instrumentation 2008: Ultraviolet to Gamma Ray. 2008: SPIE.

6. Feldman, C., *Smart X-ray optics for large and small scale applications*, in *Space Research Centre, Department of Physics and Astronomy*. 2009, University of Leicester: Leicester. p. 178.

7. Atkins, C., *Active X-ray optics for the next generation of X-ray space telescopes*, in *Physics and Astronomy*. 2009, University College London: London.

8. Chang M., Zadrozny A., Buscher D.F., Dunlop C.N. and Robinson D.J. Hysteresis correction of a piezoelectrically actuated segmented mirror, in Adaptive Optical System Technologies, Parts 1 and 2. 1998, SPIE-INT SOC OPTICAL ENGINEERING: Bellingham. p. 864-871.

9. Zhang D., Rodriguez-Sanmartin D., Button T., Meggs C., Atkins C., Doel P., Brooks D., Feldman C., Willingale R., Michette A., Pfauntsch S., Sahraei S., James A., Dunare C., Stevenson T., Parkes W., Smith A.and Wang H. The fabrication and characterisation of piezoelectric actuators for active X-ray optics. in Advances in X-ray/EUV Optics and Component IV. 2009: SPIE.

10. Zhang, D., Rodriguez Sanmartin D., Button T.W., Atkins C., Doel P., Dunare C., Feldman C., James A., Michette A., Parkes, W., Pfauntsch S., Sahraei S., Stevenson T., Wang H. and Willingale R. Development of Piezoelectric Actuators for Active X-ray Optics. Journal of Electroceramics, 2009. Online Version: DOI 10.1007/s10832-009-9566-y.

11. Feldman C., Willingale R., Atkins C., Brooks D., Button T., Doel P., James A., Meggs C., Rodriguez-Sanmartin D., Smith A., Theobald C. and Thompson S.. The performance of thin shell adaptive optics for high angular resolution X-ray telescopes. in Adaptive X-ray Optics. 2010. San Diego: SPIE.

CHAPTER 9

SUMMARY, CONCLUSIONS AND FURTHER WORK

9.1 Context and aims of the smart X-ray optics project

Active/adaptive optics have been extensively exploited in the visible domain, and is a concept which is finding applications in an increasing number of fields. In X-ray optics, several research groups have already built active Kirpatrick-Baez (line focus) and elliptical (point focus) X-ray optics for use in synchrotron facilities in the last decade. However, these technologies are based on using push/pull type actuators to control the surface of large X-ray mirrors(1, 2), which have large dimensions and are not appropriate for all X-ray applications.

The Smart X-ray optics consortium, created after a proof of concept project carried out at UCL in 2006, aimed to develop two new types of active X-ray optics with the actuation provided by piezoelectric actuators.

The first strand of research was Microstructured Optical Arrays (MOA’s), a concept based on polycapillarity and microchannel plate optics(3), where the X-rays would be focused after a double reflection on two consecutive arrays of microchannels etched on silicon substrates. The MOA’s would focus the X-rays by reflection rather than diffraction, such as in zone plates, and the optics would provide increased flux enabling the use of this technology in laboratory X-ray sources for applications, such as X-ray microscopy, which are currently only possible in cost-prohibiting synchrotron facilities. In addition, if the MOA structures are bent then they could be used to de-magnify the spot size of micro-focus X-ray source.

As discussed in Section 3.5.1, the MOA concept has been explored prior to this work(4), but its success was limited by two technical challenges which needed to be met in order for the MOA concept to work: firstly, the surface roughness of the channels needed to be below 2nm to avoid the scattering of the optical surfaces to be dominant; secondly, the MOA structure needed to be bent to a radius of 5cm to provide sufficient de-magnification of the micro-focus X-ray source.

The second strand of research of the SXO consortium was the development of large active X-ray optics. As has been discussed in Section 3.3, current X-ray telescopes need compromise between their resolution, which is related to how accurately the optics conform to the theoretical Wolter I shapes(5), and their sensitivity, which is a function of how many shells are nested inside each other. Future X-ray missions will need optics that would have to be both thin, below 500µm, and with very well defined shape conforming to the Wolter I theoretical configuration. It is generally accepted in the X-ray optics research community that to achieve this the optics would need to be active to be able to compensate for aberrations introduced during manufacturing, launch and also due to gravitational effects.

The concept involved the manufacturing of thin nickel optics by electroforming, with actuation provided by net-shaped piezoelectric actuators which would conform to the back of the nickel surfaces. The aim of the project was to obtain an X-ray optic which would enable a telescope design capable of achieving better resolution and sensitivity than those currently available by the Chandra and XMM-Newton missions.

A different approach to provide the actuation is being pursued at Harvard in collaboration with the Pennsylvania State University in which a different manufacturing route for the piezoelectric actuators would be used. Their X-ray optics would be coated directly with a layer of PZT by a thin or a thick film process which would entail: an annealing step, which with current piezoelectric manufacturing methods would need to use temperatures up to 650^{o}C; the patterning of electrodes; and poling procedures.

The main technical challenge of the Harvard approach, and which they are currently investigating, is to demonstrate the ability to integrate the manufacturing processes of the X-ray optics and the annealing of the PZT actuators. In addition, current thin film and thick film manufacturing methods of piezoelectric materials are limited to thickness of about 2µm and 20µm respectively as discussed in Section 4.3.3, thereby limiting their capability as actuators, as discussed n Section 8.2.2 where FEA analysis was carried out to analyze the effect of relative PZT and substrate thicknesses. This implies that for the Harvard approach to be successful the X-ray optic after the annealing of the piezoelectric actuator would have to be very close to the ideal Kirkpatrick-Baez geometry in order for the actuators to be able to improve the resolution of the X-ray optic(6, 7).

The work presented in this thesis, which needs to be viewed within the context of the SXO project, comprises the develelpment of actuation techniques for smart X-ray optics applications. Common to both large and small X-ray optics projects were the following objectives: i) To consider different piezoelectric actuator technologies and manufacturing methods. Determine if current piezoelectric devices could be adapted to bend the MOA arrays to a 5cm ROC. ii) Design, manufacturing and optimization of piezoelectric actuated devices using FEA tools. iii) Develop characterisation techniques for the piezolectric actuators. Curvature measurements of piezoelectric shells and testing of prototype devices. iv) Consider packaging/assembly issues. The conlclussions for each strand of reasearch are presented in the following sections.

9.2 Conclusions: spider actuators for the MOA's

FEA analysis and displacement measurements from prototype devices demonstrate that bending the MOA structures to the required 5cm radius of curvature using conventional actuators alone is not possible, unless both the actuator and the silicon are thinned to thicknesses below 20µm. Therefore an alternative actuator structure needed to be sought.

A spider array design has been proposed as a possible actuation alternative in which piezoelectric and mechanical actuation are combined by etching trenches all the way through the silicon wafer, to form levers to amplify the bending due to the piezoelectric effect alone. FEA analysis of the initial spider array design show that the required 5cm radius of curvature in the MOA chip can be obtained. This has been confirmed by measurements of the curvature in the centre region of test samples mounted on pre-curved clamps and by using piezoelectric actuated samples. To take advantage of the 1.2nm surface roughness of the vertical walls of the MOA channels achieved at Edinburgh University using a wet etch process, a novel spider arrangement has been designed which uses trenches parallel to the {111} planes in (110) silicon wafers. This means that both the MOA arrays and the lever structure can be wet etched in the same manufacturing step and integrated in the same silicon wafer. Several spider MOA structures, with six different spider designs, have been successfully manufactured.

Preliminary results of a wet etched spider device actuated with two 150μm thick piezoelectric strips show that the MOA can be bent to a radius of 6.5cm without failure of the MOA channels. This is consistent with FEA models of the wet etched spider MOA design and with those of the initial spider MOA model showing that a two piezo-strip actuator configuration could bend the MOA structure to a ROC below 5cm if the thickness ratios of the PZT and the Silicon are optimized.

An alternative actuator arrangement with segmented electrodes has also been designed and modelled. The FEA results indicate that extra capabilities such as more control over the curvature profile; +/-20μm z control; and +/-3mrad control over the tip/tilt angles could be obtained if precise micro machining of the actuator layer and assembly onto the MOA chip could be achieved.

Design drawings of an actuator with segmented electrodes have been made and an integration procedure, including packaging and mounting procedures have been conceived.

9.3 Conclusions: Actuators for large X-ray optics

Net shaped unimorph piezoelectric actuators have been manufactured and used to build the first large adaptive X-ray optic (LAXRO) prototype. X-ray tests and metrology of the reflecting surface were carried out at the University of Leicester and at the Daresbury Laboratory respectively and were successful in demonstrating that the reflecting surfaces could be controlled using the piezoelectric actuators and the resolution of the optic improved. The measurements carried out using a long trace profilometer at the Daresbury Laboratory indicated that the most important aberration introduced by the bonding of the piezoelectric devices to the nickel optic where kinks occurred between adjacent actuators.

Finite element analysis (FEA) models of a simplified structure were set up to study this kink effect. Two conclusions were extracted from the FEA models: The kink effect has a linear dependence on the size of the gap between adjacent piezoelectric devices; and that for a given gap size the kink effect is further reduced if the gaps are filled, either by PZT material or by the bonding material, as the filling material would aid the mechanical coupling.

Two sets of piezoelectric actuators (32×75×0.19mm) have been manufactured and were used to produce the second generation X-ray optics prototypes, NEMO1 and NEMO2. The novel features of the actuators with respect of the first X-ray optic prototype included firstly, the use of co-sintered platinum electrodes, instead of Au and Cu sputtered electrodes, which greatly improved the bond strength between the PZT ceramic and the electrode; Secondly, a new sintering procedure was developed which allowed the sintering of piezoelectric elements more than twice the size; and finally laser machining was successfully introduced as a technique to define the electrodes within the same piezoelectric element and for the precise control of its dimensions. Thickness and ROC measurements of the piezoelectric elements used show that: target thickness of 190μm can be achieved with 3% tolerances; For the ROC a wider distribution was obtained, which in principle is desirable as the optic also varies its ROC along its length, and the measurements show that samples with a target ROC within the bracket 160mm to 200mm with 6mm tolerances could be obtained using the same manufacturing methods.

From a design perspective the dimensions of the piezoelectric devices were chosen so they would cover the whole of the nickel surface, leaving very small gaps between piezoelectric devices. The devices were bigger, with to actuation areas instead of a single one, and were placed on the optic in a brick-wall arrangement which aided their alignment during assembly. According to the FEA models previously presented in Section 8.2.10 this should reduce the kink effects that were present in the first prototype. An integration procedure of the piezoelectric devices, the nickel shell, and the support structure has been developed. The combination of the doctor blade technique to apply the glue and the use of 80μm glass beads allows control of the glue thickness. The precise laser machining of the piezoelectric devices enabled their alignment over the nickel surface.

For NEMO1 the piezoelectric device integration and harnessing were carried out once the optic was released from the mandrel and a glue leak damaged part of the reflecting surface of the optic. For NEMO2 the nickel optic was left attached to the mandrel during the integration and harnessing procedures which made both these processes easier as the mandrel served the function of a temporary support structure and lessons learned from the integration of NEMO1 were applied to NEMO2. The problem with the second method is that the condition and metrology of the optical surfaces are unknown until the device is complete, and the nickel optic needs to be left over the mandrel longer, which in turn may allow contaminants to enter the interface between the nickel shell and the mandrel.

9.4 Suggestions for further work

On the spider MOA project, future work should concentrate, as soon as availability of resources allows, on the manufacturing on the laser machining of the piezoelectric actuators with segmented electrodes and device integration with the spider silicon chips and the support structures which have already been manufactured. Once these issues are solved the intention is to carry out X-ray testing of devices to establish their capability as an X-ray optic.

If X-ray testing due to be carried out at KCL is successful, the spider MOA could be redesigned to provide a point focus, rather than a line focus, and therefore reduce cross-shaped aberrations when a tandem/pair of spiders MOA's are used to obtain a point focus.

On the large optic project, Further X-ray test and metrology of the NEMO1 and NEMO2 are scheduled to be conducted at University College London and at University of Leicester, and detailed analysis of those results is needed in order to fully understand the impact of the design modifications of the NEMO with respect to the LAXRO device. Another possibility being considered is to use the same production methods for the piezoelectric actuators but to bond them to slumped glass rather than electroformed nickel substrates. NASA's Goddard Space Flight Centre has delivered two slumped glass optics, with dimensions 225mm×66mm×0.2mm, a 126mm ROC, and a 5nm iridium coating on the reflecting surface, to the University of Leicester which could be used for this purpose.

Once the NEMO devices are fully characterised, future work on the large optic would concentrate on improving the manufacturing procedure of the piezoelectric devices. The curvature tolerances could be improved if: i) further research to understand the effects of each manufacturing process on the curvature were carried out; ii) other aspects of the manufacturing process, such as the thickness of the green material, were more precisely controlled; iii) the manufacturing of the piezoelectric devices were scaled up to produce a larger number of devices than required and only the best devices were selected. Follow on research would also require investigating all aspects related to space proving the technology.

Finally, the spider structure has demonstrated that silicon processing techniques could be used to create patterns on silicon wafers which in turn change the properties of the structure, allowing the design of devices where small ROC could be achieved. FEA models show that the combination of these pattern structures with piezoelectric actuators results in devices where curvature and tip/tilt angles could be controlled, but this would need to be verified by using prototype devices. These capabilities could have applications for other devices. One possible application being investigated is the production of active/adaptive focusing micro-mirrors for laser applications.

9.5 References

1. Eng P.J., Newville M., Rivers M.L., Sutton S.R. Dynamically figured Kirkpatrick Baez x-ray micro-focusing optics. X-Ray Microfocusing: Applications and Techniques, 1998. 3449: p. 145-156.
2. Howells M.R., Cambie D., Duarte R.M., Irick S., MacDowell A.A., Padmore H.A., Renner T.R., Rah S. and Sandler R., Theory and practice of elliptically bent x-ray mirrors. Optical Engineering, 2000. 39(10): p. 2748-2762.
3. MacDonald, C.A. and W.M. Gibson, *Applications and advances in polycapillary optics.* X-Ray Spectrometry, 2003. **32**(3): p. 258-268.
4. Prewett, P.D. and A.G. Michette, *MOXI: A novel microfabricated zoom lens for x-ray imaging.* Advances in X-Ray Optics, 2001. **4145**: p. 180-187.
5. Wolter, V.H., *Verallgemeinerte schwarzschildsche spiegelsysteme streifender reflexion als Optiken fur riinfgenstrahlen (Generalized schwarzchil mirror systems with glancing incedence as optics for X-rays).* Annalen der Physik, 1952. **6**(10): p. 286-295.
6. Reid, P.B., Davis W.N., Schwartz D.A., Trolier-McKinstry S., Wilke R.H.T. Technology challenges of active X-ray telescopes for astronomy. in Adaptive X-ray optics, SPIE. 2010. San Diego.
7. Schwartz, D.A., Brissenden R.J., Freeman M.D., Gaetz T.J., Gorenstein P., Jerius D.H., Juda M., Reid P.B., Saha T.T., Trolier-McKinstry S. and Wilke R.H.T. On-orbit adjustment comcepts for the Gen-X observatory. in Adaptive X-ray optics, SPIE. 2010. San Diego.

APPENDIX I

THE SMART X-RAY OPTICS CONSORTIUM

The Smart X-ray Optics (SXO) project is a UK based consortium funded by a Basic Technology research grant from the Engineering and Physical Sciences Research Council (Grant number: EP/D04880X/1)). The project had one proof-of-concept year (2005) and has since run for four years up to its conclusion (2006-2010). The consortium comprises eight UK institutions investigating adaptive/active optics for both large and small X-ray optics applications.

Both projects are extensively described in Chapters VII and VIII with an emphasis on the development of the development of the actuation devices, but it would not have been possible without the contribution of the SXO collaborators. Some aspects of the SXO have only been briefly summarised, such as the fabrication of the Nickels shells at UCL and the testing procedures at UoL, or completely left out, as the development of the X-ray testing facilities for the MOAs and the development of the micro-focus X-ray source at KCL, which are/will be described in other PhD theses and publications of the SXO consortium.

Below is a brief description of the contributions of each institution, but it should be highlighted that throughout the duration of the SXO project there was great degree of synergy between the groups and overlaps, aided by quarterly project meetings, that contributed enormously to the general success of the project.

The Mullard Space Science Laboratory (MSSL), Ady James and Alan Smith

MSSL provided the role of project manager (Ady James), as well as technical support (Graham Willis and Craig Theobald). Laser machining of the piezoelectric devices for both X-ray optics, the manufacturing of the large optic carriage structure, harnessing of the large optic, and the manufacturing of the packaging structure for the MOA's were carried out at MSSL.

University College London (UCL), Peter Doel (PI)

UCL has been leading, under the guidance of Peter Doel, the large optic project since its conception in 2005. Carolyn Atkins completed her PhD whilst working at UCL, Hongchang Wang held a postdoctoral position for a year in 2008 before going on to get a permanent position at Diamond light source and David Brooks provided technical assistance. Full scale modelling of the piezoelectric actuators for the large optic, manufacturing the large scale adaptive prototype using electroforming of nickel shells and metrology of test samples were some of the tasks carried out at UCL.

Kings College London (KCL), Alan Michette (PI)

The MOA project has been led from KCL, PI Alan Michette, taking forward previous work on this concept dating back to 2002. David Hart, who started developing a micro-focus X-ray source at the Gray Cancer Institute, has since moved to KCL where he has completed the work on the micro-focus X-ray source. As part of his PhD work, Matthew Shand has developed the X-ray testing facility of the MOA's. Modelling of actuation techniques concepts for the MOA's has been also carried out by Shahin Sahraei as part of his PhD work. Finally, Slawka Pfauntsh participated in shared experiments and worked on the development of the micro-focus X-ray source and the development of the X-ray testing facility for the MOA project.

The University of Leicester (UoL), Richard Willingale (PI)

The UoL have been involved in the design process of both large and small X-ray optics. In 2009 Charly Feldman completed her PhD whilst working the SXO project at Leicester and carried on working for the SXO until the end of the project. Some of the tasks carried out at UoL included X-ray tracing modelling of on both optics using the Q software developed at the UoL, design of the large X-ray optic prototype, and testing of the Large X-ray optic prototype and the MOA prototypes at the X-ray testing facilities at the UoL.

The Scottish Micro-electronic Centre (SMC) at the University of Edinburgh UoE, Tom Stevenson (PI)

The SMC has been involved in the design and investigation of the production methods of the MOA devices. Camelia Dunare has carried out the manufacturing of MOA devices using dry and wet etching techniques and the production of spider-MOA chips. William Parkes has also provided insightful advice on the manufacturing of the spider MOA structures.

The University of Birmingham (UoB), Tim Button (PI)

The UoB has carried out the work described in this thesis including, the design, modelling, fabrication and characterisation of piezoelectric actuated devices. The author of this thesis worked on his PhD from May 2007 to April 2011. Dou Zhang worked full time for the SXO project (Sept. 2006 to Sept. 2009), during this time he developed the manufacturing methods for the piezoelectric devices used for LAXRO, moving on to gain a permanent position in Central South University, Changsha, China. Carl Meggs, who worked in part time basis throughout the project, has provided technical assistance and manufacturing expertise. He developed the sintering method for the piezoelectric actuators used in the NEMO optics and designed the assembly and packaging structure for the spider MOA's. Hana Hughes worked on an ad-hoc basis for the SXO project in 2010, when she providing assistance with SEM imaging.

The Science and Technologies Facilities Council (STFC) Daresbury Laboratory, Andy Smith

Reflectivity tests on the small scale optic and metrology using the Long Trace Profiler (LTP) on the large scale optic and mandrel. STFC Daresbury Laboratory has also been involved in the design concepts of both devices.

Silson SL, Peter Anastasi, was an associate member of the SXO consortium, and contribution his technical insights at the project meetings.

APPENDIX II

{111} PLANES IN (110) SILICON WAFERS

The two sets of {111} crystallographic planes perpendicular to the surface of (110) silicon wafers were used in the MOA project as a design rule for the drawing of the spider actuator structure. This allowed for the wet etching of both elements of the device in a single manufacturing step. Figure II-1 below depicts a 3D representation of the crystallographic planes in a (110) silicon wafer, “Fundamentals of microfabrication”, Madau, M., CRC Press, New York, 1997.

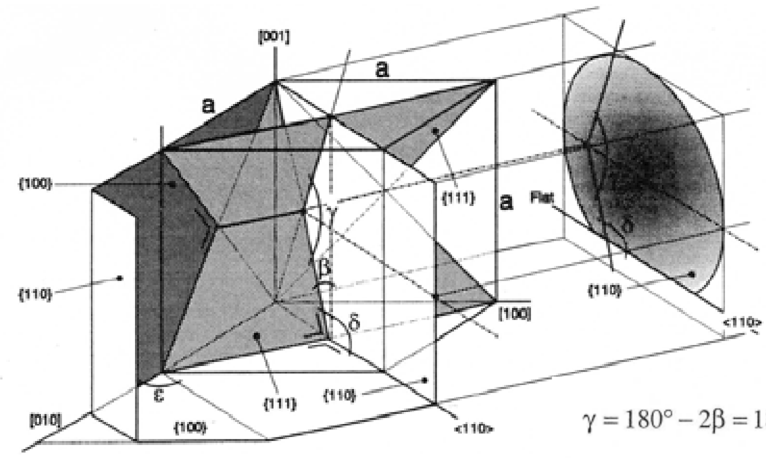

$$\gamma = 180^\circ - 2\beta = 180^\circ - 2\arctan\left(\frac{\sqrt{2}}{2}\right) = 109.47^\circ$$

$$\delta = 90^\circ + \beta = 90^\circ + \arctan\left(\frac{\sqrt{2}}{2}\right) = 125.26^\circ$$

$$\varphi = 270^\circ - \delta = 144.74^\circ$$

Figure II-1: {111} Planes in (110) silicon wafers from “Fundamentals of microfabrication”, Madau, M., CRC Press, New York, 1997.

A complete description of the angles between the {111} crystallographic planes can be found in Madou’s reference book.

The angles between different sets of {111} planes can also be visualised using the standard stereographic projections of cubic crystals shown in Figure II-2a for a (110) silicon wafer, where it can also be seen that there are two sets of {111} planes perpendicular to the silicon surface.

Most silicon manufacturers also use the {111} silicon planes to determine the orientation of (110) silicon wafers, i.e. which side is which, by means of aligning primary and secondary flats of the wafer to the silicon {111} planes perpendicular to the wafer surface as shown in the schematic representation in Figure II-2b below.

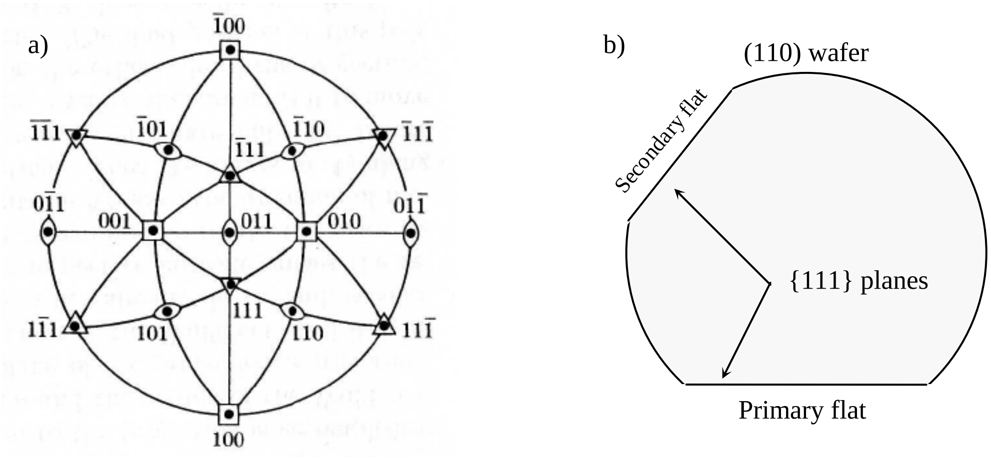

Figure II-2: a) Standard stereographic projections of cubic crystals for a (110) orientated substrate. b) The usual manufactures convention is to align the primary and secondary flats in (110) silicon wafers with the directions of the {111} planes perpendicular to the surface.

APPENDIX III

LABVIEW INTERFACES AND BLOCK DIAGRAMS

III-1 Program for the control up to 32 piezoelectric actuators

This program was used for the control of the piezoelectric actuators on the NEMO1 and NEMO2 optics. The program reads two files, one which contains an array with the current voltages applied to the piezoelectric actuators, V_i^{old}, and another which contains an array with the new voltage values, V_i^{new}, where the index i identifies each active area on the optic. It is also specified on the control interface, which control method is used, control method I or control method II and the parameters defining the control method as follows:

V_{max}	is the maximum voltage
V_{min}	is the minimum Voltage
V_{ref}	is the reference voltage
N	Controls the frequency of the oscillation in control method I
k	is the decay rate for the control method I or the ascent/descend rate for control method II.

Control method I:

The voltage has a transient period where a decaying oscillating voltage around the target new value V_i^{new} is used according to III-1 where k determines how fast the amplitude of the oscillated voltage decays over time, N determines the frequency of the oscillation. Stop conditions for the oscillation and safeguards to avoid using the maximum voltages where embedded in the code.

$$V_i(t) = V_i^{new} - Ae^{-kt}Cos(2\Pi t / N) \qquad \textbf{Equation III-1}$$

Control method II:

The voltage is first ramped, from the current V_i^{old} value to the reference voltage and then ramped from the reference voltage to the target voltage V_i^{new} as shown in III-2, where the rate of ascent and descend is controlled by the constant k.

$$\begin{array}{lll} Ramp\ to\ the\ reference\ voltage: & V_i(t) = V_i^{old} + kt & (V_i(t) < V_{ref}) \\ Ramp\ to\ the\ t\arg et\ voltage: & V_i(t) = V_{ref} - kt & (V_i(t) > V_i^{new}) \\ Stationary\ voltage: & V_i(t) = V_i^{new} & \end{array} \qquad \textbf{Equations III-2}$$

When the run button is pressed, the program checks if $V_i^{old}=V_i^{new}$? If the answer is positive, nothing else happens to those voltages. For those voltages where $V_i^{old} \neq V_i^{new}$, and in order to minimise hysteresis effect as described in section XX, the voltages go through the transient period corresponding to the control method I or II respectively. The interface and block diagrams of the programs are shown in Figures III-1 and III-2 below:

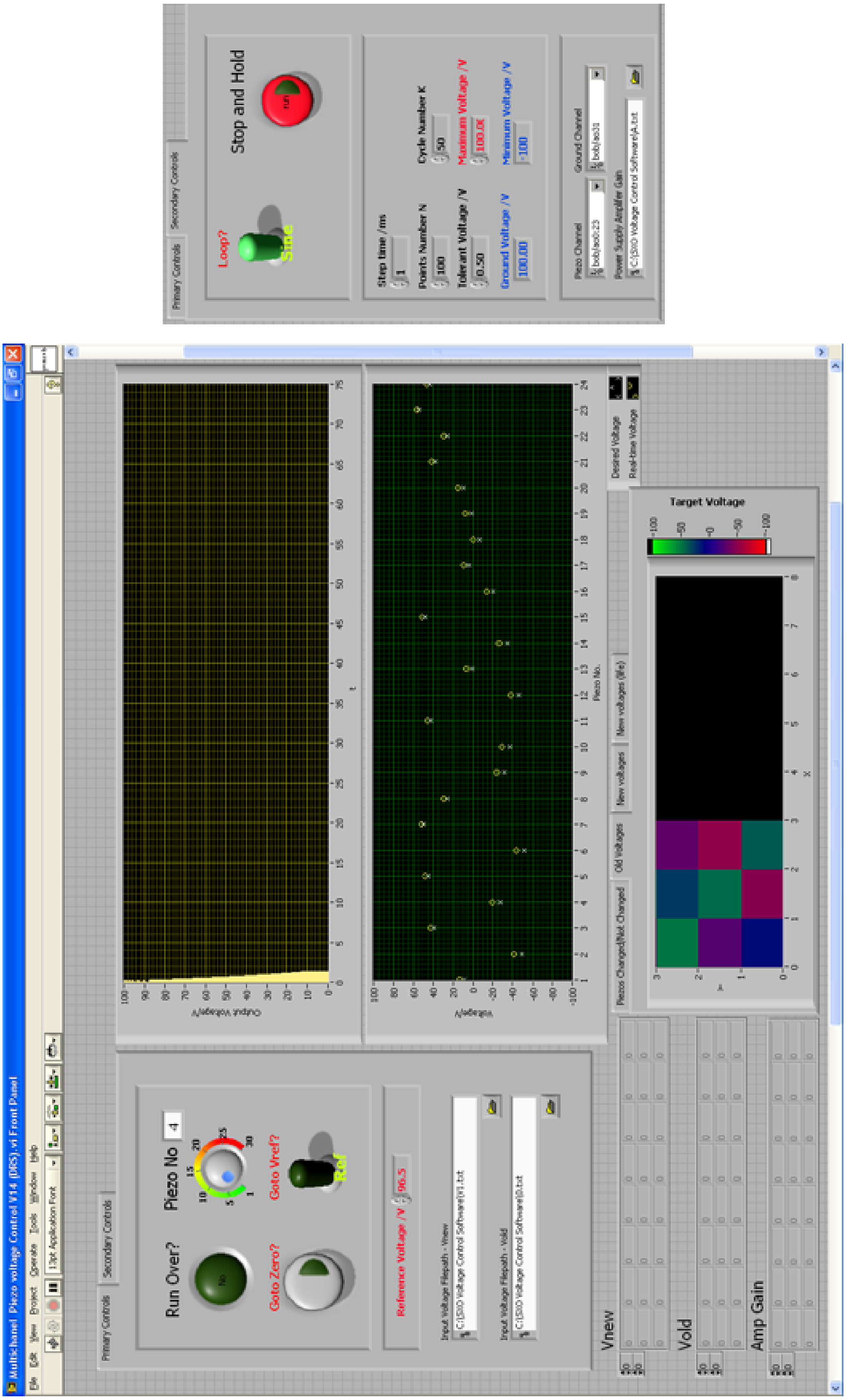

Figure III-1: LabView interface of the program designed for the control of the piezoelectric devices. The insert shows the secondary controls of the program.

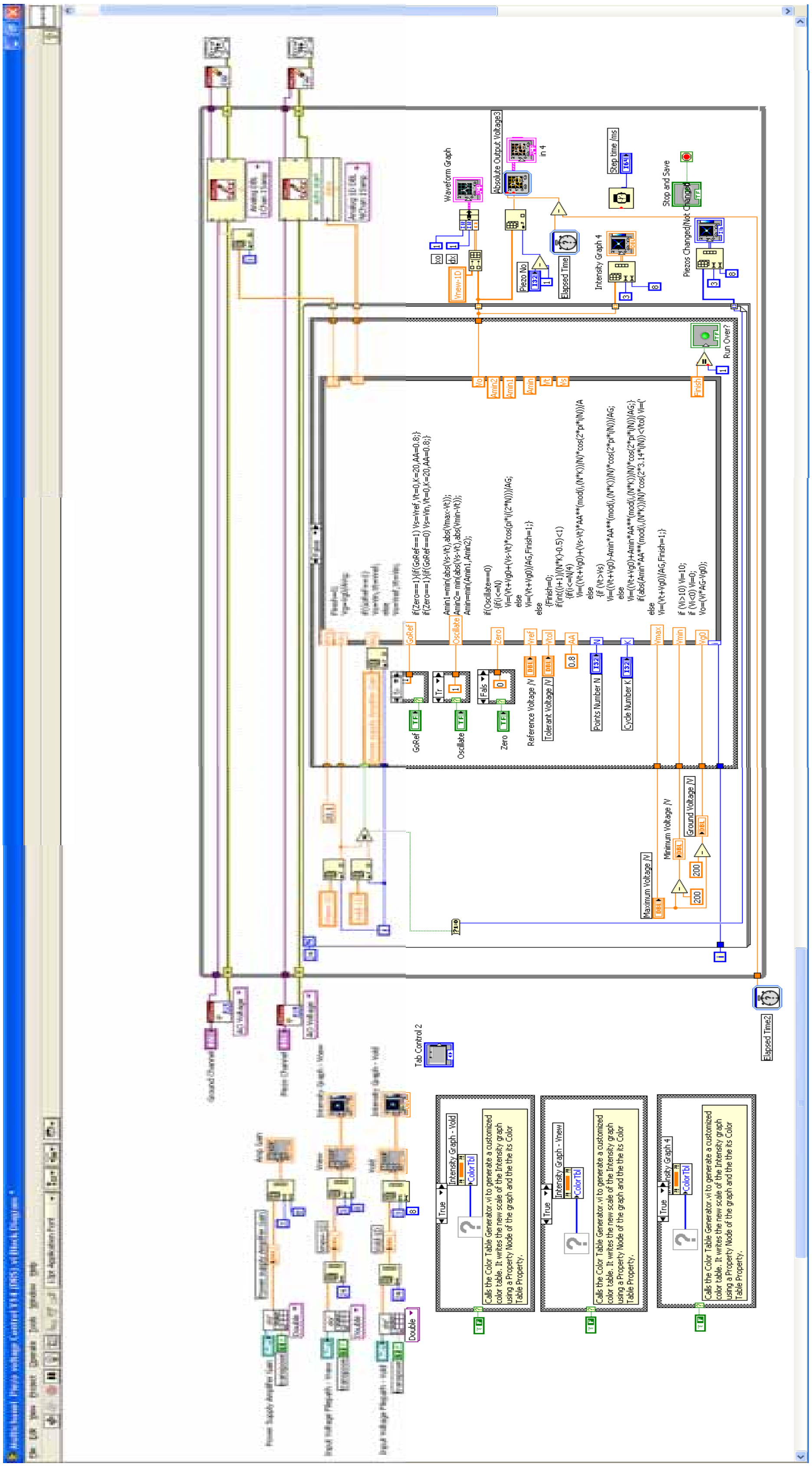

Figure III-2: LabView block diagram of the program designed for the control of the piezoelectric devices

III-2 Program for the measurement of hysteresis loops

A LabView program was also designed to carry out the measurement of the displacement vs. applied voltage hysteresis curves using the experimental set-up described in Section 6.4.4. The interface and block diagram of this program are shown in the Figures III-3 and III-4 below.

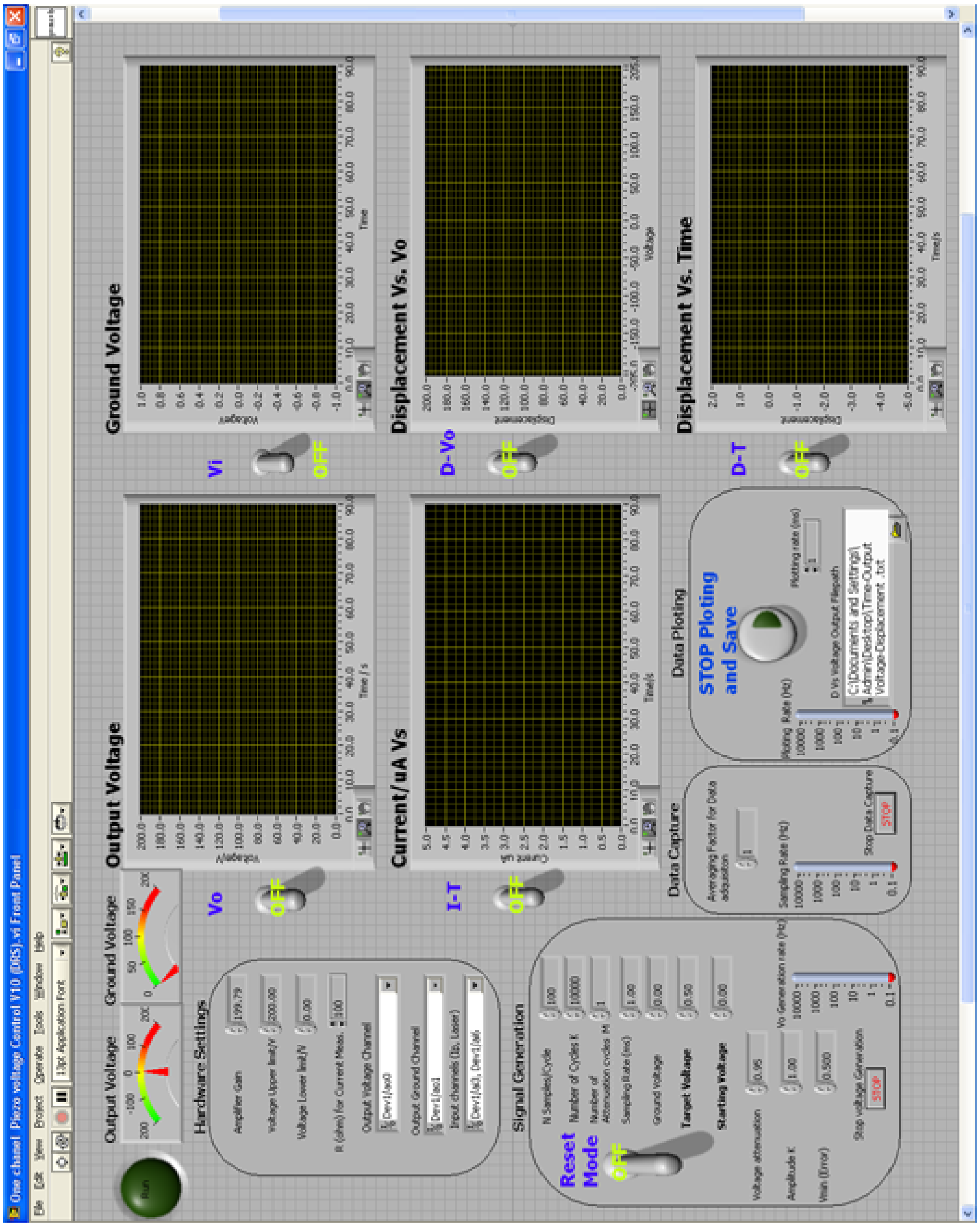

Figure III-3: Computer interface of the lab-view program for the measurement of the voltage/displacement hysteresis loops.

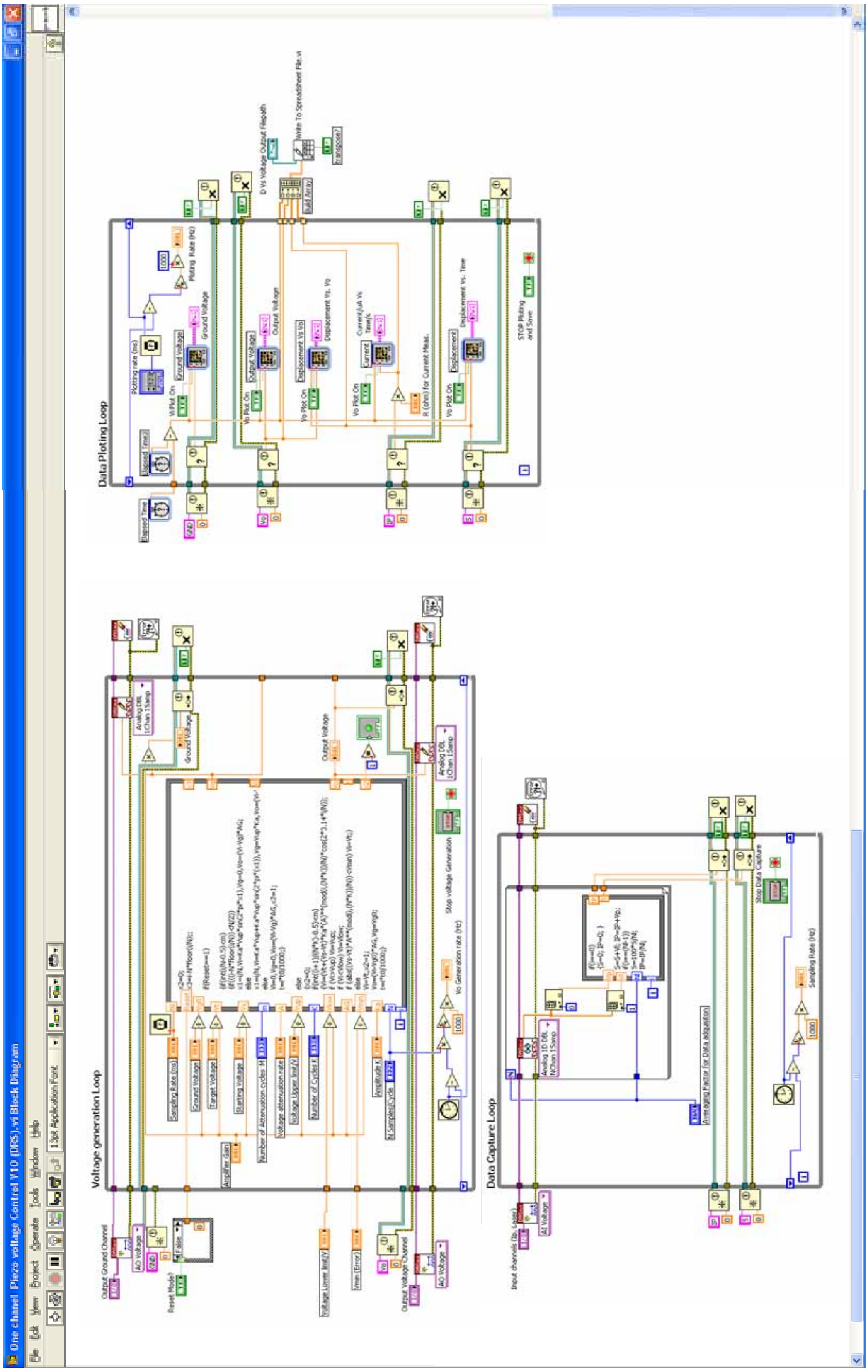

```
x2=0;
x3=i-N*floor(i/N);;

if(Reset==1)

{if(int(i/N-0.5)<m)
{if(((i-N*floor(i/N))<N/2))
x1=i/N,Vi=Ka*Vup*sin(2*pi*x1),Vg=0,Vo=(Vi-Vg)*AG;
else
x1=i/N,Vi=Ka*Vup+Ka*Vup*sin(2*pi*(x1)),Vg=Vup*Ka,Vo=(Vi-
else
Vi=0,Vg=0,Vo=(Vi-Vg)*AG,x2=1;
t=i*t0/1000;}

else
{x2=0;
if(int((i+1)/(N*K)-0.5)<m)
{Vi=(Vt+(Vs-Vt)*Ka*(A)**(mod(i,(N*K))/N)*cos(2*3.14*i/N));
if (Vi>Vup) Vi=Vup;
if (Vi<Vlow) Vi=Vlow;
if (abs((Vs-Vt)*A**(mod(i,(N*K))/N))<Vmin) Vi=Vt;}
else
Vi=Vt,x2=1;
Vo=(Vi-Vg0)*AG,Vg=Vg0;
t=i*t0/1000;}
```

```
if(i==0)
{S=0; IP=0; }

S=S+Vi; IP=IP+Vp;
if(i==(Ni-1))
S=100*S/Ni;
IP=IP/Ni;
```

Figure III-4: Block diagram of the LabView program designed for the measurement of the voltage/displacement hysteresis curves.

III-3 Program for the scanning of curved surfaces

This LabView program has two modes of operation for the experimental set-up described in Section 6.4.4: The moving mode which allows for the x and y positioning; and the 1D scanning mode. End detection was included in the code to avoid jamming of the motorised positioning stages. The program was used for scanning the piezoelectric samples used for the NEMO1 & 2 large X-ray optics prototypes. This data was then used to obtain a measurement of the radius of curvature along the length of each individual device. The block LabView interface and block diagram are shown on the Figures III-5 and III-6 below.

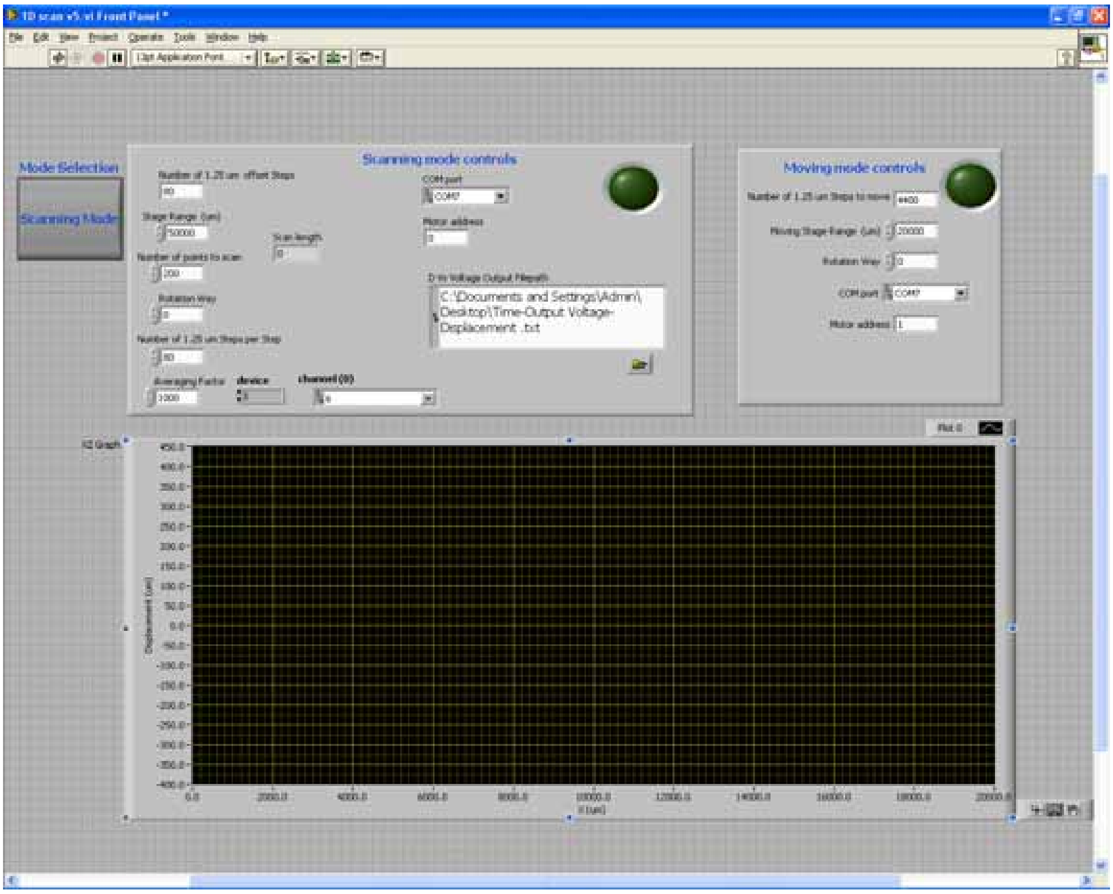

Number of 1.25 um offset Steps: 80
Stage Range (um): 50000
Scan length: 0
Number of points to scan: 200
Rotation Way: 0
Number of 1.25 um Steps per Step: 80
Averaging Factor: 1000
device: 1
COM port: COM7
Motor address: 3
D-m Voltage Output Filepath: C:\Documents and Settings\Admin\Desktop\Time-Output Voltage-Displacement .txt

Number of 1.25 um Steps to move: 4400
Moving Stage Range (um): 20000
Rotation Way: 0
COM port: COM7
Motor address: 1

Figure III-5: Interface of the LabView programme used for scanning curved surfaces.

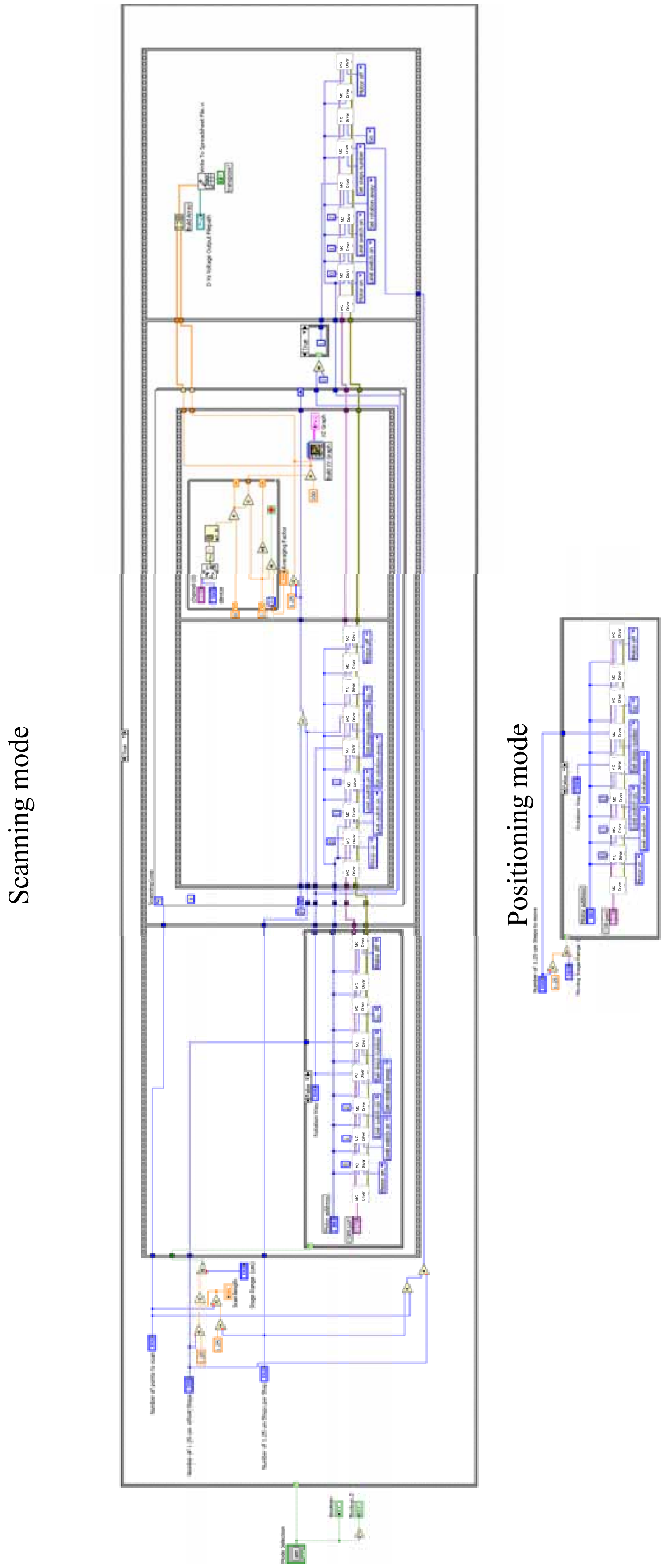

Figure III-6: Block diagram of the LabView program used to scan curved surfaces.

APPENDIX IV

MEASUREMENT OF THE BREAKING STRESS OF SILICON WAFERS

The flexural stress of a silicon wafer can be measured using a three point bending experimental set-up as described in schematic representation Figure IV-1:

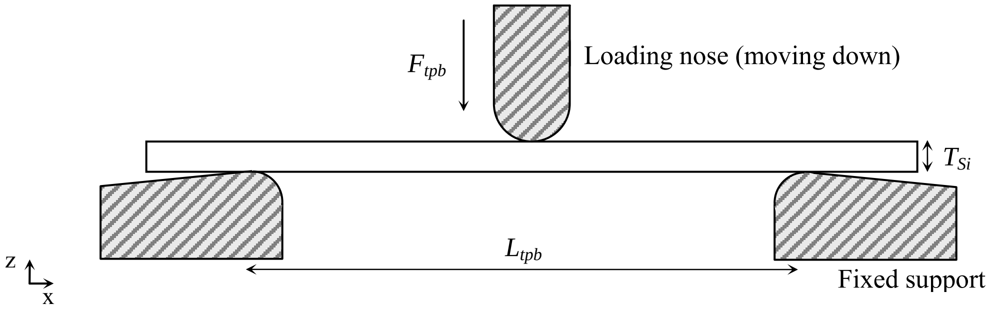

Figure IV-1: Schematic representation of a three point bending experimental set-up for the measurement of the flexural stress of a silicon wafer.

The flexural stress is then described by the expression IV-1 below(1):

$$\sigma_f = \frac{3F_{tpb}L_{tpb}}{2W_{Si}T_{Si}^2}$$ **Equation IV-1**

Where:

σ_f is the flexural stress, in MPa;

F_{tpb} is the applied force in the three point bending set-up, in newtons;

L_{tpb} is the span, in millimetres;

W_{Si} is the width of the silicon specimen (y direction), in millimetres;

T_{Si} is the thickness of the silicon specimen, in millimetres.

the maximum stresses of 108MPa do not exceed the breaking stress of silicon measured as 260MPa by a three-point bending test on silicon wafers as shown in Figure and using 7.1 to calculate the flexural stress for a three point bending set-up.

Figure IV-2a shows a picture of the three point bending set-up to measure the breaking stress of silicon wafers. The two bottom clamps were placed 2mm apart. The top clamp move at a constant rate of 100μm/min. whilst the applied load is simultaneously measured. Figure IV-b shows the load-displacement measurements for three silicon wafers. Using the equation IV-1, this experimental results indicated that the breaking stress of silicon wafer of 260MPa.

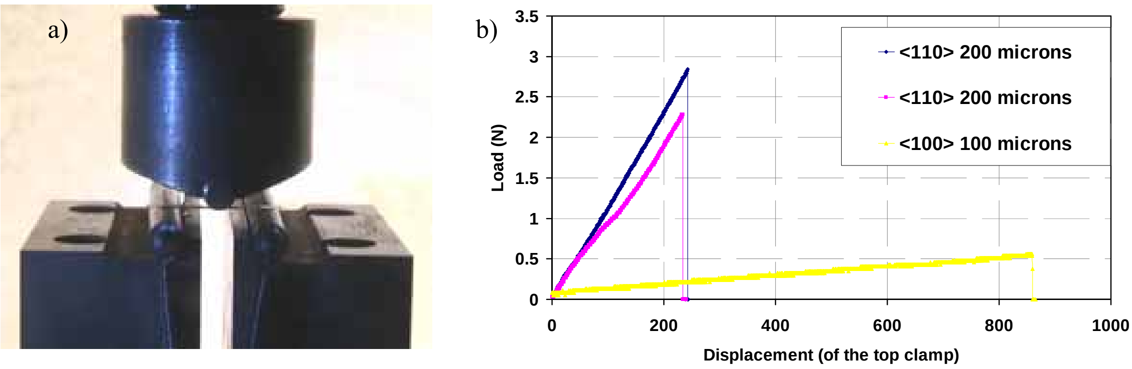

Figure IV-2: b) Picture of the three point bending set-up to measure the breaking stress of silicon wafers. The two botton clamps are placed 2mm apart. The top clamp moves at a constant rate of 100μm/min. whilst the applied load is simultaniously meassured. c) Load-Displacement measurements for three silicon wafers.

Reference:

1. S. Schoenfelder et al., Investigations of the influence of dicing techniques on the strength properties of thin silicon, Microelectronics Reliability, 47, pp 168–178, 2007.

APPENDIX V

LIST OF PUBLICATIONS

1. **Rodriguez-Sanmartin D**, Zhang D, Button T, Meggs C, Atkins C, Doel P, Brooks D, Feldman C, Willingale R, Michette A, Pfauntsch S, Sahraei S, Shand M, James A, Dunare C, Stevenson JT, Parkes W, Smith A. *Development of spider micro-structured optical arrays for X-ray optics*, Paper 7803-5, *"Adaptive X-ray optics conference"*, Proc SPIE, San Diego, 2010.
2. **Rodriguez-Sanmartin D,** Zhang D, Button T, Meggs C, Atkins C, Doel P, Brooks D, Feldman C, Willingale R, Michette A, Pfauntsch S, Sahraei S, Shand M, James A, Dunare C, Stevenson JT, Parkes W, Smith A. *Development of net-shape piezoelectric actuators for large X-ray optics*, Paper 7803-20, *"Adaptive X-ray Optics Conference"*, Proc. SPIE, San Diego, 2010.
3. Feldman C, Willingale R, Doel P, Brooks D, Thompson S, **Rodriguez-Sanmartin D**, Button T, James A, Theobald C, Smith A, *The performance of thin shell adaptive optics for high angular resolution X-ray telescopes*, Paper 7803-21, *"Adaptive X-ray Optics Conference"*, Proc. SPIE, San Diego, 2010.
4. Willingale R, Feldman C, Michette A, Button T, Dunare C, Folkard M, Hart D, McFaul C, Morrison G, Parkes W, Pfauntsch S, Powell A, **Rodriguez Sanmartin D**, Sahraei S, Stevenson T, Vojnovic B, Zhang D, *Active micro-structured optical arrays of grazing incidence reflectors , J. X-ray Optics Instruments, 2009*
5. Zhang D, **Rodriguez-Sanmartin D**, Button TW, Atkins C, Brooks D, Doel AP, Dunare C, Feldman C, James A, Michette AG, Parkes W, Pfauntsch SJ, Sahraei S, Stevenson T, Wang H, Willingale R, *Development of piezoelectric actuators for active X-ray optics, Journal of Electroceramics,* DOI 101007/s10832-009-9566-y, 2009
6. **Rodriguez-Sanmartin, D**, Dou Zhang, Tim Button, Carolyn Atkins, Peter Doel, Hongchang Wang, David Brooks, Charlotte Feldman, Richard Willingale, Alan Michette, Slawka Pfauntsch, Shahin Sahraei, Matthew Shand, Ady James, Camelia Dunare, Tom Stevenson, William Parkes and Andy Smith, *Progress on the development of active micro-structured optical arrays for x-ray optics, "Advances in X-Ray/EUV Optics and Components IV"*. Proc. SPIE, 2009.
7. Zhang D, **Rodriguez Sanmartin D**, Button T, Meggs C, Atkins C, Doel P, Brooks D, Feldman C, Willingale R, Michette A, Pfauntsch S, Sahraei S, James A, Dunare C, Stevenson T, Parkes W, Smith A, Wang H 2009. *The fabrication and characterisation of piezoelectric actuators for active X-ray*

optics, "Advances in X-Ray/EUV Optics and Components IV", Proc SPIE, San Diego, 2009.

8. Feldman C, Willingale R, Atkins C, Wang H, Doel P, Brooks D, Thompson S, Button T, Zhang D, **Rodriguez-Sanmartin D**, James A, Theobald C, Smith A, *First results from the testing of the thin shell adaptive optic prototype for high angular resolution X-ray telescopes*, in *"EUV and X-Ray Optics: Synergy between Laboratory and Space"*, Proc SPIE 7437 74371G, 2009.
9. Atkins C, Doel P, Wang H, Brooks D, Thompson S, Feldman C, Willingale R, Button T Zhang D, **Rodriguez-Sanmartin D**, James A, Theobald C, Smith, *Advances in active X-ray telescope technologies, , in "EUV and X-Ray Optics: Synergy between Laboratory and Space",* Proc SPIE, San Diego, 2009.
10. Michette AG, Pfauntsch SJ, Sahraei S, Shand M, Morrison GR, Hart D, Vojnovic B, Stevenson T, Parkes W, Dunare C, Willingale R, Feldman C, Button T, Zhang D, **Rodriguez-Sanmartin D**, Wang H 2009 Smart x-ray optics J Phys: Conf Series 186 012067
11. Michette AG, Pfauntsch SJ, Sahraei S, Shand M, Morrison GR, Hart D, Vojnovic B, Stevenson T, Parkes W, Dunare C, Willingale R, Feldman CH, Button TW, Zhang D, **Rodriguez-Sanmartin D**, Wang H, Smith, AD, *Active microstructured X-ray optical arrays*, Proc SPIE 7360 736007, 2009.
12. Atkins C, Wang H, Doel P, Brooks,D, Thompson S, Feldman C, Willingale R, Button T, Rodriguez Sanmartin D, Zhang D, James A, Theobald C, Willis G, Smith A 2009 *Active X-ray optics for the next generation of X-ray telescopes* Proc SPIE 7360 736008
13. Dunare C, Parkes W, Stevenson T, Michette A, Pfauntsch S, Sahraei S, Shand M, Zhang D, **Rodriguez-Sanmartin D**, Button T, Feldman C, Willingale R, Doel P, Wang H, James A, *Microstructured optical arrays for smart X-ray optics,* Proc SPIE, 7360 736015, 2009.
14. Atkins C, Wang H, Doel P, Brooks D, Thompson S, Feldman C, Willingale R, Button T, **Rodriguez Sanmartin D**, Zhang D, James A, Theobald C, *Future high resolution X-ray telescope technologies: prototype fabrication methods and finite element analysis,* Proc SPIE 7011 70110X-1, 2008.
15. Feldman C, Willingale R, Atkins C, Wang H, Doel P, Brooks D, Thompson S, Button T, Zhang D, **Rodriguez Sanmartin D**, James A, Theobold C 2008 *Development of thin shell adaptive optics for high angular resolution X-ray telescopes,* Proc SPIE 7011 70110Y-1, 2008.
16. Michette AG, Button T, Dunare C, Feldman C, Folkard M, Hart D, McFaul C, Morrison GR, Parkes W, Pfauntsch SJ, Powell AK, **Rodriguez-Sanmartin D**, Sahraei S, Stevenson T, Vojnovic B, Willingale R, Zhang D, *Active micro-structured arrays for X-ray optics* Proc SPIE 6705 670502, 2007.

APPENDIX V

SELECTED PUBLICATIONS

1. **Rodriguez-Sanmartin D**, Zhang D, Button T, Meggs C, Atkins C, Doel P, Brooks D, Feldman C, Willingale R, Michette A, Pfauntsch S, Sahraei S, Shand M, James A, Dunare C, Stevenson JT, Parkes W, Smith A. *Development of spider micro-structured optical arrays for X-ray optics*, Paper 7803-5, *"Adaptive X-ray optics conference"*, Proc SPIE, San Diego, 2010.
2. **Rodriguez-Sanmartin D**, Zhang D, Button T, Meggs C, Atkins C, Doel P, Brooks D, Feldman C, Willingale R, Michette A, Pfauntsch S, Sahraei S, Shand M, James A, Dunare C, Stevenson JT, Parkes W, Smith A. *Development of net-shape piezoelectric actuators for large X-ray optics*, Paper 7803-20, *"Adaptive X-ray Optics Conference"*, Proc. SPIE, San Diego, 2010.
3. **Rodriguez-Sanmartin, D**, Dou Zhang, Tim Button, Carolyn Atkins, Peter Doel, Hongchang Wang, David Brooks, Charlotte Feldman, Richard Willingale, Alan Michette, Slawka Pfauntsch, Shahin Sahraei, Matthew Shand, Ady James, Camelia Dunare, Tom Stevenson, William Parkes and Andy Smith, *Progress on the development of active micro-structured optical arrays for x-ray optics, "Advances in X-Ray/EUV Optics and Components IV"*. Proc. SPIE, 2009.
4. Zhang D, **Rodriguez-Sanmartin D**, Button TW, Atkins C, Brooks D, Doel AP, Dunare C, Feldman C, James A, Michette AG, Parkes W, Pfauntsch SJ, Sahraei S, Stevenson T, Wang H, Willingale R, *Development of piezoelectric actuators for active X-ray optics, Journal of Electroceramics,* DOI 101007/s10832-009-9566-y, 2009.

Development of spider micro-structured optical arrays for X-ray optics

Daniel Rodriguez Sanmartin,*[a] Dou Zhang,[a] Tim Button,[a], Carl Meggs,[a] Carolyn Atkins,[b] Peter Doel,[b] David Brooks,[b] Charlotte Feldman,[c] Richard Willingale,[c] Alan Michette,[d] Slawka Pfauntsch,[d] Shahin Sahraei,[d] Matthew Shand,[d] Ady James,[e] Graham Willis,[e] Camelia Dunare,[f] Tom Stevenson,[f] William Parkes,[f] and Andy Smith[g]
[a]University of Birmingham, School of Metallurgy and Materials,
Edgbaston, Birmingham, B15 2TT, U.K.
[b]University College London, Department of Physics and Astronomy,
Gower Street, London WC1E 6BT, U.K.
[c]University of Leicester, Department of Physics and Astronomy, Leicester, LE1 7RH, U.K.
[d]King's College London, Department of Physics, Strand, London WC2R 2LS, U.K.
[e]Mullard Space Science Laboratory, University College London,
Holmbury St. Mary, Dorking, Surrey, RH5 6NT, U.K.
[f]Scottish Microelectronics Centre, University of Edinburgh,
The King's Buildings, West Mains Road, Edinburgh EH9 3JF, U.K.
[g]STFC - Daresbury Laboratory, Keckwick Lane, Warrington, Cheshire, WA4 4AD, U.K.

ABSTRACT

The Smart X-Ray Optics (SXO) project comprises a U.K.-based consortium developing active/adaptive micro-structured optical arrays (MOAs). These devices are designed to focus X-rays using grazing incidence reflection through consecutive aligned arrays of microscopic channels etched in silicon. Adaptability is achieved using a combination of piezoelectric actuators, which bend the edges of the silicon chip, and a spider structure, which forms a series of levers connecting the edges of the chip with the active area at the centre, effectively amplifying the bend radius. Test spider structures, have been bent to a radius of curvature smaller than 5 cm, indicating that in complete devices a suitable focal length using a tandem pair configuration could be achieved.

Finite Element Analysis (FEA) modelling has been carried out for the optimization of the spider MOA device design. Prototype devices have been manufactured using a Viscous Plastic Processing technique for the PZT piezoelectric actuators, and a single wet etch step using {111} planes in a (110) silicon wafer for both the silicon channels and the spider structure. A surface roughness of 1.2 nm was achieved on the silicon channel walls.

Characterisation techniques have been developed in order to evaluate the device performance in terms of the bending of the MOA channels produced by the actuators. This paper evaluates the progress to date on the development of spider MOA's comparing FEA modelling with the results obtained for prototype structures.

Keywords: Smart X-ray Optics, Micro-structured optical arrays, Piezoelectric actuators, PZT, Finite Element Analysis.

1 INTRODUCTION

The concept of micro-structured optical arrays (MOAs) was discussed at a SPIE meeting in 2001(3) and at the international X-ray Microscopy conference in Grenoble in 2002;(4) some progress followed(5, 6) but it was limited by lack of funding until the UK Smart X-Ray Optics (SXO)(7) consortium received funds initially for a pilot study (in 2004) and then for a full programme of research, starting in 2006, under the Research Council UK's Basic Technology scheme.(8) Work in different aspects of the project has been carried out since.(1, 2, 9-11)

---

*dxr493@bham.ac.uk; phone: +44 121 414 3443; fax: +44 121 414 3441/7639; http://www.irc.bham.ac.uk/powder/fmg/.

The MOA concept is largely based on polycapillary(12) and microchannel plate(13) optics, in which X-rays are guided by multiple reflections along a large number of small channels. The main differences in MOAs are that the layout of the channels is more flexible and that there are single reflections in successive arrays which reduce aberrations as the Abbe sine condition is approximately satisfied. This is shown schematically at the left of figure 1, where X-rays from a point source (at the bottom of the figure) are brought to a (quasi-) point focus at the top by two reflections. A central stop in the first array prevents unreflected X-rays from reaching the focus. In practice many more channels would be used. In the case shown the second reflection is from a bent array and, by varying the radius of curvature the focal length can be changed.

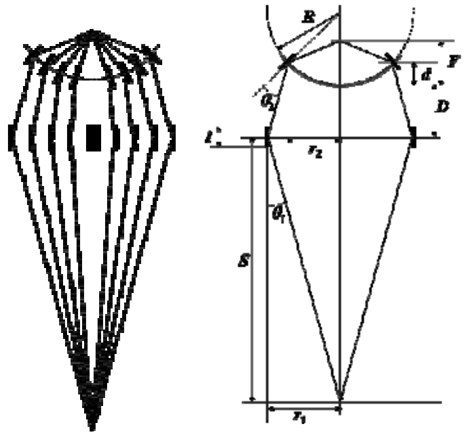

Figure 1. Left: schematic of a two-reflection MOA. Right: definition of the geometry of a two-reflection MOA.(2)

As previously reported,(2) a tandem pair MOA configuration with a 5cm radius of curvature (ROC) in the second array would provide a demagnification of a factor of three for a microfocus X-ray source. In addition, a surface roughness below 2nm would provide two orders of magnitude increase in focused flux compared to a zone plate of similar focal length. Such an optic would enable, as an exemplary application, the study of radiation induced cancers.

From the manufacturing perspective, dry etching, which is not crystal plane dependent and therefore independent of the wafer type and orientation, and anisotropic wet etching which can only be performed on (110) silicon wafers using the {111} planes, have been pursued at the Scottish Microelectronics Centre as routes to obtain the channel walls.(1) The later provided smother walls with surface roughness of 1.2 nm, which was also in agreement with X-ray reflectivity tests of unbent MOAs carried out in Leicester and at SFTC Daresbury Laboratory.(10) Figure 2 shows SEM pictures of the wet etched silicon channels; 10μm wide channels with 20μm pitch in 100μm silicon wafers have been achieved using wet etch(1).

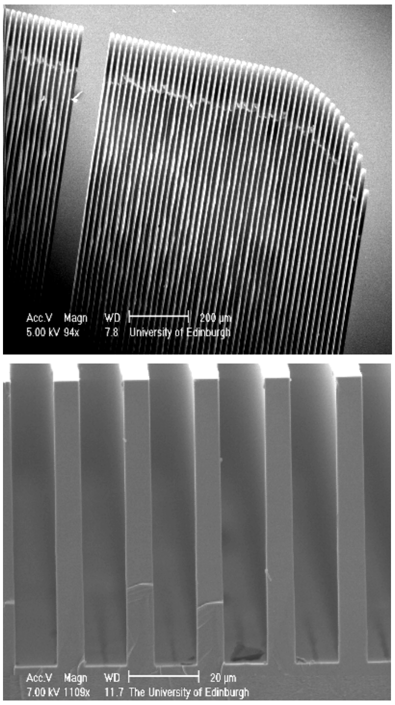

Figure 2. SEM pictures of the wet etched Silicon Channels manufactured at the University of Edinburgh.(1)

The use of piezoelectric actuators to bend MOA’s is desirable because they would provide an electrically driven and compact solution. However, in previous work it has been shown that piezoelectric actuation alone was not sufficient to bend MOA structures etched in 100μm silicon wafers to the required radius. One possible solution was to use a new arrangement, the spider design, in which the piezoelectric strips are used to actuate a series of levers, in effect amounting to a mixed piezoelectric and integrated mechanical bending solution(11).

This paper reports progress on the design, Finite Element Analysis (FEA) modelling carried out using COMSOL multiphysics software, fabrication and characterisation of the spider MOA structures. In section 2 the initial spider MOA design is described, including FEA models and characterisation of test samples. In section 3, a wet etch compatible spider design, FEA models of the device with an actuator with segmented electrodes and examples of test samples are presented. Section 4 describes a proposed manufacturing and integration procedure of an actuator arrangement with segmented electrodes onto the wet etched spider structure and a packaging design. Finally section 5 describes the conclusions and planned further investigations.

2 THE INITIAL SPIDER MOA DESIGN

2.1 Initial spider design and FEA modelling

Since the direct use of the piezoelectric actuation alone has been shown not to produce sufficient actuation, a new arrangement in which the piezoelectric strips are used to actuate a series of levers, in effect amounting to a mixed piezoelectric and integrated mechanical bending solution, has been modelled. Detailed drawings were discussed in previous work(11). The levers can be made by dry etching angled channels all the way through into the silicon chip resulting in silicon levers which move independently when the piezoelectric strips are actuated. These levers effectively play the role of amplifying the curvature of the channels at the centre of the chip.

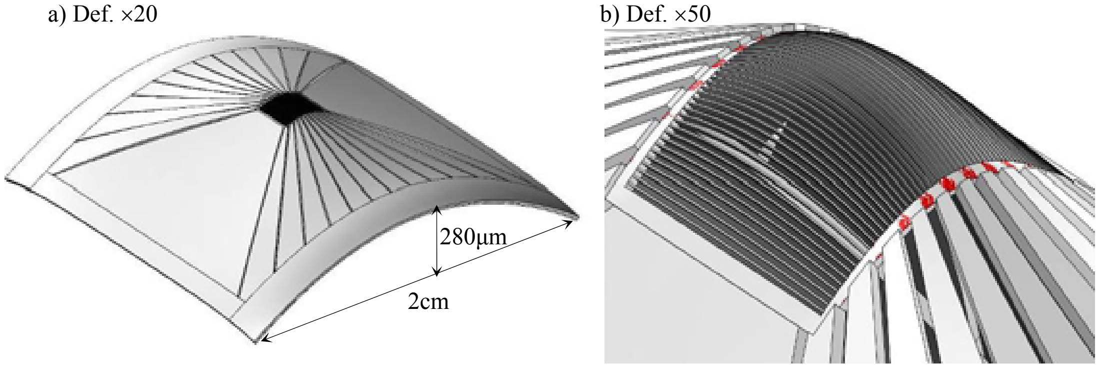
a) Def. ×20

b) Def. ×50

Figure 3. a) Modelling of the displacements (×20) on the Spider array when a voltage Vi=150Volts was applied to the piezoelectric actuators. b). Displacements (×50) on the channels. The highlighted areas are the points with highest stresses (up to 109MPa).

FEA models were set with the spider MOA pattern drawn on a 100µm thick silicon wafer. The piezoelectric coefficients chosen were those corresponding to a PZT-5H ceramic and the bonding layer between the actuator and the silicon wafer was assumed to have zero thickness. The two piezoelectric strips with dimensions L_{PZT}=2cm, W_{PZT}=2mm and a thickness T_{PZT}=75µm were used in the FEA models as it would maximise the actuation for a T_{Si}=100µm(11).
In figure 3, FEA modelling of the deformation (×20) of a 2×2cm spider array on a 100µm thick silicon wafer and an applied voltage of 150Volts to the piezoelectric actuators are shown. The z displacements at the edges of the chip are 280µm, compatible with the curvature predicted for an unimorph cantilever. Figure 3(b) shows the displacements (×50) in the channels area with the highlighted areas at the end of the levers in the beam connecting the MOA channels at the centre of the chip representing the areas with highest tensile stresses on the chip (up to 100MPa). The ROC in the centre 2mm of the chip (across the channels) was smaller than the 5cm target.

2.2 Initial spider design: Manufactured test Samples

Test spider structures were manufactured at the University of Edinburgh using a using a dry etching process(1) with the intention to demonstrate the capability of the spider design to bend the centre 2x2mm of the chip to the required radius of curvature without breaking.

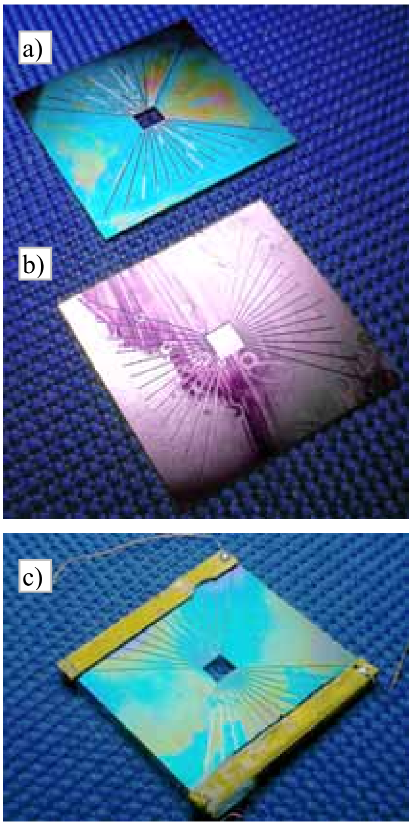

Figure 4. a) and b) Dry etched spider pattern on a 2cm×2cm×100µm Si wafers. c) 2cm×2mm×120µm PZT piezoelectric actuators mounted on one spider device.

Figure 4a shows test samples where the spider pattern has been etched all the way through the wafer and Figure 4b when the etching process was stopped about 20µm before reaching the bottom face of the silicon wafer. Figure 4c shows a picture of a test device where two PZT actuators have been mounted onto the dry etched silicon wafer.

2.3 Characterisation results

Some of the samples which were not etched all the way through the wafer were mounted on pre-curved clamps with a 25cm ROC fitted on the outer 2mm as shown in figure 5a. The flat side of the sample is effectively a mirror for which the curvature can be measured. The curvature measurements of the centre were carried out using three different methods: a) Using a Talysurf profilometer to obtain a trace along the edge of the centre 2×2mm; b) using an interferometer; and c) measuring the size of a reflected laser image shown in Figure 5d of the surface. The laser beam was deliberately defocused to illuminate the whole of the test sample surface. The three measurements were consistent indicating that the clamped sample presents a ROC of 3cm at its centre. Figures 5b and 5c show the difference in displacement using as a reference a flat surface and a 3cm ROC surface respectively. Figure 5d shows the reflective image.

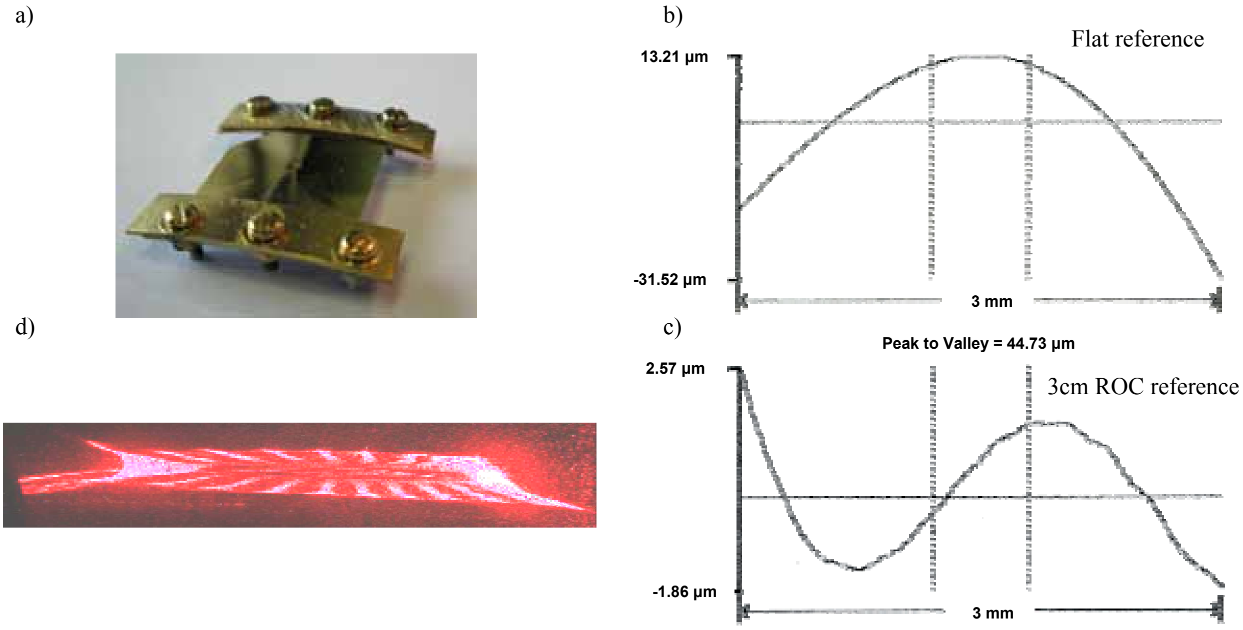

Figure 5: a) Clamped spider sample in a pre-curved jig. The sample was not dry etched all the way through so the top surface and centre area could be used as a mirror and characterised. b) Curvature profile over the beam adjacent to the centre area measured using a Talisurf profilometer with a flat reference and c) with a 3cm ROC reference. D) Reflecting image off a laser light source when the whole of the top surface is illuminated.

Reflective images where also obtained for devices mounted with 2cm×2cm×150µm piezoelectric actuators as shown in Figure 4c. The reflective images indicated that the devices could be bent from flat to an 8cm ROC at their centre which is consistent with the values predicted by the FEA models as the PZT actuators were not at their optimum thickness of 75µm for 100µm thick silicon wafers.

3 WET ETCHING COMPATIBLE SPIDER MOA'S

Characterisation results of the surface roughness of the MOA channels presented previously⁽¹⁾, together with the results shown in section 2 mean that the two main technical challenges of the of the MOA technology, i.e. smooth channel walls with a surface roughness <2nm and controllable curvature to a ROC<5cm have been achieved. The difficulty now lies on integrating both aspects of the design onto the same device.

Two spider and wet etched channels integration options were considered:

i) To use a double sided process on a silicon on insulator (SOI) wafer, where the spider pattern could be dry etched on one side of the wafer and the MOA channels wet etched on the other side with the oxide layer acting as a buffer zone. This was very challenging from the manufacturing perspective;

ii) Re-design the spider pattern so it can be wet etched in the same manufacturing step as the MOA channels. This was much more attractive from the manufacturing perspective but it had the implication of having as design rule to use the direction of the {111} silicon crystallography planes on (110) silicon wafers; i.e. parallel to the silicon channels or at a 79.53^{o} angle. The directions of both sets of planes are generally indicated by the directions of the main and secondary flat on (110) silicon wafers. Other sets of silicon planes could also be used to etch trenches on the silicon, such as the {110} planes, but their side walls would not be normal to the surface of the wafer when they are wet etched.

The second alternative was chosen, as it would produce more stable structures and would also be easier from the manufacturing perspective. It led to the design described below.

3.1 Wet etched spider: Design of the Silicon wafer

Figure 6 shows an alternative spider arrangement on a 2×2cm silicon chip. As with the previous arrangement the micro-channels would be etched on the centre 2×2mm region, piezoelectric actuators, with dimensions 2cm×2mm×75μm, would be glued onto the 2mm wide strips at the top and bottom of the silicon chip. As with the model shown in the previous section the piezoelectric coefficients of PZT-5H were used and the thickness of the bonding layer was considered to be zero. The difference is that the levers of the spider MOA structure are drawn using two sets of planes: either parallel to the silicon channels; or at an angle of 70.53^{o} which coincides with the second set of {111} planes on (110) silicon; and therefore can be wet-etched in a single step.

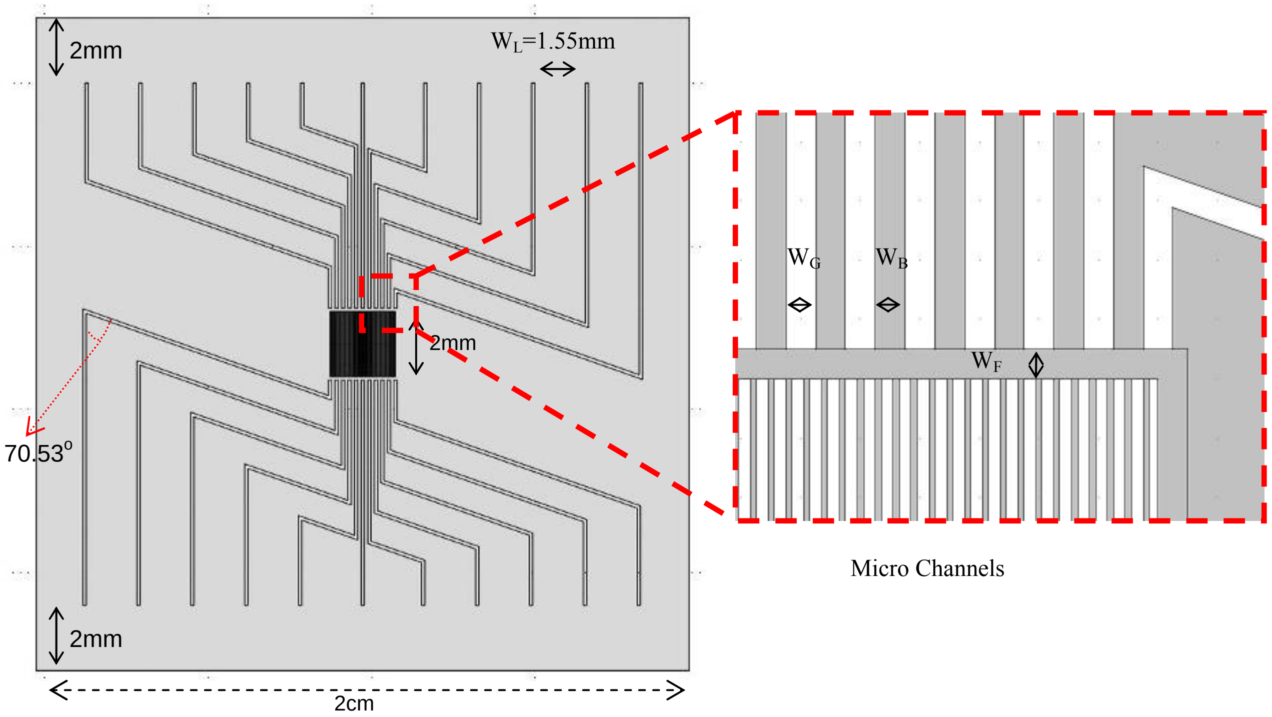

Figure 6: Wet etch compatible model definition for an spider design with number of legs N_L=20. The micro-channels are located in the centre 2×2mm region. The trenches are drawn parallel to the silicon channels and at an angle of 70.53^{o} coinciding with the {111} planes in (110) silicon. The insert depicts the levers meeting the micro-channels.

The main design parameters are: the number of legs (N_L); the widths of the levers when they meet the frame enclosing the micro-channels (W_B), the gap between them (W_G); and the width of the frame supporting the micro-channels (W_F).

Figure 6 depicts a version of the model with N_L=20 and W_G=W_B=W_F=100μm, but other combinations would also be possible.

3.2 Manufactured samples

Several spider-MOA structures have been manufactured using a wet etching process which is being developed at the University of Edinburgh. They included 6 different designs, with N_L W_B and W_G values shown in Table 1, which will allow in future comparison of FEA models with test results, and optimization of N_L, W_B, W_F. The micro channels in the centre 2×2mm are 8μm wide with 6μm gaps for all six models. Samples corresponding to all six models have been successfully manufactured. Critical issues from the manufacturing perspective were alignment, handling and control of the wet-etch rates. Further details with respect of the samples manufacturing will be presented elsewhere(14).

Model	**N_L**	**W_B**	**W_G**
M1	24	80	80
M2	20	100	100
M3	28	70	70
M4	20	80	120
M5	24	100	60
M6	20	120	80

Table 1: Design parameters of the six different spider-MOA designs which were wet etched in silicon.

3.3 Proof of concept: Preliminary results

Figure 7 shows two spider MOA samples manufactured at the University of Edinburgh for two different designs (M1 and M3). Samples with all the six models in Table 1 were successfully manufactured using the wet etching process.

Figure 8a shows one of the spider MOA's with a silicon thickness T_{Si}=120μm with two piezoelectric strips, 2cm×2mm×120μm, glued onto one of the surface of. The PZT piezoelectric strips were manufactured using a Viscous Plastic Processing process and co-sintered with platinum electrodes, this process is described in another paper at the present meeting (Ref to large optic paper). The sample was then mounted onto a holder at two pivot points at the centre of the sample so the lever action was not restricted. The top surface of the sample was then used as a mirror to estimate the ROC of the MOA once the spider structure was actuated.

Figure 8b show images obtained when the whole of top surface of the MOA device is used as a mirror and is illuminated with laser light. Different applied voltages, Vi, to the piezoelectric strips were used. For Vi=0 the image is a line, corresponding to a flat sample. As the voltage is increased the image starts to split and for Vi=60Volts a central hole appears which corresponds to the place where the channels would be in the sample. The dimensions of this centre area were used to estimate the ROC of the MOA which was ~11cm at 60 Volts. When Vi was increased to 195Volts the dimensions of the image increased, i.e. the sample was more curved, but became less symmetric. The curvature MOA calculated from the dimensions of the image varies from 6.5cm on the left to 5cm on the right.

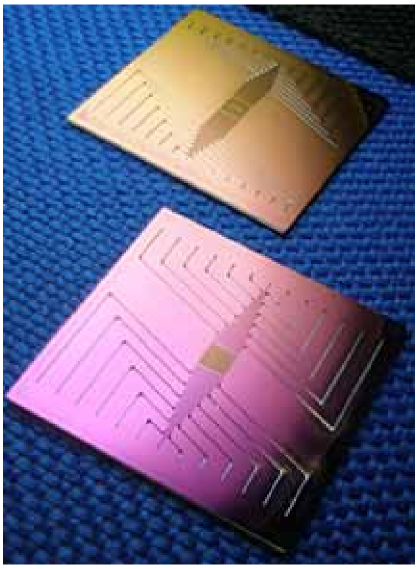

Figure 7: Spider-MOA's wet-etched in a 200μm silicon wafer. Model M3 (top) and M1 (bottom).

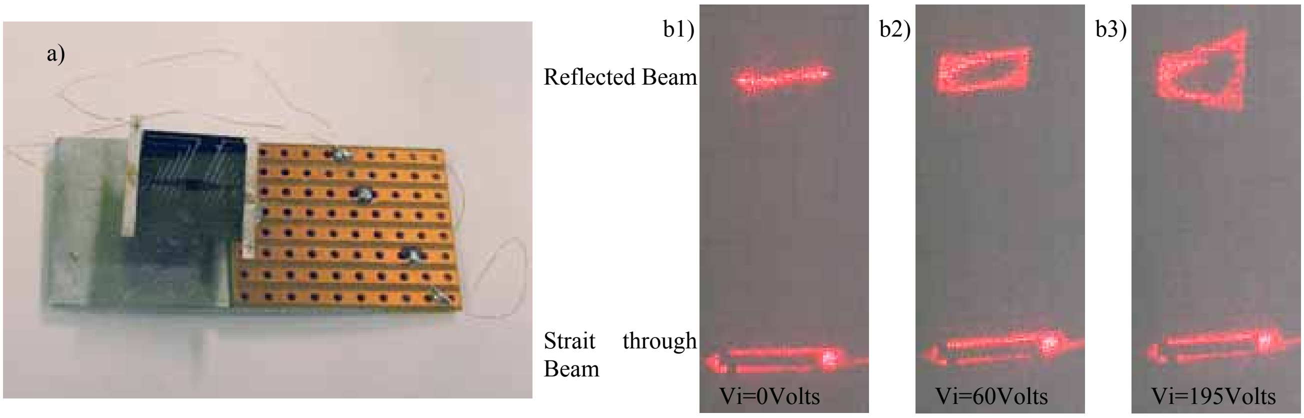

Figure 8: a) Spider MOA with two piezoelectric strips at its edges and mounted onto a holder. b) Reflective images of the top surface or the spider MOA (top) and straight through light (bottom) for 0, 60 and 195Volts applied to both piezoelectric actuators (b1, b2 and b3 respectively).

The condition of the MOA's was inspected after a few actuation cycles, and all of them remained intact without added defects on the channels themselves.

3.4 Optimization of the Actuator Layout

The actuator configuration modelled for the initial spider model, two piezoelectric strips of dimensions 2cm×2mm×75μm bonded to the outside 2cm×2mm edges, was modelled for a 20 leg version of a wet etched spider MOA in 100μm silicon. As with the initial spider design the FEA models predicted a ROC below 5cm when maximum voltages of 150Volts were applied to the piezoelectric strips for the wet etched version.

However, this simple actuator arrangement could be improved to add extra capabilities to the spider-MOA chip in two ways: i) The piezo strips could have segmented electrodes which would bring the added benefit of controlling the curvature profile on the MOA channels and possibly cancelling out slight differences in the thicknesses of the piezoelectric and bonding layers. ii) Extending the piezoelectric actuators over the spider legs to actuate more areas of the silicon. This could have the benefit of adding extra degrees of freedom on the control of each individual leg of the spider.

To investigate these effects a FEA model was assembled in where the PZT actuator layer would cover most of the silicon chip and would have trenches coincident with those on the silicon, was set up. The same assumptions as in previous models were taken: piezoelectric coefficients equivalent to those in PZT-5H; and zero thickness of the bonding layer. In the FEA model different areas of the actuator, depicted in blue in Figure 9 were separately addressed.

A 20 leg MOA spider configuration was modelled where the electrodes were arranged in four different levels: Level A, which would correspond with the piezoelectric strips in the simpler actuator design and provide the curvature and levels B, C and D. The areas not labelled in Figure 9 were not actuated in the models in order to keep where possible actuated areas of similar sizes and try to maintain symmetry on the actuator layer of the chip. The labelling

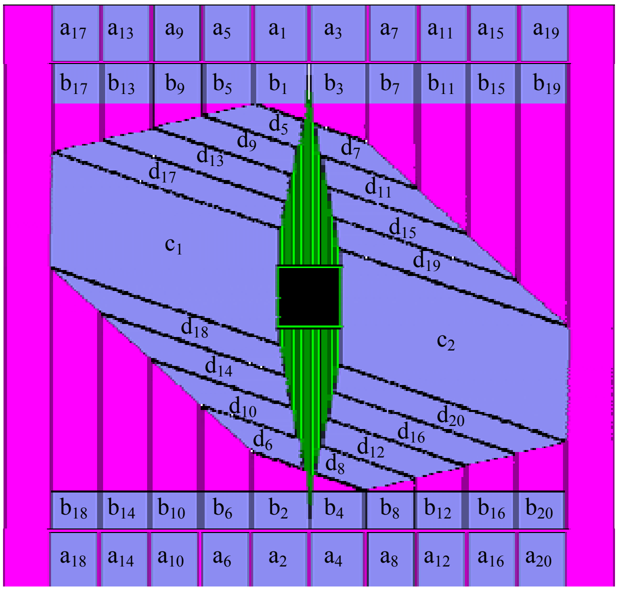

Figure 9: Modeled electrode areas for the wet-etched MOA configuration.

convention was to assign a number n=1, 2… 20 to each one of the legs with odd numbers at the top and even numbers at the bottom.

When all the electrodes in Level A are actuated to their maximum 150Volts and the electrodes in levels B, C and D are kept to 0 the silicon MOA channels are bent radius below 5cm in agreement with the initial simple model with two piezoelectric strips providing actuation. To investigate the effect on the MOA positioning of actuating several voltage combinations for the Levels B, C and D were modelled whilst voltages at the Level A where maintained at 150Volts. The FEA analysis shows that that the applied voltages on the Levels B and C could be used to control the z positioning (+/-20µm) and tip/tilt angles (+/-3mrad). The applied voltages to the Level D could be use to cancel out the unwanted bending along the y direction.

The Figure 10 depicts the FEA model of the actuated spider MOA where the deformations have been amplified by a factor of 20 and 50 for visualization purposes. The voltages in the Level D where selected to suppress the un-wanted bending along the y direction. The coloured areas in Figure 10b represent those regions of the chip with the highest stress (maximum of 220MPa bellow the maximum stress in silicon of 250MPa).

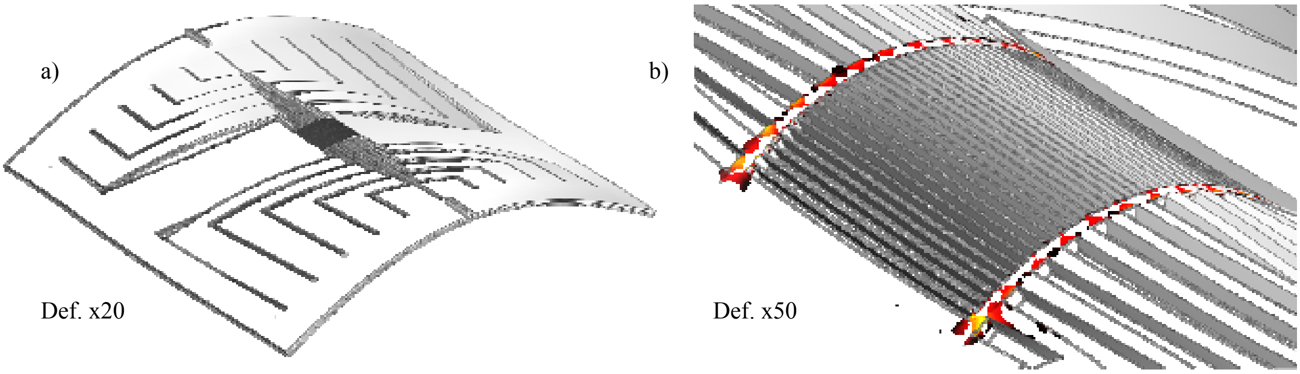

Figure 10: Results from the FEA models of a 20 leg spider MOA configuration. The deformations are multiplied by a factor of 20 and 50 respectively for visualization purposes. a) View of the whole spider MOA chip from the silicon side, the actuator would be beneath. b) Zoom image of the MOA area. The areas depicted in colour are where highest stresses in the structure are.

4 ACTUATOR ASSEMBLY AND PACKAGING CONSIDERATIONS

4.1 Segmented electrodes on the PZT actuators

The FEA analysis shown in the previous section was a useful theoretical exercise which allowed us to understand the effect of actuating different areas of the spider design. However, practical issues regarding how the actuator is going to be fabricated and assembled onto the spider MOA chip also need to be considered. For example, the number of actuated areas should be minimised to simplify both the hardware and software used for their control. Modelling using X-ray tracing techniques (Q software) was carried out at the University of Leicester to investigate the effect of the un-wanted curvature along the y direction on the MOA performance and it was found that it was the less critical of the issues in terms of reducing the width of the focused X-ray beam. Therefore the decision was taken to design the actuators without the Level D of actuation. In addition, adjacent electrodes on the Level A of actuation were joined together to reduce the number of electrodes.

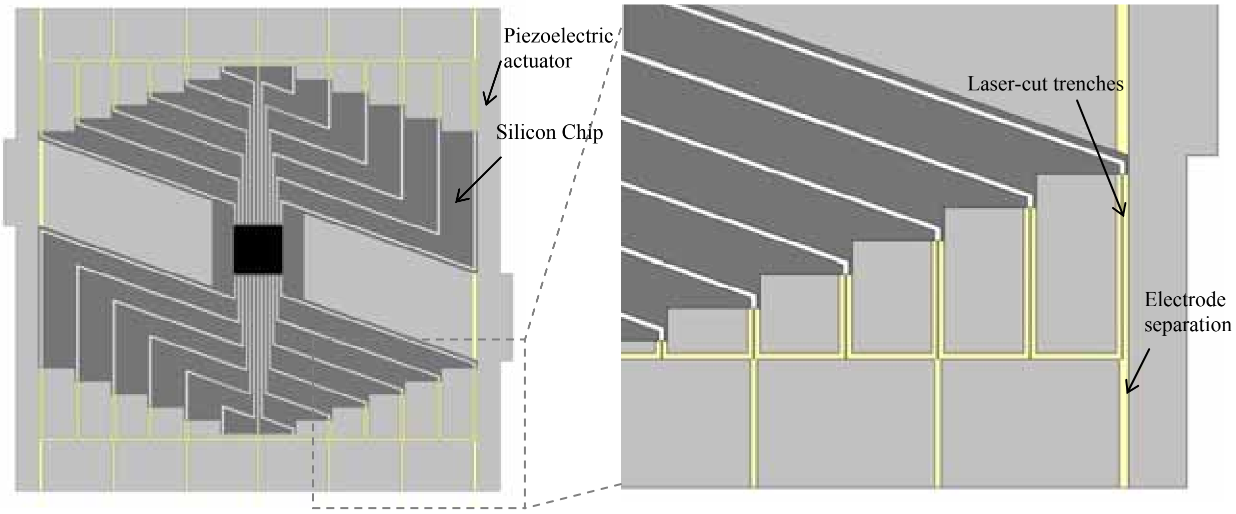

Figure 11: Proposed actuator design with 30 actuated areas for a 24 legs spider MOA configuration, 12 in the Level A, 16 in the Level B and 2 in the Level C, mounted on top of the spider MOA silicon chip.

An actuator design was proposed as shown in Figure 11, and which could be manufactured by following the steps:

i) Manufacture a 3cm×3cm×75µm PZT piezoelectric actuator with co-sintered platinum electrodes using Viscous Plastic Processing (VPP).
ii) Remove selected areas of platinum to define the segmented electrodes.
iii) Cut out the outer edges and the centre hole of the PZT actuator.
iv) Bond the PZT actuator and the spider MOA etched in silicon.
v) Cut trenches on the PZT actuator to define lever on the actuator layer. At present laser machining is being investigated as a manufacturing technique for machining the PZT actuators.

The capability for the VPP fabrication and laser machining of PZT actuators has been demonstrated for another SXO project and is described in another talk at this meeting(15).

4.2 Packaging design for the spider MOA

Figure 12 shows an exploded view of the packaging design for the spider MOA which will provide a mounting method without restricting the lever action of the design. The packaging dimensions are such that the device would fit on a 6 way cross with a 35mm diameter like the one being used at the X-ray facility at Kings College London. The packaging consist of: a chassis with two raised points where spider MOA would be mounted: a printed circuit board which will be glued to the chassis with the function of making the electrical connections to the segmented actuator of the spider MOA; and back and front covers for the device protection and filtering of the incident X-rays. During the packaging and device assembly an alignment jig to guarantee the relative alignment of the printed circuit board (PCB) and the spider MOA and the chassis whilst the glues joining different parts set.

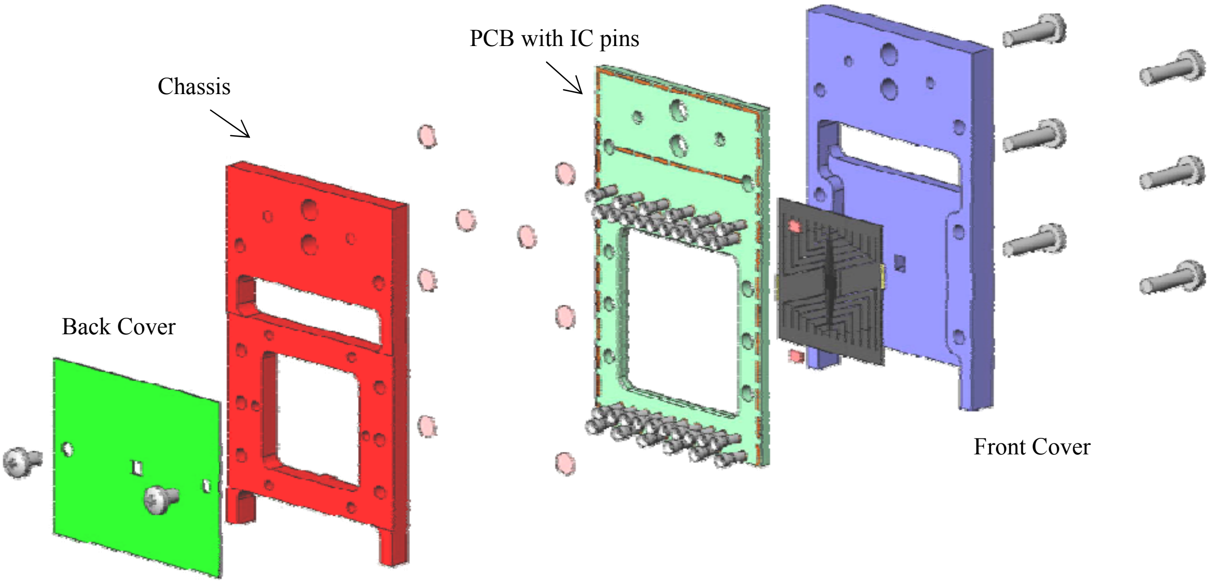

Figure 12: Exploded view of a proposed packaging structure for the Spider MOA.

5 CONCLUSIONS AND FURTHER INVESTIGATIONS

A spider array design is proposed as a possible actuation alternative in which piezoelectric and mechanical actuation are combined by etching trenches all the way through the silicon wafer, which in turn form levers to amplify the bending due to the piezoelectric effect alone. FEA analysis of the initial spider array design show that the required 5cm radius of curvature in the MOA chip can be obtained. This has been confirmed by measurements of the curvature in the centre region of test samples mounted on pre-curved clamps and using piezoelectric actuated samples. To take advantage of the 1.2nm surface roughness of the vertical walls of the MOA channels achieved at Edinburgh University using a wet etch process, a new spider arrangement has been design which uses trenches parallel to the {111} planes in (110) silicon wafers. This means that the both the MOA arrays and the lever structure can be wet etched in the same manufacturing step and integrated in the same silicon wafer. Several spider MOA structures, with six different spider designs, have been successfully manufactured.

Preliminary results of a wet etched spider device actuated with two piezoelectric strips show that the MOA can be bent to a radius of 6.5cm without failure of the MOA channels. This is consistent with FEA models of the wet etched spider MOA design and with those of the initial spider MOA model showing that a two piezo-strip actuator configuration could bend the MOA structure to a ROC below 5cm if the thickness ratios of the PZT and the Silicon are optimized.

An alternative actuator arrangement with segmented electrodes has also been modelled. The FEA results indicate that extra capabilities such as: more control over the curvature profile; +/-20µm z control; and +/-3mrad control over the tip/tilt angles could be obtained if precise micro machining of the actuator layer and assembly onto the MOA chip could be achieved.

Design drawings of an actuator with segmented electrodes have been made and an integration procedure, including packaging and mounting procedures have been conceived. Future work will concentrate on the manufacturing of an actuator arrangement with segmented electrodes, the manufacturing of the packaging structure and the device integration. Once these issues are solved the intention is to carry out X-ray testing of devices to establish their capability as an X-ray optic.

6 ACKNOWLEDGEMENTS

The Smart X-Ray Optics consortium is funded by the UK Research Councils' Basic Technology programme, grant code D04880X. The members of the consortium are University College London (including the Mullard Space Science Laboratory), King's College London (KCL), the University of Leicester, the Scottish Microelectronics Centre at the University of Edinburgh, the University of Birmingham and STFC Daresbury Ltd. Silson Ltd. is an associate member. KCL has also received support from the European Science Foundation COST Action P7 "X-Ray and Neutron Optics" and COST Action MP0601 "Short Wavelength Laboratory Sources".

REFERENCES

1. Dunare, C., et al., *Microstructured optical arrays for smart x-ray optics.* EUV and X-Ray Optics: Synergy between Laboratory and Space, 2009. **7360**(1): p. 736015.
2. Michette, A., et al. *Active microstructured arrays for x-ray optics*. in *Advances in X-Ray/EUV Optics and Components II*. 2007: SPIE.
3. Prewett, P.D. and A.G. Michette, *MOXI: A novel microfabricated zoom lens for x-ray imaging.* Advances in X-Ray Optics, 2001. **4145**: p. 180-187.
4. Michette, A.G., et al., *Novel microstructured adaptive X-ray optics.* Journal De Physique IV, 2003. **104**: p. 277-280.
5. Al Aioubi, M.Y., et al., *Design and fabrication of micro optical system for x-ray analysis of biological cells.* Opto-Ireland 2005: Optoelectronics, Photonic Devices, and Optical Networks, 2005. **5825**: p. 640-646.
6. Al Aioubi, M.Y., et al., *A novel MOEMS based adaptive optics for X-ray focusing.* Microelectronic Engineering, 2006. **83**(4-9): p. 1321-1325.
7. *http://smartxrayoptics.org/*.
8. *http://www.rcuk.ac.uk/basictech/default.htm*.
9. Zhang, D., et al., *Development of Piezoelectric Actuators for Active X-ray Optics.* Journal of Electroceramics, 2009. **Online Version: DOI 10.1007/s10832-009-9566-y**.
10. Michette, A.G., et al., *Active microstructured x-ray optical arrays.* EUV and X-Ray Optics: Synergy between Laboratory and Space, 2009. **7360**(1): p. 736007.
11. Rodriguez-Sanmartin, D., et al. *Progress on the development of active micro-structured optical arrays for x-ray optics*. in *Advances in X-Ray/EUV Optics and Components IV*. 2009: SPIE.
12. MacDonald, C.A. and W.M. Gibson, *Applications and advances in polycapillary optics.* X-Ray Spectrometry, 2003. **32**(3): p. 258-268.
13. Price, G.J., et al., *Hard X-ray imaging with microchannel plate optics.* Nuclear Instruments & Methods in Physics Research Section a-Accelerators Spectrometers Detectors and Associated Equipment, 2002. **490**(1-2): p. 290-298.
14. Dunare, C., et al. *MicroMachinning Optical Arrays (Accepted).* in *International Conference of Semiconductors*. 2010. Sinaia, Romania.
15. Rodriguez-Sanmartin, D., et al. *Development of net-shape piezoelectric actuators for large X-ray optics*. in *Adaptive X-ray Optics*. 2010. San Diego: SPIE.

Development of net-shape piezoelectric actuators for large X-ray optics

Daniel Rodriguez Sanmartin,*[a] Dou Zhang,[a] Tim Button,[a], Carl Meggs,[a] Carolyn Atkins,[b] Peter Doel,[b] David Brooks,[b] Charlotte Feldman,[c] Richard Willingale,[c] Ady James,[e] Graham Willis[e] and Andy Smith[g]
[a]University of Birmingham, School of Metallurgy and Materials,
Edgbaston, Birmingham, B15 2TT, U.K.
[b]University College London, Department of Physics and Astronomy,
Gower Street, London WC1E 6BT, U.K.
[c]University of Leicester, Department of Physics and Astronomy, Leicester, LE1 7RH, U.K.
[e]Mullard Space Science Laboratory, University College London,
Holmbury St. Mary, Dorking, Surrey, RH5 6NT, U.K.
[g]STFC - Daresbury Laboratory, Keckwick Lane, Warrington, Cheshire, WA4 4AD, U.K.

ABSTRACT
The design of current X-ray telescope systems needs to reach a compromise between the resolution and sensitivity. A new area of interest of adaptive optics is the development of actively controlled thin X-ray mirrors, where aberrations would be corrected. Their assembly on an X-ray telescope would provide an instrument with both high resolution and sensitivity.

The Smart X-Ray Optics (SXO) project comprises a U.K.-based consortium developing prototypes for the next generation of X-ray telescopes. The overall aim is to produce X-ray mirrors using thin, below 1mm, structures, comprising Ni mirror shells with bonded piezoelectric unimorph actuators, and with a target resolution of ~0.1 arcs. Such an optic would enable the design of an X-ray telescope with both a greater resolution and collective area than the best currently available by Chandra (0.5arcs) and XMM Newton (1650cm^2) respectively.

Lead zirconate titanate, PZT-based piezoelectric actuators are being developed in this programme to fit precisely the curved Ni mirror shell prototypes (100×300×0.4mm, radius of curvature 167mm). Viscous plastic processing has been chosen for the fabrication of net-shaped piezoelectric unimorph actuators 75×32×0.18mm, with radius of curvature conforming to those of the X-ray optic. Laser machining has been used for precisely controlling the actuator shape and for the definition of the multi-segment electrodes. Accurate control of the thickness, surface finish and curvature are the key factors to delivering satisfactory actuators. Results are presented concerning the fabrication and characterisation of the piezoelectric actuators, and the integration procedure on the nickel optic.

Keywords: Smart X-ray Optics, Piezoelectric actuators, X-ray telescopes, Finite Element Analysis.

1 INTRODUCTION

Two new prototype adaptive X-ray optics systems are under development in a UK consortium "Smart X-ray Optics" (SXO) with the aim of approaching the fundamental diffraction limit. One proposed technology is micro-structured optical arrays (MOAs) to produce a micro-focused X-ray source for biological applications, and which uses grazing incident reflection through consecutive aligned channels obtained using deep silicon etching. The latest developments on this technology are presented on another paper at this meeting(3). The second area of interest is actively deformable mirrors in large scale optics for the next generation of X-ray telescopes, with the aim to achieve a spatial resolution better than that currently available by Chandra (0.5") whilst having high throughput. The Nickel shells fabricated by an electroforming method are employed in this application and their production methods are described elsewhere(4-6). An X-ray reflective coating is applied on one side of the nickel shell, while a series of piezoelectric actuators are bonded on the other side of the shell to provide the active control. Detailed reports on the first prototype large optic system were presented at the SPIE meeting in 2009(6-8).

---

*dxr493@bham.ac.uk; phone: +44 121 414 3443; fax: +44 121 414 3441/7639; http://www.irc.bham.ac.uk/powder/fmg/.

Lead Zirconate Titanate (PZT) membranes with controlled surface finish, thickness and curvature have been developed for the SXO project using a viscous plastic process (VPP) technique (REF). VPP generally provides improved material properties compared to conventional dry powder pressing and slip casting due to its capability of breaking down the agglomerates even in high solids loading paste systems. Good plasticity in the green state facilitates complex shaping processes and the control of membrane thicknesses, i.e. 50-200µm in this study. The sintered density and piezoelectric properties similar to the bulk values, but the process offers the flexibility of curving the membrane to the required radius of curvature.

This paper describes the production, characterisation and the harnessing procedure of the piezoelectric actuators manufactured for the second prototype large optic systems. Results from the X-ray testing of this optics are presented by Feldman et al at this meeting(9).

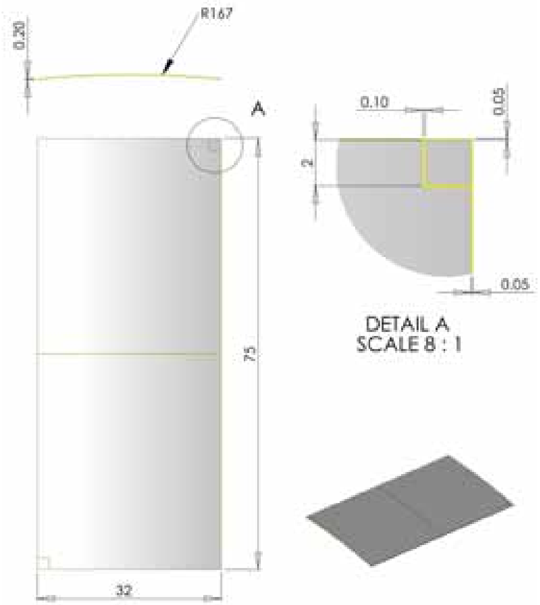

Figure 1: Drawings of the piezoelectric elements of the first prototype. All units are in mm.

2 PIEZOELECTRIC ACTUATORS DESIGN

The piezoelectric configuration of the second prototype was designed to minimise the kink effect on the reflective surface of the first X-ray optic prototype caused by the discontinuity of the piezoelectric layer bonded to the top surface. Finite element analysis (FEA) models carried out using COMSOL Multi-physics software indicated that kink effect has a dependence on the size of the gaps between piezoelectric devices and the filling material of those gaps. Therefore it was decided to minimise as much as possible those gaps, which in turn implied that a precise control over the piezoelectric dimensions and electrode configuration was required. Figure 1 shows drawings of the actuator elements with dimensions 75×32×0.2mm and 167mm ROC which matches the nickels X-ray optic. The top electrode of each element is divided in two and the ground electrode at the bottom of the piezoelectric element would be accessed using the 2x2mm square electrodes at each corner of the sample. The piezoelectric elements would not have electrodes along their 50µm edges to avoid shorting adjacent electrodes assembled in the optic. To cover the whole of the Nickel X-ray optic the elements would be staggered in a brick wall fashion the optic, using 11 full and 2 half or 10 full and 4 half elements.

3 PRODUCTION OF THE PIEZOELECTRIC ACTUATORS

3.1 Viscous plastic processing (VPP) manufacturing route for pre-curved plates

Viscous plastic processing (VPP) has been utilised for the fabrication of a wide range of net shaped ceramic structures(10). In this study TRS610C PZT powders (TRS Technologies, Inc., USA) were mixed with polyvinyl butyral (PVB), solvent and plasticisers and twin roll milled and extruded to obtain the dough. The VPP ceramic dough was shaped into membranes with controlled green thicknesses of 240µm using a calendering and laminating process. The calendered tapes were then screen printed with platinum thick film ink (Gwent Electronic Materials) to form the top and bottom (ground) electrodes and then to drying, binder removal, and sintering processes.

The sintering method used for manufacturing the samples of the first large X-ray optic prototype has been described by Zhang et al(7, 11). It consisted of

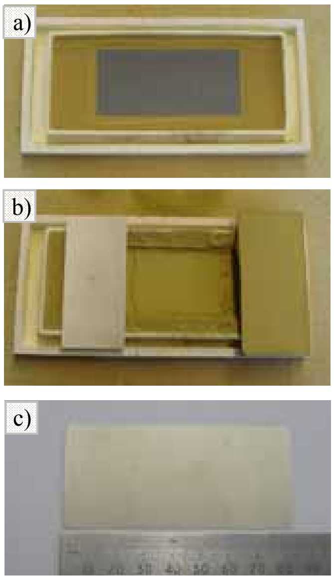

Figure 2: Sintering method to obtain large pre-curved samples.

using formers and setter plates to maintain the curvature of the samples during sintering. However, it was found that it could not be scaled to produce larger samples, which caught on the former or the setter plate during sintering, and, as the sample was shrinking, defects such as edge cracks or blister were formed.

A new sintering method was developed in which both the led stoichiometry of the PZT sample and its shape were preserved without restricting the shrinkage of the samples. This was achieved using the following steps: i) Layers of zirconia and lead oxide sand of different grain sizes were laid on a zirconia boat; ii) An indentation using a pre-formed mould of 167mm ROC was made on the sand bed; iii) The pre-curved green sample was then placed on the indentation; the sample was covered with layers of fine and coarse sand as shown in Figure 2a. This ensured a PbO-rich atmosphere and preservation of the sample curvature during sintering (1200°C for 1hr).

The bonding strength between the co-sintered platinum electrodes and the piezoelectric actuators was superior to that of electrodes applied by sputtering of Cr and Au after sintering, which was the method used for fabricating the actuators of the Large X-ray Optics prototype. The sintered piezoelectric plates were then made active using a standard poling process in an oil bath. The poling conditions used were: an applied electric field of 2.5V/µm, at 110°C for 10minutes.

3.2 Laser Machining

After the poling process the oversized piezoelectric actuators were laser machined at the Mullard Space Science Laboratory (MSSL) to obtain the dimensions described in section 2. Code with the sample coordinates was written to carry out the laser machining in two steps: i) the top platinum electrodes were removed from unwanted areas to define the two electrodes and the two ground connections. The electrodes were also removed along the perimeter of the sample to define a 50µm gap on the top electrode at the edges of the sample and to prevent the shorting the top electrodes of adjacent samples. The depth of removed material was kept at 20µm and controlled by counting the number of laser passes over the same area of the piezoelectric actuator; ii) The PZT actuators were cut to the right dimensions of length and width. The laser set up at MSSL allowed for 10µm accuracy in both tasks. Figure 3 shows SEM photographs of laser machined trenches dividing the platinum electrodes on top of the PZT layer[*].

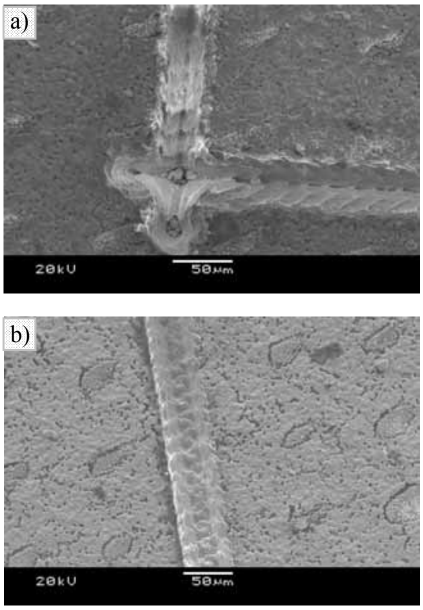

Figure 3: SEM pictures of laser machined trenches defining platinum electrodes.

3.3 Cleaning and connecting the grounds

The debris produced during the laser machining of the piezoelectric devices were cleaned using sequential cleaning in a series of solvents and an ultrasound bath. After the cleaning process the ground electrodes at the top of the sample were connected with the bottom electrodes painting the edges of the sample with thin layer of silver loaded epoxy (RS Components).

3.4 Productivity summary

From a productivity point of view a total of 20 full and 10 half were made which were used to produce the NEMO1 and NEMO2 optics with a configuration consisting of 10 full samples and 4 half's places on the corners of the optic. Some samples manufactured whist the sintering process was being improved were discarded and used instead for the calibration of the laser machining setup at MSSL and for bonding test.

---

[*] The SEM photographs of test devices shown in Figures 4 and 6 were taken with the assistance of Dr H. Hughes from the University of Birmingham.

4 CHARACTERISATION OF THE PIEZOELECTRIC ACTUATORS

The radius of curvature (ROC) of the piezoelectric devices were measured using an experimental set-up comprising the following elements: a laser probe for displacement measurement (MEL Mikroelektronik GmbH,D-85386 M5L/2), a positioning system consisting of two motorized translation stages for the X and Y axes (STANDA, models 8TM173-20-50, 8TM173-20) and a manual stage for the Z axis (STANDA, 7T173-20) which positions the laser probe above the sample. The monitoring of the laser probe and control of the motorized stages is made using a National Instruments PCI-6052E acquisition. Lab View 8.5 software to measure the ROC along the piezoelectric samples. The system was calibrated using objects of known curvature.

The radius of curvature of all the samples was measured along the length of the actuators before and after the poling procedure. It was found the ROC significantly changes during the poling, and when data from all the manufactured samples are averaged a trend emerged, the ROC of the samples increases after sintering but decreases again after poling. The averaged results are presented in Figure 4. The same data set was measured for the samples before they were poling, the results indicated that the samples decreased their ROC, on average, by 10mm after the samples were poled.

The radius of curvature measurements where used as a selection criteria for the actuators that used placed in the optics. Figure 4b show a graph summarizing all the samples where the standard deviation of the ROC for each sample is plotted against their average ROC. On the x axis plots the average ROC of each sample along its length, with most samples in the range 170-190mm. The samples from the batch 167-1 were manufactured using the initial sintering procedure and presented and smaller ROC in the 140-160mm range. The y axis represents the standard deviation of the ROC along the length of each piezoelectric actuator, with most samples with values under 7mm.

All the samples were tested using an impedance analyser (Agilent HP4294A) to ensure that they were active at the poling and laser machining processes.

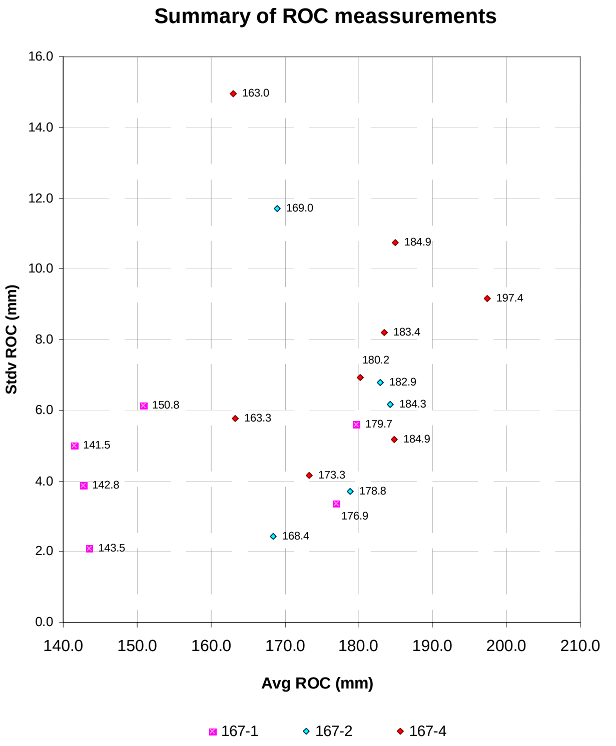

Figure 4: Average ROC and standard deviation of the ROC measured over the length of each sample after poling.

5 HARNESSING THE PIEZOELECTRIC ACTUATORS ONTO NICKEL X-RAY OPTICS

A new integration procedure of the piezoelectric nickel shell was developed. Its main objectives were to increase the control over the thickness of the glue layer, the strength of the bond and maintain the alignment between neighbour piezoelectric devices on the optic. Two full optics were assembled: NEMO1 in which the nickel shell was released from the mandrel before bonding the piezoelectric devices; and NEMO2 which was released from the mandrel after the bonding of the piezoelectric devices and the harnessing to the support structure.

To control the thickness of the glue layer a 5% volume content of glass beads with 80μm diameter was added to the EP30 glue (Master Bond Inc). The glue was applied to the optic using a doctor blade technique in which tape of defined thickness is used to define the separation between a steel blade and the nickel optic. The steel blade was then used to spread the glue leaving behind a glue layer of uniform thickness.

Initial tests were conducted to determine the weakest link of the nickel-glue-platinum electrodes-PZT structure and it was found that is was weakest at the nickel-glue interface. This was followed by another series of bonding test to investigate if a surface treatment of the nickel surface would improve the strength of the bond, and the results were positive when mechanical abrasion of the surface using sand paper, chemical etching using a 5% solution of nitric acid for 20 minutes and both surfaces treatments were added to the cleaning process. However, when the final devices were made only the cleaning of the surface was carried out as both surface treatment methods would carry the risk of damaging the reflecting surfaces of the optics. It does not appear that the bond strength has a limiting factor on the performance of the current optics, but improvements of the bond strength between the glue layer and the nickel surface will be revisited in future prototypes.

The piezoelectric devices were designed and accurately laser machined as described in sections 2 and 3.2 respectively. This enabled the devices to self align precisely with each other during assembly as long as they had a reference surface to be butted against during the bonding process. The reference surfaces were provided by two copper strips temporally bonded with double sided tape along the 2mm wide strips along the lengths of the optic. A silicone rubber mould having the same curvature profile as the optic was placed on top of the piezoelectric devices after bonding thereby adding a small even pressure along the optic and making the piezoelectric devices conform better to the curvature profile of the optic. Initially the idea was to remove the copper strips a couple of hours after bonding to avoid having them permanently glued to the optic. However, during the integration of NEMO1 this proved to be too soon as the glue had not completely set allowing glue leak onto the reflecting surface. To avoid this problem for the bonding of NEMO2, more glue trials were conducted to determine: if the copper wasters could be removed after the glue has set; and the ideal time window for the application of the EP30 after its mixing.

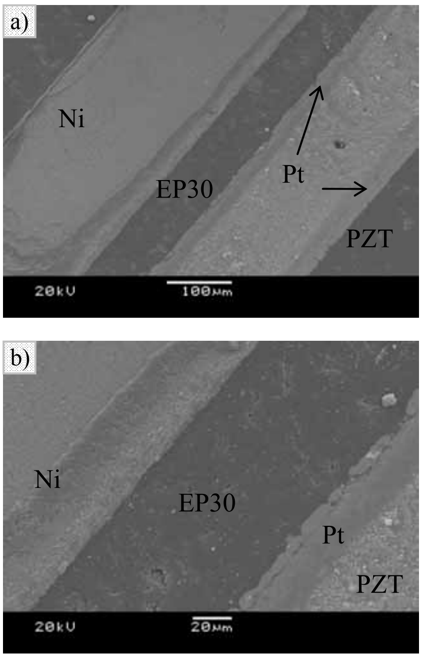

Figure 5: SEM pictures of a cross-section of a sample used for bonding test. The nickel surface was not treated prior to bonding.

The conducted glue trials and the experience gained during for the bonding of NEMO1 resulted in the bonding procedure of NEMO2 shown in Figure 6 and consisting of the following steps:

1. Thorough cleaning of the bonding surfaces: The piezoelectric devices were cleaned using sequential cleaning in a series of solvents and an ultrasound bath later left to dry on a 40^{o}C oven.
2. Double sided tape was used along the 2mm edges of the optic to temporally bond two cooper strips which would be used to align the piezoelectric devices on top of the nickel optic.
3. The edges of the optic were protected with PVC tape and to avoid glue leaks onto the reflecting surface.
4. Use 100μm PVC tapes along the two curved edges of the optic top define the glue thickness.
5. Doctor blade the low shrinkage glue, EP30, over the nickel surface as shown in Figure 6a. The glue was prepared with 80um diameter glass beads and left to set for 1h20m to achieve a suitable viscosity.
6. The piezoelectric actuators were then positioned on the optic using a vacuum tool as shown in Figures 6b and 6c. The positions of the piezoelectric devices were chosen accordingly to their curvatures to match the changing ROC on the nickel optic.
7. Once all the piezoelectric devices were micro-positioned on the optic small strips of 'magic tape' were used to join adjacent devices in order to maintain their relative alignments. The magic tape was masked over the piezoelectric boundaries so it could be removed after the glue was set even in the event of a glue leak through the gaps between piezoelectric actuators.
8. A transparent silicone rubber cast with the same curvature profile of the optic was placed on top of the actuators to keep them in position as the glue sets and to apply a small pressure over them.

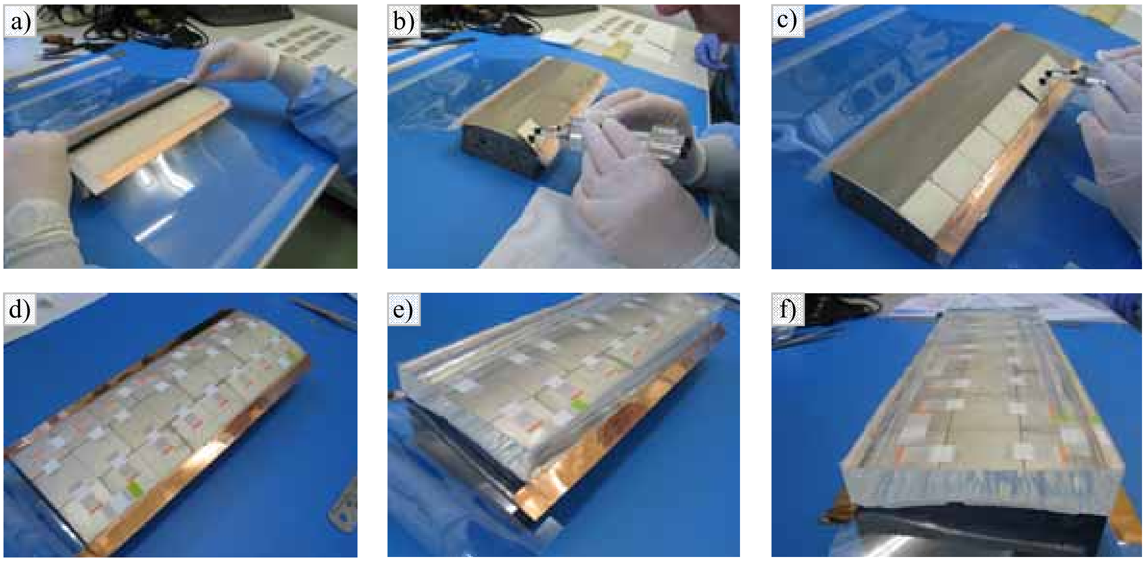

Figure 6: Bonding procedure of NEMO2. a) Applying the EP30 glue using a doctor blade technique. b) and c) Positioning the piezoelectric actuators on the optic using a vacuum peen tool. d) The piezoelectric devices were glued together using masked tape to keep their alignment. e) and f) A silicone rubber mould was used as a weight to maintain the positioning of the piezoelectric devices whilst the EP30 glue sets.

After the glue had set for 15 hours the silicon rubber, copper waster and masking tape were removed and wires soldered on the optic to provide the connections to the top and ground electrodes of the piezoelectric devices. The optic was mounted onto the support structure using two viton strips, 2mm width, which were placed in the areas uncovered by the copper wasters. The final step was to release the harnessed optic from the mandrel using thermal shock. The harnessed NEMO2 device is shown in Figure 7 below.

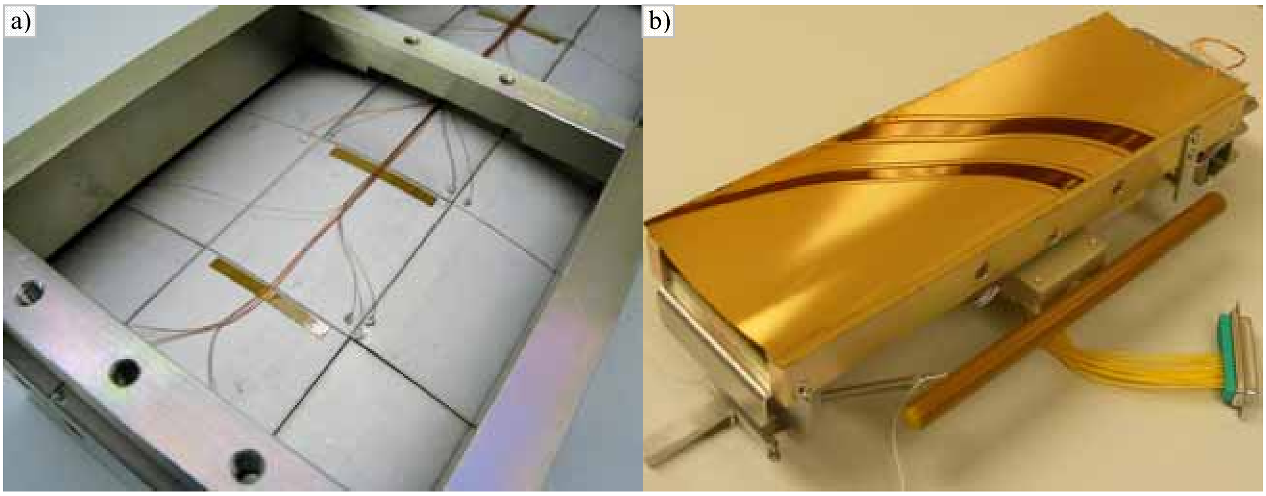

Figure 7: Harnessed NEMO2 optic. a) Actuated side of the optic. b) Reflecting side.

6 SUMMARY AND FURTHER INVESTIGATIONS

Two sets of piezoelectric actuators have been manufactured and were used to produce two second generation X-ray optics prototypes, NEMO1 and NEMO2. The novel features of the actuators with respect of the first X-ray optic prototype included: First, the use of co-sintered platinum electrodes, instead of Au and Cu sputtered electrodes, which greatly improved the bond strength between the PZT ceramic and the electrode; Secondly, a new sintering procedure was developed which allowed the sintering of piezoelectric elements more than twice the size; and finally laser machining was successfully introduced as a technique to define the electrodes within the same piezoelectric element and for the precise control of its dimensions.

From a design perspective the dimensions of the piezoelectric devices were chosen so they would cover the whole of the nickel surface, leaving very small gaps between piezoelectric devices. According to the FEA models previously presented this will reduce the kink effects that were present in the first prototype. An integration procedure of the piezoelectric devices, the nickel shell, and the support structure has been developed. The combination of the doctor blade technique to apply the glue and the use of 80µm glass beads allows the control the glue thickness. The precise laser machining of the piezoelectric devices enabled their alignment over the nickel surface.

For NEMO1 the piezoelectric devices integration and harnessing were carried out once the optic was released from the mandrel and a glue leak damaged part of the reflecting surface of the optic. For NEMO2 the nickel optic was left attached to the mandrel during integration and harnessing procedures which made both these processes easier as the mandrel served the function of temporary support structure and lessons learned from the integration of NEMO1 were applied to NEMO2. The problem with the second method is that the condition and metrology of the optical surfaces are unknown until the device is complete, and the nickel optic needs to be left over the mandrel longer, which in turn may allow contaminants to enter the interface between the nickel shell and the mandrel.

Future work would concentrate on improving the manufacturing procedure of the piezoelectric devices to improve the curvature tolerance and space proving of the technology. One particular issue to be investigated is to improve the bond strength between the glue layer and the nickel shell. X-ray testing results of NEMO1 and NEMO2, were carried out at the University of Leicester and are presented by Feldman et al at this meeting and further metrology of both optics be carried later this year.

7 ACKNOWLEDGEMENTS

The Smart X-Ray Optics consortium is funded by the UK Research Councils' Basic Technology programme, grant code D04880X. The members of the consortium are University College London (including the Mullard Space Science Laboratory), King's College London (KCL), the University of Leicester, the Scottish Microelectronics Centre at the University of Edinburgh, the University of Birmingham and STFC Daresbury Ltd. Silson Ltd. is an associate member as are Diamond Light Source Ltd. KCL has also received support from the European Science Foundation COST Action P7 "X-Ray and Neutron Optics" and COST Action MP0601 "Short Wavelength Laboratory Sources".

REFERENCES

1. Dunare, C., et al., *Microstructured optical arrays for smart x-ray optics.* EUV and X-Ray Optics: Synergy between Laboratory and Space, 2009. **7360**(1): p. 736015.
2. Michette, A., et al. *Active microstructured arrays for x-ray optics*. in *Advances in X-Ray/EUV Optics and Components II*. 2007: SPIE.
3. Rodriguez-Sanmartin, D., et al. *Development of spider micro-structured arrays for x-ray optics*. in *Adaptive X-ray Optics*. 2010. San Diego: SPIE.
4. Atkins, C., et al. *Active X-ray mirror development at UCL: preliminary results*. in *3rd International Symposium on Advanced Optical Manufacturing and Testing Technologies: Large Mirrors and Telescopes*. 2007: SPIE.
5. Atkins, C., et al., *Future high-resolution x-ray telescope technologies: prototype fabrication methods and finite element analysis (Proceedings Paper).* Proceedings of SPIE, 2008. **7011**.

6. Atkins, C., et al. *Active x-ray optics for the next generation of x-ray telescopes*. in *EUV and X-Ray Optics: Synergy between Laboratory and Space*. 2009: SPIE.
7. Zhang, D., et al. *The fabrication and characterisation of piezoelectric actuators for active X-ray optics*. in *Advances in X-ray/EUV Optics and Component IV*. 2009: SPIE.
8. Feldman, C., et al. *First results from the testing of the thin shell adaptive optic prototype for high angular resolution x-ray telescopes*. in *SPIE*. 2009. San Diego.
9. Feldman, C., et al. *The performance of thin shell adaptive optics for high angular resolution X-ray telescopes*. in *Adaptive X-ray Optics*. 2010. San Diego: SPIE.
10. Su, B., D.H. Pearce, and T.W. Button, *Routes to net shape electroceramic devices and thick films.* Journal of the European Ceramic Society, 2001. **21**(10-11): p. 2005-2009.
11. Zhang, D., et al., *Development of Piezoelectric Actuators for Active X-ray Optics.* Journal of Electroceramics, 2009. **Online Version: DOI 10.1007/s10832-009-9566-y**.

Progress on the development of active micro-structured optical arrays for X-ray optics

Daniel Rodriguez Sanmartin,*[a] Dou Zhang,[a] Tim Button,[a] Carolyn Atkins,[b] Peter Doel,[b]
Hongchang Wang,[h] David Brooks,[b] Charlotte Feldman,[c] Richard Willingale,[c] Alan Michette,[d]
Slawka Pfauntsch,[d] Shahin Sahraei,[d] Matthew Shand,[d] Ady James,[e] Camelia Dunare,[f]
Tom Stevenson,[f] William Parkes,[f] and Andy Smith[g]
[a]University of Birmingham, School of Metallurgy and Materials,
Edgbaston, Birmingham, B15 2TT, U.K.
[b]University College London, Department of Physics and Astronomy,
Gower Street, London WC1E 6BT, U.K.
[c]University of Leicester, Department of Physics and Astronomy, Leicester, LE1 7RH, U.K.
[d]King's College London, Department of Physics, Strand, London WC2R 2LS, U.K.
[e]Mullard Space Science Laboratory, University College London,
Holmbury St. Mary, Dorking, Surrey, RH5 6NT, U.K.
[f]Scottish Microelectronics Centre, University of Edinburgh,
The King's Buildings, West Mains Road, Edinburgh EH9 3JF, U.K.
[g]STFC - Daresbury Laboratory, Keckwick Lane, Warrington, Cheshire, WA4 4AD, U.K.
[h]Diamond Light Source Ltd., Harwell Science and Innovation Campus, Didcot, OX11 0DE, U.K.

ABSTRACT

The Smart X-Ray Optics (SXO) project comprises a U.K.-based consortium developing active/adaptive micro-structured optical arrays (MOAs). These devices are designed to focus X-rays using grazing incidence reflection through consecutive aligned arrays of microscopic channels etched in silicon. The silicon channels have been produced both by dry and wet etching, the latter providing smoother channel walls. Adaptability is achieved using piezoelectric actuators, which bend the device and therefore change its focal distance. We aim to achieve a 5 cm radius of curvature which can provide a suitable focal length using a tandem pair MOA configuration.

Finite Element Analysis (FEA) modelling has been carried out for the optimization of the MOA device design, consider different types of actuators (unimorph, bimorph and active fibre composites), and different Si/piezoelectric absolute and relative thicknesses. Prototype devices have been manufactured using a Viscous Plastic Processing Process for the piezoelectric actuators and dry etched silicon channels, bonded together using a low shrinkage adhesive. Characterisation techniques have been developed in order to evaluate the device performance in terms of the bending of the MOA channels produced by the actuators. This paper evaluates the progress to date on the actuation of the MOAs, comparing FEA modelling with the results obtained for different prototype structures.

Keywords: Smart X-ray Optics, Micro-structured optical arrays, Piezoelectric actuators, PZT, Finite Element Analysis.

1 INTRODUCTION

The idea of micro-structured optical arrays (MOAs) was discussed at a SPIE meeting in 2001(3) and at the international X-ray Microscopy conference in Grenoble in 2002;(4) some progress followed(5, 6) but it was limited by lack of funding until the UK Smart X-Ray Optics (SXO)(7) consortium received funds initially for a pilot study (in 2004) and then for a

---

*dxr493@bham.ac.uk; phone: +44 121 414 3443; fax: +44 121 414 3441/7639; http://www.irc.bham.ac.uk/powder/fmg/.

In addition to the institutions of the authors, the lead institution of SXO is University College of London (UCL), Department of Physics and Astronomy (A. Peter Doel). The programme is managed by the Mullard Space Science Laboratory (Ady James), part of UCL. Silson Ltd. (Peter Anastasi) is an associate member, as are Diamond Light Source Ltd (Kawal Sawhney).

full programme of research, starting in 2006, under the Research Council UK's Basic Technology scheme.(8) Work in different aspects of the project has been carried out since.(1, 2, 9, 10)

The MOA concept is largely based on polycapillary(11) and microchannel plate(12) optics, in which X-rays are guided by multiple reflections along a large number of small channels. The main differences in MOAs are that the layout of the channels is more flexible and that there are single reflections in successive arrays which reduce aberrations as the Abbe sine condition is approximately satisfied. This is shown schematically at the left of figure 1, where X-rays from a point source (at the bottom of the figure) are brought to a (quasi-) point focus at the top by two reflections. A central stop in the first array prevents unreflected X-rays from reaching the focus. In practice many more channels would be used. In the case shown the second reflection is from a bent array and, by varying the radius of curvature the focal length can be changed.

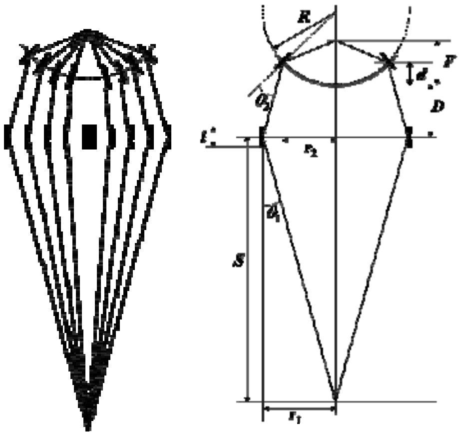

Figure 1. Left: schematic of a two-reflection MOA. Right: definition of the geometry of a two-reflection MOA.(2)

As previously reported,(2) a tandem pair MOA configuration with a 5cm radius of curvature (ROC) in the second array would provide a demagnification of a factor of three for a microfocus X-ray source. In addition, a surface roughness below 2nm would provide two orders of magnitude of focused flux compared to a zone plate of similar focal length. Such an optic would enable, as an exemplary application, the study of radiation induced cancers.

From the manufacturing perspective, dry etch, which is not crystal plane dependent and therefore independent of the wafer type and orientation, and anisotropic wet etch which can only be performed on <110> silicon wafers using the <111> planes have been pursued at the Scottish Microelectronics Centre as routes to obtain the channel walls.(1) The later provided smother walls with surface roughness of 1.2 nm, which was also in agreement with X-ray reflectivity test of unbent MOAs carried out in Leicester and at SFTC Daresbury Laboratory(10). Figure 2 shows SEM pictures of the wet etched silicon channels; 10µm wide channels with 20µm pitch in 100µm silicon wafers have been achieved using wet etch. (1)

In previous work,(9) sintered piezoelectric strips 2cm×2mm×100µm were manufactured at the University of Birmingham using a Viscous Plastic Processing (VPP) technique and bonded using epoxy to a 2cm×1cm×100µm MOA chip with the silicon channels at its centre 2mm×2mm as shown in figure 5. However bending measurements and Finite Element Analysis (FEA) results show that the radius of curvature of the channels was a factor of ten larger than the 5cm target value, which indicated that further optimization of the actuation geometry was needed.

This paper reports progress on the design, fabrication and characterisation of the actuator / MOA structure. Initial considerations for the actuation of silicon wafers are discussed in section 2, followed in section 3 by FEA modelling of different actuator arrangements for the MOAs. Experimental procedures and results for the actuation of the MOAs are discussed in section 4.

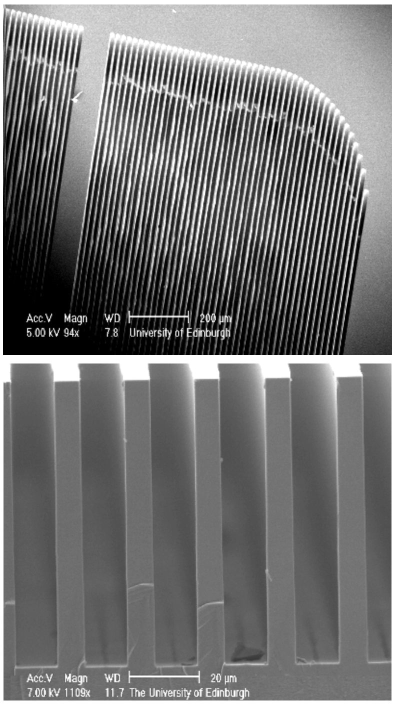

Figure 2. SEM pictures of the wet etched Silicon Channels manufactured at the University of Edinburgh.(1)

2 INITIAL COSIDERATIONS ON THE ACTUATION OF SILICON WAFERS

2.1 Advantages of piezoelectric actuation

Using Piezoelectric Actuators is desirable because it presents several advantages over other actuation methods such as mechanical bending or the use of membrane and a vacuum control system(5) to bend the channels: i) They would provide an electrically driven, compact and flat solution, with would have the advantage of freeing space in the optical system and simplifying the control mechanism. ii) As piezoelectric strips would be extended along the length of the chip, so are the stresses created, which is an advantage compared to mechanically driven three or four point bending solutions where the stresses would concentrate on the points where the forces are applied. iii) Finally, the use of segmented electrodes, thereby giving control of the curvature on the piezoelectric strips, could also make the optic adaptive, with the potential capability of reducing aberrations.

2.2 Piezoelectric manufacturing (Thick film versus VPP)

From a manufacturing point of view, the piezoelectric actuators should be produced in a way which is compatible with the manufacturing process of the silicon channels. The material most commonly used for the actuators is Lead Zirconate Titanate (PZT) because it has the highest piezoelectric coefficients. Thick film is a manufacturing route commonly used in micro electromechanical systems (MEMS), normally used as sensors, where the PZT in the green state is screen printed with the desired pattern onto a substrate such as silicon. However, thick film has its drawbacks: i) The device then needs to be sintered at high temperature (800–950°C) (13) and therefore high thermal stresses in the MOA may be produced in the silicon channels. ii) Thick films present higher porosity and therefore lower piezoelectric properties and actuation than those of bulk ceramics. iii) The thicknesses of thick films are also limited to a maximum 40μm, but thicker layers may be needed depending on the actuator arrangement. These three points indicate that an alternative to thick film needed to be sought.

Viscous Plastic Processing (VPP) is the manufacturing route chosen for manufacture the piezoelectric actuators at the University of Birmingham. VPP can produce free standing piezoelectric strips with piezoelectric properties close to those of bulk piezoelectric, and with customized thicknesses ranging from several hundreds of microns down to a minimum of about 50μm. A TRS600 powder (PZT-5H equivalent) was used. The VPP piezoelectric strips can then be bonded at room temperature to the MOA chip.(9)

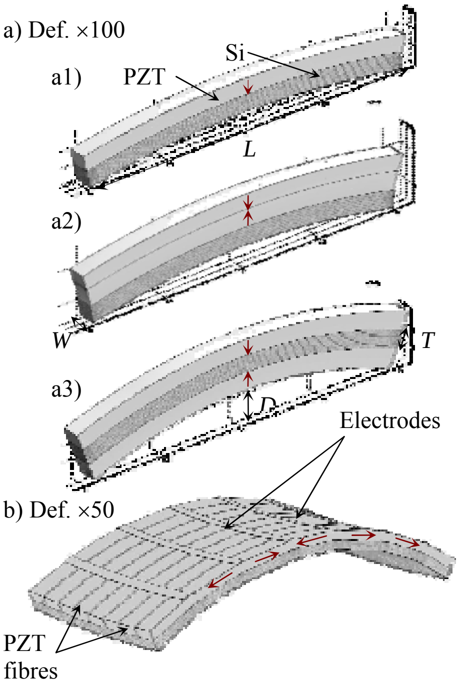

Figure 3. Deformation for different piezoelectric actuator configurations for the bending of silicon, which is depicted darker in the figures. The red arrows show the piezoelectric polarization direction. All the electric fields were set up to be 2V/μm. a) Bending of a cantilever beam of length (*L*=2mm); width (*W*=100μm) and thickness (*T*=100μm); using a unimorph (a1), a bimorph (a2) and two unimorphs. (a3). b) Bending of a silicon plate with *L*=4.5mm; *W*=1.75mm; *T*=100μm using an Active Fibre Composite. The strips at the top depict the interdigitated electrodes.

2.3 Piezoelectric configurations

Three possible configurations for the actuation of the MOA chip have been explored: unimorph, bimorph and active fibre composites (AFCs), with the unimorph single strips being the simplest of the solutions. Finite Element Analysis (FEA), using the package COMSOL Multiphysics(14) was carried out to compare different design alternatives and subsequent changes as shown in figure 3. Notice that the deformation in the figures is magnified for visualization purposes. Bimorph actuators would present only a slight (10-15%) advantage over unimorph and only if the thicknesses of the two piezoelectric layers of the bimorph are optimized, which would increase the difficulty of both manufacturing and control. Active fibre composites, which are commercially available,(15) use piezoelectric fibres in a polyimide matrix which are actuated using interdigitated electrodes, see Figure 3(b), using the d_{33} instead of the d_{31} mode ($d_{33}=–2d_{31}$), therefore providing greater and more directional actuation than unimorph actuators. However, much higher voltages with respect to a unimorph actuator would needed to exploit these advantages (200V in a 100µm in unimorph vs 1.5kV in a standard AFC). The simplest of the three configurations is the unimorph, and this concept is developed further below.

2.4 The influence of thicknesses and aspect ratios

Considering how to maximise the bending of the MOA chips, the obvious answer would be to go for thinner silicon wafers to reduce their stiffness. To take advantage of a thinner silicon wafer, thinner PZT it is also necessary as will be argued in the next paragraph. However, there are practical limits on how thin the MOA device can be. As previously reported,(2) to maintain the same amount of flux the aspect ratios (height/width) of the walls of the MOA also need to be maintained, therefore using thinner silicon wafers would make the etching of the channels more difficult which, together with handling issues, set the practical limit for thickness of the silicon wafer at 50µm minimum. From the piezoelectric perspective, free standing PZT sheets thinner than 50µm are difficult to manufacture using VPP manufacturing, and other routes such as thick film are not appropriate as discussed in section 2.2.

In the case of unimorph actuators, such as the cantilever beam shown in figure 3(a1), the relative thicknesses of the silicon and the PZT can be optimized to maximise the bending. Figure 4(a) shows 2D modelling results for the dependence of the central displacement D of a 2mm long cantilever beam for a range of silicon thicknesses for a constant electric field of 2V/µm applied to the piezoelectric actuators, which is close to the working maximum. Assuming circular bending, the displacement for the target ROC of 5cm is 10µm. As we would expect, the thinner the silicon wafer the better, but the graphs also highlight that the ratio T_{PZT}/T_{Si}~0.6 maximises the bending. The 2D modelling shown assumed a zero thickness of the bonding layer except for T_{Si}=100µm where both zero bonding and a 10µm bonding layer are shown for comparison. The bonding layer has the effect of slightly decreasing the amount of bending.

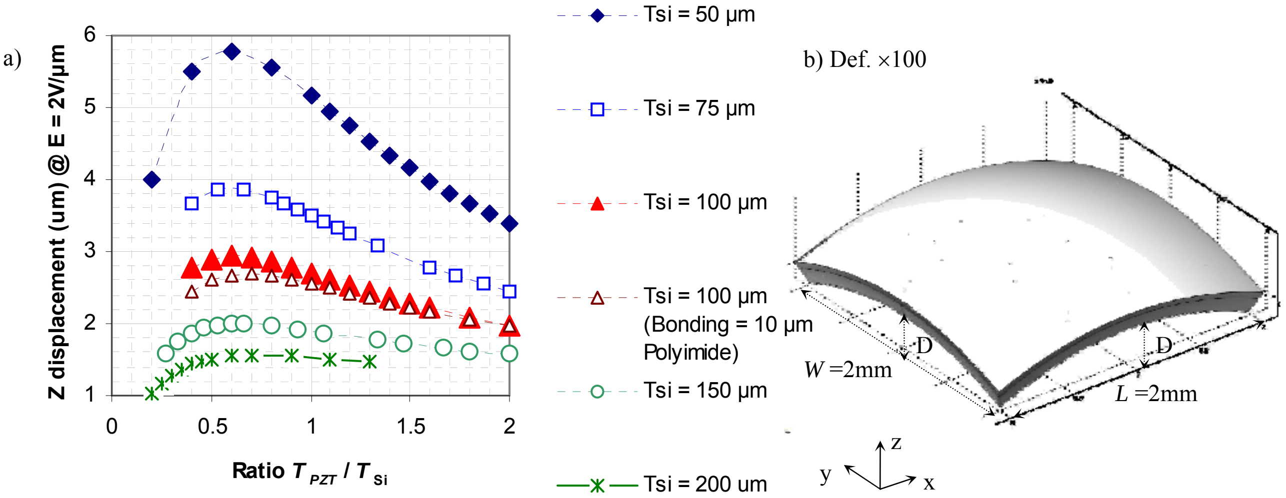

Figure 4. a) Bending displacement (D) of a silicon cantilever beam with *L*=2mm and *W*=100µm and range of silicon thicknesses (T_{Si}) as a function of the T_{PZT}/T_{Si} thicknesses ratio. The electric field on the PZT actuators are 2V/µm. b) Bending of an *L*=2mm; *W*=2mm, *T*=100µm silicon plate using a 60µm PZT unimorph. Notice that the plate bends the same amount in the x and y directions.

However, in piezoelectric material poled in the z direction, both x and y directions are equivalent. As shown in figure 4(b), a unimorph will bend the silicon wafers in both the x and y directions leading to more complicated shapes of the bent structure as described in the following sections.

3 FEA MODELLING OF DIFERENT ACTUATOR ARRANGEMENTS

3.1 The Initial Model

The actuator arrangement initially assumed in the modelling is shown in figure 5(a). The chip is made on a silicon wafer with dimensions L_{Si}=2cm, W_{Si}=1cm and a thickness T_{Si}=100µm. The silicon channels are etched in the centre 2×2mm. Two piezo strips, L_{PZT}=2cm, W_{PZT}=2mm and T_{PZT}=60µm are bonded along the length of the chip. In the modelling the bonding layer was neglected. The applied voltages for the piezoelectric actuators are 120V, which corresponds with the maximum 2V/µm electric field assumed in the previous sections. For symmetry reasons the FEA was carried out on a quarter of the chip, indicated by the red box in figure 5(a), to minimize computer overheads and allow for the use of a finer mesh. The FEA analysis indicated higher stress points, highlighted in figure 5(b), showing where the fracture would occur for a small bending radius. However, the maximum stresses of 100MPa do not exceed the breaking stress of silicon measured as 260MPa by a three-point bending test.

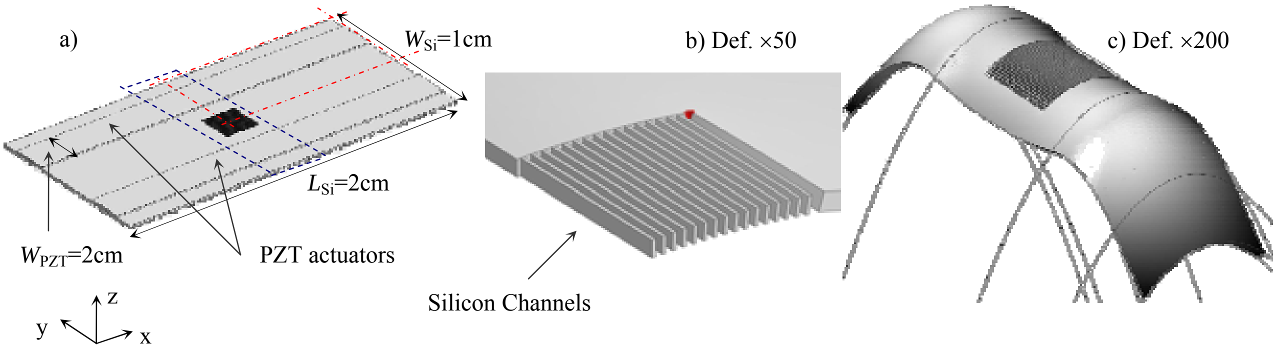

Figure 5. a) Initial model of the MOA chip. The channels are in the centre 2×2mm of the chip. The two piezo strips bonded on the chip provide the bending. b) Displacement on the channels (1.9µm) (×50), only one quarter of the MOA chip was modelled. The highlighted area shows where the biggest stresses are (up to 108MPa). c) Deformation in the centre 3mm of the chip highlighted in (a) (×200).

Figure 5(c), shows the deformation at the centre of the MOA chip highlighted in the dashed blue rectangle in figure 5(a), the deformation has been exaggerated by a factor ×200 for visualization purposes. The deformation results in a complicated shape because the piezoelectric strips, as shown in figure 4(a) bend the MOA chip in both x and y directions. The displacement in the centre 2mm in the channels is 1.9µm, compared to the 10µm necessary to achieve the 5cm ROC target. This agrees with the prediction shown in figure 4(b) for a 100µm wafer. Therefore, alternative actuation procedures needed to be addressed.

3.2 The Bridge Model

In order to maintain the handling an arrangement in which the thickness of the silicon chip itself was kept at 200µm, but the active area and the chip areas on either side of it were thinned to 50µm has been devised. The piezoelectric strips would then form bridges across the thinned area as shown in the drawing of a quarter of the chip in figure 6(a). The areas highlighted in figure 6(b) show the points of higher stresses, up to 53MPa, where the piezoelectric strips meet the edge of the bridge on the silicon. Figure 6(c) shows the deformation (×200) in the thinned silicon in the centre of the bridge, which shows less deformation in the y direction than the initial model, and bending in the centre 2mm across the channels of 2.5µm, again well below the 10µm target.

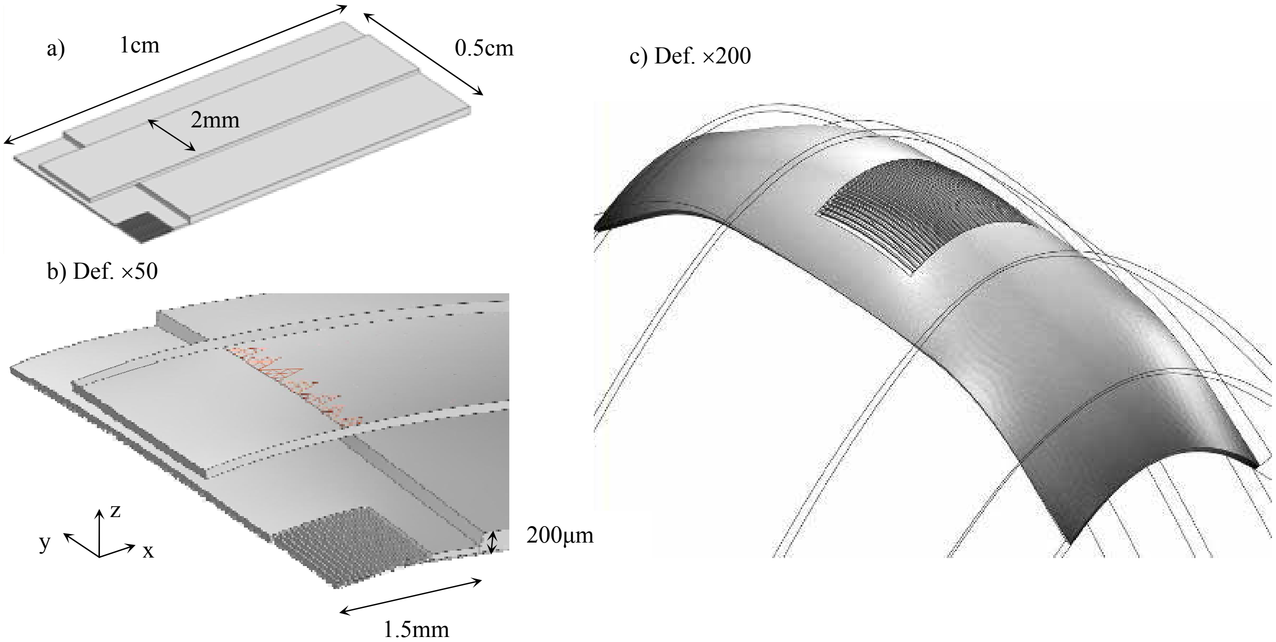

Figure 6. Bridge model. a) One quarter of the MOA chip. The piezo strip bridges the two sides of the wafer. b) Deformation (×50) on the centre of the MOA chip (2.5μm). The areas highlighted show where the highest stresses are (up to 50MPa) c) Deformation (×200) of the 3mm under the bridge.

The bending in the initial and bridge models is ultimately limited by the piezoelectric actuators d_{31}, the displacement generated in the x and y directions when a voltage is applied along the z direction for a plate poled in the z direction. Therefore a different actuator arrangement needs to be sought to obtain higher actuation in the centre arrays region of the chip.

3.3 Spider Arrays

Since the direct use of the piezoelectric actuation alone does not seem to produce sufficient actuation, a new arrangement in which the piezoelectric strips are used to actuate a series of levers, in effect amounting to a mixed piezoelectric and integrated mechanical bending solution, has been modelled. Drawings of this arrangement are shown in figures 7(a) and 7(b). Note that the chip size is now 2×2cm. The levers are made by etching angled channels all the way through into the silicon chip resulting in silicon levers which move independently when the piezoelectric strips are actuated. These levers effectively play the role of amplifying the curvature of the channels at the centre of the chip and make, contrary to the initial and bridge model, the whole length of the actuators relevant to the bending of the MOA arrays. The two PZT piezoelectric strips have the dimensions L_{PZT}=2cm, W_{PZT}=2mm and T_{PZT}=75μm. The thickness of the PZT strips was chosen as 75μm, because as shown in section 2.4, this is within the range of thicknesses which maximizes the actuation for a 100μm silicon wafer.

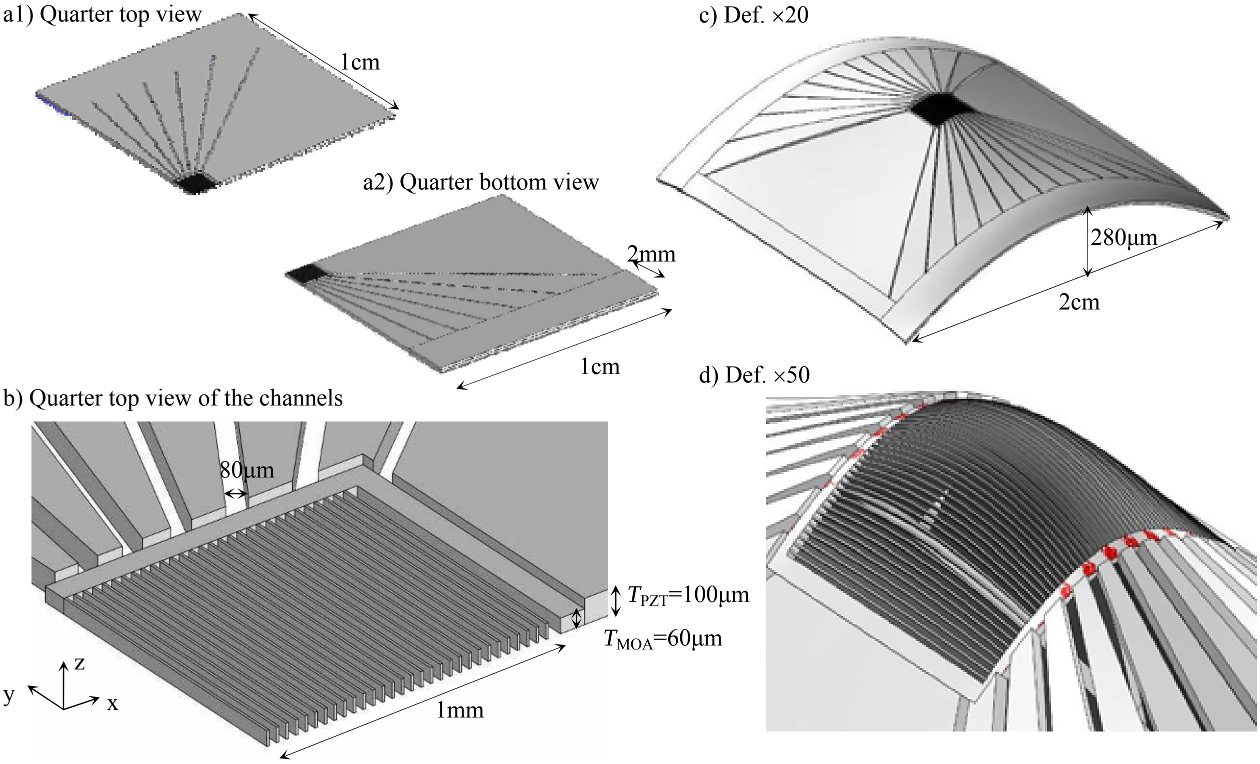

Figure 7. Drawings and FEA modelling of a Spider array. (a1) and (a2) show a top and bottom views of the drawings of quarters of the 2×2cm MOA chip. (a2) shows the position of the piezoelectric strips. c) Quarter view of the MOA channels at the centre of the chip. c) Modelling of the displacements (×20) on the Spider array. d). Displacements (×50) on the channels. The highlighted areas are the points with highest stresses (up to 109MPa).

In figure 7(c), FEA modelling of the deformation (×20) of a 2×2cm spider array on a 100µm thick silicon wafer are shown. The FEA results were also confirmed using a model of a quarter of the chip with a finer mesh. The z displacements at the edges of the chip are 280µm, compatible with the curvature predicted for the unimorph cantilever shown in figure (4a). Figure 7(d) show the displacements (×50) in the channels area with the highlighted areas representing the areas with highest tensile stresses on the chip (up to 100MPa). These high stress areas are in the beam connecting the MOA channels at the centre of the chip and the levers. The z displacement in the centre 2mm across the channels is 15µm, which translates into a ROC better than the 5cm target. The curvature in the channels is parabolic rather than circular but ray tracing(10) shows that a parabolic bend would also provide a focus.

The dimensions of the beam connecting the spider lever and the MOA channels, and the width and pitch of the levers which control the bending of the channels in the spider, are the design parameters which optimize the bending of the channels.

From the manufacturing perspective an issue which needs to be investigated is the compatibility of the manufacture of the MOA channels with the spider lever channels. One possible route is use a silicon on insulator, SOI, wafer and a double sided process to produce the levers in one side of the wafer using a dry etch process which would actuate the wet etched channels on the other side of the wafer. Another option is to manufacture both the channels and the levers in one single process using anisotropic wet etch on <110> silicon wafers. This option would require redesigning of the spiders so they can be made just using <111> planes on silicon. Both options are difficult from a technical view point and are under investigation.

A further advantage of the spider design, if the manufacturing issues are resolved, would be the use of patterned segmented electrodes on the piezoelectric strips providing an adaptive optic if the piezoelectric strips were addressed separately.

4 EXPERIMENTAL PROCEDURES AND RESULTS

4.1 Experimental set-ups

A photograph of the experimental set-up is shown in figure 8. It comprises the following elements: a laser probe for displacement measurement (MEL Mikroelektronik GmbH,D-85386 M5L/2), a positioning system consisting of two motorized translation stages for the X and Y axes (STANDA, models 8TM173-20-50, 8TM173-20) and a manual stage for the Z axis (STANDA, 7T173-20) which positions the laser probe above the sample; and a voltage Amplifier (Agilent Technologies, OEM MODEL PA05039). Monitoring of the laser probe data and control of the amplifier voltage and the motorized stages is made using a National Instruments PCI-6052E acquisition card and LabView 8.5 software.

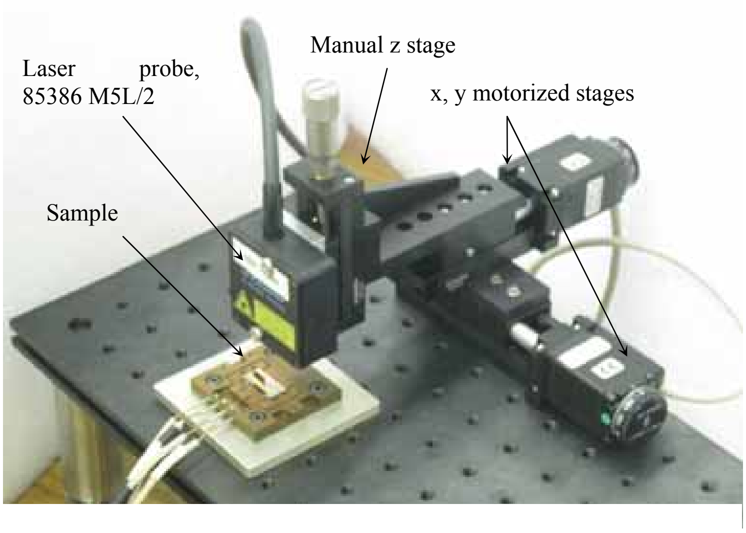

Figure 8. Photograph of one of the experimental set-ups for testing a sample consisting of a silicon MOA with two PZT strips.

LabView programs have been written to control the voltage generation and the data capture. The LabView interface allows for selection of: xy positioning of the laser probe, the voltage variation rate through the selection of changing rate of the voltage, the maximum and minimum applied voltages and the averaging factor of the displacement measurement. These features allow, for example, the determination of Displacement-Voltage hysteresis curves, or scanning the sample for a given voltage to measure a scan of z displacement for a given voltage. In both cases the data is plotted in real time, which is the main advantage of profilometer measurements. The main disadvantage is that the resolution is limited to ~2µm. The set-up has been validated by measuring samples of the initial MOA model with TalySurf and *RST-500* profilometers. (9)

4.2 Results

A MOA sample, made using the bridge design described in section 3.2, (200µm×2cm×1cm) upon which a 50µm thick bridge was etched on the centre, was tested. Two PZT piezoelectric strips, each 100µm, thick were bonded to the sample. The voltage was increased up to 200V. The results in Figure 9 show the data scanned at 200V minus the data scanned at 0V (to cancel out misalignments of the setup). The data were then fitted to a parabola to obtain the 25.3 cm ROC of the actuated bridge design.

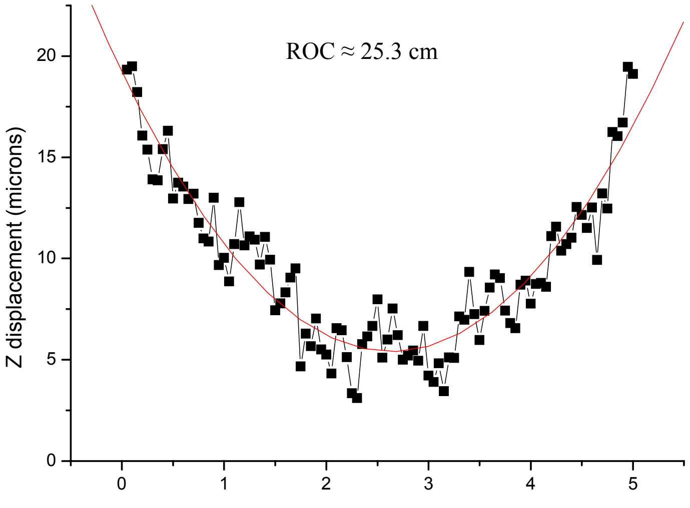

Figure 9. Displacements measurements for a bridge sample, using the set-up of figure 7.

Measurements were also carried out for the initial model actuator arrangement and are summarized in figure 10 where they are also compared to the modelling results. The vertical axis shows the FEA modelled maximum stress and the horizontal axis the minimum ROC. The horizontal dashed line shows the experimentally measured breaking stress of silicon using four point bending on 100µm silicon wafer, as a reference to avoid the failure of the samples. The vertical dashed line shows the 5cm target ROC.

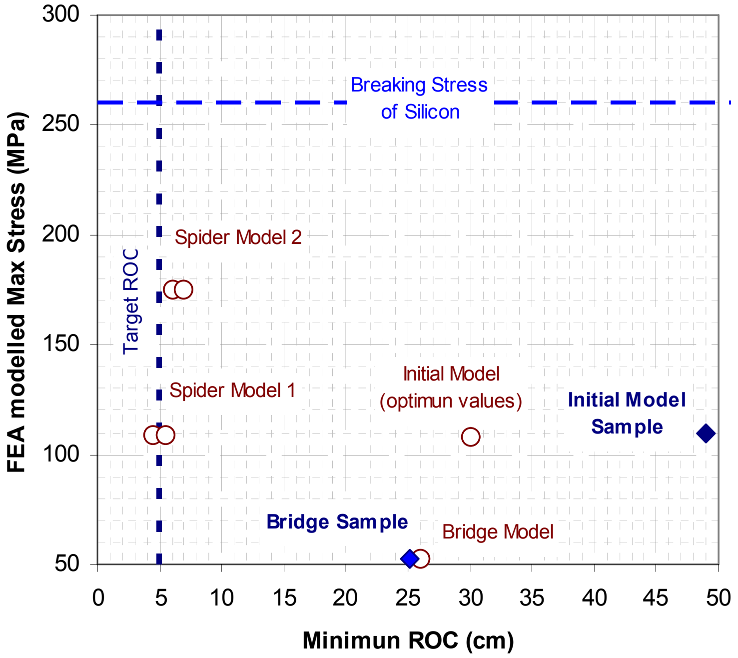

Figure 10. Summary of modelling (in empty circles) and experimental (in filled diamonds) results on a FEA modelled Max Stress Vs Channels ROC graph. The initial model area has been thinned to 60µm but the spider model 2 has not been thinned.

The graph shows good agreement between the ROC of the FEA models and the experimentally measured results for the bridge model. The discrepancy between the FEA and experimental results of the initial model is due to different parameters used in the optimum FEA model (T_{Si}=100µm; T_{PZT}= 60µm) and those of the sample (T_{Si}=200µm; T_{PZT}=100µm). The spider models 1 and 2 correspond to different variants of the design and are represented by two points because the curvature is parabolic rather than circular. In the spider model 1, the region of the channel area is 60µm thick, in contrast with the 100µm thickness of the rest of the chip. In the spider model 2, both the channel area and the sample are assumed to have the same thickness (100µm). Both versions are plotted in the diagram because the spider model 1 is more difficult to manufacture than the spider model 2. Samples with values corresponding to the spider model 2 are being manufactured and will undergo tests to verify the FEA models.

5 CONCLUSIONS AND FURTHER INVESTIGATIONS

Progress on the design, fabrication and characterisation of the actuator / MOA structure has been reported. The FEA modelling and the results from test samples show that achieving the required ROC of the channels by means of piezoelectric actuation alone is not possible, indicating an alternative actuation arrangement is needed. The Spider array design is proposed as a possible actuation alternative in which piezoelectric and mechanical actuation are combined by etching trenches all the way through the wafer, which in turn form levers. FEA analysis of the Spider arrays show that the required 5cm radius of curvature in the centre MOA chip can, in principle, be obtained.

Current work is focusing on manufacturing test samples of the spider design and solving the issues concerning the manufacturing compatibility of the spider and MOA channels. One possible route is to implement a double sided process

on a SOI wafer. The other possible option is to redesign the Spider levers to make them compatible with the anisotropic wet etch of the channels.
If the spider design materialises, it would make it possible to carry out reflectivity test on a tandem 1D MOA configuration, as other aspects of the project, mainly the fabrication of silicon channels of 10:1 aspect ratios and surface roughness under 2nm has already been achieved at Edinburgh University.

6 ACKNOWLEDGEMENTS

The Smart X-Ray Optics consortium is funded by the UK Research Councils' Basic Technology programme, grant code D04880X. The members of the consortium are University College London (including the Mullard Space Science Laboratory), King's College London (KCL), the University of Leicester, the Scottish Microelectronics Centre at the University of Edinburgh, the University of Birmingham and STFC Daresbury Ltd. Silson Ltd. is an associate member. KCL has also received support from the European Science Foundation COST Action P7 "X-Ray and Neutron Optics" and COST Action MP0601 "Short Wavelength Laboratory Sources".

REFERENCES

1. Dunare, C., et al., *Microstructured optical arrays for smart x-ray optics.* EUV and X-Ray Optics: Synergy between Laboratory and Space, 2009. Proc. SPIE **7360**(1): p. 736015.
2. Michette, A., et al. *Active microstructured arrays for x-ray optics*. in *Advances in X-Ray/EUV Optics and Components II*. 2007: Proc. SPIE. **6705:** p. 670502
3. Prewett, P.D. and A.G. Michette, *MOXI: A novel microfabricated zoom lens for x-ray imaging.* Advances in X-Ray Optics, 2001. Proc. SPIE **4145**: p. 180-187.
4. Michette, A.G., et al., *Novel microstructured adaptive X-ray optics.* Journal De Physique IV, 2003. **104**: p. 277-280.
5. Al Aioubi, M.Y., et al., *Design and fabrication of micro optical system for x-ray analysis of biological cells.* Opto-Ireland 2005: Optoelectronics, Photonic Devices, and Optical Networks, 2005. **5825**: p. 640-646.
6. Al Aioubi, M.Y., et al., *A novel MOEMS based adaptive optics for X-ray focusing.* Microelectronic Engineering, 2006. **83**(4-9): p. 1321-1325.
7. *http://smartxrayoptics.org/*.
8. *http://www.rcuk.ac.uk/basictech/default.htm*.
9. Zhang, D., et al., *Development of Piezoelectric Actuators for Active X-ray Optics.* Journal of Electroceramics, 2009. **Online Version: DOI 10.1007/s10832-009-9566-y**.
10. Michette, A.G., et al., *Active microstructured x-ray optical arrays.* EUV and X-Ray Optics: Synergy between Laboratory and Space, 2009. Proc. SPIE **7360**(1): p. 736007.
11. MacDonald, C.A. and W.M. Gibson, *Applications and advances in polycapillary optics.* X-Ray Spectrometry, 2003. **32**(3): p. 258-268.
12. Price, G.J., et al., *Hard X-ray imaging with microchannel plate optics.* Nuclear Instruments & Methods in Physics Research Section A-Accelerators Spectrometers Detectors and Associated Equipment, 2002. **490**(1-2): p. 290-298.
13. Gebhardt, S., et al., *PZT thick films for sensor and actuator applications.* Journal of the European Ceramic Society, 2007. **27**(13-15): p. 4177-4180.
14. *http://www.comsol.com/*.
15. *http://www.smart-material.com/Smart-choice.php?from=MFC*.

J Electroceram
DOI 10.1007/s10832-009-9566-y

Development of piezoelectric actuators for active X-ray optics

**Dou Zhang · Daniel Rodriguez-Sanmartin ·
Tim W. Button · Carolyn Atkins · David Brooks ·
Peter Doel · Camelia Dunare · Charlotte Feldman ·
Ady James · Alan Michette · William Parkes ·
Slawka Pfauntsch · Shahin Sahraei · Tom Stevenson ·
Hongchang Wang · Richard Willingale**

Received: 19 September 2008 / Accepted: 4 March 2009

Abstract Piezoelectric actuators are widely utilised in adaptive optics to enable mirrors having an actively controlled reflective surface for the purpose of the wavefront correction by reducing the effects of rapidly changing optical distortion. Two new prototype adaptive X-ray optical systems are under development with the aim of approaching the fundamental diffraction limit. One proposed technology is microstructured optical arrays (MOAs) involving two or four piezoelectric strips bonded to a silicon wafer to produce a micro-focused X-ray source for biological applications, and which uses grazing incidence reflection through consecutive aligned arrays of channels obtained using deep silicon etching. Another technology is large scale optics which uses a thin shell mirror bonded with 20–40 piezoelectric actuators for the next generation of X-ray telescopes with an aim to achieve a resolution greater than that currently available by Chandra (0.5UCLse Signature). PZT-based piezoelectric actuators are being developed in this programme according to the design and implementation of the proposed mirror and array structures

---

D. Zhang (✉) · D. Rodriguez-Sanmartin · T. W. Button
School of Metallurgy and Materials, University of Birmingham,
Edgbaston,
Birmingham B15 2TT, UK